UNIVERSITÀ DEGLI STUDI DI PADOVA

DIPARTIMENTO DI INGEGNERIA INDUSTRIALE
CORSO DI LAUREA MAGISTRALE IN INGEGNERIA CHIMICA E DEI PROCESSI INDUSTRIALI

Tesi di Laurea Magistrale in
Ingegneria Chimica e dei Processi Industriali

INVESTIGATION OF THE CO_2 CARBONATION REACTION: KINETIC MODELS, CFD SIMULATIONS AND THERMOGRAVIMETRIC DATA ANALYSIS

Relatore: Ing. Matteo Strumendo

Correlatore: Ing. Alberto Biasin

Laureando: Alberto Benedetti

ANNO ACCADEMICO 2013-2014

A coloro che hanno permesso di realizzare il mio sogno:

i miei genitori

Riassunto

La comunità scientifica è concorde sul fatto che gli effetti del cambiamento climatico sono evidenti e scientificamente dimostrabili. Le continue emissioni di gas serra (GHGs) hanno alterato il delicato equilibrio della troposfera e il surriscaldamento globale è uno dei principali effetti. L'*Intergovernmental Panel on Climate Change* (IPCC) riporta una dimostrazione scientifica della diretta correlazione tra l'impatto delle attività dell'uomo sull'ambiente e i cambiamenti climatici. L'aumento della temperatura media terrestre, il restringimento dei ghiacciai perenni e l'innalzamento dei mari sono tutti fenomeni documentati e dimostrati. La causa principale di questi eventi è da imputare all'emissione dei GHSs nell'atmosfera terrestre tra i quali il più rilevante è l'anidride carbonica. Le fonti di emissione sono principalmente dovute alle "grandi fonti di emissione stazionarie" che utilizzano combustibili fossili come fonte di energia termica. Tra queste sono annoverate le centrali elettriche, i cementifici, le raffinerie, le acciaierie e le industrie petrolchimiche. Tuttavia negli ultimi decenni si è assistito ad una progressiva sensibilizzazione da parte del settore industriale in materia ambientale. La comunità scientifica si quindi concentrata sulla ricerca di strategie di mitigazione.

La cattura e lo stoccaggio dell'anidride carbonica (CCS) è una di tali strategie di mitigazione e consiste in un insieme di tecnologie atte alla separazione della CO_2 da *streams* gassosi, per essere poi trasportata e stoccata in opportuni giacimenti. La strategia prevede d'integrare gli impianti con maggiori emissioni di CO_2 con queste tecnologie per ottenere benefici dal punto di vista ambientale contenendo i costi aggiuntivi richiesti per il CCS. La cattura dell'anidride carbonica con sorbenti solidi è una tecnologia che potrebbe sostituire gli impianti di assorbimento e stripping con alcanolammine, processi che, oltre ad esser costosi, presentano importanti criticità tra cui la termolabilità e corrosività delle sostanze assorbenti. La reazione di carbonatazione della CO_2 è alla base della cattura e stoccaggio con sorbenti solidi che possono essere facilmente ed economicamente reperiti in natura. Questi sorbenti sono i carbonati di calcio e magnesio ricavati, ad esempio, da rocce di origine sedimentaria come la dolomite. Segue quindi una necessaria attivazione termica chiamata attraverso una calcinazione per ottenere il sorbente attivo, l'ossido di calcio.

La carbonatazione è una reazione gas-solido non catalitica, nella quale la fase solida porosa reagisce e progressivamente viene consumata. Con l'avanzare della reazione, la struttura interna della particella evolve continuamente nel tempo.

Dal momento che il volume molare del prodotto solido (carbonato) è maggiore del volume molare del reagente (ossido), assieme alla reazione chimica si assiste al fenomeno del progressivo

restringimento dei pori fino alla loro completa chiusura, dovuta al deposito del prodotto solido all'interno del poro. In questo modo, le proprietà strutturali della fase solida reagente sono continuamente alterate a causa della reazione stessa. Tali proprietà strutturali sono la porosità e la superficie specifica. In questo modo la cinetica di reazione della carbonatazione presenta due diversi regimi: il primo è veloce ed è controllato dalla reazione stessa, il secondo invece è lento e segue una cinetica controllata dalla product layer diffusion nello strato solido che via via va accumulandosi. Inoltre, il passaggio dal regime di cinetico a quello di *product layer diffusion* avviene bruscamente, a causa della chiusura dei pori.

Questo particolare comportamento non può essere rappresentato con semplice modello cinetico volumetrico. È invece necessario un modello che tenga in considerazione l'evoluzione delle proprietà strutturali interne della particella porosa in termini di porosità e superficie specifica. Questi modelli prendono infatti il nome di "modelli strutturali". Si sono quindi analizzati i principali modelli strutturali sviluppati nel corso del XX secolo allo scopo di enfatizzarne i vantaggi e gli svantaggi. Tali modelli possono essere classificati in due categorie: i "*grain models*" e i "*pore models*". I *grain models* rappresentano la fase solida come costituita da un numero di grani, ognuno dei quali segue un modello di tipo "*shrinking core*". Tuttavia questi modelli non rappresentano in maniera opportuna l'evoluzione della struttura interna, qualora il solido poroso sia ottenuto per attivazione termica. Al contrario, si dimostrano essere utili per quei solidi ottenuti per compattazione di particelle più fini. Nel corso degli anni la letteratura scientifica si è concentrata sullo sviluppo dei *pore models*. Questi modelli definiscono due diverse superfici, la superficie del poro e quella di reazione, che rispettivamente evolvono restringendosi e allargandosi a causa della reazione stessa. Inoltre, al progredire della reazione si assiste ad un progressivo *random overlapping* delle superfici di reazione con una conseguente perdita si superficie reattiva. Conseguentemente questi modelli prendono il nome di "*random pore models*" (RPM).

È stato quindi individuato un *random pore models* che consente di rappresentare la chiusura dei pori, considerando la distribuzione iniziale dei pori ottenuta da un fitting di dati sperimentali di prove BET/BJH. Utilizzando una distribuzione lognormale continua si sono ottenuti tre parametri di fitting: il raggio medio e la varianza dei pori e la porosità della particella. In questo modo è possibile rappresentare in maniera soddisfacente l'evoluzione e la chiusura dei pori più piccoli, ritenuti responsabili della brusca transizione dal regime veloce a quello lento.

In questo lavoro, tale RPM è stato poi modificato per includere le caratteristiche specifiche della carbonatazione, che sono: la curva di equilibrio di carbonatazione e il cambio di ordine di reazione. Questo tipo di approccio fin ora non è mai stato seguito nella letteratura sulla carbonatazione della CO_2; solo il lavoro di Sun et al. [59, 58] applica il RPM alla reazione di carbonatazione, utilizzando tuttavia una distribuzione in forma discreta. Successivamente il modello è stato applicato a dati sperimentali ottenuti attraverso analisi termogravimetrica (TGA). I risultati del modello mostrano un ottimo accordo con i dati sperimentali, specie nei primi istanti di reazione. Questo RPM è quindi in grado di essere predittivo una volta nota la distribuzione iniziale dei pori in forma analitica, i parametri cinetici e il coefficiente relativo al *product layer diffusion*.

In seguito, è stato considerato l'effetto della *intra-particle diffusion* sulla cinetica di carbonatazione, la quale assume maggiore importanza all'aumentare del diametro delle particelle reagenti,

al diminuire del diametro medio dei pori e della pressione parziale di CO_2. Il RPM precedentemente modificato è stato quindi esteso al fine di accoppiare in maniera simultanea la reazione di carbonatazione con l'intra-particle diffusion. Tale accoppiamento non è mai stato sviluppato precedentemente nella letteratura sulla carbonatazione.
Le prove sperimentali utilizzate in questo lavoro sono state ottenute attraverso analisi termogravimetriche. Tuttavia, tali risultati possono essere affetti da alcune limitazioni dell'analisi termogravimetrica. Queste comprendono la diffusione esterna del reagente gassoso dal *bulk* alla superfice del reagente e l'*inter-particle diffusion*.
In questo lavoro l'*inter-particle diffusion* non è stata considerata perché può essere ridotta sperimentalmente utilizzando piccole quantità di sorbente.
È stato quindi analizzato l'effetto della diffusione esterna sulla cinetica di reazione. Allo scopo si è effettuato uno CFD al fine di determinare il campo di moto e i profili di concentrazione nei pressi e all'interno del crogiolo. Le simulazioni sono state effettuate con un codice CFD (*computational fluid dynamics*) commerciale e applicate a sistemi TGA di tipo orizzontale.
I risultati dimostrano che i profili di concentrazione alla superficie di reazione non sono constanti, bensì presentano una specifica evoluzione temporale che raggiunge in maniera asintotica la concentrazione di *bulk*. In questo modo la velocità di reazione misurata dipende dalle condizioni operative (portata di reagente gassosa) alle quali la reazione è condotta. L'effetto della diffusione esterna è tanto più accentuato quanto più cinetica di reazione è veloce.
Le simulazioni CFD mostrano che la cinetica nella TGA diventa una cinetica apparente che risulta inferiore alla cinetica intrinseca della reazione considerata.

Abstract

This work of thesis deals with the kinetics of the CO_2 carbonation reaction. Such reaction is a non-catalytic gas-solid reaction in which the solid phase is consumed as the reaction progresses. In order to represent the two stage (fast chemical kinetics controlled stage and slow product layer diffusion controlled stage) behaviour of the carbonation, the pore closure and the random pore overlapping a "structural model" is required. Among the several models analysed, a Random Pore Model (RPM) is chosen to simulate the kinetics of the carbonation. This model is modified in order to account for some specific features of the carbonation, such as the order switching of the reaction rate and the equilibrium curve. The results of these models are then compared with termogravimetric (TGA) data. Afterwards, the intra-particle diffusion is considered and the RPM is coupled with the intra-particle diffusion. Finally, a fluid-dynamic study on an horizontal TGA is presented using a computational fluid-dynamics (CFD) commercial code, in order to analyse the effects of the external mass transfer on the kinetics of the carbonation reaction.

Contents

List of Figures

List of Tables

Introduction

Human activities have changed the energy budget of the Earth by introducing in the atmosphere the greenhouse gases (GHGs) as the carbon dioxide. A significant part of these emissions are largely attributed to the industrial sector of the power generation that uses the fossil fuel combustion. The Intergovernmental Panel on Climate Change (IPCC) [62] provides a scientific demonstration of the climate change due to the GHGs emissions. During the last years the industrial and scientific sectors have focused their attention on mitigation strategies in order to reduce the atmospheric emissions of GHGs from human activities. The carbon dioxide capture and storage (CCS) is one of these strategies and has the potential of reducing the GHSs emissions. Specifically, the CO_2 separation with solid sorbents is a promising technology that can be integrated with the existing CO_2 emitting plants.

The carbon dioxide capture with solid sorbents is based on the CO_2 carbonation reaction, a fast gas-solid reaction that use cheap solid reactants.

Therefore, this works of thesis investigates the behaviour of the carbonation reaction that is characterized by two different stages: an initial fast chemical reaction controlled followed by a second slower product layer diffusion controlled stage. The goal of this work is to model the whole kinetics of the reaction as well as the pore closure observed from experimental results and the intra-particle diffusion. The carbonation is a non-catalytic gas-solid reaction in which the solid reactant is progressively consumed during the reaction. The kinetic models for such reaction must include the physical changes that occur inside the porous particle during the reaction. Thus, these models are named "structural models".
In this work of thesis, a random pore model is selected and modified in order to be applied to the CO_2 carbonation and to include the intra-particle diffusion.
Typically, carbonation conversion data are experimentally obtained through the thermogravimetric analysis (TGA). However, TGA results can be affected by mass transfer resistances, such as: the external mass transfer diffusion, the inter-particle diffusion and the intra-particle diffusion.

A second objective of this work of thesis is to analyse the influence of the external mass diffusion on the carbonation kinetics in a TGA furnace through CFD simulations.

The first chapter deals with the climate change showing the scientific and unequivocal evidences of the climate change reported by IPCC [62]. Then, the causes of change are investigated and the CCS technology is presented as one of the mitigation strategies, focusing the attention on the carbon dioxide capture with solid sorbents.

Afterwards, the carbonation reaction is considered and Chapter 2 presents the thermodynamics of the carbonation, the solid phase characterization and the TGA measurements of the carbonation conversion.
Chapter 3 deals with the "structural models" developed during the 20^{th} century. The "grain model" and the "pore model" are the two types of structural model considered. For each model an analytical development is reported as well as their advantages and drawbacks. Particularly, this chapter shows the evolution of the "structural models" over the years, up to recent years.
In Chapter 4 the pore model named "random pore model" is applied to the carbonation in order to account for the specific features of the reaction. Moreover, the chapter reports the most important literature results on the carbonation reaction of the last thirty years. The random pore model is applied to the carbonation reaction and the predictions are compared with the experimental TGA data.
The following Chapter 5 deals with the influence of the intra-particle diffusion on the carbonation. The quantities (namely, the carbonation pressure, the particle size and the pore radius size) that influences the intra-particle diffusion are analysed and discussed. Thus, a new model is presented which couples the carbonation reaction with the intra-particle diffusion.
In this work of thesis the inter-particle diffusion in the TGA experiments is assumed to be negligible considering that can its influence reduced loading a small amount of sorbent.
In Chapter 6 a fluid dynamic study of an horizontal TGA is presented. The geometry, the meshing and the used equations are presented and discussed. Finally, the CFD simulation results are reported and discussed as well as the problem of the apparent kinetics respect to the intrinsic one and the discrepancy between the apparent kinetics and the intrinsic kinetics (due to the external mass transfer) is highlighted.

Chapter 1

The CCS Technology

The Working Group I contribution to the Fifth Assessment Report of the Intergovernmental Panel on Climate Change (IPCC) provides a comprehensive assessment of the physical science basis of climate change [62]. This work puts a focus on those elements that are relevant to understand past, document current and project future climate change of the planet. The Special Report of the Working Group III of IPCC on Carbon dioxide Capture and Storage (CSS) has been developed in response to an invitation of the United Nations Framework Convention on Climate Change (UNFCCC) at its seventh Conference of Parties (COP7) in 2001. The results of this workshop were a first assessment of literature on CO_2 capture and storage, in the field of mitigation technologies for climate change. The attention is then focused on carbon dioxide capture technologies, specifically on calcium carbonate looping cycle.

1.1 Climate change

> *Warming of the climate system is unequivocal, and since the 1950s, many of the observed changes are unprecedented over decades to millennia. The atmosphere and ocean have warmed, the amounts of snow and ice have diminished, sea level has risen, and the concentrations of greenhouse gases have increased [62].*

Human activities are continuing to affect the Earth's energy budget by changing the emissions and resulting atmospheric concentrations of important gases and aerosols and by changing land surface properties. The evidences of climate change derives from observations of the atmosphere, land, oceans and cryosphere. Unequivocal evidence from in-situ observations and ice core records shows that the atmospheric concentrations of important greenhouse gases (GHGs) such as carbon dioxide (CO_2), methane (CH_4), and nitrous oxide (N_2O) have increased over the last few centuries.

Observations of the climate system are based on direct measurements and remote sensing from satellites and other platforms. Global-scale observations from the instrumental era began in the mid-19th century for temperature and other variables, with more comprehensive and diverse sets of observations available starting from 1950s. Paleo-climate reconstructions extend some records back hundreds to millions of years. Together, they provide a comprehensive view

of the variability and long-term changes in the atmosphere, the ocean, the cryosphere, and the land surface.

Global mean surface air temperatures over land and oceans have increased over the last 100 years. Temperature measurements in the oceans show a continuing increase in the heat content. Observations from satellites and in situ measurements show a trend of significant reductions in the mass balance of most land ice masses and in Arctic sea ice. The increasing of CO_2 concentrations in oceans is having a significant effect on the chemistry of sea water.

1.1.1 Atmosphere

> *Each of the last three decades has been successively warmer at the Earth's surface than any preceding decade since 1850. In the Northern Hemisphere, 1983-2012 was likely the warmest 30-year period of the last 1400 years [62].*

The globally averaged combined land and ocean surface temperature data as calculated by a linear trend, show a warming of 0.85 °C, over the period 1880 to 2012. The total increase between the average of the 1850-1900 period and the 2003-2012 period is 0.78 °C (Fig. 1.1a). For the longest period for which calculation of regional trends is sufficiently complete (1901 to 2012), almost the entire globe has experienced surface warming, as shown in Fig. 1.1b.
Confidence in precipitation change averaged over global land areas since 1901 is low prior to 1951 and medium afterwards. Averaged over the mid-latitude land areas of the Northern Hemisphere, precipitation has increased since 1901 as reported in Fig. 1.2. Changes in many extreme weather and climate events have been observed since about 1950. It is very likely that the number of cold days and nights has decreased and the number of warm days and nights has increased on the global scale. The frequency of heat waves has increased in large parts of Europe, Asia and Australia. There are likely more land regions where the number of heavy precipitation events has increased than where it has decreased. The frequency or intensity of heavy precipitation events has likely increased in North America and Europe.

1.1.2 Ocean

> *Ocean warming dominates the increase in energy stored in the climate system, accounting for more than* 90 % *of the energy accumulated between 1971 and 2010. It is virtually certain that the upper ocean* $(0 \div 700\,\mathrm{m})$ *warmed from 1971 to 2010 [62].*

On a global scale, the ocean warming is largest near the surface, and the upper 75 m warmed by 0.11 °C per decade over the period 1971 to 2010 and it is likely that it has warmed from the 1870s to 1971. There is less certainty in changes prior to 1971 because of relatively sparse sampling in earlier time periods.
It is likely that the ocean warmed between $700 \div 2000$ m from 1957 to 2009, based on 5-year averages. The ocean warmed from 3000 m to the bottom from 1992 to 2005, instead no significant trends in global average temperature were observed between 2000 and 3000 m depth from circa 1992 to 2005. Below 3000 m depth, the largest warming is observed in the Southern Ocean (Fig. 1.3).

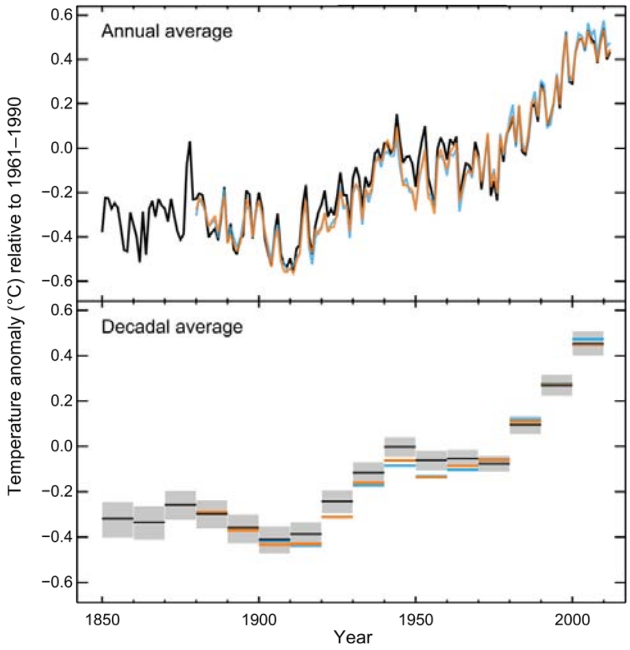

(a) *Observed globally averaged combined land and ocean surface temperature anomaly 1850-2012.*

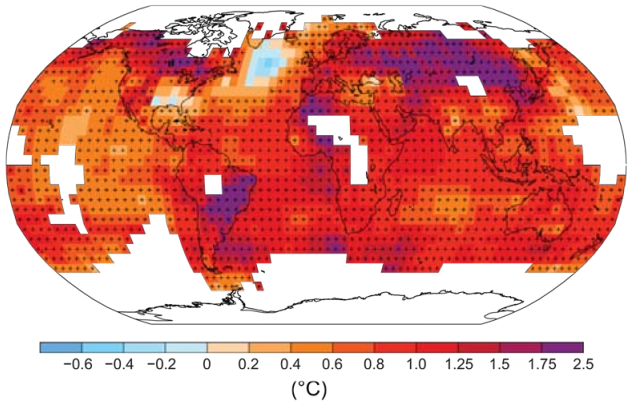

(b) *Observed change in surface temperature 1901-2012.*

Figure 1.1: (a) Observed global mean combined land and ocean surface temperature anomalies, from 1850 to 2012. Top panel: annual mean values. Bottom panel: decade mean values including the estimate of uncertainty. Anomalies are relative to the mean of 1961-1990. (b) Map of the observed surface temperature change from 1901 to 2012, according to IPCC 2013 [62].

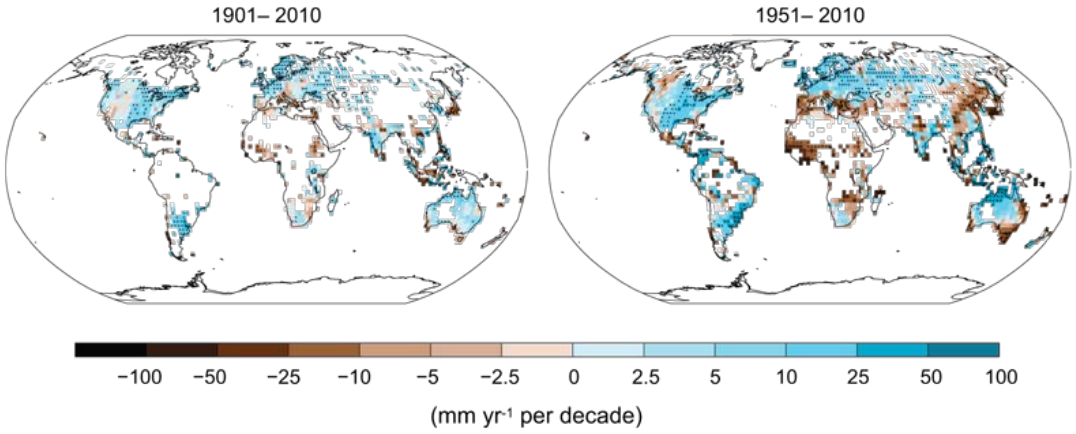

Figure 1.2: Maps of observed precipitation change from 1901 to 2010 and from 1951 to 2010, according to IPCC 2013 [62].

1.1.3 Cryosphere

> *Over the last two decades, the Greenland and Antarctic ice sheets have been losing mass, glaciers have continued to shrink almost worldwide, and Arctic sea ice and Northern Hemisphere spring snow cover have continued to decrease in extent [62].*

The average rate of ice loss from glaciers around the world, excluding glaciers on the periphery of the ice sheets, was very likely 226 Gt yr^{-1} over the period 1971 to 2009, and very likely 275 Gt yr^{-1} over the period 1993 to 2009.
The average rate of ice loss from the Greenland ice sheet has very likely substantially increased from 34 Gt yr^{-1} over the period 1992 to 2001 to 215 Gt yr^{-1} over the period 2002 to 2011.
The average rate of ice loss from the Antarctic ice sheet has likely increased from 30 Gt yr^{-1} over the period 1992-2001 to 147 Gt yr^{-1} over the period 2002 to 2011 (Fig. 1.4).
The annual mean Arctic sea ice extent decreased over the period 1979 to 2012 with a rate that was very likely in the range 3.5 to 4.1 % per decade (range of 0.45 to 0.51 million km^2 per decade), and very likely in the range 9.4 to 13.6 % per decade (range of 0.73 to 1.07 million km^2 per decade) for the summer sea ice minimum (perennial sea ice). There is medium confidence from reconstructions that over the past three decade, Arctic summer sea ice retreat was unprecedented and sea surface temperatures were anomalously high in at least the last 1450 years.

1.1.4 Sea levels

> *The rate of sea level rise since the mid-19th century has been larger than the mean rate during the previous two millennia. Over the period 1901 to 2010, global mean sea level rose by* 0.19 m *[62].*

Sea level data indicate a transition in the late 19th to the early 20th century from relatively low mean rates of rise over the previous two millennia to higher rates of rise. It is likely that the rate of global mean sea level rise has continued to increase since the early 20th century.
It is very likely that the mean rate of global averaged sea level rise was 1.7 mm yr^{-1} between

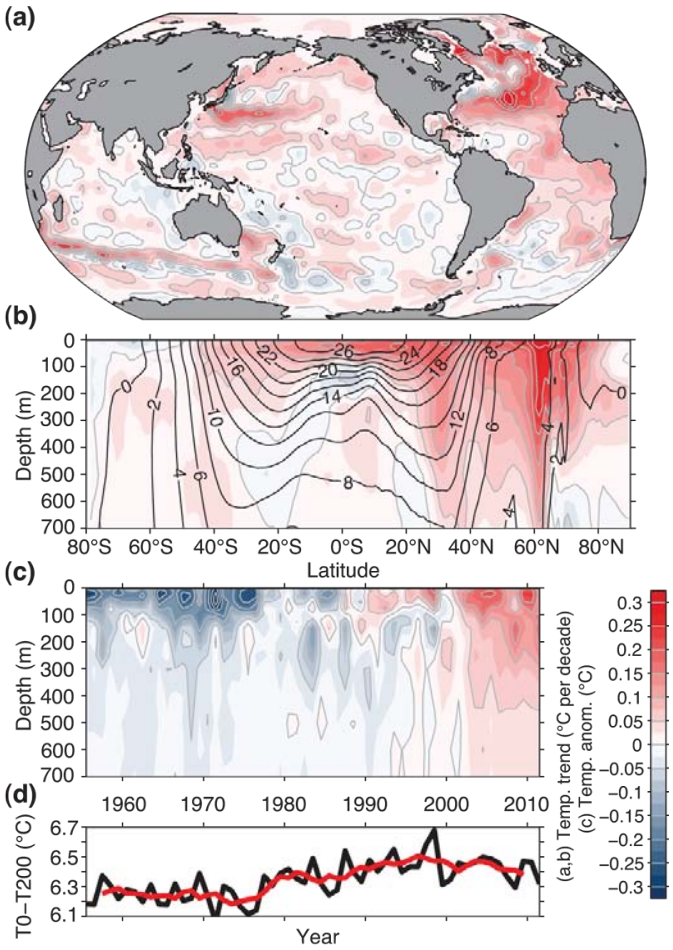

Figure 1.3: (a) Depth-averaged 0 to 700 m temperature trend for 1971-2010. (b) Zonally averaged temperature trends for 1971-2010 with zonally averaged mean temperature over-plotted (black contours in degrees Celsius). (c) Globally averaged temperature anomaly relative to the 1971-2010 mean. (d) Globally averaged temperature difference between the ocean surface and 200 m depth (black: annual values, red: 5-year running mean). Source: IPCC 2013 [62].

1901 and 2010, 2.0 mm yr^{-1} between 1971 and 2010, and 3.2 mm yr^{-1} between 1993 and 2010. Tide-gauge and satellite altimeter data are consistent regarding the higher rate of the latter period.

Since the early 1970s, glacier mass loss and ocean thermal expansion from warming together explain about 75 % of the observed global mean sea level rise. Over the period 1993 to 2010, global mean sea level rise is, with high confidence, consistent with the sum of the observed contributions from ocean thermal expansion due to warming (1.1 mm yr^{-1}), from changes in glaciers (0.76 mm yr^{-1}), Greenland ice sheet (0.33 mm yr^{-1}), Antarctic ice sheet (0.27 mm yr^{-1}), and land water storage (0.38 mm yr^{-1}). The sum of these contributions is 2.8 mm yr^{-1}.

1.2 Causes of change

Human activities have changed and continue to change the Earth's surface and atmospheric composition. Some of these changes have a direct or indirect impact on the energy balance of the

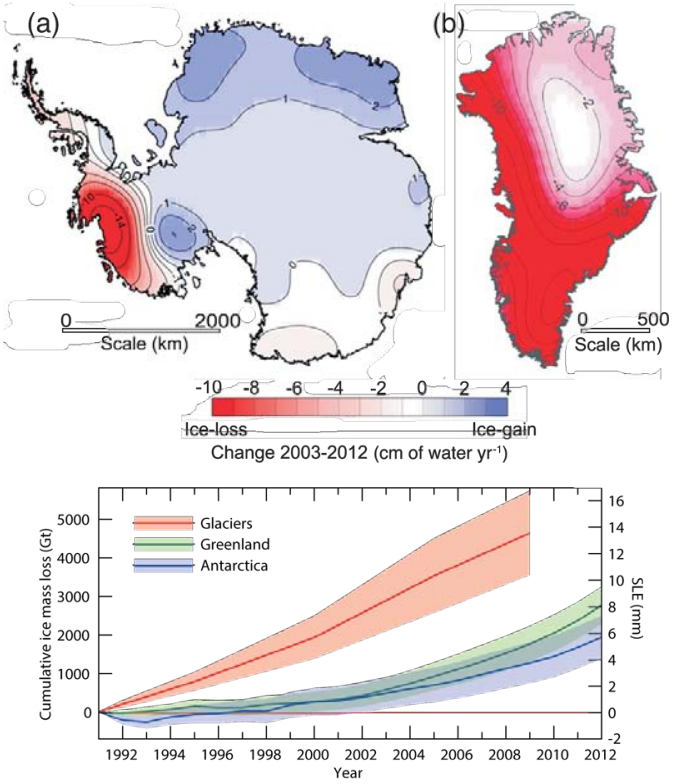

Figure 1.4: (Top) Distribution of ice loss determined from Gravity Recovery and Climate Experiment (GRACE) time-variable gravity for (a) Antarctica and (b) Greenland, shown in centimeters of water per year for the period 2003-2012. (Bottom) The assessment of the total loss of ice from glaciers and ice sheets in terms of mass (Gt) and sea level equivalent (mm) from 1992. The contribution from glaciers excludes those on the periphery of the ice sheets. Source: IPCC 2013 [62].

Earth and are thus drivers of climate change. Radiative forcing is a measure of the influence that a factor has in altering the balance of incoming and outgoing energy in the Earth-atmosphere system and it is expressed in $\mathrm{W\,m^{-2}}$. If RF is positive it leads to warming and, on the contrary, if RF is negative, it leads to a cooling. Human activities result in emissions of four principal greenhouse gases (GHG): carbon dioxide (CO_2), methane (CH_4), nitrous oxide (N_2O) and the halocarbons (a group of gases containing fluorine, chlorine and bromine). These gases accumulate in the atmosphere, causing concentrations to increase with time. The climate change responses are different for each GHG, because of their different warming influence on the global climate system due to their diverse radiative properties and lifetimes in the atmosphere. In order to compare the different influences, these may be expressed through a common metric based on the radiative forcing of carbon dioxide: the CO_2 equivalent emission[1].

Global GHG emissions have grown since pre-industrial times, with an increase of 70 % between 1970 and 2004. Carbon dioxide is the most important anthropogenic GHG because it is the most emitted anthropogenic GHG. Its annual emissions have grown between 1970 and 2004 by about 80 %, from 21 to 38 Gt, and represented 77 % of total anthropogenic GHG emissions in 2004, as

[1]It is the amount of CO_2 emission that would cause the same time-integrated radiative forcing, over a given time horizon, as an emitted amount of a long-lived GHG or a mixture of GHGs.

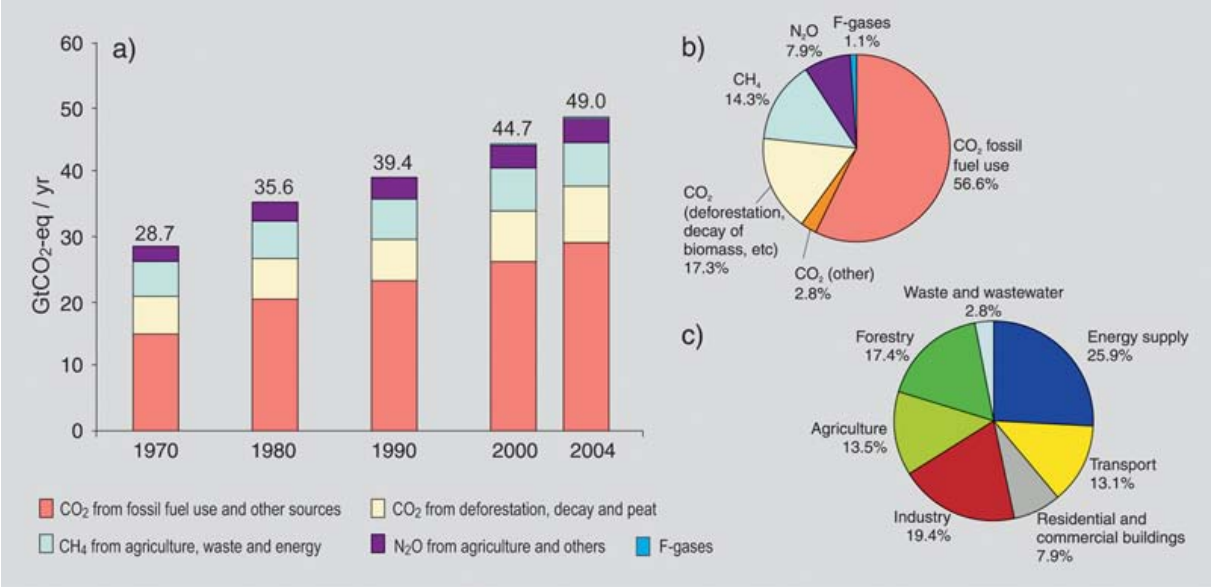

Figure 1.5: (a) Global annual emissions of anthropogenic GHGs from 1970 to 2004. (b) Share of different anthropogenic GHGs in total emissions in 2004 in terms of CO_2-eq. (c) Share of different sectors in total anthropogenic GHG emissions in 2004 in terms of CO_2-eq. Source: IPCC 2007 [55].

shown in Fig. 1.5. The rate of growth of CO_2-eq emissions was much higher during the recent 10-year period of 1995-2004 (0.92 Gt of CO_2-eq per year) than during the previous period of 1970-1994 (0.43 Gt of CO_2-eq per year). Prior to the Industrial Era, that began in 1750, the concentration of atmospheric CO_2 fluctuated roughly between 180 ppm and 290 ppm for at least 2.1 Myr (Fig. 1.6) according to IPCC 2007 [55]. Between 1750 and 2011, the combustion of fossil fuels (coal, gas, oil and gas flaring) and the production of cement have released 375 ± 30 Pg ($1\,\text{Pg} = 1 \times 10^{15}$ g) of carbon dioxide to the atmosphere. Land use change activities, mainly deforestation, has released an additional 180 ± 80 Pg. This carbon released by human activities is called anthropogenic carbon.

Of the 555 ± 85 Pg of anthropogenic carbon emitted to the atmosphere from fossil fuel, cement and land use change, less than half have accumulated in the atmosphere (240 ± 10 Pg). The remaining anthropogenic carbon has been absorbed by the ocean and in terrestrial ecosystems, named "carbon sinks" (Fig. 1.7). The power and industry sectors combined dominate the current global CO_2 emissions, accounting for about 60 % of total CO_2 emitted. Carbon dioxide emissions in these sectors are generated by boilers and furnaces burning fossil fuels and are typically emitted from large exhaust stacks. These stacks can be described as large stationary sources, to distinguish them from mobile sources such as those in the transport sector and from smaller stationary sources such as small heating boilers used in the residential sector. These last CO_2 emissions that account for the residential, commercial, transportation and agriculture sectors are not considered by IPCC 2007 [55].

The emission sources considered include all large stationary sources (larger than 0.1 Mton of CO_2 per year) involving fossil fuel and biomass. These sources are present in three main areas: fuel combustion, industrial processes and natural-gas processing. The largest CO_2 emissions by far

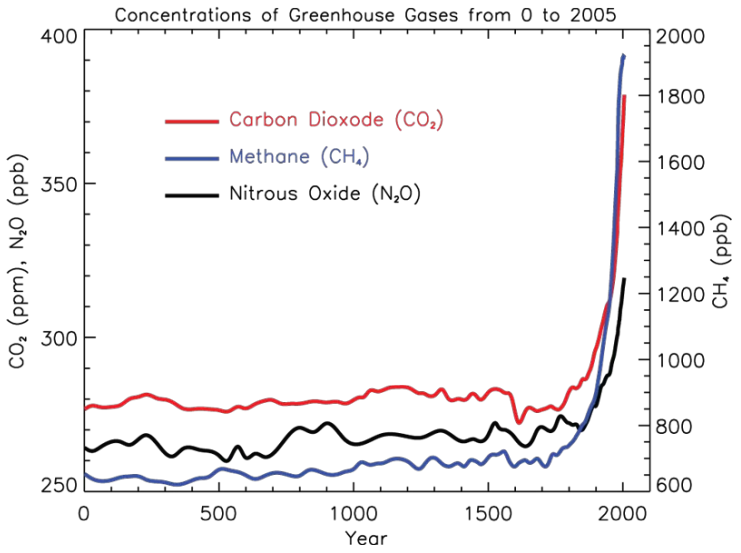

Figure 1.6: Atmospheric concentrations of important long-lived greenhouse gases over the last 2000 years. Increases since about 1750 are attributed to human activities in the industrial era. IPCC 2007 [55].

result from the oxidation of carbon when fossil fuels are burned. These emissions are associated with fossil fuel combustion in power plants, oil refineries and large industrial facilities (Tab. 1.1). The top 25 % of all large stationary CO_2 emission sources, listed in Tab. 1.2, account for over 85 % of the cumulative emissions from these types of sources. There are 330 sources with individual emissions above 10 Mton CO_2 per year. Of their cumulative emissions, 78 % come from power plants, 20 % from gas processing and the remainder from iron and steel plants.

Carbon dioxide not related to combustion is emitted from a variety of industrial production processes which transform materials chemically, physically or biologically. Such processes include: the use of fuels as feedstocks in petrochemical processes; the use of carbon as a reducing agent in the commercial production of metals from ores; the thermal decomposition (calcination) of limestone and dolomite in cement or lime production; the fermentation of biomass.

1.3 Carbon dioxide capture and storage

Carbon dioxide capture and storage (CCS) is a range of technologies that consisting of the separation of CO_2 from industrial and energy-related sources, transport to a storage location and long-term isolation from the atmosphere. It is considered as one of the options for reducing atmospheric emissions of CO_2 from human activities. CCS has the potential to reduce overall mitigation costs and increase flexibility in achieving greenhouse gas emission reductions.

The CCS involves the use of different technologies, first to collect and concentrate the CO_2 produced in industrial and energy related sources, to transport it to a suitable storage location, and then to store it away from the atmosphere for a long period of time. Thus, CCS would allow fossil fuels to be used with low emissions of greenhouse gases. Application of CCS to biomass energy sources could result in the net removal of CO_2 from the atmosphere (often referred to as "negative emissions") by capturing and storing the atmospheric carbon dioxide taken up by the

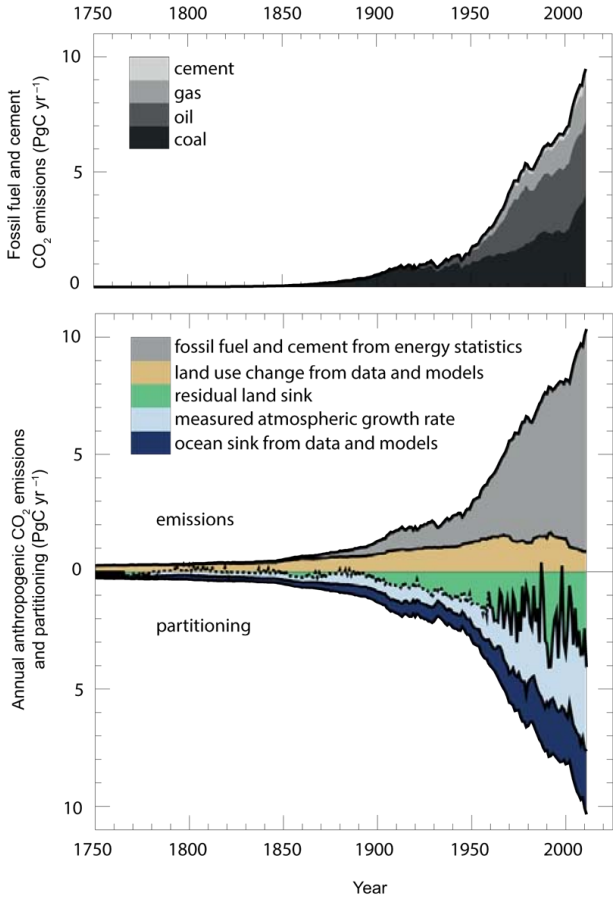

Figure 1.7: Annual anthropogenic CO2 emissions and their partitioning among the atmosphere, land and ocean ($Pg\,yr^{-1}$) from 1750 to 2011. (Top) Fossil fuel and cement CO_2 emissions by category. (Bottom) Fossil fuel and cement CO_2 emissions as above. CO_2 emissions from net land use change, mainly deforestation, are based on land cover change data and estimated for 1750-1850. Source: IPCC 2013 [62].

biomass.

The three main components of the CCS are: capture, transport and storage processes. The capture step involves separating CO_2 from other gaseous products. For fuel-burning processes such as those in power plants, separation technologies can be used to capture CO_2 after combustion or to decarbonize the fuel before combustion. The transport step may be required to carry captured CO_2 to a suitable storage site located at a distance from the CO_2 source. To facilitate both transport and storage, the captured CO_2 gas is typically compressed to a high density phase at the capture facility. Potential storage methods include injection into underground geological formations, injection into the deep ocean, or industrial fixation in inorganic carbonates. Some industrial processes also might utilize and store small amounts of captured CO_2 in manufactured products.

1.3.1 CO_2 capture technologies

Depending on the process, there are three main approaches to capture the CO_2 generated from a primary fossil fuel (coal, natural gas or oil), biomass, or mixtures of these fuels: post-

Table 1.1: Profile by process or industrial activity of worldwide large stationary CO_2 sources with emissions of more than $0.1\,MtCO_2$ per year. Source: IPCC 2005 [9].

Process	Number of sources	Emissions $[MtCO_2\,yr^{-1}]$
Fossil fuels		
Power	4942	10539
Cement production	1175	932
Refineries	638	798
Iron and steel industry	269	646
Petrochemical industry	470	379
Oil and gas processing	NA	50
Other sources	90	33
Biomass		
Bioethanol and bioenergy	303	91
Total	7887	13466

combustion systems, pre-combustion systems and oxyfuel combustion systems, Fig. 1.8.

Post-combustion systems separate CO_2 from the flue gases produced by the combustion of the primary fuel with air. These systems normally use a liquid solvent to capture the fraction of CO_2 (typically $3 \div 15\,\%$ by volume) present in a flue gas stream in which the main constituent is nitrogen (from air). For a modern pulverized coal power plant or a natural gas combined cycle power plant, current post-combustion capture systems typically employ organic solvents such as monoethanolamine (MEA), according to Dean et al. [20].

In pre-combustion systems process the primary fuel is fed in a reactor with steam and air or oxygen and converted into syn-gas. Then hydrogen, together with CO_2, is produced by reacting the carbon monoxide with steam in a second reactor ("shift reactor"). The resulting mixture of H_2 and CO_2 can then be separated into a CO_2 gas stream, and a stream of hydrogen. If the CO_2 is captured, hydrogen is a carbon-free energy carrier that can be combusted to generate power and/or heat. Although the initial fuel conversion steps are more elaborate and costly than in post-combustion systems, the high concentrations of CO_2 produced by the shift reactor and the high pressures often encountered in these applications are more favourable for CO_2 separation. Pre-combustion would be used at power plants that employ integrated gasification combined cycle technology.

Oxyfuel combustion systems use oxygen instead of air for combustion of the primary fuel to produce a flue gas that is mainly water vapour and CO_2. This results in a flue gas with high CO_2 concentrations (larger than $80\,\%$ by volume). The water vapor is then removed by cooling and compressing the gas stream. Oxyfuel combustion requires the upstream separation of oxygen from air, with a purity of $95 \div 99\,\%$ oxygen assumed in most current designs. Further treatment of the flue gas may be needed to remove air pollutants and non-condensed gases (such as nitrogen) from the flue gas before the CO_2 is sent to storage.

Table 1.2: Profile of worldwide large CO_2 stationary sources emitting more than 0.1 Mton CO_2 per year. Source: IPCC 2005 [9].

Process	CO_2 concentration in gas stream % by vol.	Number of sources	Emissions (Mton $CO_2\,yr^{-1}$)	% of total CO_2 emissions	Cumulative total CO_2 emissions (%)	Average emissions per source (Mton $CO_2\,yr^{-1}$)
Power - CO_2 from fossil fuels						
Coal	12 to 15	2025	7984	59.69	59.69	3.94
Natural gas	3	985	759	5.68	65.37	0.77
Natural gas	7 to 10	743	752	5.62	70.99	1.01
Fuel oil	8	515	654	4.89	75.88	1.27
Fuel oil	3	593	326	2.43	78.31	0.55
Other fuels	NA	79	61	0.45	78.77	0.77
Hydrogen	NA	2	3	0.02	78.79	1.27
Natural-gas sweetening	NA	NA	50	0.37	79.16	
Cement production						
Combined	20	1175	932	6.97	86.13	0.79
Refineries	3 to 13	638	798	5.97	92.09	1.25
Iron and steel industry						
Integrated steel mills	15	180	630	4.71	96.81	3.50
Other processes	NA	89	16	0.12	96.92	0.17
Petrochemical industry						
Ethylene	12	240	258	1.93	98.85	1.08
Ammonia: process	100	194	113	0.84	99.70	0.58
Ammonia: fuel combustion	8	19	5	0.04	99.73	0.26
Ethylene oxide	100	17	3	0.02	99.75	0.15
CO_2 from biomass						
Bioenergy	3 to 8	213	73			0.34
Fermentation	100	90	17.6			0.2

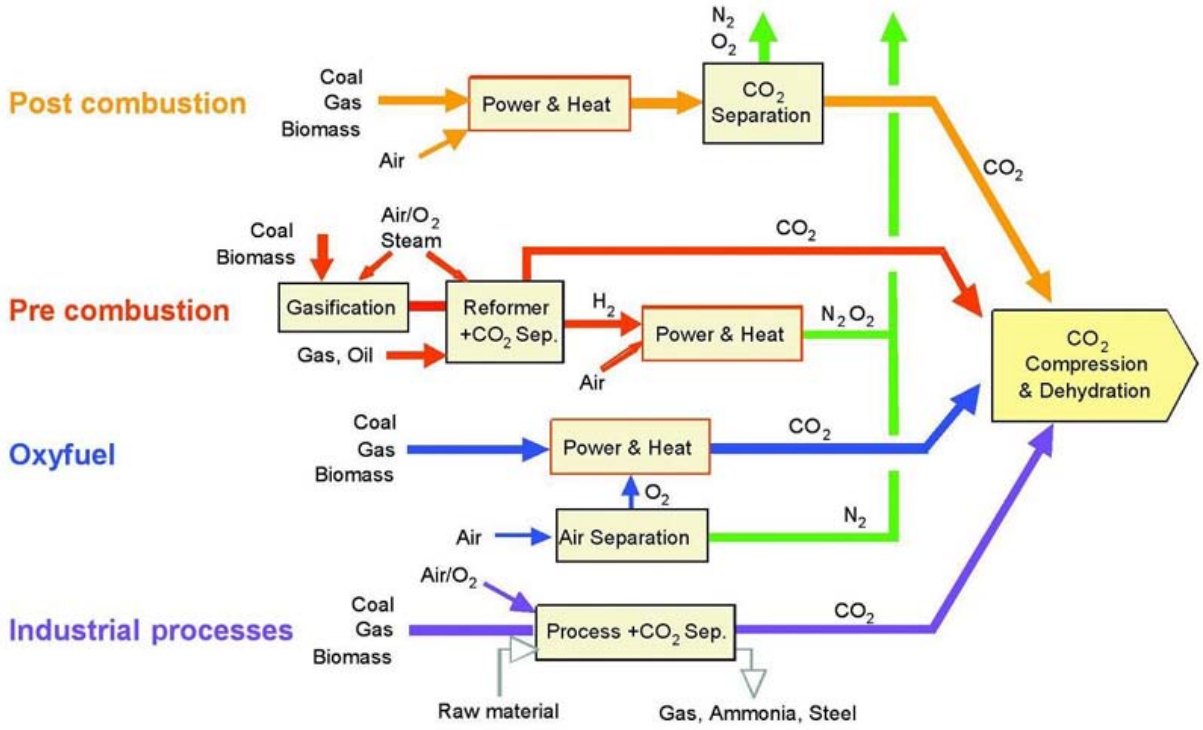

Figure 1.8: CO_2 capture systems. Source: IPCC 2005 [9].

1.3.2 Types of CO_2 capture processes

As shown in Fig. 1.9, the capturing technologies to obtain the CO_2 separation are: separation by sorbents or solvents, membranes separation and cryogenic distillation.

The separation with with sorbents/solvents is achieved by passing the CO_2-rich gas in intimate contact with a liquid absorbent or solid sorbent that is capable of capturing the CO_2. In the general case the sorbent loaded with the captured CO_2 is transported to a different vessel, where it releases the CO_2 (sorbent regeneration) after being heated or after a pressure decrease. Regenerated sorbent is sent back to the capture step establishing a cyclic process. A make-up flow of fresh sorbent is always required to compensate for the natural decay of activity and sorbent losses. One common problem of these CO_2 capture systems is that the flow of sorbent between the vessels is large because it has to match the large flow of CO_2 being processed in the power plant. Therefore, equipment sizes and the energy required for sorbent regeneration are large and tend to translate into an important efficiency penalty and added cost (IPCC 2005 [9]).

Membranes are specially manufactured materials that allow the selective permeation of a gas through them. The selectivity of the membrane to different gases is intimately related to the nature of the material, but the flow of gas through the membrane is usually driven by the pressure difference across the membrane. Therefore, high-pressure streams are usually preferred for membrane separation. Although membrane separation finds many current commercial applications in industry they have not yet been applied for the large scale and demanding conditions in terms of reliability and low-cost required for CO_2 capture systems (according to IPCC 2005 [9]).

Distillation of a liquefied gas stream and refrigerated separation requires a gas that can be

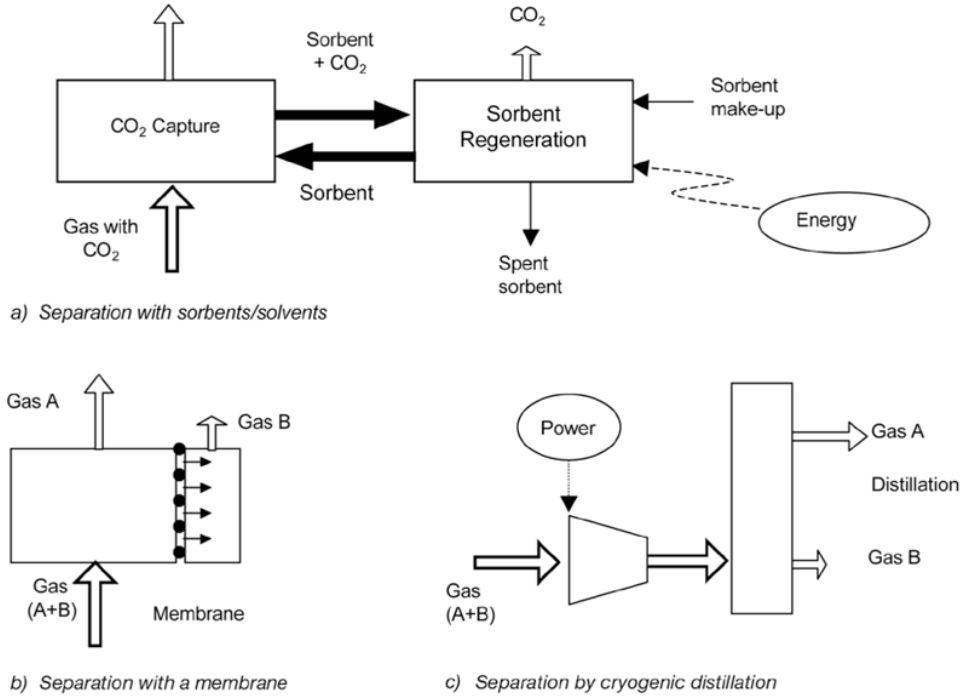

Figure 1.9: Schemes of the main separation processes relevant for CO_2 capture: (a) separation with sorbents or solvents, (b) separation with membrane, (c) separation by cryogenic distillation. Source: IPCC 2005 [9].

made liquid by a series of compression, cooling and expansion steps. Once in liquid form, the components of the gas can be separated in a distillation column. It can be used to separate impurities from relatively high purity CO_2 streams, for example, from oxy-fuel combustion and for CO_2 removal from natural gas or synthesis gas that has undergone a shift conversion of CO to CO_2.

1.3.3 Transport

Except when plants are located directly above a geological storage site, captured CO_2 must be transported from the point of capture to a storage site. Gaseous CO_2 is typically compressed to a pressure above 8 MPa in order to avoid two-phase flow regimes and increase the density of the CO_2, thereby making it easier and less costly to transport. CO_2 can also be transported as a liquid in ships, road or rail tankers that carry CO_2 in insulated tanks at a temperature well below ambient, and at much lower pressures. Pipeline transport operate in the "dense phase" mode (supercritical phase), at ambient temperature and high pressure. In most of these pipelines, the flow is driven by compressors at the upstream end, although some pipelines have intermediate compressor stations.

In some situations or locations, transport of CO_2 by ship may be economically more attractive, particularly when the CO_2 has to be moved over large distances or overseas. Carbon dioxide can be transported by ship in the same way of liquefied petroleum gases (typically at 0.7 MPa).

Road and rail tankers also are technically feasible options, transporting CO_2 at a temperature of $-20\,°C$ and at 2 MPa pressure (IPCC 2005 [9]).

1.3.4 Storage

Carbon dioxide storage consists of three main storage technologies: geological storage, ocean storage and mineral sequestration.
Underground accumulation of carbon dioxide is a geological phenomenon, with natural trapping of CO_2 in underground reservoirs. While there are differences between natural accumulations and engineered storage, injecting CO_2 into deep geological formations at carefully selected sites can store it underground for long periods of time: it is considered likely that 99 % or more of the injected CO_2 will be retained for 1000 years. Depleted oil and gas reservoirs, possibly coal formations and particularly saline formations, can be used for the aim. To geologically store CO_2, it must first be compressed, usually to a dense fluid state known as "supercritical". Depending on the rate that temperature increases with depth (the geothermal gradient), the density of CO_2 increases with depth, until at about 800 m or higher, where the injected CO_2 is in a dense supercritical state. Carbon dioxide can remain trapped underground by virtue of a number of mechanisms, such as: trapping below an impermeable, confining layer (caprock); retention as an immobile phase trapped in the pore spaces of the storage formation; dissolution in-situ formation fluids; adsorption onto organic matter in coal and shale. Additionally, it may be trapped by reacting with the minerals in the storage formation and caprock to produce carbonate minerals.

Further, captured CO_2 could be injected into the ocean at great depth, where most of it would remain isolated from the atmosphere for centuries. CO_2 can be placed on a ship, injected directly into the ocean, or deposited on the sea floor. CO_2 loaded on ships could either be dispersed from a towed pipe or transported to fixed platforms feeding a CO_2 lake on the sea floor. Such CO_2 lakes must be deeper than 3 km where CO_2 is denser than sea water. Numerical models of the ocean indicate that placing CO_2 in the deep ocean would isolate most of the CO_2 from the atmosphere for several centuries, but over longer times the ocean and atmosphere would equilibrate.

Putting CO_2 directly into the deep ocean means that the chemical environment of the deep ocean would be altered immediately and change in ocean chemistry would be greater proximate to the release location. For ocean storage of CO_2, issues remain regarding environmental consequences, public acceptance, implications of existing laws, safeguards and practices that would need to be developed, and gaps in current understanding of ocean CO_2 storage.

Mineral carbonation is based on the reaction of CO_2 with metal oxides producing insoluble carbonates, calcium and magnesium are retained to be the most attractive metals. Mineral carbonation refers to the fixation of CO_2 using alkaline and alkaline-earth oxides, such as magnesium oxide (MgO) and calcium oxide (CaO), which are present in naturally occurring silicate rocks. Chemical reactions between these materials and CO_2 produces compounds such as magnesium carbonate ($MgCO_3$) and calcium carbonate ($CaCO_3$, commonly known as limestone). This process produces silica and carbonates that are stable over long time scales and can therefore be disposed of in areas such as silicate mines, or re-used for construction purposes.
Industrial uses of CO_2 include chemical and biological processes where CO_2 is a reactant, such as those used in urea and methanol production, as well as various technological applications that use CO_2 directly, for example in the horticulture industry, refrigeration, food packaging, welding,

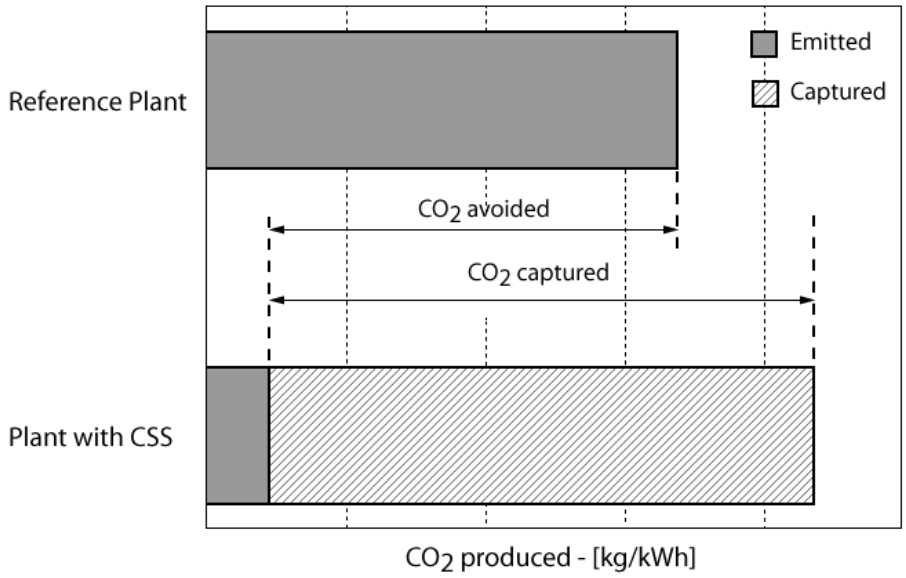

Figure 1.10: CO_2 capture and storage from power plants. The increased CO_2 production resulting from loss in overall efficiency of power plants due to the additional energy required for capture, transport and storage, and any leakage from transport result in a larger amount of CO_2 produced per unit of product (lower bar) relative to the reference plant (upper bar) without capture. Source: IPCC 2005 [9].

beverages and fire extinguishers.

1.3.5 Costs

In general, the capture, transport, and storage of CO_2 require energy inputs. For a power plant, this means that the amount of fuel input (and therefore CO_2 emissions) increases per unit of net power output. As a result, the amount of CO_2 produced per unit of product (e.g., a kWh of electricity) is larger for the power plant with CCS than for the reference plant, as shown in Fig. 1.10. To determine the CO_2 reductions one can attribute to CCS, it is necessary to compare CO_2 emissions of the plant with capture to those of the reference plant without capture. These are the avoided emissions. Unless the energy requirements for capture and storage are zero, the amount of CO_2 avoided is always less than the amount of CO_2 captured. The cost in US$ per tonne avoided is therefore greater than the cost in US$ per tonne captured.

The mitigation costs (US$ per ton CO_2 avoided) reported in Tab. 1.3 are context-specific and strongly depend on what is chosen as a reference plant. In Tab. 1.3, the reference plant is a power plant of the same type as the power plant with CCS. The mitigation costs here therefore represent the incremental cost of capturing and storing CO_2 from a particular type of plant.

1.4 CO_2 capture with solid sorbents

Emerging problems with CCS include the financial cost and energy penalty associated with the CO_2 capture step, i.e. the collection of a pure stream of CO_2 for sequestration. Currently,

Table 1.3: Ranges of total costs for CO_2 capture, transport, and geological storage based on current technology for new power plants. Source: IPCC 2005 [9].

	Pulverized Coal Power Plant	Natural Gas Combined Cycle Power Plant	Integrated Coal Gasification Combined Cycle Power Plant
Cost of electricity without CCS (US$ MWh^{-1})	43-52	31-50	41-61
Power plant with capture			
Increased Fuel Requirement (%)	24-40	11-22	14-25
CO_2 captured (kg MWh^{-1})	820-970	360-410	670-940
CO_2 avoided (kg MWh^{-1})	620-700	300-320	590-730
% CO_2 avoided	81-88	83-88	81-91
Power plant with capture and geological storage			
Cost of electricity (US$ MWh^{-1})	63-99	43-77	55-91
Electricity cost increase (US$ MWh^{-1})	19-47	12-29	10-32
% increase	43-91	37-85	21-78
Mitigation cost (US $ per ton of CO_2 avoided)	30-71	38-91	14-53
Mitigation cost (US $ per ton of C avoided)	110-260	140-330	51-200
Power plant with capture and enhanced oil recovery			
Cost of electricity (kg MWh^{-1})	49-81	37-70	40-75
Electricity cost increase (kg MWh^{-1})	5-29	6-22	(-5)-19
% increase	12-57	19-63	(-10)-46
Mitigation cost (US $ per ton of CO_2 avoided)	9-44	19-68	(-7)-31
Mitigation cost (US $ per ton of C avoided)	31-160	71-250	(-25)-120

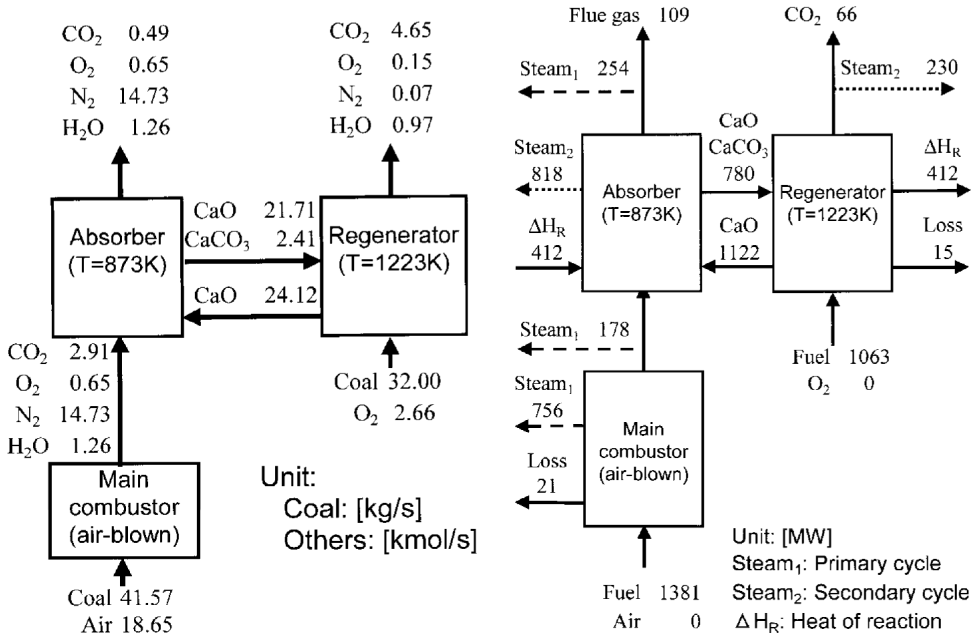

(a) *Material balance.* **(b)** *Heat balance.*

Figure 1.11: Proposed carbon oxide looping cycle process by Shimizu et al. [53].

a technology close to market for this step is post-combustion "scrubbing" of flue gases using amine-based sorbents, such as monoethanolamine (MEA). However, there are several problems associated with this technology, such as degradation of sorbents at higher temperatures, reactions with compounds present in the flue gas such as oxygen ($\sim 2\,\mathrm{vol}\,\%$) and sulphur dioxide, and cost. Additional drawbacks of this technology are due to the corrosive nature of MEA and its degradation products, which limits the wt.% of MEA in a typical power plant Dean [20].
Another technology is the oxyfuel combustion, where coal is burned with a mixture of pure O_2 and CO_2, with a portion of the flue gas being recycled to the burners to moderate the flame temperature. However, this system requires a large air separator (currently cryogenic) to produce the vast quantities of O_2 required. It is also clear that very stringent safety management is required within such power plants, and a number of issues remains regarding potential changes to ash chemistry and fouling, together with potential leaks into the plant reducing CO_2 purity. However, it appears that either oxyfuel combustion or amine scrubbing are become the first large-scale CCS technologies implemented (IPCC 2005 [9]).

Problems are associated with existing CO_2 capture technologies lead researches to investigate other methods of carbon dioxide capture, such as the reversible reaction between calcium oxide and carbon dioxide to form calcium carbonate (the calcium looping cycle). This process was originally proposed by Shimizu et al. [53] and uses CaO as a regenerable sorbent to capture CO_2 from combustion flue gases, Fig. 1.11.
Both pre-combustion and post-combustion applications of the calcium looping cycle follow similar principles, in that a calcium oxide sorbent is repeatedly cycled between two vessels, as shown in Figs. 1.12 and 1.13. In one vessel (the carbonator) carbonation of CaO occurs, stripping the flue gas of its CO_2. The $CaCO_3$ formed is then fed to another vessel where calcination occurs

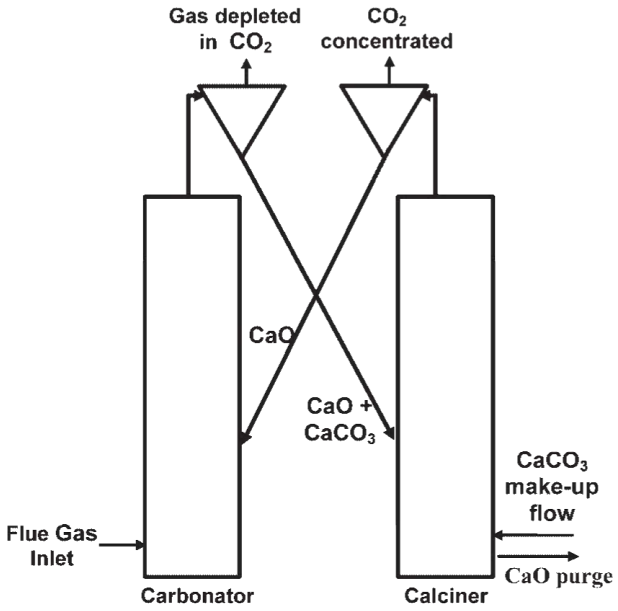

Figure 1.12: Schematics of the carbonation-calcination loop [24].

(the calciner) and the CaO formed is passed back to the carbonator leaving a pure stream of CO_2 suitable for sequestration. This cycle is continued and spent (unreactive) sorbent is continuously replaced by fresh (reactive) sorbent. The carbonation can either occur in-situ (i.e. within the gasifier/combustor) or ex-situ (i.e. on the product gases), with the former resulting in a reduction in plant complexity at the expense of a higher rate of degradation of sorbent due to contact with ash, sulphur and other impurities in the fuel burned. Heat from the exothermic carbonation of lime can be used to run a steam cycle, making up for some of the energy losses. The conditions in the calciner must be a compromise between the increased rate of reaction obtained at higher temperatures and the reduced rate of degradation of sorbent at lower temperatures. The conditions in the carbonator must strike a balance between the increased equilibrium conversion obtained at lower temperatures and the increased rate of reaction at higher temperatures.

The design of the carbonator requires a fondamental understanding of the carbonation reaction rates of the CaO particles that are fed to the carbonator from the calciner. High reaction rates between the CO_2 in the flue gas and the sorbent particles are necessary to design absorbers of a reasonable size. Fresh calcined lime is known to be a very reactive solid in the carbonation reaction. However, the average sorbent particle must undergo many carbonation-calcination cycles as a result of which sorbent capture capacity decreases rapidly. After a fast, chemically controlled initial reaction stage, a second slower reaction stage controlled by the diffusion in the product layer ($CaCO_3$) takes place. It has also been observed that the transition between the fast and slow regimes takes place quite suddenly at a given level of conversion, and that this level of conversion decreases as the number of carbonation/calcination cycles increases [24].

Since carbonation reaction does not present a trivial kinetics, in order to estimate the carbonator size a deep understanding on the kinetics of the carbonation reaction is needed. Several models have been proposed to describe the carbonation kinetics between CaO and CO_2. These

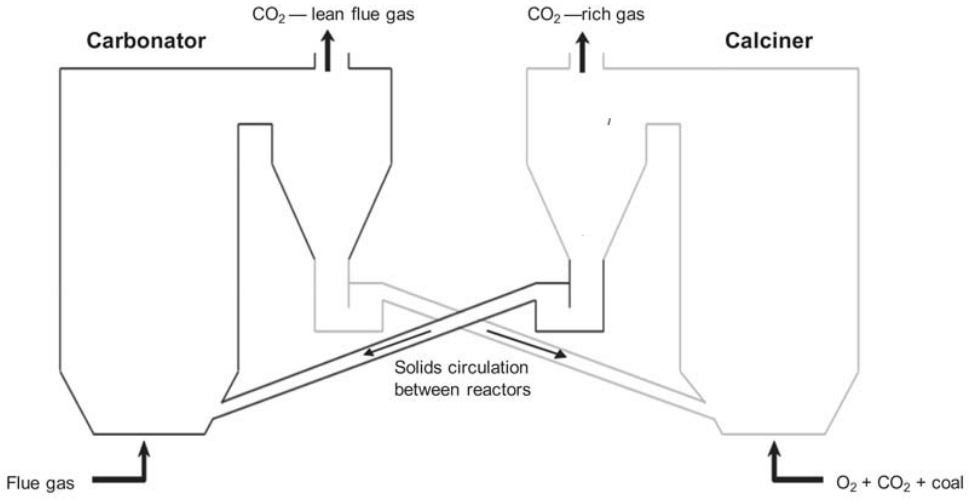

Figure 1.13: Dual interconnected circulating fluidized bed reactors for calcium oxide looping cycle [39].

models can be classified into several types: apparent models [34], shrinking core models [61], random pore models (RPM) [11], [12], [12], [13], [14], [10], [24] and grain models (GM) [65], [37]. RPM and GM are especially relevant for the study of the carbonation reaction. The RPM model correlates the carbonation rate with the internal pore structure, while the GM model assumes that the sorbent is composed of small grains that are dispersed in gas, and each grain is converted according to the shrinking core model.

Chapter 2

The Calcium Oxide Carbonation Reaction

One of the strategies for the carbon dioxide capture and storage using solid sorbents is based on the carbonation reaction, which is an heterogeneous reaction involving a gas species that reacts with a porous solid. During the reaction the solid phase undergoes structural changes, conditioning the reaction itself. Building a mathematical model of the process requires to elaborate a structural model able to simulate morphological changes of solid. Intrinsic kinetic parameters are required and can be estimated from thermo-gravimetric analysis data. This chapter presents the thermodynamics of the carbonation reaction, the solid phase characterization, a detailed description of thermo-gravimetric analysis and a critical review of the several phenomena that occur during the reaction.

2.1 Introduction

Calcium oxide can be an effective sorbent for separating carbon dioxide at high temperature and this reaction is the basis for the CO_2 capture systems when coupled with the calcination step to produce a pure carbon dioxide stream. However, if the calcination step is very rapid and goes to completion under a wide range condition, the carbonation one has not a trivial kinetics, specifically, under isothermal and isobaric conditions, after a fast chemical controlled stage, it shows a strong slowing down of the conversion leading to incomplete reaction, as reported by [13], [42], [1], [24] and [50]. It was also observed that the transition between the fast and slow regimes takes place quite suddenly at a given level of conversion, which decreases when the number of carbonation/calcination cycles increases. These features make the study of the carbonation reaction rate the most critical one.

Since the chemical species employed in this treatment are calcium oxide, carbon dioxide and calcium carbonate, it is useful to list some of their chemical, physical and thermodynamic properties in Tab. 2.1, where all the reported values are obtained from [36].

[1] melting point.

Table 2.1: Chemical, physical and thermodynamic proprieties of calcium oxide, carbon dioxide and calcium carbonate from [36]. All proprieties are estimated at 25 °C and 1 bar.

Property	CaO (s)	CO_2 (g)	$CaCO_3$ (s)
IUPAC name	calcium oxide	carbon dioxide	calcium carbonate
CAS number	1305-78-8	124-38-9	471-34-1
Appearance	white/pale yellow powder	colorless gas	white powder
M_i $[\mathrm{g\,mol^{-1}}]$	56.077	44.01	100.087
ρ_s $[\mathrm{g\,cm^{-3}}]$	3.34	-	2.71
MP[1] [°C]	2898	-78.5	1330
ΔH_f° $[\mathrm{kJ\,mol^{-1}}]$	-634.9	-393.5	-1207.6
ΔG_f° $[\mathrm{kJ\,mol^{-1}}]$	-603.3	-394.4	-1129.1
S° $[\mathrm{J\,mol^{-1}\,K^{-1}}]$	38.1	213.8	91.7
Cp° $[\mathrm{J\,mol^{-1}\,K^{-1}}]$	42	37.1	83.5

2.2 The carbonation reaction

The carbonation reaction is an equilibrium reaction that can be represented by the chemical equation reported in Eq. (2.1):

$$\mathrm{CaO}_{(s)} + \mathrm{CO}_{2(g)} = \mathrm{CaCO}_{3(s)} \qquad \Delta H_r^\circ = -178\,\mathrm{kJ\,mol^{-1}}. \tag{2.1}$$

From the reaction enthalpy of Eq. (2.1) the carbonation reaction is exothermic, while the backward step is endothermic and its name is calcination.

The carbonation reaction is an heterogeneous reaction between a porous solid species and a gas species, that evolves producing a solid product. The overall volume of the solid phase increases due to the relative density between the carbonate and the calcium oxide.

In order to specify the operative conditions for the carbonation step, a compromise must be take into account between high temperatures, which favour the speed of the reaction rate, and low temperatures, that favour the equilibrium conversion maintaining the equilibrium partial pressure of carbon dioxide at low values. From several contributions (such as [13], [3], [1], [42] or [24]) it is well known that this reaction takes place in two stages: an initial rapid one followed by a slow stage, which approaches a conversion plateau. In addition, all the cited authors report a CaO conversion below to 100 %, that means calcium oxide is not totally converted into carbonate. This trend can be study analyzing the kinetic curves of the carbonation reaction that can be obtained using a Thermo-Gravimetric Analyzer (TGA), a typical instrument employed in kinetic studies of gas-solid reactions.

2.3 Thermodynamics of carbonation: the reversibility of the carbon dioxide capture

The conditions at which the gas-solid reaction between CaO and CO_2 takes place can be predicted from thermodynamics: calcium oxide reacts with carbon dioxide when the CO_2 partial

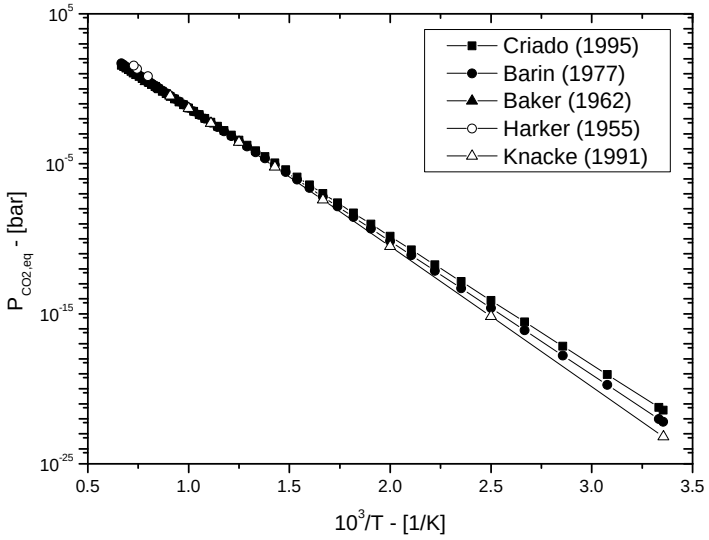

Figure 2.1: The equilibrium partial pressure of CO_2 resulting from decomposition of $CaCO_3$. Data reproduced from [7], [8], [18], [27] and [30].

pressure in the reactant gas is greater than the equilibrium partial pressure; conversely, $CaCO_3$ decomposes to form CaO and CO_2 when carbon dioxide partial pressure is lower than the equilibrium partial pressure.

Determination of the equilibrium conditions namely the equilibrium partial pressure ($p_{CO_2,\,eq}$) of carbon dioxide was performed by several investigators such as [7], [8], [18], [27] and [30]. In these works, according to Eq. (2.1), the equilibrium vapor pressure of CO_2 over CaO was calculated as a function of the system temperature. Specifically, a linear relationship can be emphasized in a plot of $\log\left(p_{CO_2,\,eq}\right)$ against $10^3/T$, as showed in Fig. 2.1, where T is expressed in K. From Fig. 2.1 the various calculated values are in good agreement among the cited works, specially for high temperatures.

In order to predict the equilibrium of carbonation, the frequently quoted equilibrium equation of [7] is reported in Eq. (2.2),

$$\log p_{CO_2,\,eq} = 7.079 - \frac{38000}{4.574\,T}, \tag{2.2}$$

where $p_{CO_2,\,eq}$ is in atm and T in K. Fig. 2.2 plots Eq. (2.2): for partial pressures of CO_2 larger than the equilibrium curve at a given temperature favors the carbonation, while in conditions below the curve calcination takes place. It is clear that above 1000 K carbonation cannot occur at atmospheric pressure because chemical equilibrium is strongly shifted to the reactants of Eq. (2.1), identifying the thermodynamics condition for sorbent regeneration.

2.4 Solid phase characterization

In this work the selected precursor material employed for studying the carbonation reaction is pure calcium carbonate, produced by AppliChem GmbH. The company declares that $CaCO_3$

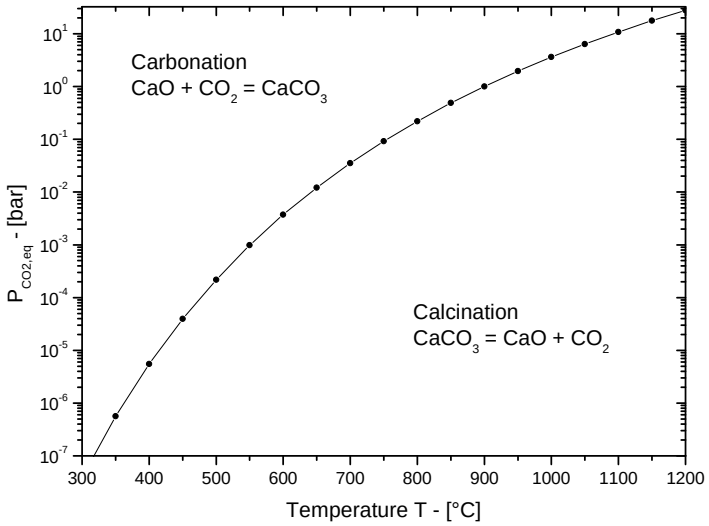

Figure 2.2: The equilibrium partial pressure of CO_2 above CaO. Data reproduced using Eq. (2.1) from [7].

purity is close to 99 % without any trace of organic solvents and, further, it reports that the material was obtained from marble granular.

The powder was sieved and classified on the basis of mean particle diameter and, only the $150 \div 160\,\mu m$ class was considered for TGA tests. This specific particle size is retained to be a good compromise between a low particle volatility and a negligible resistance particle diffusion during reaction process. In fact, during experimentations too light particles may be lifted by the gas flow, dirtying the instrumentation; the light particles are cohesive and may lead to inter-particle sintering. Intra-particle diffusion will be discussed in the further chapters. Actually, every single particle of calcite of $150\,\mu m$ is completely covered by very fine particles having a mean diameter lower than $10\,\mu m$, as shown in Fig. 2.3. Indeed, this fine powder is likely linked to the $CaCO_3$ by van der Waals'Forces, weak interactions that can be easily annulled using, for example, an inorganic solvent as water. Sedimentation with water can be used to remove the fine phase and in the following sections their influence on carbonation reaction will be demonstrated. Otherwise, if fine particles were to be removed from calcined material, CaO, a non-polar solvent should be used such as n-hexane or cyclohexane. However, if organic solvents are to be avoided it is recommended to separate the fine powder directly from calcium carbonate with water.

In order to obtain porous calcium oxide starting from limestone the reversibility of Eq. (2.1) was exploited. As reported in Fig. 2.2 the calcination reaction occurs at high temperature and at low carbon dioxide partial pressure. Therefore, calcination reactions were conducted at atmospheric pressure inside a muffle where the temperature was controlled by a temperature profile specified by the user. typically, calcination reactions were conducted between $700 \div 900\,°C$ starting from room temperature and imposing an heating rate (HR) of $10\,°C\,min^{-1}$. Furthermore, the entire process was operated at atmospheric pressure with air. In bulky samples decomposition may be inhibited because of the local high CO_2 concentration, which is held in the pores of the particle, or in the interstices of the bed. This inconvenient was reduced charging low quantity

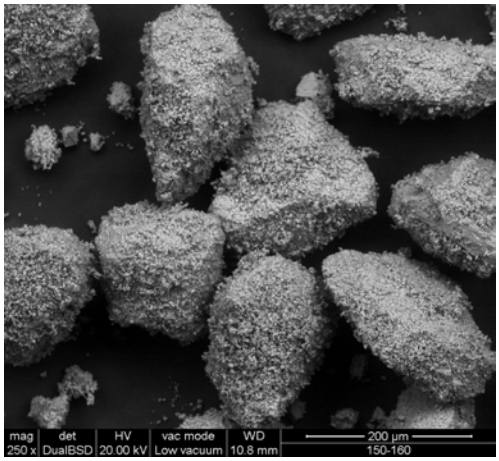

(a) *Limestone particle.*

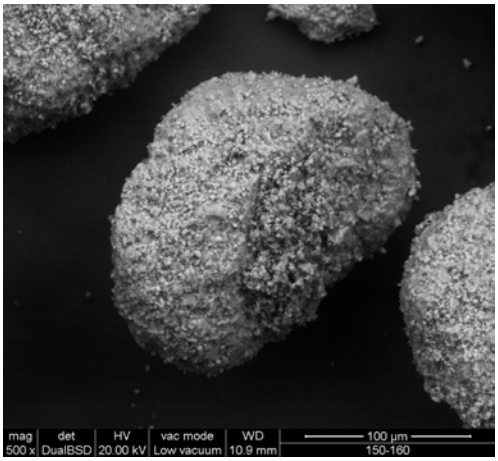

(b) *Detail of a single limestone particle covered by fine ones.*

Figure 2.3: SEM images of limestone with mean particle diameter of $150 \div 160\,\mu m$. The fine particles are clearly visible.

of limestone and arranging particles to obtain a thin layer. In this work maximum 2 g of calcite was charged in the crucible muffle.

Calcined samples were first degassed using vacuum and then stored under nitrogen in a dry-box, in fact, it is extremely important to avoid the hydration reaction that gives calcium hydroxide, on the basis of Eq. (2.3):

$$CaO_{(s)} + H_2O_{(g)} \rightleftharpoons Ca(OH)_{2(s)} \qquad \Delta H_r^\circ = -108.5\,kJ\,mol^{-1}. \tag{2.3}$$

SEM images of material before and after calcination are reported in Fig. 2.4 and Fig. 2.5 respectively. It is interesting to focusing on Fig. 2.5d which shows one of many structural fractures on calcium oxide particle generated during reaction. In fact calcite particles undergo structural fractures, that are inter-granular cracking, and this phenomena causes a double effect on material: it exposes unreacted carbonate core and it contributes to the increase of particle specific surface.

2.4.1 BET analysis

Gas-solid reactions as calcination or carbonation depend on the structural properties of the solid in terms of interphase area and for this reason the solid phase is employed in the form of particles in order to increase the interphase surface area. However, the gain in surface due to particles is low compared to porous particles, because of the pore network, that generates an internal surface which is significantly larger than the external particle surface. Indeed, this is one of the main goals of the preliminary calcination: the thermal activation of the solid material in terms of pore opening and specific surface increase.

Therefore, it is important to evaluate the total specific surface of calcium oxide because it influences the kinetics of the carbonation: high specific surface means high reactivity, because of

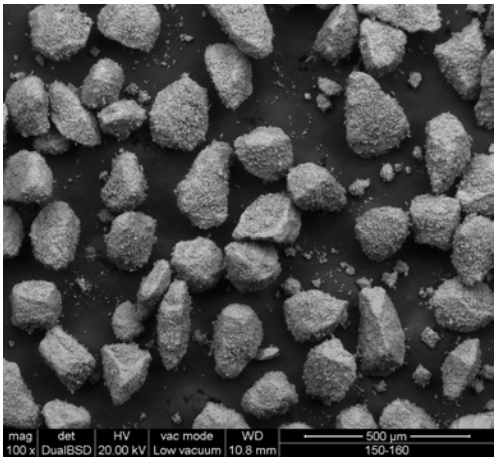

(a) *Calcite particle overview.*

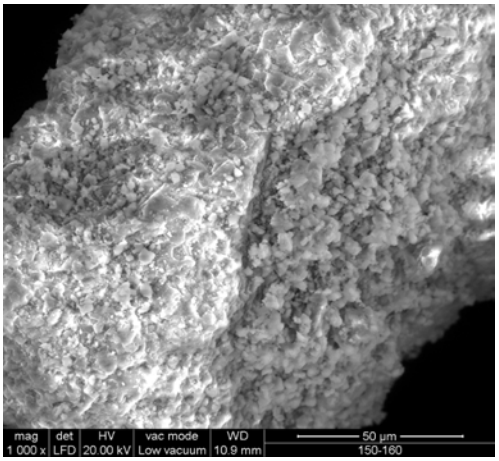

(b) *Particle detail with Large Field Detector (LFD).*

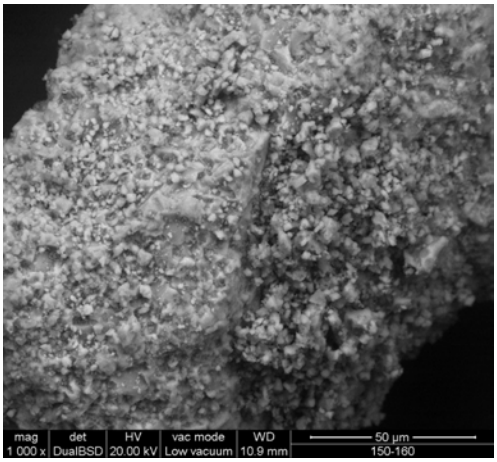

(c) *Particle detail with Back Scattered Detector (BSD).*

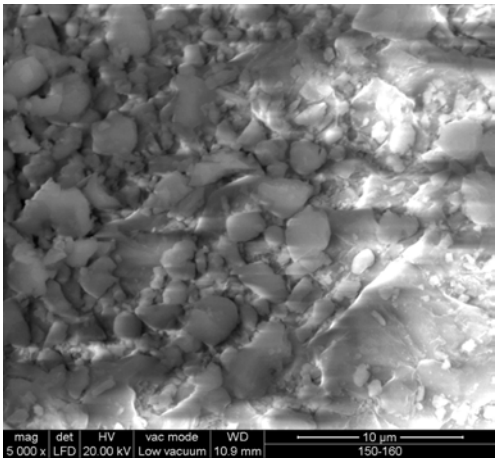

(d) *Surface detail.*

Figure 2.4: SEM images of precursor $CaCO_3$ with mean particle diameter of $150 \div 160\,\mu m$.

the high gas-solid interface that is established; instead a solid with a low specific surface presents a poor reactivity and it may undergo to incomplete conversion. For these reasons BET analysis (Brunauer, Emmett, Teller) was employed to estimate the total specific surface area, using nitrogen as gaseous adsorbent (a Quantachrome Autosorb iQ-MP instrument was used).

Brunauer, Emmett, and Teller, in 1938 [16], extended Langmuir's kinetic theory of monolayer adsorption to multilayer adsorption. The BET theory assumes that the uppermost molecules in the adsorbed layer are in dynamic equilibrium with the vapor. This means that where the surface is covered with only one layer of adsorbate, an equilibrium exists between that layer and the vapor; where two layers are adsorbed, the upper layer is in equilibrium with the vapor, and so forth. Since the equilibrium is dynamic, the actual location of the surface sites covered by one, two or more layers may vary but the number of molecules in each layer remain constant, according to [38].

First of all a BET analysis was performed on the calcium carbonate (precursor) sample in

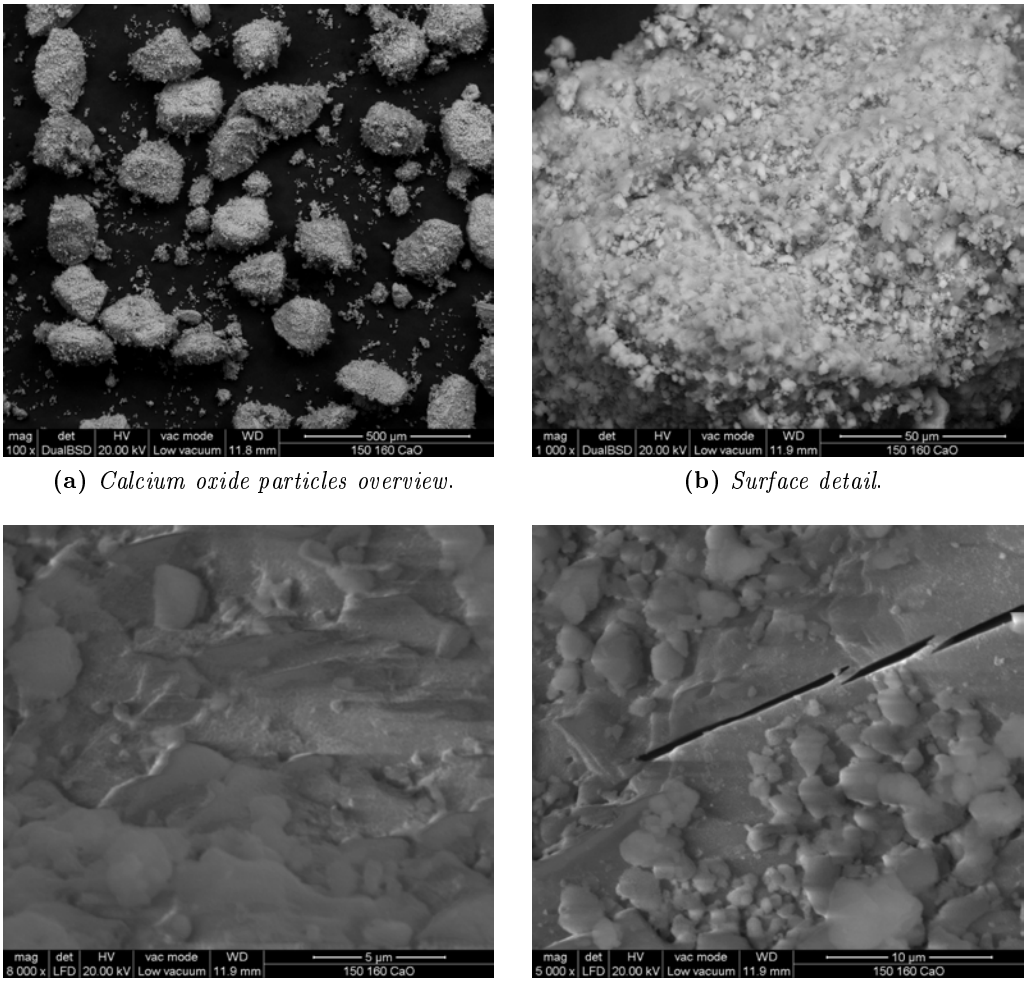

(a) *Calcium oxide particles overview.*

(b) *Surface detail.*

(c) *Enlarged surface detail.*

(d) *Fracture in the crystalline structure during calcination.*

Figure 2.5: SEM images of CaO obtained from limestone particles diameter of $150 \div 160\,\mu m$, calcined at $900\,^{\circ}C$ for $120\,min$ with an heating rate (HR) of $10\,^{\circ}C\,min^{-1}$.

order to estimate its initial specific surface and Fig. 2.6 shows BET results on material. The values are elaborated by a software that implement the Brunauer-Emmett-Teller method and in this particular case the specific surface area is $1.347\,m^2\,g^{-1}$. This result suggests that calcite has not a very extended pore network, rather, it seems to be a non-porous solid.

During the calcination reaction the solid phase is both converted into calcium oxide and thermally activated, so that the internal structure evolves up to generate an internal pore network that defines the specific surface of the material. Clearly, this process of pore enlargement is influenced by the operative conditions with which calcination reaction is carried out, namely calcination temperature, heating rate, permanence time and sample weight. Heating rate normally adopted was $10\,^{\circ}C\,min^{-1}$. Sample weight around $2\,mg$ are retained to sufficient low to reduce particle layer diffusivity. Material is arranged inside the muffle in such a way to ensure high CO_2 mass transport avoiding calcination inhibition. High temperatures and permanence times will favour sintering processes with a consequently loss of internal surface and a gain in pore volume.

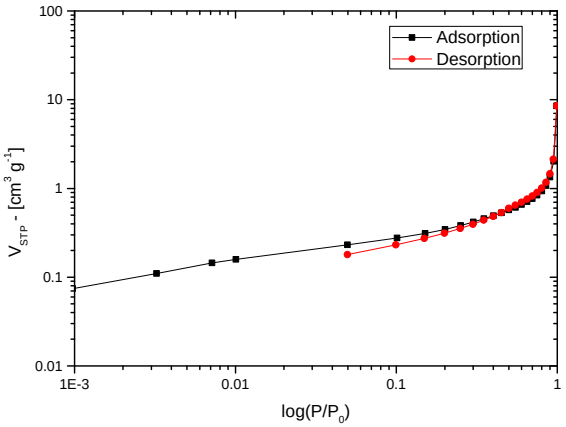

(a) *Isotherm: semi-log scale.*

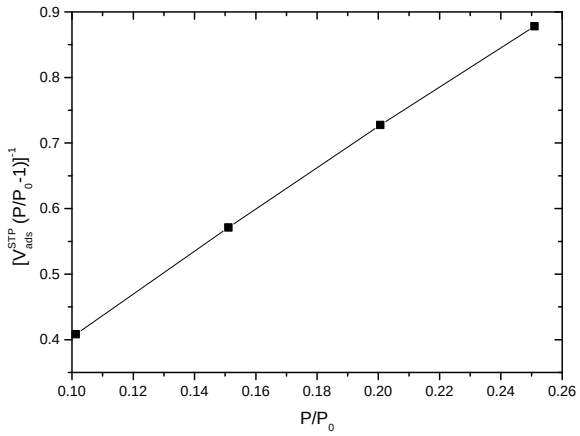

(b) *Multipoint BET method.*

Figure 2.6: BET analysis results of precursor calcium carbonate with particle diameter of $150 \div 160\,\mu m$. P_0 refers to the bulk fluid saturation pressure.

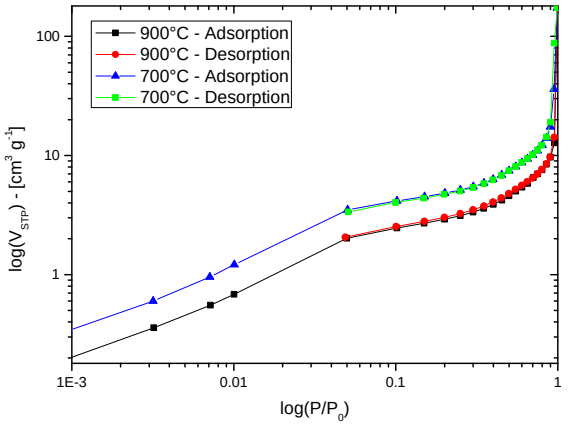

(a) *Isotherm: log-log scale, to emphasize the profiles.*

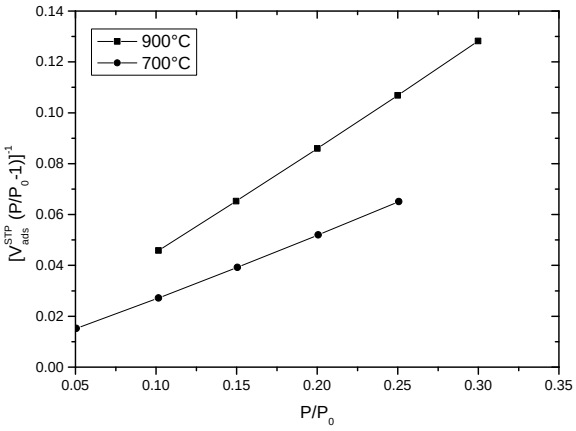

(b) *Multipoint BET method.*

Figure 2.7: Comparison of BET analysis results between two calcium oxide samples obtained with a calcination temperature of 900 °C and 700 °C respectively, HR of 10 °C min^{-1} and permanence time of 120 minutes.

Fig. 2.7 shows a comparison between two samples both calcined under 10 °C min^{-1} for 120 min, respectively at 900 °C and 700 °C. The low temperature calcined sample presents higher adsorption (and also desorption) profile than the high temperature one, that means an higher specific surface: the first one is 10.518 m^2 g^{-1}, because of high temperature that favours sintering; the second one is 17.296 m^2 g^{-1}. Though sintering is reduced the low temperature disadvantages the reaction equilibrium and the reaction rate, consequently, the sample was not completely converted and 14.6 % of calcium carbonate remained unreacted.

2.4.2 BJH analysis

The physical and kinetic properties of porous solids are strictly influenced by the void fraction that is determined by the pore network. Pore arrangement inside a particle can be extremely

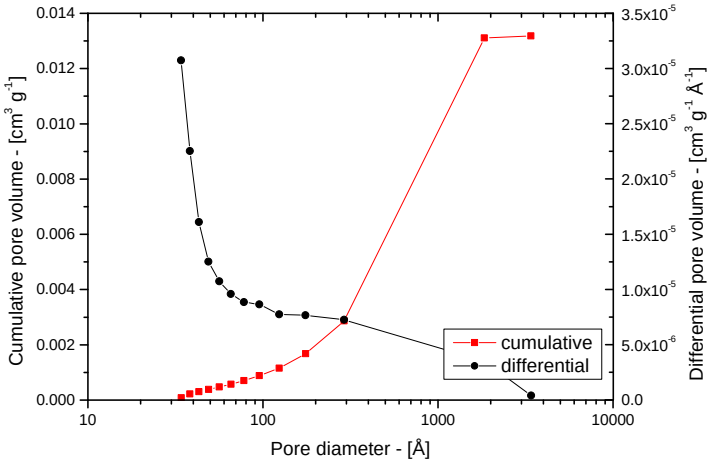

Figure 2.8: BJH analysis of precursor limestone, differential and cumulative distribution are reported.

complicated: actually straight pores do not exist, they have different diameters, different shapes and length and they can intersect each other. BJH method (Barrett, Joyner, Halenda) is a useful technique for estimating the pore size distribution using nitrogen isotherms.
IUPAC nomenclature classifies pores on the basis of their internal pore diameter[2] (assuming cylindrical shape pores) dividing pores in three main categories:

1. *micropore*: pore of internal diameter less than 2 nm;
2. *mesopore*: pore of internal diameter between 2 and 50 nm;
3. *macropore*: pore of internal diameter greater than 50 nm.

Most of the pores of the calcium oxide employed in this work belong to the mesopore category, indeed BJH method is particularly indicated for this pore size. The method is based on the physical adsorption of a fluid (nitrogen). Inside pores the most important phenomenon observed is pore condensation, which represents a first order phase transition from a gas state to a liquid state of the pure fluid occurring at a pressure P lower than the corresponding saturation pressure P_0 of the bulk fluid. The relative pressure when this condensation occurs depends on the pore diameter. The relationship between the pore size and the relative pressure when capillary condensation occurs can be described by the classical Kelvin equation.

First in Fig. 2.8 the pore size distribution of a calcium carbonate sample is reported that suggests a very low porosity, as confirmed by BET results of Fig. 2.6. Applying the BJH method to these results the sample has a total pore volume of $0.0131\,\mathrm{cm^3\,g^{-1}}$ and a total pore surface area of $1.2017\,\mathrm{m^2\,g^{-1}}$. The total pore volume multiplied by the particle bulk density provides the void fraction which is 0.042. This value is extremely low for considering calcium carbonate a porous solid.
As previously done with BET analysis, two calcined samples at 900 °C and 700 °C respectively (HR of $10\,^{\circ}\mathrm{C\,min^{-1}}$ and permanence time of 120 min) are employed for BJH analysis and the

[2]For slit pore the diameter corresponds to the distance between opposite walls.

Table 2.2: Summary of results of calcium oxide sample analysis: BET, BJH and XRD (sample composition in terms of mass fraction). HR of $10\,°C\,min^{-1}$, sample mass of 2 g in calcination.

sample	$T_{calc.}$ [°C]	time [min]	S_g $[m^2\,g^{-1}]$	ε $[m^3\,m^{-3}]$	% CaO [–]	% CaCO3 [–]
1	900	120	10.518	0.4912	96.1	0
2	700	120	17.296	0.4755	74.4	14.6
3	900	5	15.595	0.5197	44.7	1.2
4	900	10	15.308	0.4841	85.4	0.4
5	900	15	15.402	0.4859	81.6	1.4
6	900	30	14.002	0.4920	93.2	1.1

results are shown in Fig. 2.9. Sample calcined at higher temperature presents a total pore volume of $0.290\,cm^3\,g^{-1}$ and a total pore surface area of $10.518\,m^2\,g^{-1}$; the lower temperature one is characterized by a total pore volume of $0.272\,cm^3\,g^{-1}$ and a total pore surface area of $17.296\,m^2\,g^{-1}$, that means an higher pore volume opening and a lower pore surface is obtained at elevated temperature.

Fig. 2.11 shows BJH analysis on four samples calcined at different residence times. Typically, the higher residence times the lower specific surface area of the samples.
The differential pore size distributions showed in Figs. 2.9 and 2.11 appear to have a bimodal behavior. In reality, the pore size distributions presents only a maximum, that is the real mean pore diameter. The second maximum is due to the low number of the experimental points of BJH analysis. Fig. 2.10 shows how an higher number of experimental points allows a more accurate estimation of the differential pore size distributions.

All the previous results are summarized in Tab. 2.2, where the results of BET, BJH and XRD[3] analysis are listed.

2.4.3 Fine particle removal

Removing fine particles has the advantage to improve powder fluency and reducing packing, however it also causes a loss in interphase surface area due to fine particles. In order to separate a significant quantity of particles ($10 \div 20\,mg$), a sedimentator was built using water as solvent to suspend the particles. Powder was loaded in a vessel of cylindrical shape with a volume of about 3 L, then it was filled with water. Water was continuously fed above the particles in order to ensure particle good mixing. Because of difference of weight, heavier particles stratified on the bottom, whereas lighter particles remained suspended into the fluid. Once the vessel was completely filled, water overflowed bringing the suspended fine particles outside. As soon as water inside the vessel was completely clarified, water flow was stopped, sedimented particles were filtered and then dried.
Images of calcium carbonate particles before and after washing them are reported in Fig. 2.12. Fine phase is clearly visible even with an optical microscope. Fig. 2.13 reports BJH analysis on calcined calcium oxide after removing fine particles. This result must be compared with

[3]XRD analysis was used in order to determinate CaO composition.

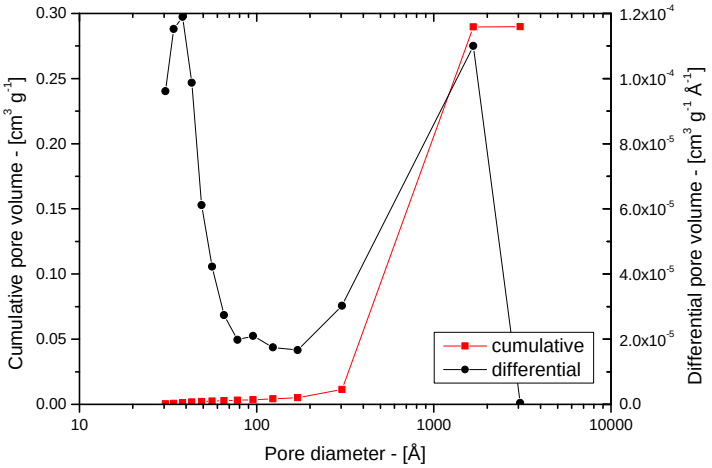

(a) *Calcination temperature at* 900 °C.

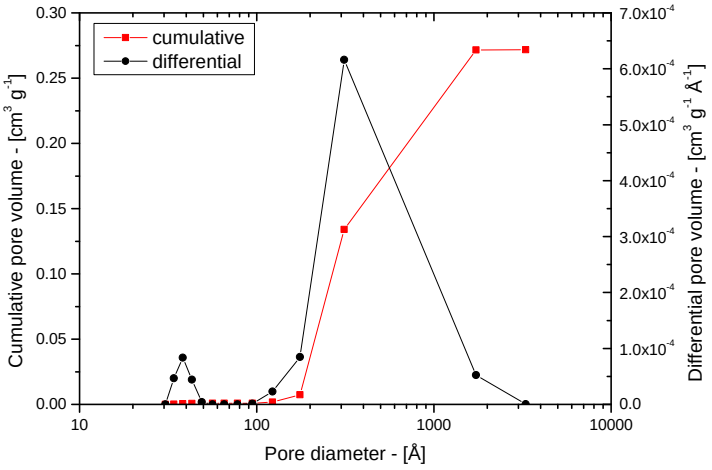

(b) *Calcination temperature at* 700 °C.

Figure 2.9: Comparison between BJH analysis of two calcined samples at temperature of 900 °C and 700 °C respectively, HR of 10 °C min^{-1} and residence time of 120 min.

Fig. 2.11a, where a sample of CaO with fine particles was calcined at the same conditions. The sample without fine particles is characterized by a total pore volume of 0.317 cm^3 g^{-1}, a total pore surface area of 13.078 m^2 g^{-1} and a void fraction of 0.514. These results seem to be lower than the alues of calcium oxide with fine particle (Tab. 2.2). Specifically, the specific surface area shows about 2.5 m^2 g^{-1} less.

2.5 Kinetic measurements: the Thermo-gravimetric analysis

2.5.1 General description

Thermo-gravimetric analysis (TGA) is an analytical technique used to determinate the thermal stability of a material and its fraction of volatile components by monitoring the weight change that occurs as a specimen is heated. More specifically, this approach is widely used in the scientific literature in the investigation of the gas-solid reactions. Referring to carbonation

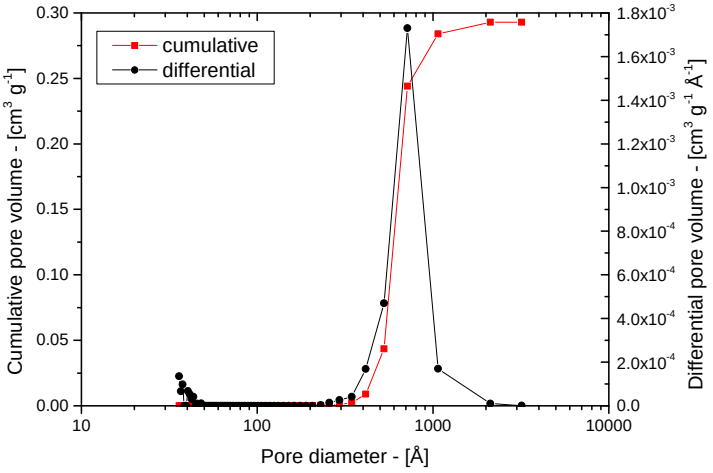

(a) *Calcination temperature at* 900 °C*, residence time* 180 min.

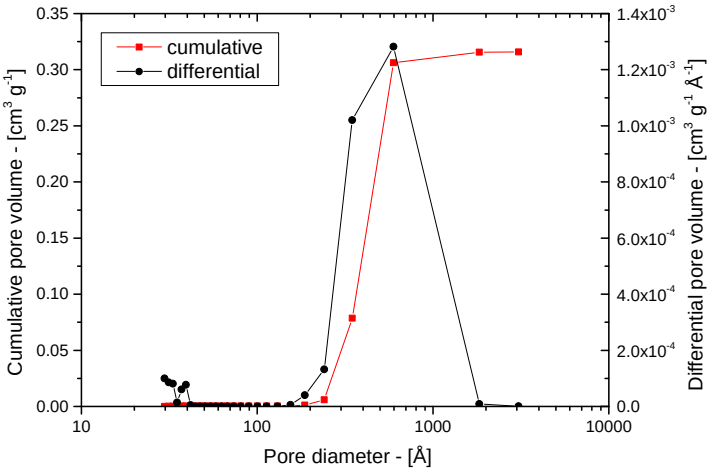

(b) *Calcination temperature at* 800 °C*, residence time* 120 min.

Figure 2.10: BJH analysis with large experimental values ($\sim$ 216 points). HR is 10 °C min^{-1}.

reaction, the calcium oxide samples are introduced in a reactor chamber, named furnace, with a controlled atmosphere, a temperature program is planned and the resulting changes in weight are measured by a balance and then registered by a computer software. TGA instruments can be divided into two general types: vertical and horizontal balances. The vertical ones have a specimen pan hanging from the balance or located above the balance on a sample stem; the horizontal ones normally have two pans and they can perform differential thermo-gravimetry (DTG) and differential thermal analysis (DTA) measurements.

2.5.2 TA SDT Q600

In this work of thesis the TA SDT Q600 was used only for a computational fluid dynamics (CFD) study. Thus, a detailed knowledge of the components and geometry is necessary.

The TA SDT Q600 is an horizontal thermo-balance which can work at temperatures up to 1500 °C at atmospheric pressure. As shown in Fig. 2.14, the instrument is composed by sev-

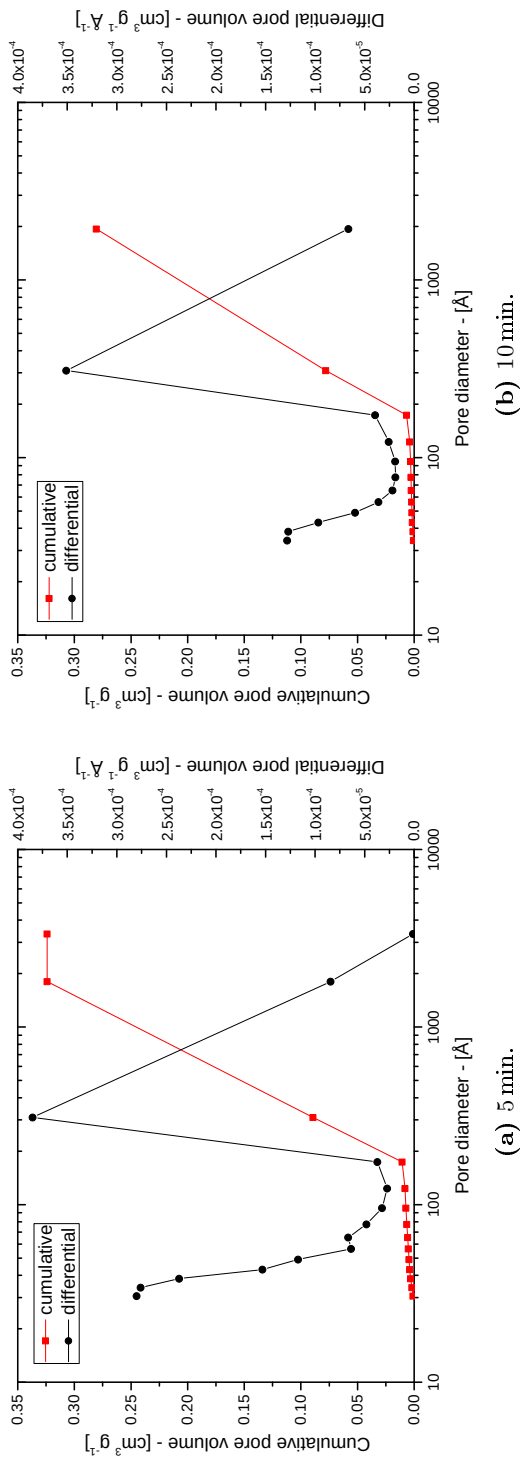

(a) 5 min.

(b) 10 min.

(c) 15 min.

(d) 30 min.

Figure 2.11: Comparison between BJH analysis of samples calcined at different residence times. Calcination was performed at 900 °C, HR of 10 °C min^{-1}.

(a) *Limestone with fine particles.*

(b) *Limestone with fine particles.*

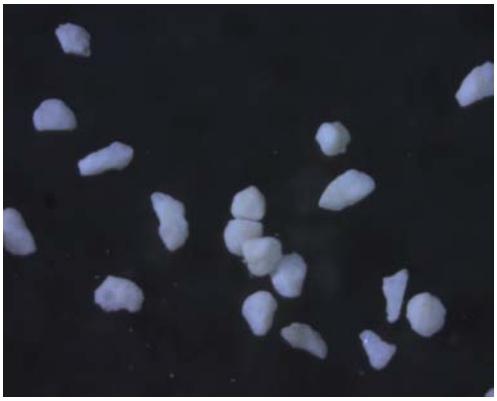

(c) *Washed particle limestone.*

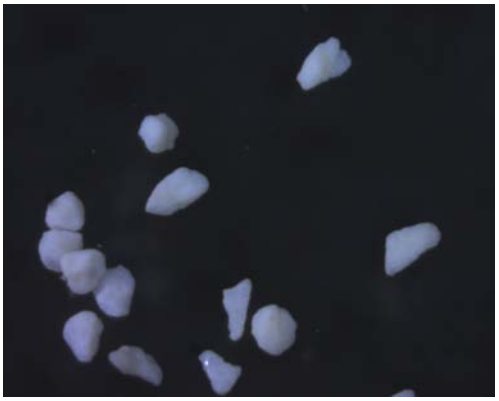

(d) *Washed particle limestone.*

Figure 2.12: Optical images of $150 \div 160\,\mu m$ limestone particles before and after washing.

eral components: a balance, an heating system, a tubular furnace, an unit for the temperature measurement and a recording system. The heater warms up the reaction chamber following a specific temperature profile set up by the user, inside the tubular furnace there are two beams that hold two crucibles at their extremities, where the sample is charged. The beams are linked to a thermo-balance that measures the temperature of the crucibles (by a thermocouple) and the change of the sample weight. The furnace atmosphere is fed from the reactive gas tube connected to a specific line of inert or reactive gases. Downstream of the crucibles the reaction chamber tapers until reaches the purge gas zone, where exhaust gases leave the reaction chamber. The horizontal purge gas system has a digital mass flow control and the design prevents back diffusion and removes efficiently decomposition products from the sample area.
The TA SDT Q600 provides simultaneous measurement of the weight change (TGA) and differential heat flow (DSC), the instrument being equipped with two crucibles. One works as reference weight the other is designed to contain the sample, so the instrument can perform heat flow measurements starting from differential temperature measurements. Instruments that can perform only TGA measurements are provided with only one sample holder.

The material of which the crucible is made must not influence the sample reaction, thus, in general, alumina (aluminium oxide) crucibles are used for TGA measurements and in this work

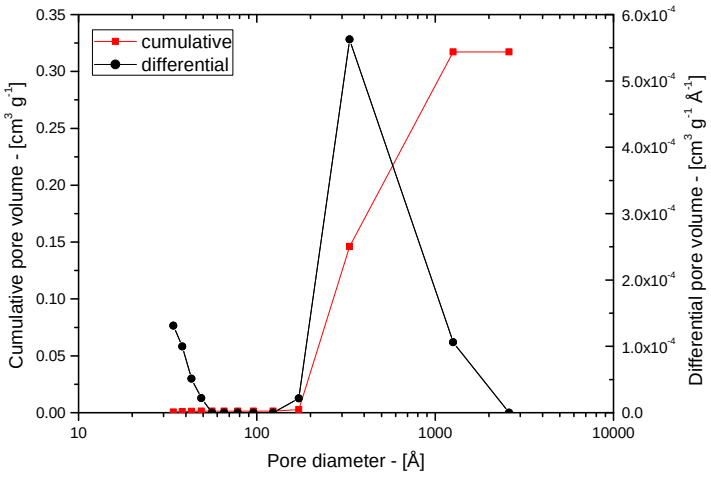

Figure 2.13: BJH analysis of calcined calcium oxide after removing fine particles. Calcination conditions: 900 °C, HR of 10 °C min^{-1} and residence time of 5 min.

of thesis crucibles of this material were employed. These have the advantage that they can be heated up to 1600 °C. A schematic representation of the crucible geometry is reported in Fig. 2.15 which shows the crucible placed into the sample holder, below which there is a thermocouple that measures the local temperature. The entire structure is supported by an alumina beam arm linked to the balance of the instrument.

2.5.3 Geometry

In this work the crucibles used are two cylindrical basket of different heights and a schematic representation is shown in Fig. 2.15.

The total furnace length is 8.5 in (215.9 mm) and as shown in Fig. 2.14 its geometry is made of three parts: the first one is a constant diameter section where the heater, the balance beams with crucibles and the reactive gas tube are placed. The second one is a tapering section that starts with a 0.9 in inner diameter and tapers to 0.15 in (22.86 mm and 3.81 mm respectively), this portion has an extension of 1.07 in (27.18 mm). The last part is a constant diameter section with a length of 0.58 in (14.72 mm) that conveys the gas to the instrument outlet.

Fig. 2.16 shows a side view of the first region (names and values of the abbreviations are reported in Tab. 2.3.) The length of this region is 174 mm and crucibles are placed in the center of the furnace axis at 87 mm from the wall.

Reactants gases are fed into the TGA through the reactive gas tube so that they are axially injected into the furnace by a sudden expansion that goes from 1/32 in (reactive gas tube inner diameter) to 0.9 in (furnace inner diameter), namely 0.7937 mm and 22.86 mm respectively. The sudden expansion allows the reactant gases to reduce their mean velocity. The gases flow above the crucibles and reactants diffuses into the solid material. Reaction products, unreacted gas and inert gas are then discharged outside the furnace.

The first crucible is where the sample is loaded, the second one is the reference sample for DSC measurements. As represented in Fig. 2.17, the first crucible has an internal diameter of

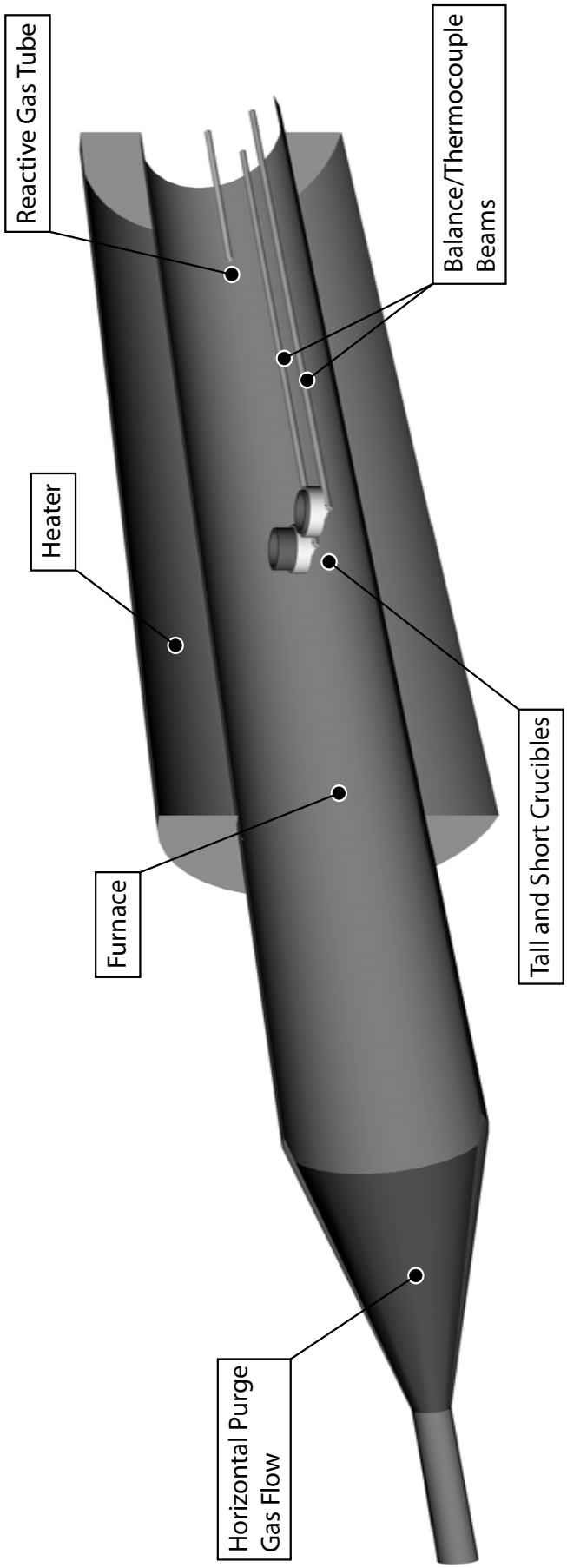

Figure 2.14: A schematic of the TA SDT Q600 geometry.

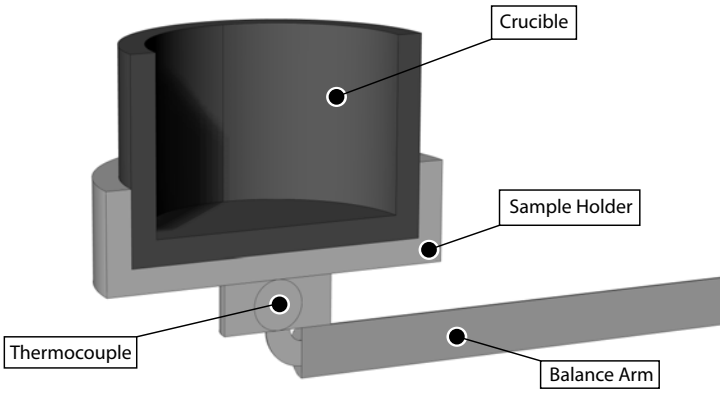

Figure 2.15: A schematic representation of the crucible geometry of TA SDT Q600.

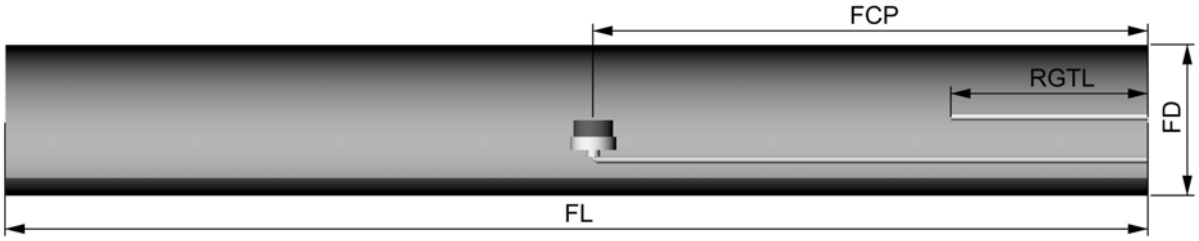

Figure 2.16: TA SDT Q600 side geometry.

5 mm and an height of 2 mm. This crucible was selected in order to reduce the diffusion resistance in the gas phase of the chemical reactive species, that flow from the bulk to the internal of the crucible.

The reactive gas tube is horizontally centered and it is placed at 7.6 mm from the top of the furnace. The beams are placed at 7.6 mm from the bottom of the furnace and their distance from each other is 7.66 mm as shown in Fig. 2.18 in which an overhead view of the furnace is presented.

2.5.4 Crucible and particle layer morphology

When a mass of particles of calcium carbonate between $2.5 \div 10$ mg is poured into the crucible, a particle layer is established and its thickness increases with the weight of the sample following. On the contrary, the lower sample weight, more difficult is the particle layer thickness estimation.

In fact as the sample weight decreases till 2.5 mg the particles of CaO do not cover the entire internal section of the crucible and they distribute with empty regions, regions where particles organize themselves establishing a mono-layer and regions where particles overcome each other generating two, three or four layers.

Fig. 2.19 shows some photos about a crucible loaded with 2.5 mg of calcium carbonate shot by an optical microscope, above which a digital photo-camera was installed. The material was poured and then tapered in order to obtain a uniform particle layer, however, as shown in

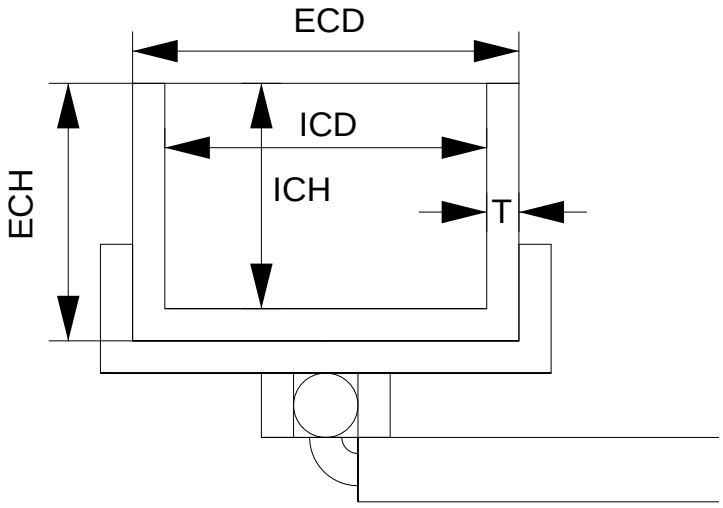

Figure 2.17: Two dimensional crucible geometry.

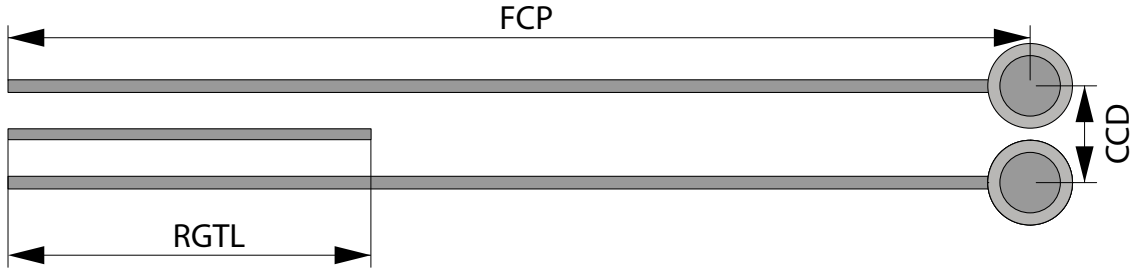

Figure 2.18: TA SDT Q600 overhead view.

Fig. 2.19, this was difficult to achieved, consequently, some area remains empty and some are covered by one o more layer of particles.
Observing the particle distribution inside the crucible it can be noticed a central zone where particles are more concentrated than in the rest of the surface. This suggests that the crucible bottom surface is not levelled and seems to have a circular concentric depression where particles sit on.

Fig. 2.20a shows two optical microscope images of the empty crucible surface. Clearly, the crucible surface area is not smooth but it shows asperities and roughness that reduce the ability of homogenization of the particle layer. Furthermore, Fig. 2.20b shows clearly the circular depression region where the particle tend to accumulate. In order to investigate the roughness of the crucible bottom an optical profilometer was used to scan the surface obtaining a 3D map. The scanned areas have a diameter of 3.5 mm from the center of the crucible and the obtained images are reported in Fig. 2.21.

Figs. 2.21 and 2.22 show that the crucible surface is extremely heterogeneous and is characterized by a large number of asperities of different shape and size. However, most of them only offer attrition to the motion of the particles determining a more difficult homogenization of the particle layer. Instead, the concentric depression has an important impact to the material distribution which tends to concentrate toward the center of the crucible.

Table 2.3: List of quantities and depth shown in Figs. 2.16, 2.17 and 2.18.

Furnace geometry		
abbr.	description	value [mm]
FD	furnace diameter	22.86
FL	furnace length	174.00
RGTL	reactive gas tube length	40.00
FCP	crucible position in the furnace	87.00
CCD	crucible center distance	7.66
Crucible geometry		
abbr.	description	value [mm]
ECD	external crucible diameter	6.5
DICD	internal crucible diameter	5.5
T	crucible thickness	0.5
ICH (1)	first internal crucible height	2.0
ECH (1)	first external crucible height	1.5
ICH (2)	second internal crucible height	3.5
ECH (2)	second external crucible height	4.0

Fig. 2.23 reports the profile depression. Roughly, it has a 2.4 mm of diameter with a depth of 70 µm. The path slope from the lateral zone to the central one is not sharp, but occurs with an inclination of about 20°. Since the particle diameter is 150 µm, the single particle of material is inside the valley for the half of its diameter.

2.5.5 Experimental procedure

The first TGA tests were conducted in TA SDT Q600. However, the best TGA results were obtained with DynTHERM MP-ST by RUBOTERM GMBH that is a vertical TGA and the sample weight measurement is performed by a suspension magnetic balance.

The carbonation reaction was performed by loading a known mass of CaO and running a specify temperature program. The temperature and the sample weight are continuously recorded on a computer. In order to obtain reproducible results it is important to follow a procedure that was developed. The aim of the whole procedure is to avoid the potential phenomena that occur can during the reaction time, with the purpose to obtain intrinsic kinetics data (such as resistances due to external mass transfer, inter-particle and intra-particle molecular diffusion).

A fully calcined calcium oxide is weighted and than loaded into the crucible; typically a mass between $2.5 \div 10$ mg is used. The granular material is poured into the crucible which is tapered in order to obtain a uniform (in as much as possible) particle layer. Afterwards, the crucible is placed into the sample holder inside the furnace[4], then some times should be waited before the beginning of the experiment until the weight measurement does not vary. When the weight measure is sufficiently stable, the test can start. The furnace temperature at which the sample is

[4]The furnace can be accessed to the user by an opening and closing system, in fact the furnace can axially move exposing the crucibles.

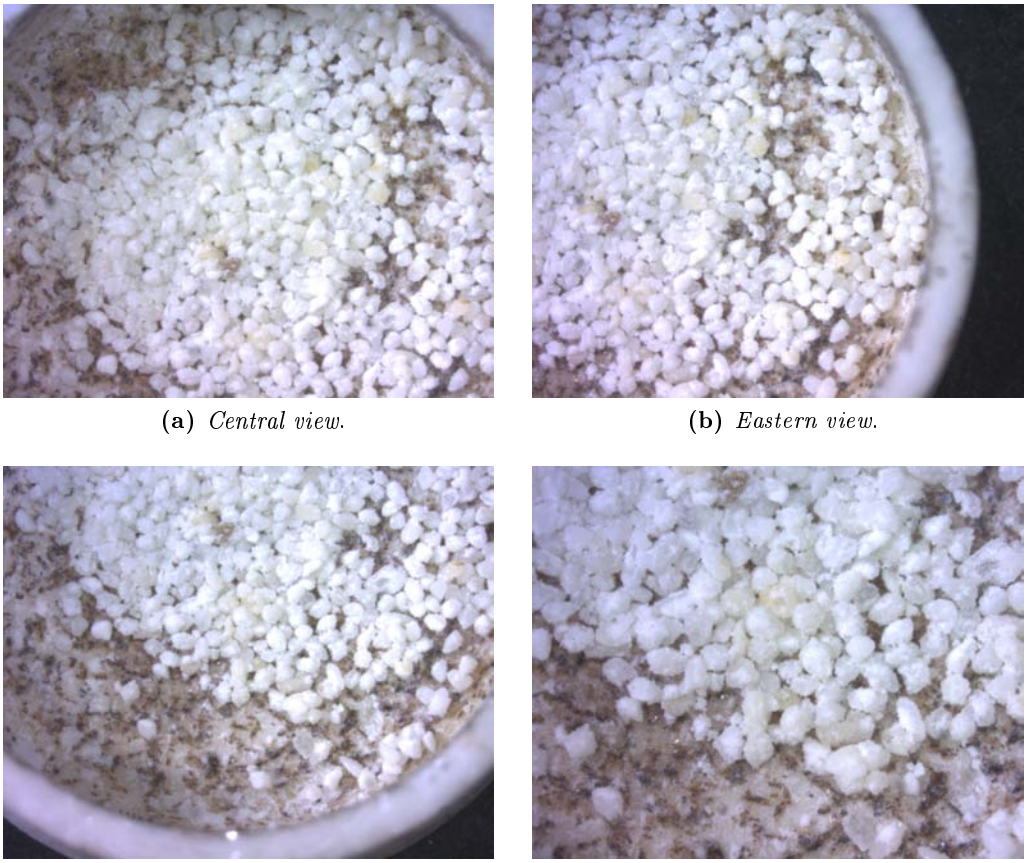

(a) *Central view.* **(b)** *Eastern view.*

(c) *South view.* **(d)** *Detail of particle layers.*

Figure 2.19: Shots of the particles in the crucible.

loaded is around $20 \div 30\,°C$, this range allows to obtain a stable weight measure because of the low difference between the room and furnace temperature. After the test is started, the heater begins a temperature ramp (typically $50\,°C\,min^{-1}$) meanwhile the reaction chamber is fluxed by pure nitrogen (typically $200\,mL\,min^{-1}$). The furnace is heated till $450 \div 650\,°C$ depending on the equilibrium conditions, indeed, it is important to establish a sufficient driving force in terms of CO_2 partial pressure[5] in order to allow reaction Eq. (2.1) to occur. To achieve this, it is useful to consult Eq. (2.2) and Fig. 2.2. When isothermal conditions are reached, a gas switch is performed from the inert atmosphere to the reactive gas which consists of a mixture of nitrogen and carbon dioxide. Volume fraction of carbon dioxide should be varied on the basis of carbonation temperature, in order to obtain a sufficient driving force in terms of CO_2 partial pressure. Isothermal reaction conditions under reactant gas are maintained for about 20 min, than the heater turns off and the furnace slowly cools down. When the reaction chamber reaches the room temperature, the crucible can be taken out and unloaded.

In the meanwhile, the computer software has recorded time, weight, temperature, heat flow, temperature difference between crucibles and the derivative of the weight with respect to time or the temperature.

[5]The TGA SDT Q600 can operate at atmospheric conditions, so that reaction occurs at isobaric conditions.

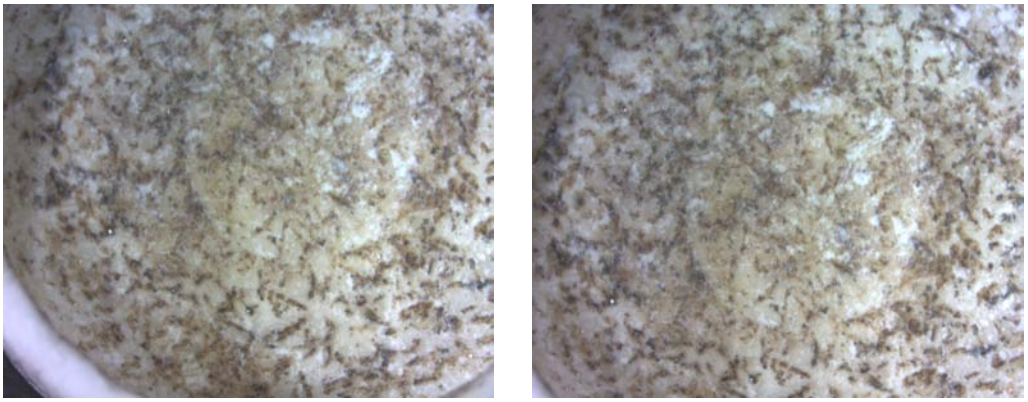

(a) *Overview of the superficial roughness.* **(b)** *Detail of the depression zone.*

Figure 2.20: Shots of the surface of the crucible.

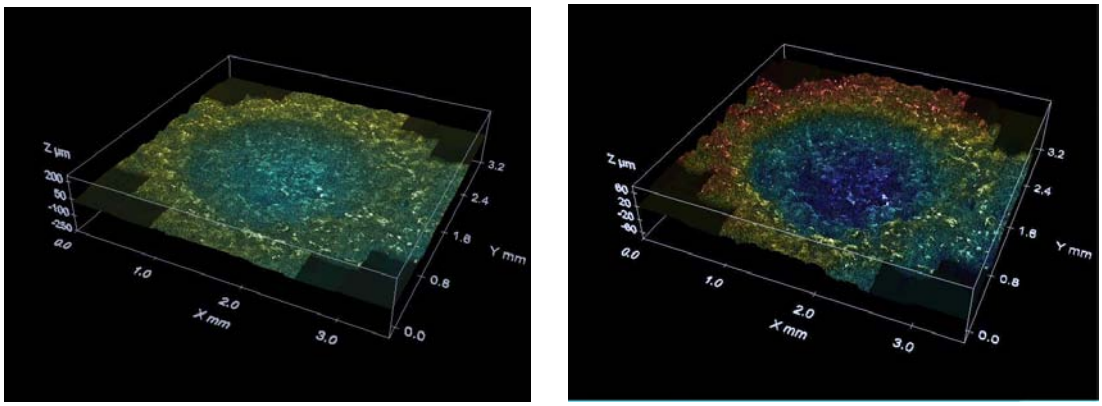

(a) *Tree-dimensional map of the crucible surface.* **(b)** *Rescaled tree-dimensional map of the crucible surface.*

Figure 2.21: Bottom surface of the alumina crucible obtained by optical profilometer.

2.5.6 Experimental results

The whole procedure is summarized in Fig. 2.24 which represents the mass and temperature change during a typical experiment with about 10 mg of sample. In this case also a preliminary calcination step is reported , through which porous CaO is obtained from $CaCO_3$ (non-porous) before the carbonation.

Considering only the carbonation step, it is common to express TGA tests in dimensionless form through the fractional conversion X defined as

$$X = \frac{(m - m_{\text{calcined}})\ M_{\text{CaO}}}{m_{\text{calcined}}\ M_{\text{CO}_2}\ \chi}, \tag{2.4}$$

where m_{calcined} is the initial mass of the fully calcined sample, m is the measured mass of the sample during the carbonation reaction, χ is the mass fraction of the active CaO in the sample, which takes the value of 1 in this work due to the high purity of $CaCO_3$ that decomposes into calcium oxide, M_{CO_2} and M_{CaO} are respectively the molar mass of carbon dioxide and calcium

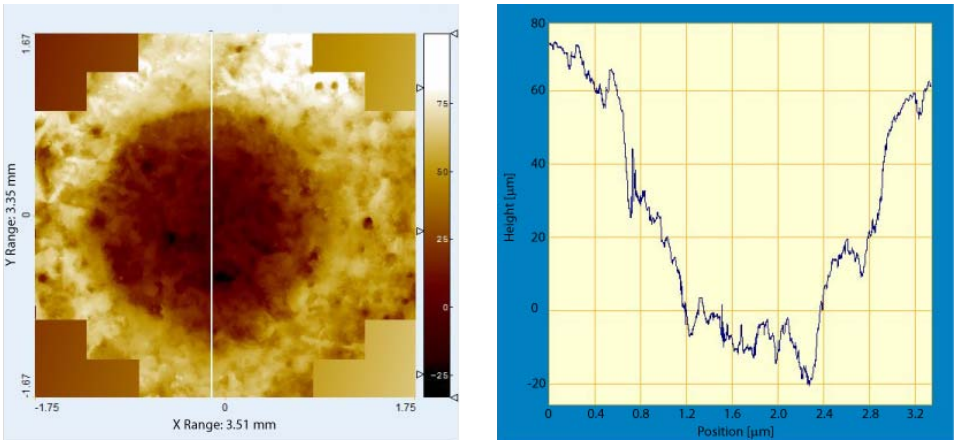

(a) *Two-dimensional overview of the crucible surface. The values of the color map on the right side are in* µm.

(b) *Surface profile along the vertical line at* $x \approx 0$.

Figure 2.22: Surface profile along a vertical line from profilometer.

oxide. If impurities are present in the starting material, such as mayenite or hematite, χ will be less than one.
It is known [2] that TGA results may be affected by physical limitations of the instrument and experimental procedures employed. There are many factors which influence a TGA curve and they may be due to the instrumentation, to operative condition or to the sample properties. The main factors which affect the precision and the accuracy of the experimental results in thermogravimetry are listed as follows:

1. *operative conditions*: temperature, gas flow rate, furnace atmosphere;
2. *instrumental factors*: geometry of the crucible, composition of the sample container, sensitivity of the recording system;
3. *sample properties*: sample weight, particle size, heat of reaction, sample packing.

In the previous sections the crucible geometry and the particle layer morphology were discussed. The other effects are reported in the following paragraphs.

Influence of the temperature on the carbonation kinetics

A typical plot showing the effect of the temperature on the carbonation kinetics is shown in Fig. 2.25. The conversion-time curve obtained at 450 °C appears to have a weak temperature dependence rather than 550 °C and 650 °C curves. No strong influence is shown for temperature higher than 550 °C, whereas, for low reaction temperature, conversion curve are strongly affected by experimental conditions. Certainly this phenomena can be explained with kinetic constant, that increases its value in an exponential way following the Arrhenius equation. However, it is important to emphasize that TGA curves may records apparent reaction kinetics which may account several physical limitations.

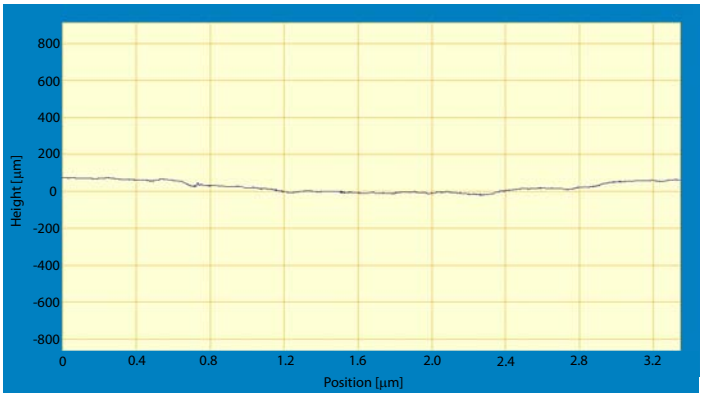

(a) *Real dimensions.*

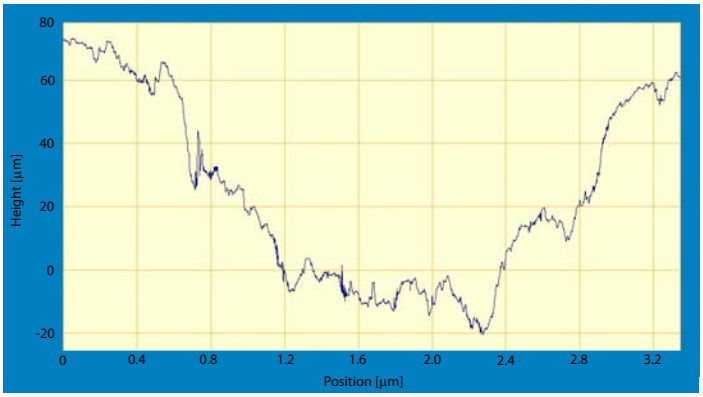

(b) *Rescaled dimensions.*

Figure 2.23: Crucible depression profile along a straight line at $x \approx 0$.

Influence of the gas composition on the TGA measurements

Reaction kinetics depends on the gas reactant composition, namely a higher CO_2 partial pressure means a higher driving force at the same temperature (Fig. 2.2). A typical plot showing the effect of the gas composition on the conversion-time curves is shown in Fig. 2.26. In fact, the intrinsic kinetics of the carbonation reaction depends by $(p_{CO_2} - p_{CO_2,eq})$ that is the real driving force of the reaction. Furthermore, following Sun et al.'s work [59], when $(p_{CO_2} - p_{CO_2,eq}) \leq 10\,\text{kPa}$ the reaction follows a first order kinetics, otherwise, beyond 10 kPa in CO_2 driving force the carbonation reaction becomes zero-order.

Influence of the gas flowrate on the TGA measurements

When isothermal conditions are reached, the preselected program switches the injected gas from the inert gas to the reactant gas. The higher gas flow rate, the faster the reaction front reaches the sample surface, reducing induction the time. Furthermore, when the reactant gas flows with an higher spatial velocity gas mass transport from the bulk to the particle layer is increased.

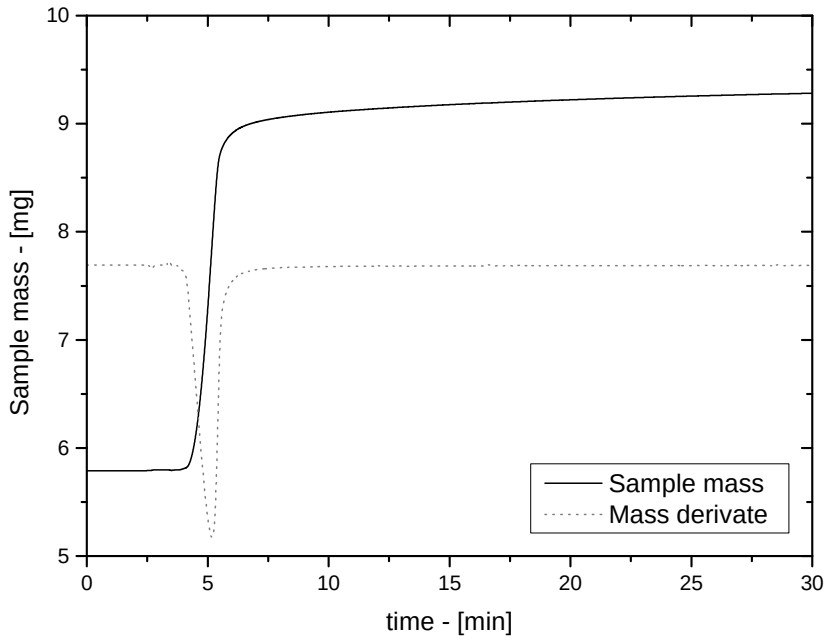

Figure 2.24: Typical experiment starting from calcium carbonate. Carbonation takes place at isobaric condition.

Effect of sample weight on the TGA measurements

The kinetic rate of the reaction can be obtained by TGA conversion-time curves that they should be independent from the mass of reactant. As can be seen in Fig. 2.27 the increase of sample mass clearly improves the quality of the measurements. This means that the intrinsic kinetics is not measured, because this should be independent from the extension of system. In reality TGA results produce an apparent kinetic rate of the process due to the increase of mass sample that means a higher sample height. This experimental situation increases diffusion resistance inside the particle layer (inter-particle diffusion, through the void space around solid particles), establishing a more pronounced concentration gradient of the gaseous reactant.

Effect of particle size on the TGA measurements

Generally the particle size causes a change in the intra-particle diffusion of gases which alter the reaction rate and hence the curve shape. The smaller the particle size, the greater the extent of conversion at any given temperature. Tests conducted using samples with different particle sizes reveal that TGA curves of large particle size seem to be slower in first instants of reactions, whereas they reach higher conversion values for high reaction times. Furthermore, the particle size interval of $45 \div 75\,\mu m$ and $200 \div 400\,\mu m$ yielded identical conversion curves, which is an indication that intra-particle diffusional resistance affect the results only above a specific particle size, e.g., $600 \div 800\,\mu m$ (Fig. 2.28).

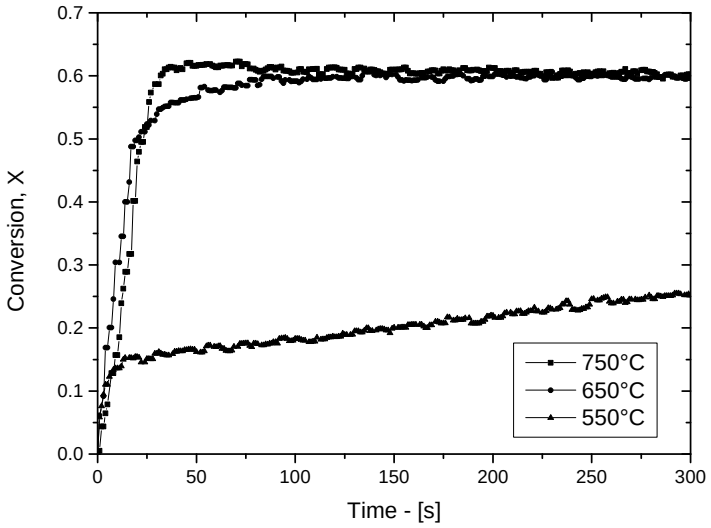

Figure 2.25: Conversion of CaO versus time at different carbonation temperatures obtained with DynTHERM MP-ST. Sample weight of 65 mg, 5 bar, 100 % of CO_2, particle size 150 ÷ 160 µm.

Sources of error in TGA

There are several sources of error in TGA and they can lead to inaccuracies of the recorded temperature and of mass data. Specifically, a buoyancy effect arises when the crucible is heated in the furnace atmosphere or when the bulk gas switches to another gas species. When the crucible is empty or the mass sample is low, there is usually an apparent weight change as temperature increases. This is due to the change in buoyancy of the gas in the sample environment with the temperature. Even if this effect is low, a blank run with an empty crucible is recommended. The resultant record can be used as a correction curve for the subsequent experiment performed in the same conditions. Buoyancy effects may arise when the furnace atmosphere is switched from the inert gas to the reactant gas.

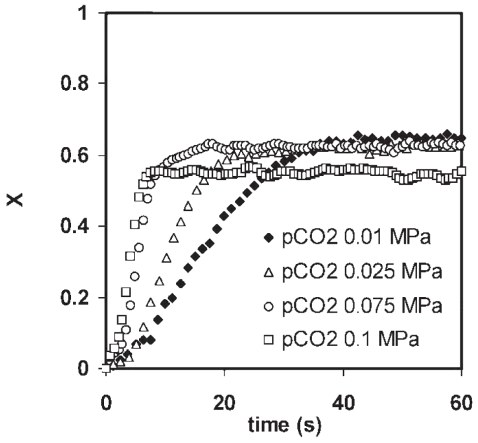

Figure 2.26: Conversion of CaO versus time for different CO_2 partial pressure. Carbonation temperature 650 °C. Source: Grasa et al. [24].

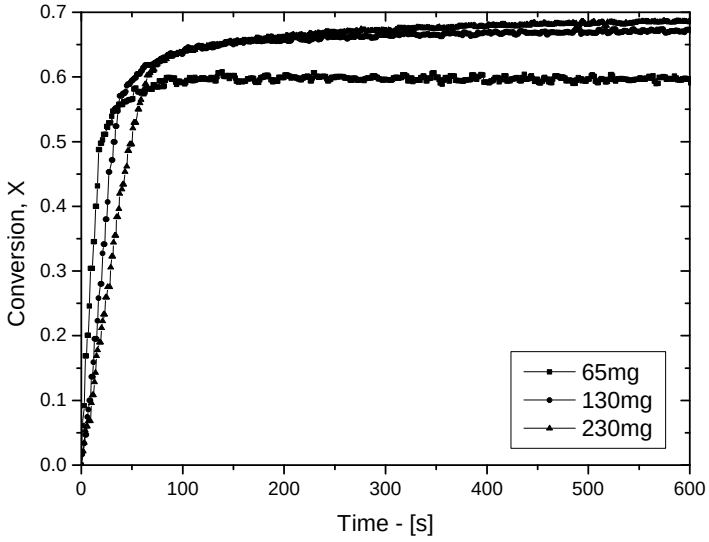

Figure 2.27: Conversion of CaO versus time using different sample size. Test performed with the DynTHERM MP-ST at 650 °C, 5 bar, 100 % of CO_2, particle size $150 \div 160$ µm.

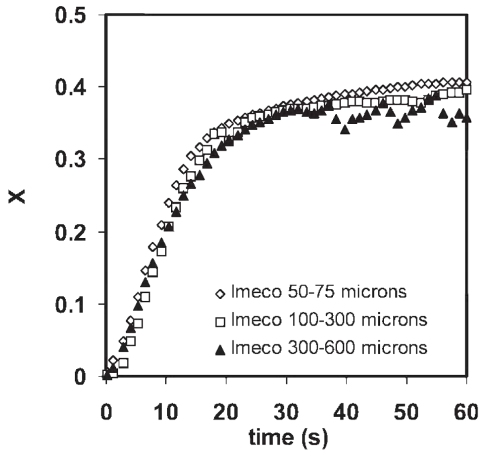

Figure 2.28: Conversion of CaO versus time for different particle sizes. Carbonation temperature 650 °C, 0.01 MPa of CO_2. Source: Grasa et al. [24].

Additionally, several experimental tests showed that fluctuations of the balance mechanism and convection effects of the gas flow (specially at high flow rate) may add noise to the TGA results.

2.6 Physical limitations in TGA tests: the intrinsic kinetics problem

From the discussion at previous sections, it should be clear that many phenomena occur during TGA tests and each one of them has its own rate.Such phenomena may verify simultaneously or one after the other depending of the operative conditions. With the aim to determinate kinetic parameters of the carbonation reaction, physical limitations should be reduced. This can

be achieved when all other processes are faster than the chemical reaction, so that they can be neglected ("kinetic controlled regime").

Typically, TGA tests measure an apparent kinetic rate which is the combination of the rates of several phenomena. This may lead to measure kinetic parameters that are affected by heat and mass transfer resistances. The problem to estimate the intrinsic kinetic rate is extensively discussed in the scientific literature in a several contributions such as [13], [14], [1], [3], [59], and [24].

When the TGA furnace has reached isothermal conditions, the gas flow rate is switched from inert gas to carbon dioxide. In this precisely instant several physical limitations start , specifically such resistances are due to:

1. *external diffusion*: the reactant gas employs a certain time to reach the crucible positions from the outlet of the reactive gas tube and this can be regarded as a delay related to the gas flow rate. When the front arrives to the crucible, mass transport of carbon dioxide occurs from the bulk flow to the sample surface, adding another time delay to the process;

2. *inter-particle diffusion*: the reactant gas must diffuse within the sample through molecular diffusion from the particle layer surface down to the bottom of the crucibles. A concentration profile is established inside the sample;

3. *intra-particle diffusion*: the carbon dioxide diffuses inside the pore network of each particle realizing a concentration profile inside the solid particles;

4. *product layer diffusion*: during the early stages the reaction takes place inside the pore surface and this fast kinetic regime occurs until a thick product layer is generated. Afterwards, the reactant gas must be adsorbed on the product layer surface and diffuse inside the solid matrix reaching the unreacted calcium oxide where reaction occurs. This last stage becomes the slower one when a critical product layer is reached and changes the process regime in the product diffusion controlled one.

Several strategies have been developed in order to eliminate the mass transfer resistances that affect the intrinsic kinetic measurements.

The first one consists to increase the gas flow rate up to reduce the external diffusion, but it cannot be completely eliminated because the TGA only works in laminar conditions. Further, high flow rates influence balance measurements giving noisy responses. For this reason crucibles with short height should be preferred. However, crucible height can not be too low because the gas flow rate may drift the sample particle causing instrument degradation.

Particle layer resistance increases with the sample thickness and the particle packing. Low sample mass means low particle layer thickness. If the sample mass is small enough, a mono-layer can be generated. This can be considered as an ideal situation because of the difficulty to obtain an homogeneous layer and because of crucible bottom asperities (Figs. 2.19 and 2.20). Mono-layer generation is difficult with cohesive powders and this situation can be improved removing fine particles phase as reported in § 2.4.3.

Intra-particle limitation is due to the molecular diffusion of the reactant gas inside the particle pores. Larger particle diameters produce steep concentration profiles that may become the controlling step with low particle porosity or high particle tortuosity.

When carbon dioxide reaches the active sites of calcium oxide, the reaction shows an initial rapid and chemically controlled step, followed by a second slower one controlled by product layer diffusion. This transition takes place quite suddenly at a given extent of conversion and due to the growing particle layer thickness and to the small pores closure (which determines a loss in gas solid interface area). Intrinsic kinetics depends on temperature carbonation and gas reactant partial pressure. Specifically, low temperature and CO_2 partial pressure favours kinetic/ product layer diffusion controlled regions. Product layer diffusivity can vary only with temperature following following an Arrhenius's like equation.

Chapter 3

Kinetic Models for Non-Catalytic Gas-Solid Reactions

This chapter deals with the structural kinetic models for non-catalytic gas-solid reactions that were developed during the 20^{th} century. The aim of this chapter is to underline the advantages and the drawbacks of different kinetic models in order to find the most suitable one for carbonation reactions. The first and simpler model that is presented is the "grain model". The governing equations of the model are derived for kinetic controlled regime, product layer diffusion controlled regime and for simultaneous reaction and diffusion.
Because of the several drawbacks of this model, the scientific literature focused on modeling the particle porosity and this kind of models take the name of "pore models". By this way, Petersen model is than presented and it may be retained one of the first pore models accounting pore intersections and overlap for kinetic controlled processes. However, its empirical assumptions made the model unable to describe structural changes in solid phase during reaction. Afterwards, in § 3.4 the random pore model of Bhatia and Perlmutter [11] is described, which assumes that the solid reactant is made of random overlapping capillaries. Even though the assumptions of this model are reasonable, a good agreement with experimental data is obtained only for limiting regimes (kinetic or product layer diffusion regime). The last model presented was independently developed by Bhatia [10] and by Sotirchos et al. [57] and models gas-solid reactions under conditions of simultaneous reaction and product layer diffusion. Furthermore it accounts for pore closure and incomplete conversion when gas-solid reactions occur with solid product generation and when the molar volume of the product layer is larger than the solid reactant.

3.1 Introduction

The reaction of a porous particle with a gaseous species is a complex process whose complete analysis needs consideration of a large number of physical and chemical processes. It involves mass transport of gaseous reactants and products in the surrounding gas phase, mass transport in the interior of the porous particle, diffusion in the product layer and reaction on the product-reactant interface. For exothermic or endothermic reaction systems, it may also be necessary to

consider the effects of heat transport in the surrounding gas phase or even in the interior of the porous particle.
These processes are not uniquely related to non-catalytic gas-solid reactions, but they are also met in the catalytic gas-solid systems. However the distinguishing feature of non-catalytic gas-solid systems is the evolution of the pore structure that takes place because of the physical and chemical changes the reacting solid undergoes. Hence the necessity to built a suitable mathematical model that takes into account not only the gas-solid chemical reaction at the interface, but also the physical changes of the solid structure due to the reaction in terms of pore size, internal and external surface, product layer thickness and pore overlapping. Furthermore the porous network can be extremely complex, consequently, a pore size distribution should be considered in order to take into account the different pore sizes that may evolve during the reaction process.

The mathematical analysis of the pore structure evolution is further complicated by the deposition of the solid product on the surface of the reacting solid, consequently, the gaseous reactants must diffuse through this layer in order to reach the unreacted solid. Because of the high diffusional resistance of the product layer, the concentration of the gaseous reactant at the reaction interface may be non-uniform even under uniform temperature and concentration in the porous network, thus, the reaction rate may be non-uniform among pores. As a result, the structural properties depend non only on the conversion but also on the relative rates of reaction (intrinsic kinetic) and mass transport in the product layer. Interesting situations result when the specific volume of the solid product is larger than the solid reactant one, in which case pore plugging and incomplete conversion may arise.

Additional complications may arise when the solid reactant consists of particles which can be of different size, and set into a confined system so that a porous bed of particle is realized. In this case the particle mass transport resistance must be evaluated, as well as the particle bed one. These resistance may modify the concentrations of reactants at the reaction interface, especially when the particle size and the particle bed thickness are sufficiently large to establish pronounced concentration and temperature gradients.

3.2 Gas-solid reaction models

A mathematical model that takes into account the evolution of the internal porous network of a solid, it is able to describe the structural changes as the gas-solid reaction proceeds, thus, these models takes the name of "structural models". Several structural models are available in the literature for gas-solid reactions and they are usually classified in "grain models" and "pore models" according to Szehely and Evans [60] and Ishida and Wen [28].

The grain model was first proposed by Szekely et al. [60] and assumes that the porous solid phase is made of a matrix of dense solid grains[1] usually having the shape of a sphere, a long cylinder or a flat plate. The solid phase may consist of porous particles of spherical, cylindrical and plate-like geometry. Usually, the grain model has been applied assuming spherical particles made of spherical grains. The grain size may be uniform or may be described by a grain size

[1] Assumed to be non-porous.

distribution. As reaction occurs they can overlap and react with a shrinking core model.

The pore models represent the porous network by a collection of capillaries, usually cylindrical that may overlap during the reaction. One of the first pore model was developed by Petersen [46] and considered two-dimensional overlapping of pores of uniform size randomly distributed in space. More refined pore models for a distributed pore system were presented by Gavalas [22] and Bhatia and Pelmutter [11] in 1980.

In this chapter the class of gas-solid reactions in which a fluid phase reacts with a solid is considered. In general reaction products may be fluid or solid or both. Such heterogeneous reactions may be represented by

$$a\,A_{(f)} + b\,B_{(s)} = p\,P_{(f)} + q\,Q_{(s)} \tag{3.1}$$

where a, b, c and d are the stoichiometric coefficients, the subscripts f and s refers to the fluid phase and solid phase respectively. The overall volume of solid may increase or decrease depending on the relative density of the solid product compared with that of the solid reactant. In some cases, however, the change is rather small that the overall size may be regarded as constant. When solid reactants are non-porous there is a sharp interface between fluid and solid reactants, whereas, in the general case of a porous solid, there is a gradual change in the degree of conversion throughout the particle. The product layer, made of solid phase completely reacted, increases toward the interior of the particle, so that the reaction within the partially reacted zone occurs simultaneously with the diffusion of fluid reactants.

3.2.1 Definition of reaction rate

In heterogeneous reactions ones the rate of reaction may be defined in different ways which differ for the extensive variable on which they are based. Thus, it is important to clarify some definitions and to emphasize their relationships in order to avoid any kind of misunderstanding. If the rate of change of the number of moles of component i due to a reaction is dn_i/dt, then the rate of reaction can be defined in several forms.

Following the IUPAC definition by Cohen et al. [49], the reaction rate, based on the unit of volume of reacting fluid,

$$R_v = \frac{1}{\tilde{V}}\frac{d\xi}{dt}, \tag{3.2}$$

where $\tilde{V}$ is the geometrical volume of the considered system[2] and ξ is the extent of reaction of Eq. (3.1). In gas-solid reaction $\tilde{V}$ refers to the volume of the solid phase.
The reaction rate, based on unit interface between two different phases (e.g. unit surface of solid in gas-solid systems) is defined as,

$$R_s = \frac{1}{\tilde{S}}\frac{d\xi}{dt}, \tag{3.3}$$

[2]The symbol $\tilde{}$ refers to a generic extensive variable.

where $\tilde{S}$ is expressed in term of square length, according to Cohen et al. [49]. The relation between Eqs. (3.2) and (3.3) is

$$\begin{aligned} \tilde{V}\, R_v &= \tilde{S}\, R_s \\ R_v &= \frac{\tilde{S}}{\tilde{V}}\, R_s = S\, R_s, \end{aligned} \tag{3.4}$$

where S is the specific surface area in terms of area per unit of geometrical volume. S is frequently expressed in terms of area per unit of solid mass S_g, and the relationship between these two quantities is:

$$S = S_g\, \rho_s\, (1 - \varepsilon_s)\,, \tag{3.5}$$

in which ρ_s is the skeleton density of the solid reactant (s), and ε_s is the void fraction (void volume per unit of geometrical volume).

In gas-solid reactions it is common to express the local intensive reaction rate in term of a power law

$$R_j = k_j\, C_A^n\, C_s, \qquad \text{with} \quad j = v,\, s, \tag{3.6}$$

where k_j is the kinetic constant of the chemical reaction commonly evaluated with the Arrhenius' law[3], C_A is the molar concentration of the fluid species A, n is the reaction order and C_s is the molar concentration of the solid reactant that can be expressed as:

$$C_s = \frac{\rho_s}{M_s}\, (1 - \varepsilon_s)\,. \tag{3.7}$$

C_s is usually retained to be constant during the reaction and it may be incorporated in k_j resulting in the following equation,

$$R_j = k'_j\, C_A^n, \qquad \text{with} \quad j = v,\, s, \tag{3.8}$$

and combining Eq. (3.6) and Eq. (3.8), the following relation may be derived

$$k'_j = k_j\, C_s, \qquad \text{with} \quad j = v,\, s. \tag{3.9}$$

Depending on the reaction rate definition, the kinetic constant may assume different dimensions. The various conversion factors of the kinetic constant for every reaction rate are reported in Tab. 3.1.

It is useful to express a reaction rate in terms of the conversion of species i, X, defined for a

[3] Arrhenius' laws is defined as $k = A \exp\left(-Ea/\left(R_{\text{gas}}\, T\right)\right)$, where A is the pre-exponential factor, Ea is the activation energy of the reaction, R_{gas} is the universal constant of gases and T is the temperature of the system expressed in K.

Table 3.1: Dimensions and conversion factors for the different reaction rate definitions.

from/to	k_v	k'_v	k_s	k'_s
k_v	$\mathrm{m^3/mol/s}$	$k_v\,C_s$	k_v/S	$k_v\,C_s/S$
k'_v	k'_v/C_s	$\mathrm{s^{-1}}$	$k'_v/\left(S\,C_s\right)$	k'_v/S
k_s	$k_s\,S$	$k\,C_s\,S$	$\mathrm{m^4\,mol^{-1}\,s^{-1}}$	$k_s\,C_s$
k'_s	$k'_s\,S/C_s$	$k'_s\,S$	k'_s/C_s	$\mathrm{m\,s^{-1}}$

batch process as

$$X = \frac{n_{i,0} - n_i(t)}{n_{i,0}} = \frac{w_{i,0} - w_i(t)}{w_{i,0}}, \tag{3.10}$$

where $n_{i,0}$ and $n_i(t)$ are respectively the number of moles of specie i at initial time and at the generic time t, whereas $w_{i,0}$ and $w_i(t)$ is the weight of i respectively at the initial conditions and after a time t. If Eqs. (3.2) and (3.3) are expressed in terms of conversion, they change into the general relation

$$R_j = -\frac{n_{i,0}}{\nu_i}\,\frac{1}{j}\,\frac{dX}{dt}, \qquad \text{with} \quad j = v,\, s, \tag{3.11}$$

where ν_i is the stoichiometric coefficient of species i and Eq. (3.10) is differentiated to give $dn_i = -n_{i,0}\,dX$[4].

In gas-solid reactions it is common to express Eq. (3.6) in terms of partial pressure:

$$R_j = k'_{j,p}\,p_A^n, \qquad \text{with} \quad j = v,\, s, \tag{3.12}$$

whatever basis is used in the reaction rate (volume of surface), the order of reaction unchanged, however, the chosen basis affects the dimensions of $k'_{j,p}$. In the case of Ping Sun et al.'s works, [59] and [58], the kinetic law employed is like Eq. (3.12) based on the unit surface area of the solid phase[5]. Their kinetics follow Eq. (3.3) with the difference that the amount of reactant A is expressed in terms of partial pressure. For these reasons the kinetic constant $k'_{s,p}$, when the reaction order is one, has the units of $\left[\mathrm{mol\,m^{-2}\,s^{-1}\,Pa^{-1}}\right]$, thus, a conversion factor is needed and can be obtained from a comparison between the two reaction rates. Eqs. (3.12) and (3.8) lead to

$$k'_s = k'_{s,p}\,R_{\mathrm{gas}}T, \tag{3.13}$$

where a first order reaction ($n = 1$) is assumed as well as the ideal gas state $p_A = R_{\mathrm{gas}}T\,C_A$.

Considering a reversible chemical reaction like Eq. (3.1), a limit in terms of concentration of species A is imposed by thermodynamics, hence, a driving force must be considered in the reaction rate equation with respect to the equilibrium conditions. Consequently, an equilibrium

[4]Following the extent of reaction definition, that is $\xi = (n_i - n_{i,0})/\nu_i$, the differential relationship between ξ and n_i is $dn_i = \nu_i\,d\xi$.

[5]For simplicity here the equilibrium term is neglected, that term will be included afterwards in this thesis.

concentration $C_{A,\mathrm{eq}}$ is needed, so that Eq. (3.8) becomes

$$R_j = k'_j \, (C_A - C_{A,\mathrm{eq}})^n \,, \qquad \text{with} \quad j = v,\, s, \tag{3.14}$$

that can be obviously expressed in terms of partial pressure.
For gas-solid systems and especially for Thermo-Gravimetric Analysis (TGA), it is common to express the reaction rate in terms of reactivity R_m [33] defined as

$$R_m = -\frac{1}{w_i}\frac{dw_i}{dt} = \frac{1}{1-X}\frac{dX}{dt} \tag{3.15}$$

where w is the weight of the solid reactant at any time. Eq. (3.15) has units $\left[\mathrm{s}^{-1}\right]$ and can be considered as a reaction rate based on the unit of mass of solid reactant.
Based on the previous definitions the rate of reactant formation or of disappearance of each species can be defined (according to Levenspiel [35]), using the global rate of the reaction R_j and adopting the stoichiometry of Eq. (3.1),

$$r_{j,i} = \pm \nu_i \, R_j \qquad \text{with} \quad j = v,\, s \qquad \text{and} \quad i = A,\, B,\, P,\, Q \tag{3.16}$$

where ν_i is the stoichiometric coefficient of species i[6]. $r_{j,i}$ is positive or negative depending whatever the reacting species is a reactant or a product.

3.3 The grain model

A chemical reaction involving fluid-solid reactants following Eq. (3.1) is considered, and, for simplicity, a spherical particle of solid reactant made of non-porous spherical[7] grains of uniform radius r_g is assumed. Reaction occurs by diffusion of fluid reactant into the particle to the reactive surface of the grains. As time progresses a layer of porous Q builds up around grains and it is also assumed that the relative density between the solid product and the solid reactant is one, so that the grain shape remains constant during the whole reaction period. Thus the shrinking-core model (SCM) is applicable to each grain, but not to the particle as a whole. This feature makes the model well suited for explaining data where the conversion is less than 100 %, due to the formation of a non-porous passivated product layer around the grain reactive surfaces. In the general case of porous reactants the reaction occurs in a partially converted region where reaction and fluid diffusion occur simultaneously. For the non-porous grains the reaction is supposed to occur at a sharp interface between the product layer and the solid reactant, so that the fluid phase must diffuse through the dense solid phase product. The nomenclature and geometry of the model are shown in Fig. 3.1.

If Eq. (3.1) is retained to be irreversible and if it is assumed that the chemical transformation occurs at isothermal conditions, generally the whole process includes the following steps:

[6] The stoichiometric coefficient ν_i is a, b, ..., according to Eq. (3.1).
[7] Spherical shape is not strictly necessary, grains may assume different geometrical configurations, such as long cylinders and flat plates.

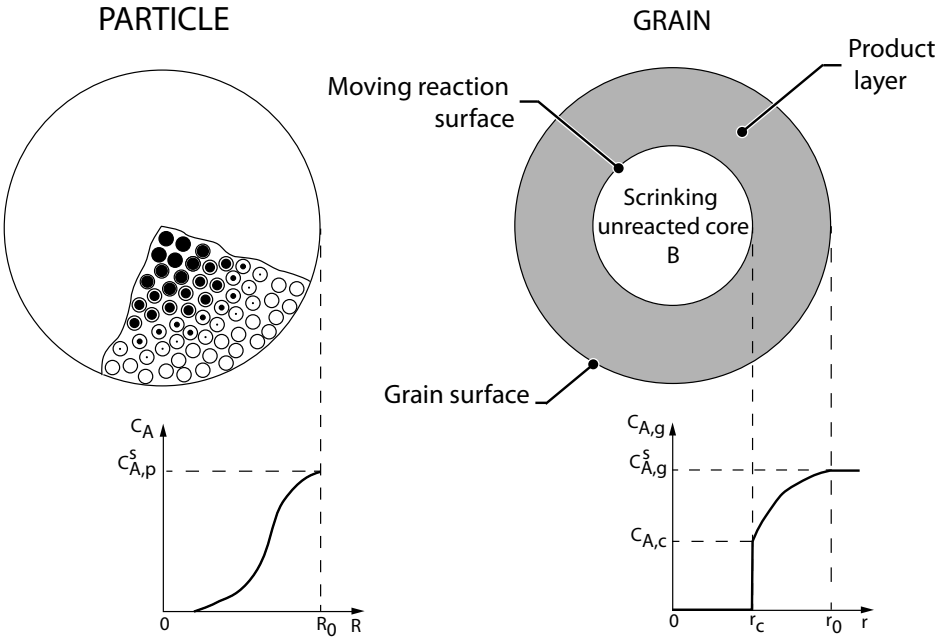

Figure 3.1: Representation of the grain model for reaction of a porous solid with a fluid phase, according to Szekely et al. [29] and Levenspiel [35]. R_0 is the particle radius, $C^s_{A,p}$ is the concentration of A at the particle surface, r_0 and r_c are respectively the grain and the core radius, $C^s_{A,g}$ and $C_{A,c}$ are the concentration of A at grain surface and at core surface respectively.

1. external mass transport of reactant from the bulk fluid to the outer surface of the porous solid;

2. diffusion of the reactant fluid within the pores of the solid;

3. chemical reaction at the reactant-product interface, including the adsorption of the reactants on the solid surface and the desorption of the products, and the solid diffusion within a product layer;

4. diffusion of the fluid products through the porous solid;

5. mass transfer of the products into the bulk fluid stream.

The external mass transport and the intra-particle diffusion may affect the overall rate. Therefore, it becomes important to eliminate these resistances or, on the contrary, when these phenomena cannot be neglected, it is necessary to built appropriate models that take into account all the mentioned resistances. Clearly, if the solid particles are stored in a particle layer, inter-particle diffusion should be considered as well. Specifically, these steps do not occur one after the other, but they may be occur simultaneously, e.g. inter-particle diffusion occurs together with intra-particle diffusion and reaction.

In this chapter, only reaction and diffusion in the solid state are considered and the other processes are neglected.

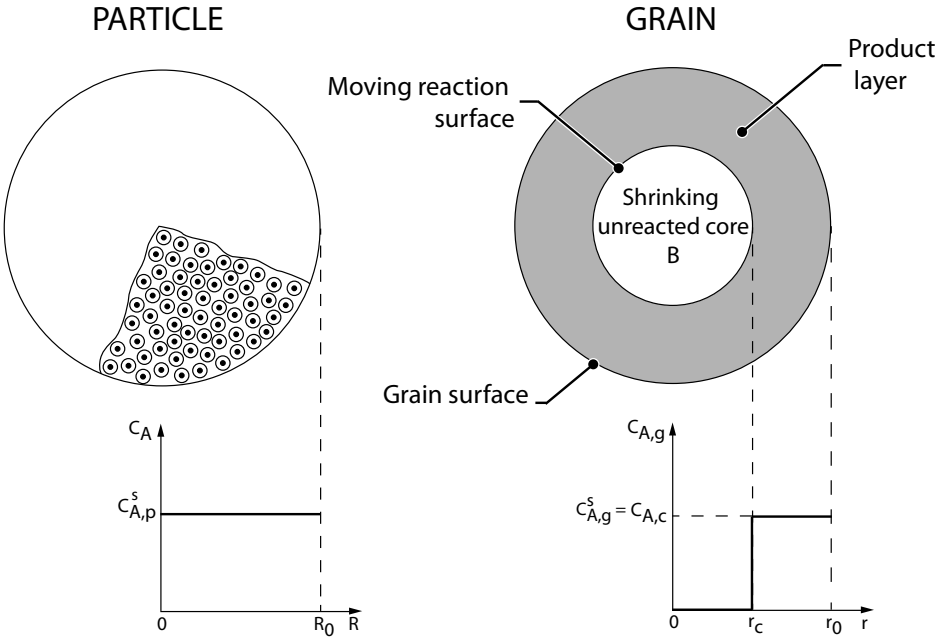

Figure 3.2: The grain model for the case of a solid reacting under kinetic controlled conditions, following Szekely et al. [29] and Levenspiel [35].

When the chemical reaction represents the larger resistance to the overall progress of reaction, the concentration of the fluid reactant is constant everywhere, and the reaction occurs uniformly throughout the volume of the solid: this state is named "kinetic control" (or similarly "chemical controlled regime"). If, on the other hand, diffusion through the solid phase (product layer) represents the larger resistance, the reaction occurs in a narrow boundary between the unreacted and completely reacted zones (that is the product layer), where the fluid concentration becomes zero (or takes its equilibrium value in the case of reversible reaction): the process in this case is named "diffusion controlled".

3.3.1 Chemical reaction control

This situation occurs when the rate of diffusion through the dense product layer presents a negligible resistance to the progress of reaction and thus chemical kinetics controls the process. According to the grain model, such a system is considered as an agglomerate of individual reacting grains. Thus the fluid concentration reactant is uniform throughout the solid as shown in Fig. 3.2. Since the grains are non porous, within each one the reaction front retains its geometrical shape as reaction proceeds. Thus, the rate of reaction expressed in terms of unit surface of unreacted core, on the basis of Eq. (3.1) is

$$\frac{dn_B}{dt} = -b\, R_s\, \tilde{S}_{\text{core}} = -b\, k'_s\, C_{A,\,c}\, \tilde{S}_{\text{core}}, \tag{3.17}$$

where k'_s is the kinetic constant of the reaction based on the unit of surface area, $C_{A,\,c}$ is the molar concentration of A at the core surface that is equal to the concentration of A at grain surface $C^s_{A,\,g}$ and $\tilde{S}_{\text{core}}$ is the surface of the core interface that is $4\pi r_c^2$. If ρ_s is the mass density of solid B and $\tilde{V}_g$ is the volume of the unreacted grain, the amount of B present in the particle is

$$n_B = \frac{\rho_s}{M_B}\,\tilde{V}_g, \tag{3.18}$$

and the change of moles, volume or radius of the unreacted core due to the reaction is

$$dn_B = \frac{\rho_s}{M_B}\,d\tilde{V}_g = \frac{\rho_s}{M_B}\,d\left(\frac{4}{3}\pi r_c^3\right) = 4\pi r_c^2\,\frac{\rho_s}{M_B}\,dr_c. \tag{3.19}$$

Substituting Eqs. (3.18) and (3.19) into Eq. (3.17), it becomes

$$\frac{\rho_s}{M_B}\,\frac{dr_c}{dt} = -b\,k'_s\,C^s_{A,\,g}, \tag{3.20}$$

whose solution is

$$r_c\,(t) = r_g - \frac{b\,k'_s\,C^s_{A,\,g}\,M_B}{\rho_s}\,t, \tag{3.21}$$

having care to consider the initial solution $r_c = r_g$ at $t = 0$.
In order to express the previous results in terms of conversion, substituting Eq. (3.18) into Eq. (3.10), conversion is expressed as:

$$X = 1 - \frac{\tilde{V}_c}{\tilde{V}_g} = 1 - \frac{r_c^3}{r_g^3}, \tag{3.22}$$

where $\tilde{V}_c$ is the unreacted solid volume. From Eq. (3.22) $r_c = (1 - X)^{1/3}\ r_g$ and in differential form is

$$dr_c = -\frac{r_g}{3}\,\frac{dX}{(1-X)^{2/3}}. \tag{3.23}$$

Consequently, Eq. (3.17) in terms of conversion becomes

$$\frac{dX}{dt} = b\,k'_S\,C^s_{A,\,g}\,(1-X)^{2/3}\,\frac{3}{r_g}\,\frac{M_B}{\rho_s}, \tag{3.24}$$

where $3/r_g$ is the surface area per unit of volume of each the spherical grain (S_{grain}). However, according to the grain model assumption the solid particle is made of a number of grains, consequently, Eq. (3.24) should be rescaled to the whole particle by multiplying by the ratio of the

volume of one grain to the geometrical volume of the particle[8]:

$$S_g = \frac{\tilde{S}_g}{\tilde{V}_g} = \frac{n_g\,\tilde{S}_g}{\tilde{V}_p}\,\frac{\tilde{V}_p}{n_g\,\tilde{V}_g} = \frac{S_p}{1-\varepsilon_p} \tag{3.25}$$

where $\tilde{V}_g$ and $\tilde{V}_p$ are respectively the volume of a single grain and the volume of the particle, n_g is the number of grains inside a particle and ε_p is the particle porosity. Hence, the product between S_g and $(1-\varepsilon_p)$ gives the specific surface area of the particle,

$$S_g\,(1-\varepsilon_p) = S_p. \tag{3.26}$$

It is useful to express the kinetic constant k'_s in terms of k_s in order to obtain a density-independent term. The relationship between the two kinetic constants is given by Eq. (3.9) (or Tab. 3.1), having care to pay attention that each grain is a non-porous solid:

$$k'_s = k_s\,\frac{\rho_s}{M_B}. \tag{3.27}$$

Multiplying Eq. (3.24) by Eq. (3.25) and substituting Eqs. (3.26) and (3.27) the following equation is obtained:

$$\frac{dX}{dt} = \frac{b\,k_s\,C^s_{A,\,g}\,S_p\,(1-X)^{2/3}}{(1-\varepsilon_p)}, \tag{3.28}$$

which is the classic rate expression of the grain model under kinetic control for spherical particles. Once integrated Eq. (3.27) gives

$$\hat{t} = \frac{t}{\tau_{\mathrm{GM,\,kin}}} = 3\left[1-(1-X)^{1/3}\right], \tag{3.29}$$

where $3\,\tau_{\mathrm{GM,\,kin}}$ is the time required for complete conversion when $r_c = 0$,

$$\tau_{\mathrm{GM,\,kin}} = \frac{(1-\varepsilon_p)}{b\,k_s\,C^{\mathrm{sup}}_{A,\,g}\,S_p} = \frac{r_g}{3\,b\,k_s\,C^s_{A,\,g}}. \tag{3.30}$$

As reported in Eq. (3.30), the time required to attain a certain conversion is proportional to the grain size, whereas for non-porous solids it is proportional to the overall size of the particle. This relationship enables to determine from experimental conversion data the intrinsic reaction rate constant plotting $\left[1-(1-X)^{1/3}\right]$ vs time, giving a straight line whose slope is $(3\,\tau_{\mathrm{GM,\,kin}})^{-1}$. The experiments for this purpose must be performed under conditions where the pellet offers no resistance to the diffusion of the reacting species (external, inter-particle, intra-particle diffusion and product layer diffusion).

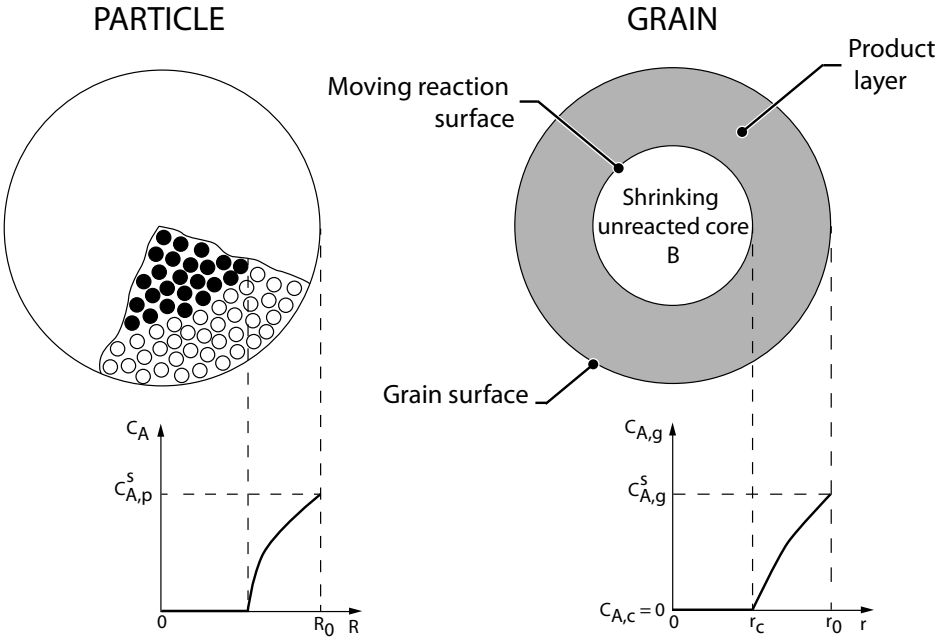

Figure 3.3: The grain model for the case of a reacting solid undergoing reaction when diffusion through the product layer is the controlling resistance, following Szekely et al. [29] and Levenspiel [35].

3.3.2 Product layer diffusion control

If the chemical reaction step presents a negligible resistance compared with the resistance due to the dense product layer diffusion, the overall rate is controlled by the product layer diffusion. The reaction occurs in a narrow zone separating the unreacted core and the completely reacted layer where the reactant concentration drops to zero, as shown in Fig. 3.3.
In order to obtain the rate of diffusion (hence the overall rate), the pseudo-steady-state approximation is assumed so that the molar balance of A in the product layer is

$$\frac{d}{dr}\left(D_{pl}\, r^2\, \frac{dC_A}{dr}\right) = 0 \tag{3.31}$$

where D_{pl} is the molecular diffusivity coefficient of A in the product layer Q, retained to be constant (isotropic product layer). Two boundary conditions must be considered in order to obtain a unique solution to Eq. (3.31):

$$\begin{aligned} C_A &= C^s_{A,g} && \text{at } r = r_g \\ -D_{pl}\,\frac{dC_A}{dr} &= \frac{1}{4\pi r_c^2}\,\frac{dn_A}{dt} && \text{at } r = r_c. \end{aligned} \tag{3.32}$$

[8] The whole particle volume is retained to be the total geometrical volume including void and solid spaces.

Once integrated, Eq. (3.31) becomes

$$-\frac{dn_A}{dt}\left(\frac{1}{r_c}-\frac{1}{r_g}\right)=4\pi\, D_{pl}\, C^s_{A,g}, \tag{3.33}$$

considering $C_{A,c}$ equal to zero because the reaction kinetics is assumed to be fast in comparison to the product layer diffusion. According to the stoichiometry of Eq. (3.1) $-dn_B/b = -dn_A/a$ and substituting Eq. (3.19) into Eq. (3.33) this becomes:

$$\frac{dr_c}{dt}=-\frac{b}{a}\frac{M_B}{\rho_s}\frac{D_{pl}\, C^s_{A,g}}{r_c\left(1-\frac{r_c}{r_g}\right)}. \tag{3.34}$$

Once integrated with the initial condition $r_c = r_g$ at $t = 0$, Eq. (3.20) becomes:

$$t=\frac{a\, r_g^2\, \rho_s}{6\, b\, D_{pl}\, C^s_{A,g}\, M_B}\left[1-3\left(\frac{r_c}{r_G}\right)^2+2\left(\frac{r_c}{r_g}\right)^3\right], \tag{3.35}$$

and expressing this result in terms of conversion using Eq. (3.22),

$$t=\frac{a\, r_g^2\, \rho_s}{6\, b\, D_{pl}\, C^s_{A,g}\, M_B}\left[1-3\,(1-X)^{2/3}+2\,(1-X)\right]. \tag{3.36}$$

Finally, it is useful to express Eq. (3.36) in differential form,

$$\frac{dX}{dt}=\frac{3\, b\, D_{pl}\, C^s_{A,g}\, M_B}{a\, r_g^2\, \rho_s}\frac{(1-X)^{1/3}}{1-(1-X)^{1/3}}. \tag{3.37}$$

All the previous equations are referred to a single grain, hence, it is necessary to multiply by $(1-\varepsilon_p)$ to obtain the reaction rate under diffusion control for a single solid particle. Furthermore, the time required for complete conversion of a particle is given by:

$$\tau_{GM,\,\mathrm{diff}}=\frac{a\, r_g^2\, \rho_s\, (1-\varepsilon_p)}{6\, b\, D_{pl}\, C^s_{A,g}\, M_B}. \tag{3.38}$$

3.3.3 Simultaneous chemical reaction and diffusion

When chemical reaction and diffusion in the product layer are comparable, the overall process is simultaneously controlled by both phenomena. According to [17], reaction occurs by diffusion of fluid reactant into the particle to the reactive surface of grains. As time progresses a layer of dense solid Q builds up around each grain. Hence, continued reaction occurs by diffusion of A through the layer of Q. This feature makes the model well suited for explaining data where the conversion approaches a constant value less than 100 % at long times, due to formation of a passivated product layer around reactive surfaces. In the analysis that follows it will be assumed that there is no change of particle size with reaction.

Reaction surface changes during the reaction according to Eq. (3.17) and, in order to develop a relationship of the conversion of solid B as a function of time, the pseudo-steady-state approxi-

mation of species A in the product layer is assumed. Eqs. (3.31) and (3.32) give

$$C^s_{A,g} - C_{A,c} = -\frac{dn_A}{dt}\,\frac{1}{4\pi D_{pl}\, r_c}\left(1 - \frac{r_c}{r_g}\right) \tag{3.39}$$

where in this case $C_{A,c}$ is not zero and it is substituted by Eq. (3.17), solving for dn_A/dt, giving

$$\frac{dn_A}{dt} = -\frac{a\, k'_s\, C^s_{A,g} 4\pi r_c^2}{1 + \dfrac{a\, r_c\, k'_s}{D_{pl}}\left(1 - \dfrac{r_c}{r_g}\right)}. \tag{3.40}$$

Substituting $dn_B = b/a\, dn_A$ and considering Eq. (3.19), Eq. (3.40) becomes

$$\frac{dr_c}{dt}\,\frac{\rho_s}{M_B} = -\frac{b\, k'_s\, C^s_{A,g}}{1 + \dfrac{a\, r_c\, k'_s}{D_{pl}}\left(1 - \dfrac{r_c}{r_g}\right)} \tag{3.41}$$

and taking into account Eqs. (3.22), (3.26) and (3.27), Eq. (3.41) assumes the form

$$\frac{dX}{dt} = \frac{b\, k_s\, S_p\, C^s_{A,g}\, (1-X)^{2/3}}{(1-\varepsilon_p)\left\{1 + \dfrac{a\, k_s\, r_g\, \rho_s}{M_B\, D_{pl}}\left[(1-X)^{1/3} - (1-X)^{2/3}\right]\right\}}. \tag{3.42}$$

Once integrated, Eq. (3.42) becomes:

$$\hat{t} = \frac{t}{\tau} = 3\left[1 - (1-X)^{1/3}\right] + \frac{3}{4}\beta\left[1 - 3\,(1-X)^{2/3} + 2\,(1-X)\right] \tag{3.43}$$

where

$$\tau = \frac{(1-\varepsilon_0)}{b\, k_s\, C^n_A\, S_0}, \qquad\qquad \beta = \frac{2\, a\, k_s\, \rho_s\, (1-\varepsilon_0)}{M_B\, D_{pl}\, S_p}. \tag{3.44}$$

Eq. (3.42) represents the differential form of the grain model in the general case when neither kinetic nor diffusion resistance controls the overall process. This situation is represented in Fig. 3.1.

3.3.4 Drawbacks of the grain model

The grain model considers the reaction to occur on the surface of non-porous grains. Calvelo and Smith and Szekely and Evans, in their works respectively [17] and [29], consider the shrinking core behaviour of uniformly sized non-porous grains of a solid reactant. Each particle is retained to be composed by grains which represent the solid fraction of the particle. This particular geometry may be realistic for those particles formed by compacting fine grains of small particles with or without some binding agents. The overall shape may be approximated with a slab, a long cylinder or a sphere. However, it is not so easy to characterize the shape of the individual grains that form the pellet. Difficulties will arise because the grains are usually of irregular shape and are distributed in size; moreover, their shape may change in the course of the reaction.

On the other hand, porous particles formed by a complex pore network can be regarded as solids made of pores of different shape and size. The solid phase of the porous medium is visualized as a matrix of dense solid grains of some geometrical shape. In this case the grain model is only a mathematical representation of the real system, the solid phase volume is described by the total volume of grains and void volume becomes the space among each grain. In this manner the porous network is modeled in a simple way using simple geometries as spheres. However, it is not easy to identify the grain size because, in this case, it is only a representation of the solid fraction of the system.

Eq. (3.42) incorporates the structural parameters of the solid in terms of porosity and surface area that allow an high versatility of the model. However, it predicts a monotonically decrease of the reaction rate because of the receding of the reacting surface of each grain. Some systems exhibit a maximum in the reaction rate, such as gasification or carbonation reactions, as reported by Bhatia and Pelmutter [11]. This is attributed to an increase in the reacting surface area during the early stages of reaction. The grain model does not account for such change of the structure occurring during the reaction.
Moreover, reactions may occur with the formation of a product layer that can be more or less dense of the solid reactant. On the basis of the ratio of the volume of solid phase after reaction to that before reaction (Z) grain surface (pore surface) may increase or decrease. As reaction progresses, if $Z > 1$ each grain grows and it is inevitable that neighboring surfaces will intersect one another, determining grains overlapping, or generally, structural overlapping. Clearly, these features are not contemplated by the grain model.

Furthermore, the grain model does not account for pore closure due to the product layer deposition as reaction occurs. In this case, the solid phase undergoes to specific surface loss determining a slow down of the kinetic rate.

3.4 The random pore model

The disadvantages of the previous models lead Bhatia and Pelmutter (in their works [11] and [12]) in 1980 to propose a general model for gas-solid reactions that accounts for reacting surfaces randomly overlapping as they grow by extending a theory originally developed by Avrami in 1939-1940 ([5] and [6]) for the analysis of the geometry of crystal aggregates. No assumption was made on the shapes of pores.
By using the characteristic parameters of a random pore size distribution, the Random Pore Model (RPM) avoids the need to assume an idealized structure having uniformly size distributed pores and it accounts for the intersection of reaction surfaces as they grow. One of the most important features of the RPM is that it predicts the reaction surface area at any given conversion as a function of an initial pore structure parameter.

3.4.1 Isothermal kinetic control

Consider an isothermal chemical reaction of particles of solid B with a fluid A according to the stoichiometry of Eq. (3.1). The reaction starts on the surfaces of pores in the solid phase B.

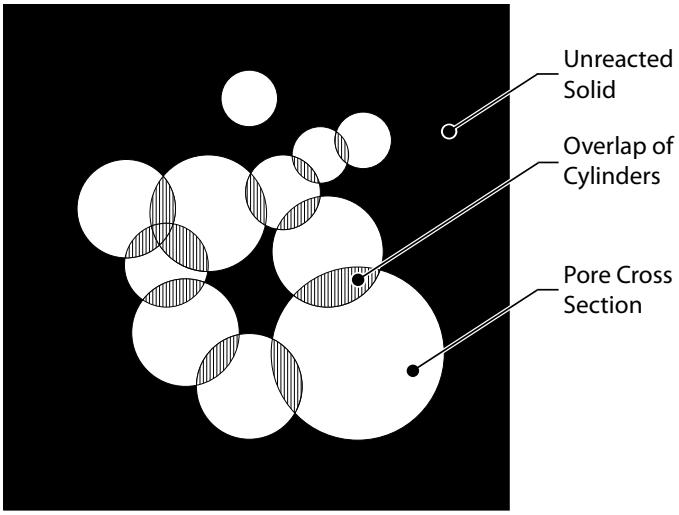

Figure 3.4: Overlapping of cylindrical surfaces. The hatched area shows the overlapped portion. The blackened area represents unreacted solid B. The reaction surface is the interface between the non overlapped portion of the cylindrical surface and the unreacted solid. The product layer that is deposited at the reaction surface is not shown. Source Bhatia and Pelmutter [11].

As further reaction occurs, a layer of product Q is formed around each pore which separates the growing reaction surface of the solid B from the fluid reactant A within the pores. Reactant A diffuses through the product layer to the reaction surface where the chemical reaction occurs.
As reaction progresses, each pore of the particle is associated with a growing reaction surface which initially corresponds to the inner surface of the pore. As the various reaction surfaces in the particle grow, neighboring surfaces intersect one another as the solid B separating them is consumed and replaced by the product Q (Fig. 3.4).
The actual reaction surface of the solid B at any time is assumed to be the result of the random overlapping of a set of cylindrical surfaces with pore size distribution $l(r)$ where $l(r)\,dr$ is the total length of the cylindrical surfaces per unit of volume of space having radii between r and $r + dr$. The following properties are defined:

$$L_E = \int_0^\infty l(r)\,dr, \tag{3.45}$$

$$S_E = 2\pi \int_0^\infty r\,l(r)\,dr, \tag{3.46}$$

$$V_E = \pi \int_0^\infty r^2\,l(r)\,dr, \tag{3.47}$$

as the total length, total surface area and total enclosed volume of non-overlapped cylindrical system per unit of volume. A balance over the pore size distribution of the growing cylinders yields:

$$\frac{\partial l\,(r)}{\partial t} + \frac{\partial}{\partial r}\left[l\,(r)\,\frac{dr}{dt}\right] = 0 \tag{3.48}$$

where it is assumed that no cylinders are created or destroyed.

The growth of the total reaction surface may be followed in terms of the radial growth of a given set of overlapping cylinders as shown in Fig. 3.4. Following Eqs. (3.3) and (3.6), the reaction rate is

$$\frac{dn_B}{dt} = -b\,k_s\,C_A^n\,C_s\,\tilde{S}_{\text{pore}}, \tag{3.49}$$

where $\tilde{S}_{\text{pore}}$ is the surface of the pore and C_s is ρ_s/M_B. Since $dn_B = \rho_s/M_B\,d\tilde{V}_{\text{pore}}$[9] and $d\tilde{V}_{\text{pore}} = -\tilde{S}_{\text{pore}}\,dr$, Eq. (3.49) becomes

$$\frac{dr}{dt} = b\,k_s\,C_A^n, \tag{3.50}$$

which states that each element of the actual surface must belong to the non-overlapped portion of some cylinder. Eq. (3.50) differs to Bhatia and Pelmutter's work [11] in the stoichiometry coefficient b[10]. Combining Eqs. (3.48) and (3.50)

$$\frac{\partial l\,(r)}{\partial t} = -b\,k_s\,C_A^n\,\frac{\partial l\,(r)}{\partial r}. \tag{3.51}$$

Integrating Eq. (3.51) with respect to r, $2\pi r$ and πr^2, and using Eqs. (3.45), (3.46) and (3.47) together with the conditions $l\,(0) = l\,(\infty) = 0$

$$\frac{dL_E}{dt} = 0, \tag{3.52}$$

$$\frac{dS_E}{dt} = 2\pi\,b\,k_s\,C_A^n\,L_E, \tag{3.53}$$

$$\frac{dV_E}{dt} = b\,k_s\,C_A^n\,S_E. \tag{3.54}$$

Eq. (3.52) expresses that the total pore length in the non-overlapping system remains constant with time. With some algebra, Eqs. (3.52), (3.53) and (3.54) can be solved to give

$$S_E = \sqrt{S_{E_0}^2 + 4\pi L_{E_0}\,(V_E - V_{E_0})} \tag{3.55}$$

$$V_E = V_{E_0} + S_{E_0}\,(b\,k_s\,C_A^n\,t) + \pi\,L_{E_0}\,(b\,k_s\,C_A^n\,t)^2\,, \tag{3.56}$$

which describe the evolution of the non-overlapped surface and volume as conversion proceeds. It remains to relate these quantities to the corresponding properties of the actual surface, that is the overlapped system. Avrami ([5] and [6]) found that on the average the increment in the volume enclosed by the actual system (overlapped) is only a fraction of the growth in the non-overlapped cylindrical system. Moreover, this fraction is $(1 - V)$ where V is the overlapped volume of enclosed by the reaction surface. The fractional volume of space occupied by solid B

[9] The negative sign is due to the pore geometry: as reaction occurs, the pore volume continuously recedes.

[10] In Bhatia and Pelmutter's work [11] each stoichiometric coefficient is normalized by the stoichiometric coefficient of the solid phase.

is

$$dV = (1 - V)\, dV_E. \tag{3.57}$$

With the observation that $V \to 0$ as $V_E \to 0$, Eq. (3.57) can be integrated to

$$V = 1 - \exp(-V_E). \tag{3.58}$$

To obtain a relationship between the surface areas of the overlapped and non-overlapped systems, the increase in volume of the overlapped system by an amount dV in time dt is considered,

$$\frac{dV}{dt} = S\ (b\, k_s\, C_A^n\, t)\,. \tag{3.59}$$

Combining Eqs. (3.54), (3.58) and (3.59)

$$S = S_E\ (1 - V) \tag{3.60}$$

that relates the surface area per unit of volume of the overlapped system to that of the non-overlapped one. Following Bhatia and Pelmutter [11], as the overlapped system increases in amount dV, the change in the total length of the system due to additional intersections may be written as

$$dL = -\frac{L}{(1 - V)}\, dV, \tag{3.61}$$

and since no overlapping is possible for $V = 0$, $\lim_{V \to 0} L = L_E$. Integrating Eq. (3.61) gives

$$L = L_E\ (1 - V)\,. \tag{3.62}$$

Structural parameters such as the total pore length, total pore surface and total pore volume (particle porosity) of the solid phase can be obtained from BET or BJH analysis. Assuming that pores in the solid phase start from a overlapped configuration, experimental analysis determines overlapped structural parameters:

$$V_0 = \varepsilon_0 = 1 - \exp(-V_{E_0}) \tag{3.63}$$

$$S_0 = (1 - V_0)\ S_{E_0} \tag{3.64}$$

$$L_0 = (1 - V_0)\ L_{E_0}. \tag{3.65}$$

Integrating Eq. (3.57)

$$\int_{V_0}^{V} \frac{dV'}{(1 - V')} = \int_{V_{E_0}}^{V_E} dV'_E \tag{3.66}$$

gives

$$V = 1 - (1 - V_0) \exp\left[-\frac{b\,k_s\,C_A^n\,t}{(1 - V_0)}\,(S_0 + \pi\,L_0\,b\,k_s\,C_A^n\,t)\right] \tag{3.67}$$

and using Eq. (3.60)

$$S = S_0\,\frac{(1 - V)}{(1 - V_0)}\,\sqrt{1 - \frac{4\pi L_0\,(1 - V_0)}{S_0^2}\ln\left(\frac{1 - V}{1 - V_0}\right)}. \tag{3.68}$$

Finally, for a spherical particle of radius R_0 in the regime of reaction control,

$$X = 1 - \frac{1 - V}{1 - V_0}\left(1 - \frac{b\,k_s\,C_A^n\,t}{R_0}\right)^3, \tag{3.69}$$

where the following conversion definition is considered:

$$\begin{aligned} X &= \frac{\text{volume of initial solid - volume of solid at time } t}{\text{volume of initial solid}} \\ &= \frac{(1 - \varepsilon_0) - (1 - \varepsilon)}{(1 - \varepsilon_0)} = \frac{\varepsilon - \varepsilon_0}{1 - \varepsilon_0}, \end{aligned} \tag{3.70}$$

Considering the following change of variables

$$\psi = \frac{4\pi L_0\,(1 - \varepsilon_0)}{S_0^2}, \qquad \hat{t} = \frac{t}{\tau} = \frac{b\,k_s\,C_A^n\,S_0}{(1 - \varepsilon_0)}\,t, \qquad \sigma = \frac{R_0 S_0}{(1 - \varepsilon_0)} \tag{3.71}$$

in dimensionless form Eq. (3.67) and (3.68), upon combining with Eq. (3.69) become

$$S = S_0\,\frac{1 - X}{\left(1 - \dfrac{\hat{t}}{\sigma}\right)^3}\,\sqrt{1 - \psi\,\ln\left[\frac{1 - X}{\left(1 - \dfrac{\hat{t}}{\sigma}\right)^3}\right]}, \tag{3.72}$$

and

$$X = 1 - \left(1 - \frac{\hat{t}}{\sigma}\right)^3 \exp\left[-\hat{t}\,\left(1 + \frac{\psi\,\hat{t}}{4}\right)\right]. \tag{3.73}$$

Conversion-time behaviour

Eq. (3.73) provides conversions at each dimensionless time in terms of the initial pore structure parameter ψ and the particle size parameter σ. In order to characterized the effect of particle size, Eq. (3.73) is used to compute the time required for 50 % of conversion at various of ψ. Such results are presented in Fig. 3.5, where it is evident that no significant change occurs for $\sigma \geq 100$ when the particle external surface is negligible in comparison with the internal surface. On the other hand, for small enough particles ($\sigma < 0.25$), the reaction time is independent of internal structure for $\psi \leq 100$. Between the limits there is a transition region in which both internal

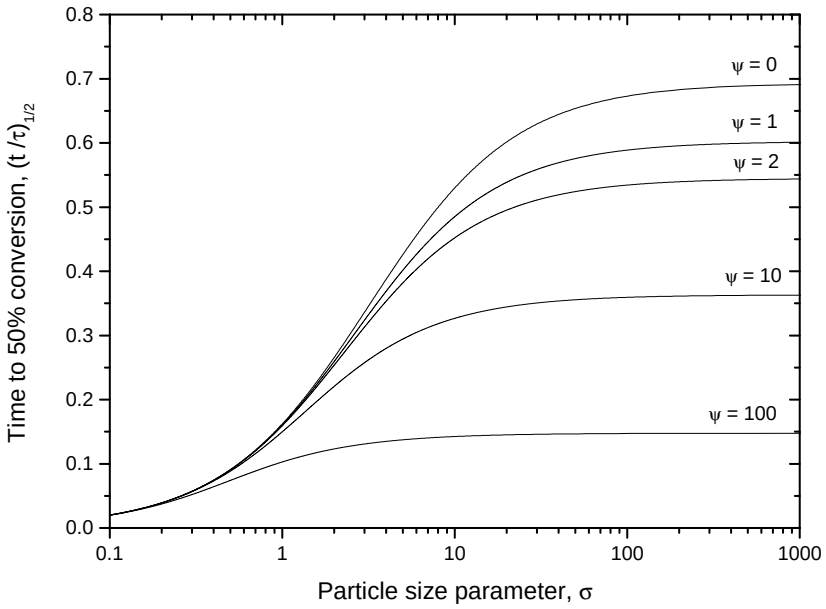

Figure 3.5: The effect of particle size on time required for 50 % of conversion for various values of the pore structure parameter. Source: Bhatia and Pelmutter [11].

and external surfaces have comparable influence, according to Bhatia and Pelmutter [11]. In the range of parameters where the external surface is negligible, the choice of $\sigma \to \infty$ is a convenience and the conversion-time curve may be computed for each choice of the pore structure parameter [11]. Such results are presented in Fig. 3.6, from which it can be noticed that the rate (slope) usually decreases with conversion as wall collapse progressively acts to reduce the total reaction surface area.

Reaction surface

Eq. (3.72) relates the reaction surface area to the conversion through the pore structure and particle size parameters. The results shown for $\sigma \to \infty$ in Fig. 3.7 indicate that a maximum surface occurs when the value of the parameter ψ is large, but not for small values. The maximum arises from two opposing effects: the growth of reaction surfaces associated with the pore and the loss of these surfaces as they progressively collapse by intersection [11]. The latter effect overshadows the first at all levels of conversion when the pore structure parameter is small enough.

By differentiating Eq. (3.72), the conversion corresponding to the maximum surface for $\sigma \to \infty$ is obtained as

$$X_M = 1 - \exp\left(\frac{2-\psi}{2\,\psi}\right). \tag{3.74}$$

The maximum exists over the range $2 \leq \psi < \infty$ and gives $0 \leq X_M < 0.393$.

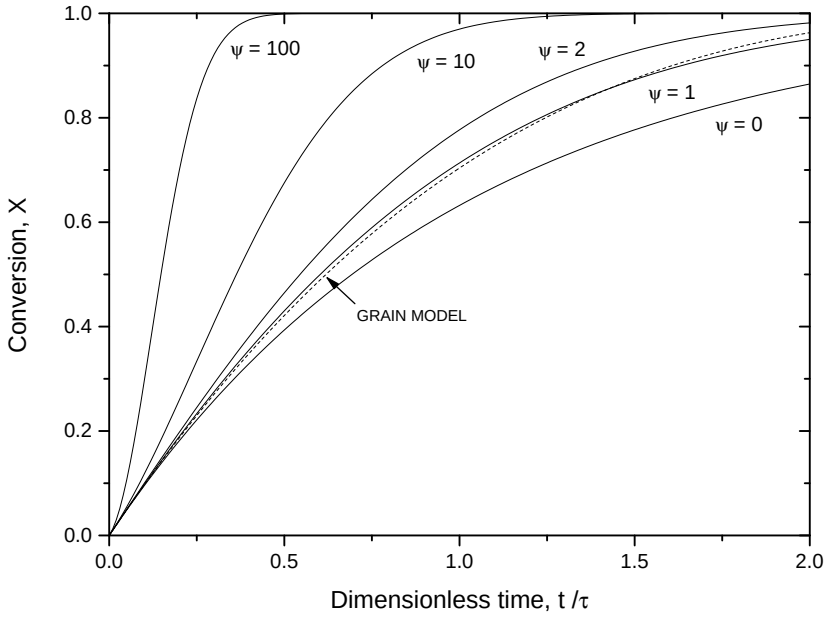

Figure 3.6: The effect of reaction time on overall conversion for different pore structures with negligible external surface. Source: Bhatia and Pelmutter [11].

Comparison with other models

To draw a comparison between the results of the RPM and the other models, it is convenient to differentiate Eq. (3.73), for $\sigma \to \infty$, to give

$$\frac{dX}{d\hat{t}} = (1-X)\,\sqrt{1-\psi\,\ln(1-X)}, \tag{3.75}$$

underlining that $(1-X)$ is $\exp\left[-\hat{t}\,\left(1+\frac{\psi\,\hat{t}}{4}\right)\right]$[11]. This reduces exactly to the volume reaction model if $\psi = 0$. For non-zero values of ψ, the volume reaction model will still be a good approximation for all X such that

$$\psi\,\ln\left(\frac{1}{1-X}\right) \ll 1. \tag{3.76}$$

In terms of the grain model, Eq. (3.28) may be rewritten in dimensionless form as

$$\frac{dX}{d\hat{t}} = (1-X)^{2/3}\,. \tag{3.77}$$

The results are reported in Figs. 3.6 and 3.7. In either figures, it is clear that grain model predictions match for $\psi = 1$.

[11] It is easy to demonstrate that $\sqrt{1-\psi\,\ln(1-X)}$ is equal to $\left(1+1/2\,\psi\,\hat{t}\right)$.

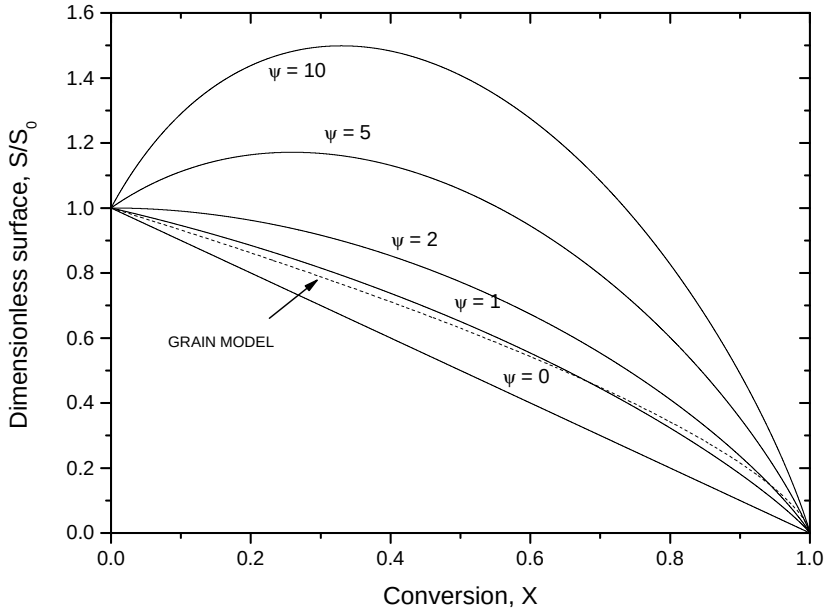

Figure 3.7: Development of the reaction surface with conversion according to the random pore model, compared with the grain model. Source: Bhatia and Pelmutter [11].

Comparison with experimental data

The three parameters ε_0, S_0 and l_0 are the core features of the RPM. The determination of the initial pore structure is discussed in Chapter 2 referring to BET and BJH analysis from which the initial pore volume distribution is obtained. The three parameters of interest are then obtained from

$$\varepsilon_0 = \int_0^\infty \varepsilon_0(r)\, dr, \tag{3.78}$$

$$S_0 = 2\int_0^\infty \frac{\varepsilon_0(r)}{r}\, dr, \tag{3.79}$$

$$L_0 = \frac{1}{\pi}\int_0^\infty \frac{\varepsilon_0(r)}{r^2}\, dr, \tag{3.80}$$

where $\varepsilon_0(r)$ is the probability density function (PDF) inherent to the porosity distribution of the solid phase.

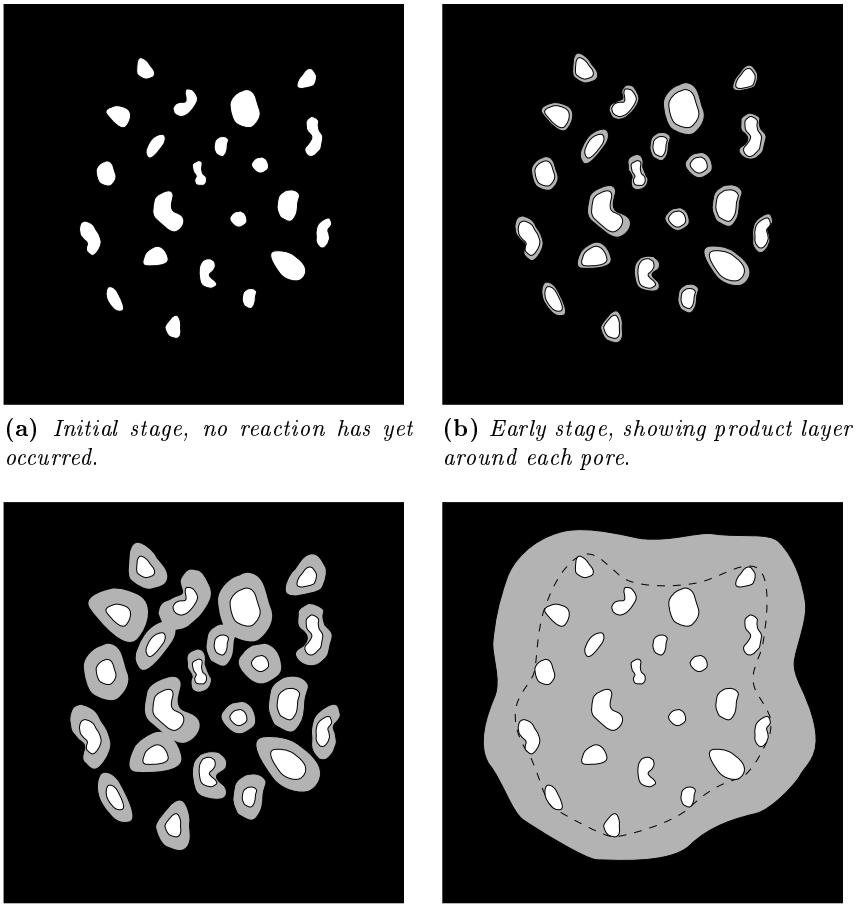

(a) *Initial stage, no reaction has yet occurred.*

(b) *Early stage, showing product layer around each pore.*

(c) *Intermediate stage, showing some overlapping reaction surfaces.*

(d) *Later stage, showing full development of the product layer and the reaction surface for the particular view chosen.*

Figure 3.8: Development of reaction surface. The blackened areas represent unreacted solid B, the gray areas the product layer, while the white areas represent pores. Source: Bhatia and Pelmutter [12].

3.4.2 Isothermal diffusion control

The RPM for kinetic controlled fluid-solid reactions is generalized to include transport effects arising from product layer diffusion following Bhatia and Pelmutter [12]. According to [12], the reaction starts on pore boundaries resulting in a set of growing surfaces at each radial position within the particle. The product Q accumulates in the space between the growing reaction surfaces and the pore boundaries offering a diffusional resistance to the flow of fluid A. As well as in the previous case, as reaction proceeds it is inevitable that neighboring surfaces will eventually intersect, with an accompanying loss in area.

Considering a first order irreversible reaction respect to reactant A and proportional to the surface area, Eqs. (3.50) and (3.59) become

$$\frac{dr}{dt} = b\, k_s\, C_{A,\text{int}}\,, \tag{3.81}$$

and

$$\frac{dV}{dt} = b\, k_s\, C_{A,\text{int}}\, t\, S. \tag{3.82}$$

where $C_{A,\text{int}}$ is the concentration of fluid reactant A, assumed to be uniform over the entire reaction surface at any radial position within the particle. Moreover, Eq. (3.75) remains the same as well as its whole procedure of derivation, but the bulk concentration C_A is replaced for this case by $C_{A,\text{int}}$:

$$\frac{dX}{dt} = \frac{b\, k_s\, S_0\, C_{A,\text{int}}}{(1-\varepsilon_0)}\,(1-X)\,\sqrt{1-\psi\,\ln(1-X)}. \tag{3.83}$$

It remains to relate the interfacial concentration $C_{A,\text{int}}$ to the concentration in the pores at any radial position in the pellet. To this end the two-dimensional sketch shown in Fig. 3.8 is considered, which represents a micro-region at some radial position of the particle in four stages of development: an initial stage in which no reaction has yet occurred; an early stage in which the reaction surfaces have formed around each pore; an intermediate stage in which some of the reaction surfaces intersected; a later stage in which all of the surfaces in that micro-region intersected.
In each case the space between the pore surfaces and the reaction surfaces is filled with reaction product through which the fluid A must diffuse. It should be noticed that the pores and the reaction surfaces associated with them are not necessarily parallel, but can have any orientation in three dimensional space. Thus, although no pore intersection is represented in Fig. 3.8, the pore system forms a single overlapping network, according to Bhatia and Pelmutter [12]. It is assumed that the reaction surface grows normal to itself, so that any point of its boundary traces a non-planar curve in three dimensions. Along this curve the diffusion distance for reactant A is then the distance separating the reaction surface from the surface of the pore closed to it. Thus, as shown in Fig. 3.8d the diffusion thickness is the distance between the reaction surface and the dashed curve representing the periphery of the nearest pores.

Since the molar volume of the solid before reaction and the molar volume of the solid after reaction may be different, it is convenient to define Z as the ratio of the volume of product formed to the volume of solid reacted,

$$\begin{aligned} Z &= \frac{\text{volume of solid phase after reaction}}{\text{volume of solid phase before reaction}} \\ &= \frac{(1-\varepsilon)-(1-V)}{(1-\varepsilon_0)-(1-V)} = \frac{V-\varepsilon}{V-\varepsilon_0}. \end{aligned} \tag{3.84}$$

Eq. (3.84) becomes

$$V-\varepsilon = Z\,(V-\varepsilon_0)\,, \tag{3.85}$$

and combining Eqs. (3.81) and (3.85) gives the rate of formation of product as a result of reactions,

$$\frac{d\,(V-\varepsilon)}{dt} = Z\,b\,k_s\,C_{A,\text{int}}\,S. \tag{3.86}$$

Denoting Δ as the mean thickness of the diffusion layer, and considering it to be small in comparison to the size of the reaction surface,

$$\frac{d\Delta}{dt} = \frac{1}{S}\,\frac{d\,(V-\varepsilon)}{dt}. \tag{3.87}$$

Combining Eqs. (3.86) and (3.87) results

$$\frac{d\Delta}{dt} = Z\,b\,k_s\,C_{A,\text{int}}\,, \tag{3.88}$$

Eqs. (3.83) and (3.88) provide

$$\frac{d\Delta}{dX} = \frac{Z\;(1-\varepsilon_0)}{S_0\;(1-X)\;\sqrt{1-\psi\,\ln(1-X)}} \tag{3.89}$$

which, upon integration with initial condition $\Delta = 0$ when $X = 0$, yields

$$\Delta = \frac{2\,Z\;(1-\varepsilon_0)}{\psi\,S_0}\;\left[(1-X)\;\sqrt{1-\psi\,\ln(1-X)}-1\right], \tag{3.90}$$

as the effective local thickness of the diffusion layer, at any local conversion X.
Bhatia and Pelmutter [12] assumed a thin product layer Q, so that a linear concentration gradient of species A is established in the diffusion layer of thickness Δ. With the hypothesis of pseudo-steady-state approximation of A in the product layer, a material balance of A provides

$$D_{pl}\,\frac{C_A - C_{A,\text{int}}}{\Delta} = \frac{a\,k_s\,C_{A,\text{int}}\,\rho_s}{M_B}. \tag{3.91}$$

Combining Eqs. (3.75), (3.90) and (3.91) yields an expression for the local reaction rate

$$\frac{dX}{dt} = \frac{b\,k_s\,S_0\,C_A\;(1-X)\;\sqrt{1-\psi\,\ln(1-X)}}{(1-\varepsilon_0)\;\left[1+\dfrac{\beta\,Z}{\psi}\;\left(\sqrt{1-\psi\,\ln(1-X)}-1\right)\right]}, \tag{3.92}$$

where β is a dimensionless quantity that expresses the relative magnitude between the reaction kinetics and the diffusion in the product layer:

$$\beta = \frac{2\,a\,k_s\,\rho_s\;(1-\varepsilon_0)}{M_B\,D_{pl}\,S_0}. \tag{3.93}$$

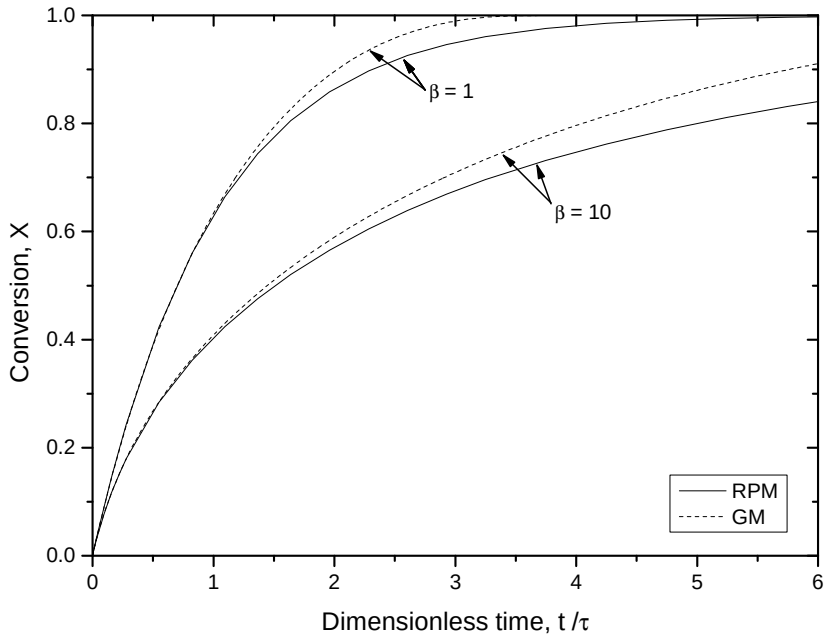

Figure 3.9: Comparison of conversion-time behaviour predicted by the random pore model and the grain model, in presence of chemical reaction and product layer diffusion. The random pore model lines are obtained with $\psi = 1$. In all cases $Z = 1$. Source: Bhatia and Pelmutter [12].

Using the definition of Eq. (3.71), Eq. (3.92) becomes

$$\frac{dX}{d\hat{t}} = \frac{\hat{C}_A\,(1-X)\,\sqrt{1-\psi\,\ln(1-X)}}{1+\dfrac{\beta\,Z}{\psi}\left(\sqrt{1-\psi\,\ln(1-X)}-1\right)} \tag{3.94}$$

where

$$\hat{t} = \frac{t}{\tau} = \frac{b\,k_s\,C_{A,\,\mathrm{bulk}}\,S_0}{(1-\varepsilon_0)}\,t, \qquad\qquad \hat{C}_A = \frac{C_A}{C_{A,\,\mathrm{bulk}}}. \tag{3.95}$$

Conversion-time behavior

When chemical kinetics and product layer diffusion control the overall reaction rate, Eq. (3.94) may be integrated to

$$X = 1 - \exp\left\{\frac{1}{\psi} - \frac{\left[\sqrt{1+\beta\,Z\,\hat{t}} - \left(1-\dfrac{\beta\,Z}{\psi}\right)\right]^2\psi}{\beta^2\,Z^2}\right\} \tag{3.96}$$

The comparable expression for the spherical grain model with $Z = 1$ is reported in Eq. (3.44) in implicit form. Fig. 3.9 shows a comparison of the predictions of Eq. (3.44) with those of Eq. (3.96) for $Z = 1$ and $\psi = 1$. In general, the agreement is better for smaller values of β, and for small conversions. As expected, the conversion process is slowed down as the diffusional resistance in the product layer increases (D_{pl} decreases), as shown in Fig. 3.10.

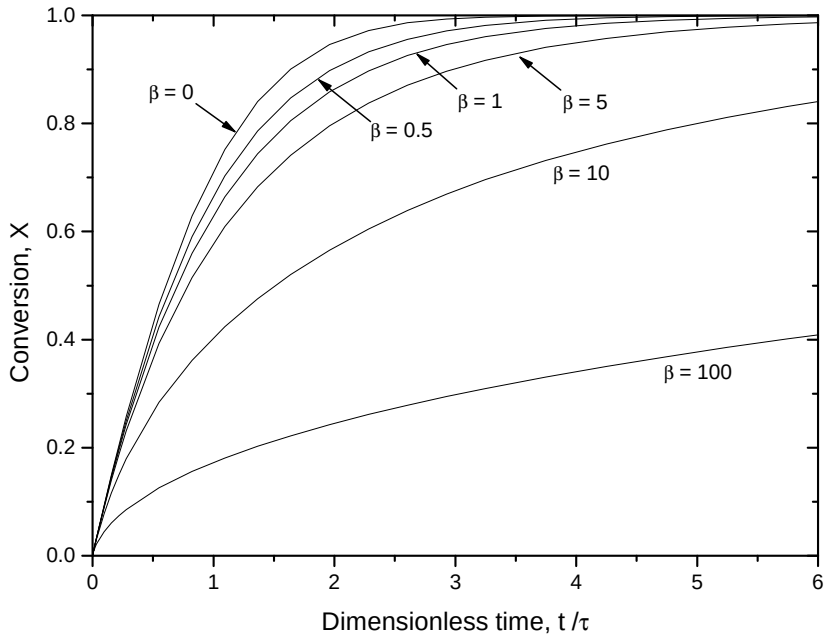

Figure 3.10: Comparison of conversion-time behavior predicted by the random pore model at various values of β. In all cases $Z = 1$.

Product layer diffusion resistance

From a comparison between Eq. (3.83) and Eq. (3.92) a function of conversion is introduced in order to represent the diffusion resistance in the product layer that may be named $F_\psi(X)$ as reported in Eq. (3.97),

$$F_\psi(X) = \frac{\beta Z}{\psi}\left(\sqrt{1-\psi\ln(1-X)}-1\right). \tag{3.97}$$

Depending on β, diffusion in the product layer may be more or less strong. When $F_\psi(X)$ is less than 1, the overall process is controlled by chemical reaction, otherwise, when $F_\psi(X)$ magnitude is larger than 1 diffusion regime is controlling. When $F_\psi(X)$ assumes intermediate values, the overall process is both chemical and diffusion controlled. Fig. 3.11 shows $F_\psi(X)$ plots against conversion for different values of β. When β is large, diffusion resistance is high even when for small values of X, in other cases it becomes considerable only when X approaches to 1. Consequently, for heterogeneous reactions whose β is very high, it seems that the whole process is diffusion controlled even at low degree of conversion.

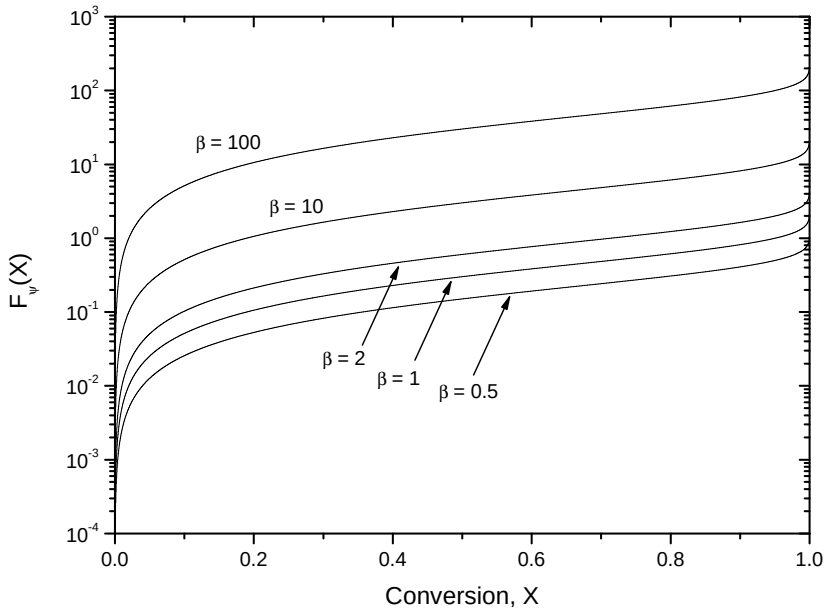

Figure 3.11: Profiles of $F_\psi(X)$ with conversion X for different values of β. In all cases $Z = 1$ and $\psi = 1$. Source: Bhatia and Pelmutter [12].

Estimation of Z

Eq. (3.84) gives the definition of Z as the ratio of the volume of the solid phase after reaction to that before reaction. Its value can be estimated starting from Eq. (3.84), that becomes

$$Z = \frac{\dfrac{M_r}{\rho_r}\,(n_{r,0} - \Delta n_r) + \dfrac{M_p}{\rho_p}\,(n_{p,0} + \Delta n_r)}{\dfrac{M_r}{\rho_r}\,n_{r,0} + \dfrac{M_p}{\rho_p}\,n_{p,0}}, \tag{3.98}$$

where the subscripts r and p refer respectively to the solid reactant and to the solid product, the subscript 0 refers to the initial time and $\Delta n_r = n_r - n_{r,0}$ is the number of moles of reactant disappeared due to the reaction. Eq. (3.98) assumes that the porous solid is initially composed by both reactant and product. Considering the conversion definition reported by Eq. (3.10), $X = \Delta n_r / n_{r,0}$ so that Eq. (3.98) is changed into

$$Z = \frac{\dfrac{M_r}{\rho_r}\,(1 - X) + \dfrac{M_p}{\rho_p}\left(\dfrac{n_{p,0}}{n_{r,0}} + X\right)}{\dfrac{M_r}{\rho_r} + \dfrac{M_p}{\rho_p}\,\dfrac{n_{p,0}}{n_{r,0}}}. \tag{3.99}$$

However, if the solid consists of pure reactant, $n_{p,0} = 0$ and Eq. (3.99) becomes

$$Z = 1 + \frac{\rho_r}{M_r}\left[\frac{M_p}{\rho_p} - \frac{M_r}{\rho_r}\right] X. \tag{3.100}$$

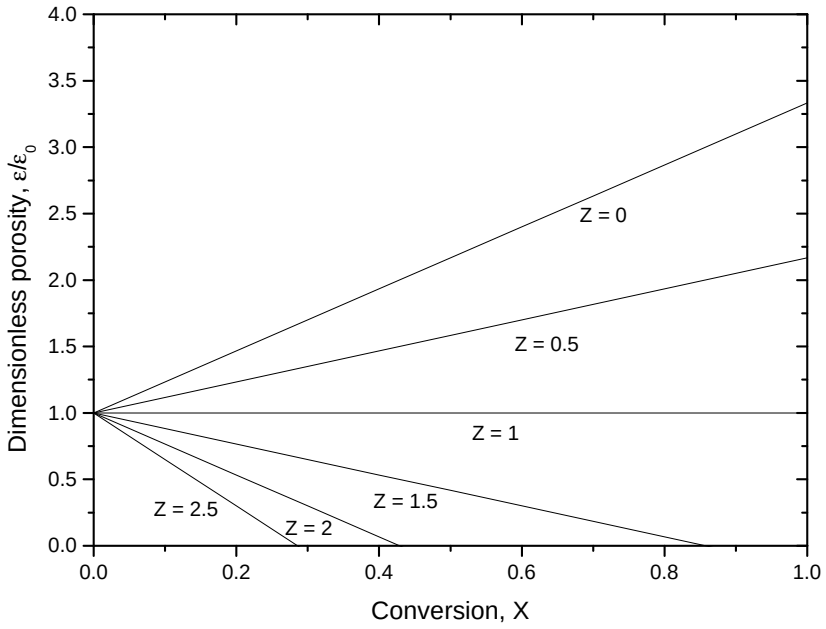

Figure 3.12: Porosity-conversion profile for various values of Z ($\varepsilon_0 = 0.3$).

Moreover, the value of Z for $X = 1$ is

$$Z(X=1) = \frac{M_p}{\rho_p}\,\frac{\rho_r}{M_r}, \tag{3.101}$$

that is the volumetric ratio between the molar volume of the product to the reactant.
Referring to Eq. (2.1) and Tab. 2.1, and assuming that the initial solid density is $\rho_r = \rho_{\mathrm{CaO}}$[12], Eq. (3.101) assumes the value of 2.2.

Porosity-conversion behaviour

As reaction occurs the solid reactant undergoes to structural chances in its internal morphology, which means that both internal reaction surface and porosity change with conversion. From Eq. (3.72) with $\sigma \to \infty$ the reaction surface varies with conversion according to

$$S = S_0\,(1-X)\,\sqrt{1-\psi\,\ln(1-X)}, \tag{3.102}$$

that may shows a maximum depending on ψ value as reported in Fig. 3.7.
Since the porosity varies during the reaction, its relationship with conversion can be found starting from the definition of Z reported by Eq. (3.84), that gives

$$\varepsilon = V - Z\,V + Z\,\varepsilon_0. \tag{3.103}$$

[12]During calcination step, calcium carbonate is completely decomposed to calcium oxide.

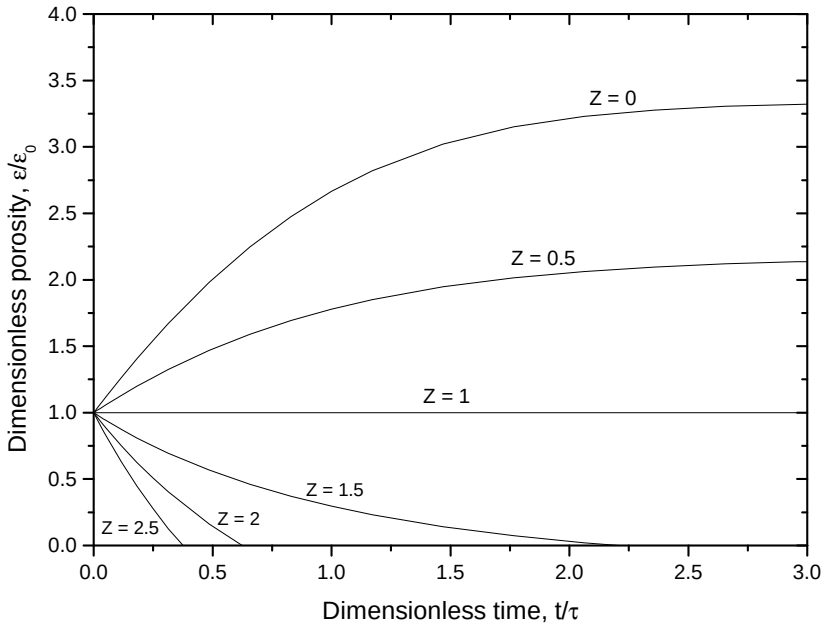

Figure 3.13: Porosity-dimensionless time profile for various values of Z ($\varepsilon_0 = 0.3$).

Eq. (3.69) may be solved for V (assuming $\sigma \to \infty$), giving

$$V = \varepsilon_0 + (1 - \varepsilon_0)\, X. \tag{3.104}$$

Substituting Eq. (3.104) into Eq. (3.103),

$$\varepsilon = \varepsilon_0 + (1 - Z)\, (1 - \varepsilon_0)\, X, \tag{3.105}$$

and defining a dimensionless porosity $\hat{\varepsilon} = \varepsilon/\varepsilon_0$, it gives

$$\hat{\varepsilon} = 1 + \frac{(1 - Z)\, (1 - \varepsilon_0)}{\varepsilon_0}\, X. \tag{3.106}$$

Further, it is useful to differentiate Eq. (3.105) with time, giving

$$\frac{d\varepsilon}{dt} = (1 - Z)\, (1 - \varepsilon_0)\, \frac{dX}{dt}. \tag{3.107}$$

Fig. 3.12 plots the linear trend of Eq. (3.107) for various Z (the particular case $Z = 0$ is not physically possible). Fig. 3.13 reports the porosity profiles against the dimensionless time $\hat{t}$ with Z. Clearly, only for $Z = 1$ the total porosity remains constant during the whole process, leaving the internal structure unchanged. Depending on Z, Figs. 3.12 and 3.13 show a progressively change in pore volume, specifically, if $Z > 1$ solid phase undergoes to a pore shrinkage, whereas, $Z < 1$ pore enlargement takes place.

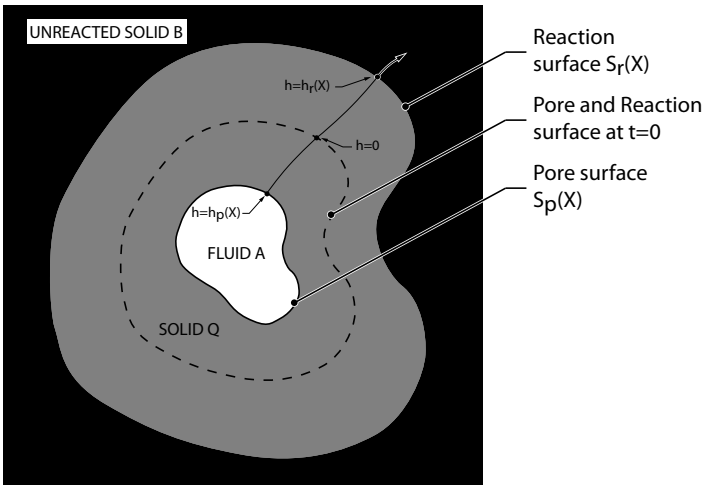

(a) $Z > 1$.

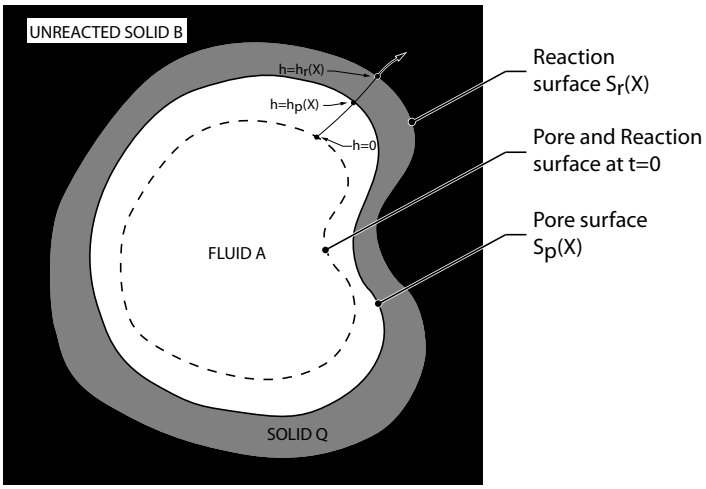

(b) $Z < 1$.

Figure 3.14: Development of pore and reaction surface in a single pore. Sketches reproduced from Bhatia and Pelmutter [14].

3.5 Additional structural effects in gas-solid reactions

Bhatia and Pelmutter in their works [11] and [12] formulated a model that accounts for the random intersections of the pores in a solid. For reactions with a solid product, they derived a reaction rate that accounts for both chemical and diffusion mechanisms, as reported in Eq. (3.92), where the parameter β characterizes the diffusional resistance to the flow of A in the layer of product Q (assumed to be sufficiently thin to allow a linear concentration profile). In this way, the RPM developed by Bhatia and Pelmutter [11] considers the pore and reaction surface areas to be equal, an approximation which is less accurate at high conversion [14].

3.5.1 Structural development

As a porous solid undergoes an isothermal irreversible reaction, structural changes (in terms of porosity and specific surface) occur on the pore walls from which reaction surfaces progress

inwards as conversion proceeds, leaving behind a layer of product Q through which the reactant fluid must diffuse. The pore surface must be distinguished from the reaction surface at all times after the initial instant. As reaction proceeds each point on the reaction surface moves into the unreacted solid B at the instantaneous speed according to Bhatia and Pelmutter [14]:

$$\frac{dh_r}{dt} = b\, k_s\, C^r_{A,\,\mathrm{int}}, \tag{3.108}$$

where h_r is the distance along the curve traced by any point on the reaction surface as it moves in the normal direction, and $C^r_{A,\,\mathrm{int}}$ is the concentration of fluid A on the reaction interface. Eq. (3.108) is formally equal to Eq. (3.50) with the difference that in this case a suitable distinction is made between pore and reaction surface. It should be emphasized that $C^r_{A,\,\mathrm{int}}$ is exactly uniform over the entire reaction surface only for solids where the surface curvature is everywhere uniform. This assumption is not strictly rigorous because pore surface, and so reaction surface, may be not uniform, however, the concentration of fluid A is to be regarded as an effective or averaged value on the reaction surface.

Because of the reaction, product Q generally occupies a different volume than the stoichiometrically equivalent reactant B and the pore surface also moves in a direction assumed always normal to itself from its initial position at $h = 0$ to $h = h_p(X)$ at conversion X. The space between h_p and h_r is filled with reaction product Q. Fig. 3.14 illustrates the motion of the pore and reaction surfaces separated by the product Q, in a single pore. In Fig. 3.14a $Z > 1$ and h_p moves in the negative h direction; in Fig. 3.14b $Z < 1$ and in this case the pore surface moves in the positive h direction. If it is assumed that diffusion through the product layer occurs unidimensionally in the h direction, all points with a distance h from the original pore surface form contours of constant concentration. Consequently, with the pseudo-steady-state approximation of reactant A in the product layer, its conservation equation is

$$\frac{\partial}{\partial h}\left[S_d(h)\,\frac{\partial C_A}{\partial h}\right], \tag{3.109}$$

where $S_d(h)$ is the surface area of the contour formed by all points at a distance h away from the original pore surface, measured along the normal direction. Since the reaction surface also moves in the normal direction, $S_d(h)$ represents the area of the reaction surface when it was at position h. Taking $Z > 1$,

$$S_d(h) = \begin{cases} S_r(h), & 0 \le h \le h_r \\ S_p(h), & h_p \le h \le 0. \end{cases} \tag{3.110}$$

The boundary condition of Eq. (3.109) are

$$\begin{aligned} C_A &= C^p_{A,\,\mathrm{int}}, && \text{at } h = h_p \\ -D_{pl}\,\frac{\partial C_A}{\partial h} &= \frac{a\,\rho_s}{b\,M_B}\,\frac{dh_r}{dt}, && \text{at } h = h_r. \end{aligned} \tag{3.111}$$

Integrating Eq. (3.109) with the boundary conditions, it provides the concentration of fluid A at reaction interface:

$$C^r_{A,\,\mathrm{int}} = \frac{C^p_{A,\,\mathrm{int}}}{\left[1 + \dfrac{a\,\rho_s\,k_s\,S_r(h_r)}{M\,D_{pl}} \displaystyle\int_{h_p}^{h_r} \frac{dh'}{S_d(h')}\right]}. \tag{3.112}$$

Expressing the local reaction rate Eq. (3.108) in term of conversion

$$\frac{dX}{dt} = \frac{S_r(h_r)}{1-\varepsilon_0}\,\frac{dh_r}{dt}, \tag{3.113}$$

and substituting Eqs. (3.108) and (3.112),

$$\frac{dX}{dt} = \frac{b\,k_s\,C^p_{A,\,\mathrm{int}}\,S_r(h_r)}{(1-\varepsilon_0)\left[1 + \dfrac{a\,\rho_s\,k_s\,S_r(h_r)}{M\,D_{pl}} \displaystyle\int_{h_p}^{h_r} \frac{dh'}{S_d(h')}\right]}. \tag{3.114}$$

To each position h' of the reaction surface or pore surface there corresponds a conversion X'. Following Bhatia and Pelmutter [14], in order to re-express the integrand of Eq. (3.114) in terms of conversion, it is convenient to introduce the following transformation that comes from Eq. (3.113)

$$X' = \frac{1}{(1-\varepsilon_0)} \int_0^{h'} S_d(h)\,dh \qquad h_p(X) \le h' \le h_r(X). \tag{3.115}$$

From Eq. (3.115), $|X'|$ represents the volume of the product lying between $h = 0$ and $h = h'$, per unit volume of the original solid phase. Therefore, the conversion corresponding to the position h' of reaction surface is

$$X'' = X', \qquad 0 \le h' \le h_r(X), \tag{3.116}$$

and similarly the conversion X'' when the pore surface was at position h' may be written using Z ratio definition, Eq. (3.84),

$$X'' = \frac{X'}{(Z-1)}, \tag{3.117}$$

over $h_p(X) \le h' \le 0$ for $Z > 1$, and over the interval $0 \le h' \le h_p(X)$ for $Z < 1$. Both h_p and X' are negative for $Z > 1$. Eqs. (3.114) and (3.115) and the above arguments provide

$$\frac{dX}{d\hat{t}} = \frac{\hat{C}^p_{A,\,\mathrm{int}}\,\hat{S}_r(X)}{1 + \dfrac{\beta}{2}\,\hat{S}_r(X) \displaystyle\int_{(1-Z)X}^{X} \frac{dX'}{\hat{S}^2_d(X')}}. \tag{3.118}$$

which, combined with Eqs. (3.110), (3.116) and (3.117), gives

$$\frac{dX}{d\hat{t}} = \frac{\hat{C}^{p}_{A,\,\mathrm{int}}\,\hat{S}_r(X)}{1+\dfrac{\beta}{2}\,\hat{S}_r(X)\displaystyle\int_0^X\left[\frac{1}{\hat{S}_r^2(X')}+\frac{Z-1}{\hat{S}_p^2(X')}\right]dX'}. \tag{3.119}$$

This is an integer-differential equation and expresses the instantaneous local reaction rate at any radial position in the particles of solid B; β and $\hat{t}$ are the same of Eqs. (3.93) and (3.95) .If intra-particle and boundary layer diffusional resistances are negligible, $\hat{C}^{p}_{A,\,\mathrm{int}} = 1$ everywhere and Eq. (3.119) may be rearranged and integrated to yield

$$\hat{t} = \int_0^X \frac{dX'}{\hat{S}_r(X')} + \frac{\beta}{2}\int_0^X\int_0^{X'}\left[\frac{1}{\hat{S}_r^2(X')}+\frac{Z-1}{\hat{S}_p^2(X')}\right]dX'\,dX''. \tag{3.120}$$

In the reaction control regime, $\beta \to 0$, and the first term in the left-hand side of Eq. (3.120) dominates; whereas, when product layer diffusion dominates, the second term becomes more important.

To obtain specific solutions for $X(t)$, it is necessary to provide models of the internal structure of the solid. Each such choice of model yields appropriate expressions $\hat{S}_r(X)$ and $\hat{S}_p(X)$ for substitution in the integrands of Eq. (3.119) or (3.120).

3.5.2 Random pore model

Bhatia and Pelmutter [11] showed that if all the cylinders are growing at the same rate, the area of the reaction surface as it grows from the original pore surface is given by Eq. (3.68) ($\sigma \to \infty$). The assumption that all the cylinders grow at the same rate is rigorously true in the absence of a product layer diffusional resistance, or when all the non overlapped cylinders have the same size. Otherwise, Eq. (3.68) also may be used for thin product layers for which the curvature of the reaction surface has little influence.

According to the previous considerations, Eq. (3.68) represents the total reaction surface of the particle and may be rewritten in terms of conversion,

$$\hat{S}_r(X) = (1-X)\,\sqrt{1-\psi\,\ln(1-X)}. \tag{3.121}$$

Since the pore surface is assumed to move in the normal direction, its evolution can also be considered to be the motion of the surface of a set of overlapping cylinders. For uniform-size cylinders, Eq. (3.68) is valid for the pore surface area, but with V replaced by the porosity ε. Combining this observation with Eqs. (3.105) and (3.68), it provides

$$\hat{S}_p(X) = [1+(Z-1)X]\,\sqrt{1-\psi\,\ln[1+(Z-1)\,X]}. \tag{3.122}$$

The local reaction rate of any conversion can be found by substitution of Eqs. (3.121) and (3.122) into Eq. (3.119), that gives

$$\frac{dX}{d\hat{t}} = \frac{\hat{C}^{p}_{A,\,\mathrm{int}}\,(1-X)\,\sqrt{1-\psi\,\ln(1-X)}}{1+\dfrac{\beta}{2}\,(1-X)\,\sqrt{1-\psi\,\ln(1-X)}\displaystyle\int_{(1-Z)X}^{X}\frac{dX'}{(1-X')^{2}\,[1-\psi\,\ln(1-X')]}}. \tag{3.123}$$

3.5.3 Grain model

For spherical grains undergoing an irreversible fist order reaction, Georgakis at al. [23] considered a changing grain size model (without overlapping) and provided the result

$$\frac{dX}{d\hat{t}} = \frac{\hat{C}^{s}_{A,g}\,(1-X)^{2/3}}{1+\dfrac{3\,\beta}{2}\left[(1-X)^{1/3}-\dfrac{(1-X)^{2/3}}{[1+(Z-1)X]^{1/3}}\right]} \tag{3.124}$$

in which it is assumed that the fluid A diffuses through a spherical shell of product Q that surrounds an unreacted core of B in each grain, before reaction at the B-Q interface. However, this kind of model can only describe systems without a maximum rate, since it treats the reaction surface as monotonically shrinking.
If the solid is treated as being composed of equally-sized grains, the variation of the reaction surface with conversion follows

$$\hat{S}_r(X) = (1-X)^{2/3}\,, \tag{3.125}$$

and for the pore surface

$$\hat{S}_p(X) = [1+(Z-1)\,X]^{2/3}\,. \tag{3.126}$$

Eq. (3.126) is derived from Eq. (3.22) and Z ratio definition which is

$$Z = \frac{V_g - V_c}{V_{g,0} - V_c}, \tag{3.127}$$

that gives

$$r_g^3 = r_{g,0}^3\,[1+(Z-1)\,X]\,, \tag{3.128}$$

where the subscripts g and c refer respectively to the grain and to the core.
Eqs. (3.125) and (3.126) may be introduced into Eq (3.119) to derive the expression of reaction rate

$$\frac{dX}{d\hat{t}} = \frac{\hat{C}^{s}_{A,g}\,(1-X)^{2/3}}{1+\dfrac{\beta}{2}\,(1-X)^{2/3}\displaystyle\int_{0}^{X}\left[\frac{1}{(1-X')^{4/3}}+\frac{Z-1}{[1+(Z-1)\,X']^{4/3}}\right]dX'} \tag{3.129}$$

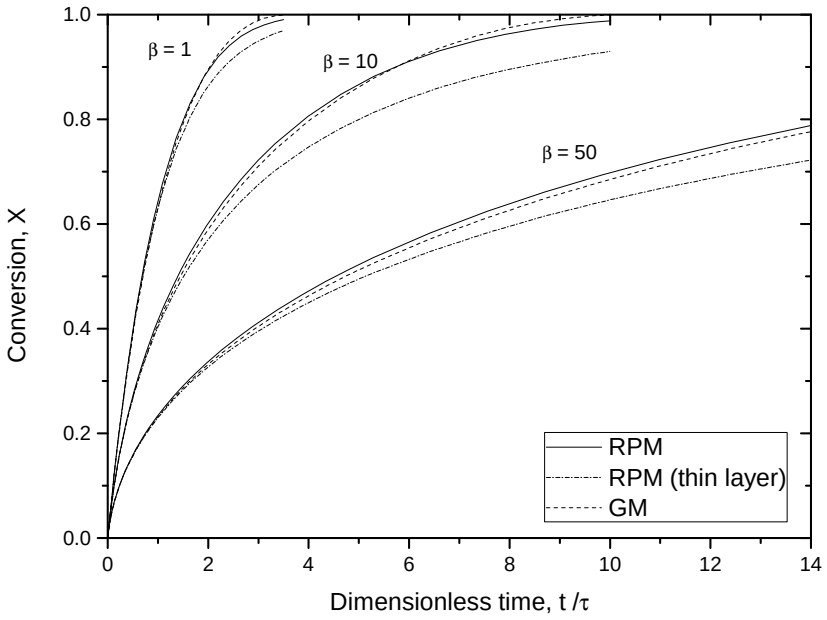

Figure 3.15: Comparison of conversion-time behavior predicted by the RPM, by the RPM with thin layer and the GM, for various values of β. Parameters are $\psi = 1$ and $Z = 1$. Source: Bhatia and Pelmutter [14].

which integrates to the result in Eq. (3.124).

3.5.4 Numerical results

In order to compare the two models, solutions were computed with Eqs. (3.123) and (3.124) for the case when intra-particle concentration gradients are negligible. To solve Eq. (3.123), the following transformation was considered

$$Y = \int_{(1-Z)X}^{X} \frac{dX'}{(1-X')^2\,[1-\psi\,\ln(1-X')]}, \tag{3.130}$$

so that

$$\frac{dY}{dX} = \frac{1}{(1-X)^2\,[1-\psi\,\ln(1-X)]} + \frac{(Z-1)}{[1+(Z-1)X]^2\,[1-\psi\,\ln(1+(Z-1)X)]} \tag{3.131}$$

and

$$\frac{dX}{d\hat{t}} = \frac{\hat{C}^{p}_{A,\,\mathrm{int}}\,(1-X)\,\sqrt{1-\psi\,\ln(1-X)}}{1+\dfrac{\beta}{2}\,(1-X)\,Y\,\sqrt{1-\psi\,\ln(1-X)}}. \tag{3.132}$$

with initial condition $X = Y = 0$ at $\hat{t} = 0$.

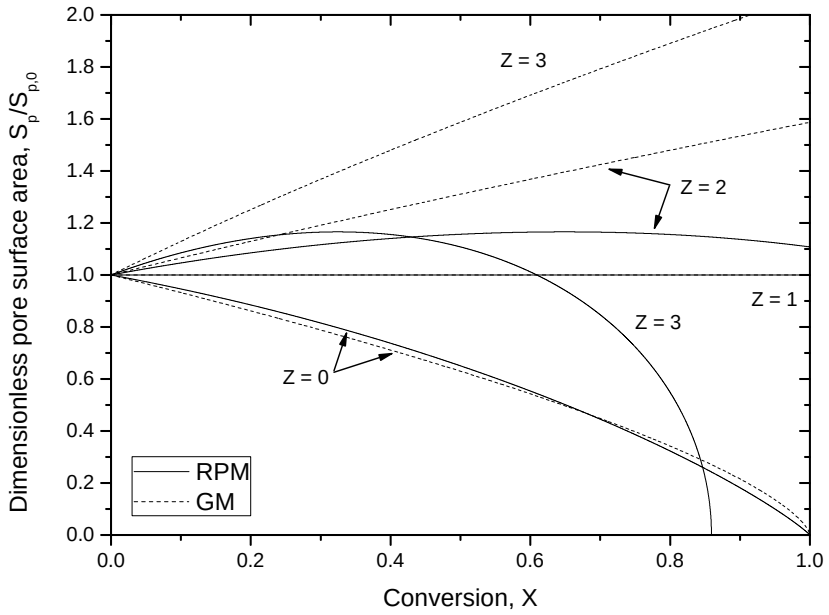

Figure 3.16: Predicted development of the pore surface for RPM and GM varying Z. For the RPM all curves are obtained with $\psi = 1$.

Conversion vs. time

The random pore model agrees well with the spherical grain model for all values of β, as reported in Fig. 3.15, for $\psi = 1$ and $Z = 1$. The simpler thin layer RPM (that is the RPM of Bhatia and Pelmutter [11]) result also agrees with these two up to about 60 % of conversion, deviating at higher conversions because of the assumption that the concentration gradient of A in the product layer is linear.

Surface vs. time

Fig. 3.16 shows a comparison between the pore surface evolution of the RPM and the GM with conversion. As mentioned the GM predicts a monotonically decrease of $\hat{S}_p$ and it well agrees with RPM prediction only for $Z = 0$. When $Z = 1$ both models are clearly in agreement since the pore surface is assumed unchanged. At values of $Z > 1$, however, the grain and random pore models are in disagreement, the former predicting a monotonically increasing pore surface, and the latter showing a decrease in the surface after some conversion. It would seem that this random pore model result is more realistic, since for Z large enough that Eq. (3.105) predicts pore closure prior to complete conversion, the model is consistent in leading to $\hat{S}_p \to 0$ with increasing conversion. There are relative large differences in the pore surfaces between the grain model and random pore models for $Z > 1$, but only small differences in predicted conversion (Fig. 3.17). Evidently, the conversion-time predictions are more strongly affected by differences in the reaction surface than of the pore surface.

Fig. 3.18 shows the influence of the structural parameter ψ on pore surface evolution of RPM, for larger values of ψ pore closure occurs at lower degree of conversion for a constant value of Z

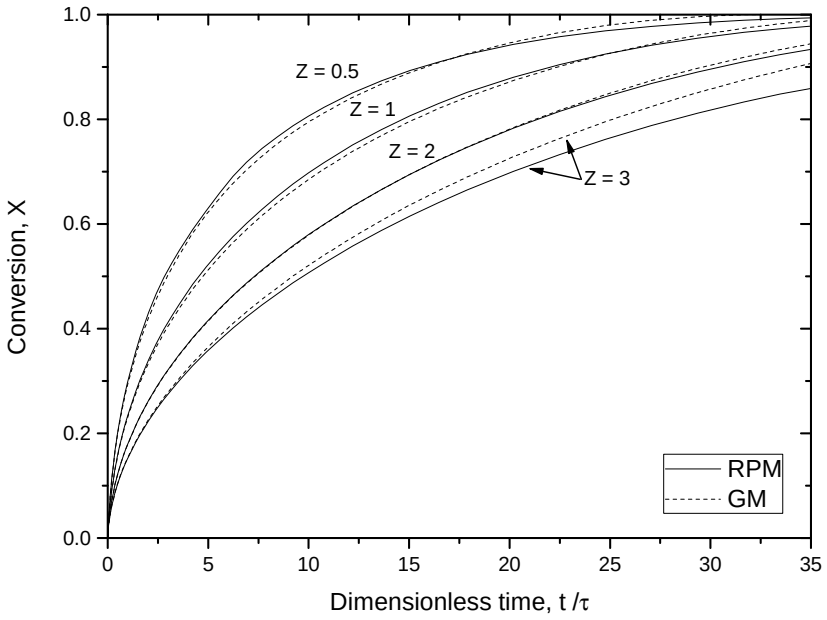

Figure 3.17: Comparison of conversions predicted by random pore and grain models. Parameters are $\psi = 1$ and $\beta = 50$.

$(Z = 2)$.

A particular feature of the random pore model is the pore surface behaviour against conversion for certain values of structural parameters. Figs. 3.16 and 3.18 show an increase of $\hat{S}_p$ up to a maximum value, after that pore surface decreases down to zero reaching pore closure. It is not clear the meaning of this behaviour and at first sight it appears to be unphysical. However, an explanation can be obtained taking the derivative of Eq. (3.122) with X that can be expressed as

$$\frac{d\hat{S}_p}{dX} = f_1(X) - f_2(X). \tag{3.133}$$

Eq. (3.133) is composed by two different contributions, namely $f_1(X)$ and $f_2(X)$ that are

$$f_1(X) = (Z-1)\sqrt{1 - \psi \ln[1 + (Z-1)X]}, \tag{3.134}$$

$$f_2(X) = \frac{1}{2}\frac{\psi\,(Z-1)}{\sqrt{1 - \psi \ln[1 + (Z-1)X)]}}. \tag{3.135}$$

Fig. 3.19 reports the behaviour of $f_1(X)$ and $f_2(X)$ with conversion, it shows that the first contribution is monotonically decreasing with X, whereas the second one is monotonically increasing. Specifically, $f_1(X)$ magnitude is larger that $f_2(X)$ for low degree of conversions, but when $\hat{S}_p$ reaches its maximum value the two functions have the same magnitude. Later, $f_2(X)$ becomes larger than $f_1(X)$ so that pore surface areas decrease until zero.

According to the previous equations, it seems that this pore surface trend is due to the RPM assumptions which may affect $\hat{S}_p$ curves making its behaviour similar to the reaction surface one.

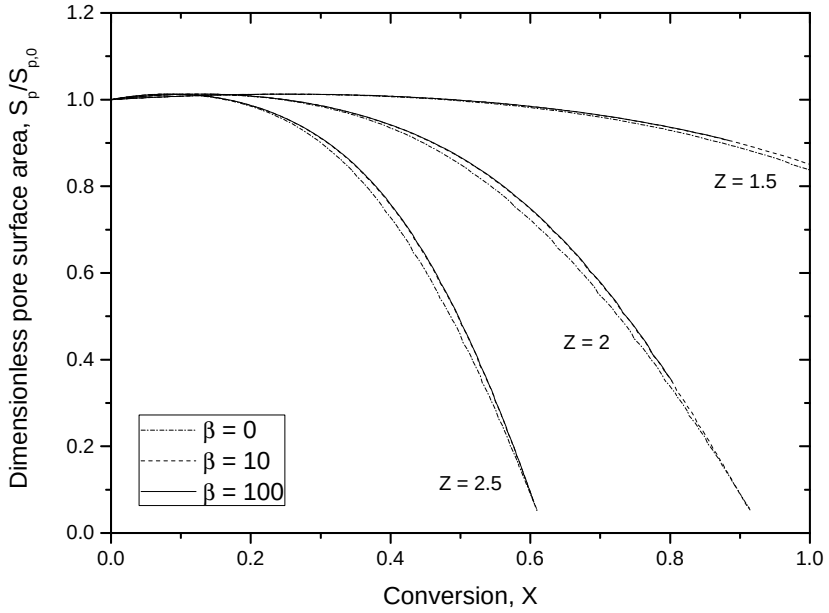

Figure 3.18: Effect of ψ on the development of pore surface for RPM. Curves were obtained for $Z = 2$.

3.6 Analysis of local structural evolution and pore closure in gas-solid reactions

The gas-solid reactions involving pore closure have the common feature that the reaction product occupies a larger volume than the reactant consumed, so that the porosity of the solid is gradually reduced with conversion. In such cases often incomplete conversion is noticed because of the pore closure at the particle surface prior to complete conversion(Bhatia [10] and Sotirchos et al. [57]). In this way the internal structure is sealed off from the exposure to the gaseous reactant.

According to Eq. (3.105), porosity varies linearly with local conversion, this means that the local porosity may reduce to zero due to pore closure. In his work [10] Bhatia suggested that porosity never really reduces to zero, but takes on a very small value permitting further reaction to continue at an extremely slow rate.

Apparently, Eq. (3.105) is able to predict the maximum conversion at pore closure. Actually, pore closure must be distributed with the smaller pores closing first and the larger pores closing later (or not at all). Bhatia [10] suggested a modification of the RPM to incorporate this effect. Furthermore he recognized the importance to include pore overlap, for otherwise in the limit of reaction control the model predicts a monotonically increasing reaction rate as the reaction surface grows with conversion.

Experimental results on the reaction between carbon dioxide and lime [13] showed incomplete conversion even when pore diffusion resistances were considered negligible and sufficient initial porosity existed for the reaction to reach completion. Inspection of the pore size distribution of the reactants showed that the bulk of the porosity existed in small pores of a narrow size range,

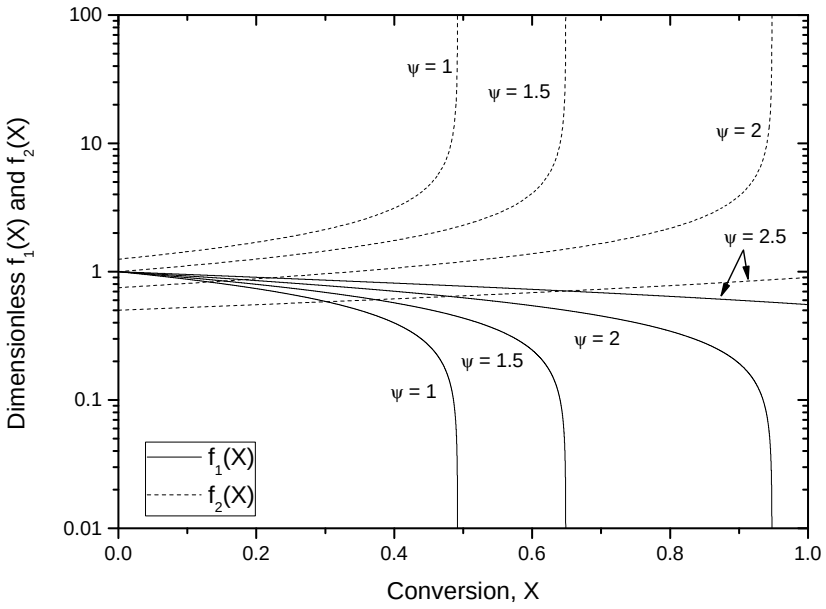

Figure 3.19: Effect of ψ on the two contributes of the derivative of $\hat{S}_p$ with conversion.

with a small amount of pore volume in larger pores of a wide size range. Incomplete conversion was then attributed to closure of the smaller pores, with the large pores being much less active and showing only a small amount of residual reactivity.

Bhatia [10] and Sotirchos et al. [57] independently developed a RPM accounting for pore size distribution, modeling the local closure of pores, assuming that pores and reaction surfaces are uniformly distributed.

3.6.1 Model development

A first order irreversible reaction of gas A with solid B is considered, according to the stoichiometry of Eq. (3.1). It is assumed that reaction is initiated inside pores of solid B, assumed to be cylindrical. As reaction progresses B is consumed and a reaction surface moves into the unreacted solid leaving behind a layer of product Q. If the product layer occupies a larger volume than the reactant B consumed, the pore surface moves inward as shown in Fig. 3.20. Furthermore, the pore and reaction surfaces are assumed to remain cylindrical as reaction proceeds and diffusion of the reactant fluid A occurs unidimensionally between them, always along the h direction for any pore. Even though pore shape is assumed to be cylindrical, the model derivation consider a generic pore geometry.

Porous network is initially formed by a collection of straight capillaries uniformly distributed in space. The structural properties of such a system were first studied by Gavalas [22], who showed that it can be completely described by a single distribution density function namely a length distribution function $l_0(r_0)$, where $l_0(r_0)dr_0$ gives the initial not overlapped total length of pore per unit of volume corresponding to capillaries in the size range $[r_0,\, r_0 + dr_0]$. The porosity

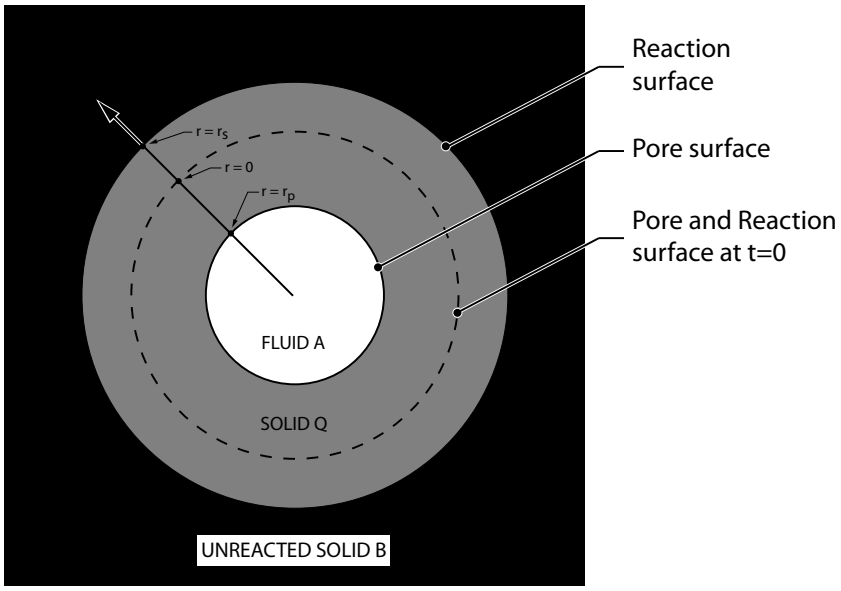

Figure 3.20: Development of pore and reaction surfaces. Sketches reproduced from Bhatia and Pelmutter [14].

and internal surface area of the porous medium are given by

$$V_0 = \varepsilon_0 = 1 - \exp\left[-\pi \int_0^\infty r_0^2\, l_0(r_0)\, dr_0\right], \tag{3.136}$$

$$S_0 = (1-\varepsilon_0)\left[2\pi \int_0^\infty r_0\, l_0(r_0)\, dr_0\right]. \tag{3.137}$$

Bhatia [10] and Sotirchos et al. [57] both assumed that all points of a pore with a distance r away from the original pore surface form contours of constant concentration. As reaction progresses, each point of the reaction surface (of radius r_s) moves in the direction normal to it with velocity proportional to the local reaction rate. The intrinsic reaction rate expression can also be written in terms of the change in r_s as

$$\frac{\partial r_s}{\partial t} = b\, k_s\, C^s_{A,\,\mathrm{int}}. \tag{3.138}$$

where r_s is the r coordinate in correspondence of the reaction surface. Eq. (3.138) implies that all points of the reaction surface of given initial r_0 move with the same velocity since the concentration of A is uniform over the reaction surface corresponding to capillaries of radius r_s. However, since pore overlapping is admitted, $C^s_{A,\,\mathrm{int}}$ is different at points of the same initial curvature, and consequently the overlapping capillaries used to represent the reaction surface progressively deviate more and more from the ideal cylindrical shape. In order to overcome similar difficulties in their uniform pore size model, Bhatia and Perlmutter [14] suggested treating the concentration of A at the reaction surface as an average quantity. In the present model, this assumption translates into using an average value for the concentration of A at points of the same initial curvature.

In this way, as Bhatia [10] and Sotirchos et al. [57], the easiest procedure for deriving an

average of $C^s_{A,\,\mathrm{int}}$ at points of reaction surface of curvature r_s is to neglect the effect of overlapping and solve the pseudo-steady-state diffusion equation of species A in cylindrical coordinates for the product layer, obtaining

$$\frac{\partial}{\partial r}\left(S(r,r_0)\,\frac{\partial C_A}{\partial r}\right)=0 \qquad r_p\le r\le r_s, \tag{3.139}$$

with boundary conditions

$$\begin{aligned} C_A &= C^p_{A,\,\mathrm{int}}, && \text{at } r=r_p\\ -D_{pl}\,\frac{\partial C_A}{\partial r} &= \frac{a\,\rho_s}{b\,M_B}\,\frac{dr_s}{dt}, && \text{at } r=r_s, \end{aligned} \tag{3.140}$$

where $S(r,r_0)dr_0$ is the surface area of iso-concentration contour at location r, for all pores of initial size in the interval $[r_0, r_0+dr_0]$. Once integrated with Eq. (3.140), Eq. (3.139) becomes

$$\frac{\partial r_s}{\partial t}=\frac{b\,k_s\,C^p_{A,\,\mathrm{int}}}{1+\dfrac{a\,k_s\,\rho_s}{M_B\,D_{pl}}\,S(r_s,r_0)\displaystyle\int_{r_p}^{r_s}\frac{dr'}{S(r',r_0)}}. \tag{3.141}$$

Since the reaction and pore surfaces always move in the normal direction, $S(r,r_0)$ must also correspond to the value of the area of the reaction surface for pores of initial size r_0 when it is at position h for $0\le r\le r_s$, and to the value of the pore surface when it is at r for $r_p\le r\le 0$. Eq. (3.141) can be used to obtain the growth of the reaction surface corresponding to any pore of initial size r_0. However, it is necessary first to relate the surface area $S(r,r_0)$ to the geometry of the moving pore and reaction surfaces. To this end Bhatia and Perlmutter in their work [11] and [12] considered that the reaction surface consists of a system of randomly overlapping growing cylinders of arbitrary size distribution. Hence, Gavalas [22] suggested that if the total volume of the non-overlapped cylinders of radius larger than r per unit of volume of space is $V_{E>r}$, then

$$V_{>r}=1-\exp\left(-V_{E>r}\right), \tag{3.142}$$

where $V_{>r}$ is the overlapped volume for surfaces of radius larger than r. Differentiating Eq. (3.142) gives

$$\frac{\partial V_{>r}}{\partial t}=\left(1-V_{>r}\right)\,\frac{\partial V_{E>r}}{\partial t}. \tag{3.143}$$

Since the pore volume is assumed randomly distributed in the solid,

$$\frac{\partial V_{>r}}{\partial t}=\left[\int_r^\infty\left(\frac{\partial S_{>r'}}{\partial r'}\right)\left(\frac{dr'}{dt}\right)\,dr'\right]+V_{<r}\frac{\partial V_{E>r}}{\partial t}, \tag{3.144}$$

where $(\partial S_{>r'}/\partial r')\,dr'$ in the integrand represents the area of reaction surfaces having radius in the range $[r',\,r'+dr']$, and the second term accounts for the growth at intersections of pores larger than r into pores smaller than r, according to Gavalas [22]. Substituting Eq. (3.144) into

Eq. (3.143) provides

$$\left[\int_r^\infty \left(\frac{\partial S_{>r'}}{\partial r'}\right)\left(\frac{dr'}{dt}\right) dr'\right] - (1-V_s)\,\frac{\partial V_{E>r}}{\partial t} = 0 \tag{3.145}$$

where V_s represents the total overlapped volume enclosed by reaction surfaces. Since

$$\frac{\partial V_{E>r}}{\partial t} = \int_r^\infty \left(\frac{\partial S_{E>r'}}{\partial r'}\right)\left(\frac{dr'}{dt}\right) dr', \tag{3.146}$$

Eq. (3.145) becomes

$$\int_r^\infty \left[\frac{\partial S_{>r'}}{\partial r'} - (1-V_s)\,\frac{\partial S_{E>r'}}{\partial r'}\right]\left(\frac{dr'}{dt}\right) dr' = 0. \tag{3.147}$$

However, since the growth rate dr'/dt is in general an arbitrary function of r', it means that Eq. (3.147) is rewritten as

$$\frac{\partial S_{>r'}}{\partial r'} = (1-V_s)\,\frac{\partial S_{E>r'}}{\partial r'}, \tag{3.148}$$

which relates overlapped and non overlapped areas of reaction surfaces of radius larger than r'. Once integrated Eq. (3.148) yields

$$S\big(r_s\,(r_0,t)\,,r_0\big) = (1-V_s)\;S_E\big(r_s\,(r_0,t)\,,r_0\big), \tag{3.149}$$

where $S_E\big(r_s\,(r_0,t)\,,r_0\big)\,dr_0$ represents the area of non-overlapped surfaces at time t of initial radii in the range $[r_0,\, r_0+dr_0]$. Eq. (3.149) therefore can be written as

$$S\big(r_s\,(r_0,t)\,,r_0\big) = 2\pi r_s\,l(r_0)\;(1-V_s)\,. \tag{3.150}$$

Since initially the overlapping surfaces must correspond with the pore surface,

$$(1-V_s) = (1-X)\;(1-\varepsilon_0)\,, \tag{3.151}$$

and substituting Eq. (3.151) into Eq. (3.150),

$$S\big(r_s\,(r_0,t)\,,r_0\big) = 2\pi r_s\,l(r_0)\;(1-X)\;(1-\varepsilon_0)\,. \tag{3.152}$$

Similarly, considering the pore surfaces of initial radius in the range $[r_0,\, r_0+dr_0]$ as being moving overlapping cylinders gives

$$S\big(r_p\,(r_0,t)\big,r_0\big) = 2\pi r_p\,l(r_0)\;(1-V_p)\,, \tag{3.153}$$

where $V_p = \varepsilon$. Taking into account the porosity evolution with conversion by following Eq. (3.105), Eq. (3.153) becomes

$$S\big(r_p\,(r_0,t)\,,r_0\big) = 2\pi r_p\,l(r_0)\;[1+(Z-1)X]\;(1-\varepsilon_0)\,. \tag{3.154}$$

Defining the following transformation

$$y = 2\pi\,l(r_0)\int_{r_p}^{r_s}\frac{dr'}{S(r',r_0)}, \tag{3.155}$$

Eqs. (3.141), (3.152), (3.154) and (3.155) are combined to give

$$\frac{\partial r_s}{\partial t} = \frac{b\,k_s\,C_{A,p}}{1+\dfrac{a\,k_s\,\rho_s}{M_B\,D_{pl}}\,r_s\;(1-\varepsilon_0)\;(1-X)\;y}. \tag{3.156}$$

In order to solve (3.156), that is an integral-differential equation, Eq. (3.155) is differentiated giving

$$\frac{\partial y}{\partial t} = \left[\frac{1}{r_s\;(1-X)}\left(\frac{\partial r_s}{\partial t}\right) - \frac{1}{r_p\;[1+(Z-1)X]}\left(\frac{\partial r_p}{\partial t}\right)\right]\frac{1}{(1-\varepsilon_0)}. \tag{3.157}$$

Afterwards, it is necessary to relate r_p and X to r_s in order to obtain the conversion-time behavior using Eqs. (3.156) and (3.157). To obtain the relation between r_s and r_p, Bhatia and Perlmutter (in their works [11], [12] and [14]) assumed that the reaction and pore surfaces are comprised of randomly overlapping cylinders of arbitrary size distribution. Using the properties of randomly overlapping surfaces as in Eq. (3.142)

$$V_s = 1-\exp\left(-V_{E,s}\right), \tag{3.158}$$

$$V_p = 1-\exp\left(-V_{E,p}\right), \tag{3.159}$$

where $V_{E,s}$ and $V_{E,p}$ are the volumes enclosed by the non-overlapped cylinders corresponding to the reaction and pore surfaces respectively. As reaction occurs

$$\frac{dV_p}{dt} = -(Z-1)\,\frac{dV_s}{dt} \tag{3.160}$$

and combining Eq. (3.160) with Eqs. (3.158) and (3.159)

$$(1-V_p)\;\frac{dV_{E,p}}{dt} = -(Z-1)\,(1-V_s)\;\frac{dV_{E,s}}{dt}. \tag{3.161}$$

$V_{E,s}$ and $V_{E,p}$ may be rewritten in terms of the length size distribution function $l(r_0)$ to yield

$$(1-V_p)\int_0^\infty 2\pi\,l(r_0)\,r_p\,\frac{\partial r_p}{\partial t}\,dr_0 = -(Z-1)\,(1-V_s)\int_0^\infty 2\pi\,l(r_0)\,r_s\,\frac{\partial r_s}{\partial t}\,dr_0 \tag{3.162}$$

and, since $\partial r_p/\partial t$ is in general arbitrary and $r_p = r_p(r_s, r_0)$, Eq. (3.162) reduces to

$$(1 - V_p)\, r_p \frac{\partial r_p}{\partial t} = -(Z-1)\,(1 - V_s)\, r_s \frac{\partial r_s}{\partial t}. \tag{3.163}$$

Recognizing that $V_p = \varepsilon$, and combining Eq. (3.162) with Eqs. (3.141) and (3.151)

$$\frac{\partial r_p}{\partial t} = -\frac{(Z-1)\,(1-X)\, r_s}{[1 + (Z-1)X]\; r_p} \frac{\partial r_s}{\partial t}. \tag{3.164}$$

Substituting Eq. (3.164) into Eq. (3.157),

$$\frac{\partial y}{\partial t} = \left[\frac{1}{r_s\;(1-X)} + \frac{(Z-1)(1-X)\, r_s}{r_p^2\;[1 + (Z-1)X]^2}\right] \frac{1}{(1-\varepsilon_0)} \left(\frac{\partial r_s}{\partial t}\right), \tag{3.165}$$

where $\partial r_s/\partial t$ is expressed by Eq. (3.156).
To relate X to r_s, Eqs. (3.151) and (3.158) are combined to yield

$$X = 1 - \frac{\exp\left(-V_{E,s}\right)}{1 - \varepsilon_0}, \tag{3.166}$$

and since

$$V_{E,s} = \int_0^\infty \pi r_s^2(r_0, t)\, l(r_0)\, dr_0, \tag{3.167}$$

Eq. (3.166) is re-expressed as

$$X = 1 - \frac{\exp\left[-\displaystyle\int_0^\infty \pi r_s^2(r_0, t)\, l(r_0)\, dr_0\right]}{1 - \varepsilon_0}. \tag{3.168}$$

Eqs. (3.156), (3.163), (3.165), and (3.168) must be simultaneously solved to obtain the conversion-time behavior, in the absence of intra-particle concentration gradients.
Considering the following change of variables

$$a_0 = \frac{r_0}{M_0}, \quad \eta_s = \frac{r_s}{M_0}, \quad \eta_p = \frac{r_p}{M_0}, \quad \beta = \frac{a\, k_s\, \rho_s\, M_0\;(1-\varepsilon_0)}{M_B\, D_{pl}}, \quad \hat{t} = \frac{b\, k_s\, C_{A,p}}{M_0}\, t = \frac{t}{\tau}, \tag{3.169}$$

where M_0 is the mean pore radius.
Eqs. (3.156), (3.163), (3.165), and (3.168) may be written in dimensionless form as

$$\frac{\partial \eta_s}{\partial \hat{t}} = \frac{1}{1 + \beta\, \eta_s\, y\, (1-X)}, \tag{3.170}$$

$$\frac{\partial \eta_p}{\partial \hat{t}} = -\frac{(Z-1)\,(1-X)\, \eta_s}{[1 + (Z-1)X]\; \eta_p} \left(\frac{\partial \eta_s}{\partial \hat{t}}\right), \tag{3.171}$$

$$\frac{\partial y}{\partial \hat{t}} = \left[\frac{1}{\eta_s\;(1-X)} + \frac{(Z-1)(1-X)\, \eta_s}{[1 + (Z-1)X]^2\; \eta_p^2}\right] \frac{1}{(1-\varepsilon_0)} \left(\frac{\partial \eta_s}{\partial \hat{t}}\right), \tag{3.172}$$

and

$$X = 1 - \frac{\exp\left[-\int_0^{\infty} \pi M_0^3\, \eta_s^2(a_0,t)\, l(a_0)\, da_0\right]}{1-\varepsilon_0}, \tag{3.173}$$

with the initial conditions $\eta_s = \eta_p = a_0$, $y = 0$ at $\hat{t} = 0$.
In comparison with the prior development [12] of the random pore model for thin product layers, the new equations above contain the same parameters β[13], Z, and ε_0, but require the microscopic details of the pore size distribution $l(r_0)$, in place of the averaged macroscopic property (ε_0, $S_{E,0}$ $L_{E,0}$).

3.6.2 Numerical results

The simultaneous solution of Eqs. (3.170), (3.171), (3.172) and (3.173) provide the conversion-time profile for a given gas-solid reaction. A numerical method is needed in order to solve the integral of the pore size distribution that appears in Eq. (3.173); a second numerical method is required to solve the system of ordinary differential equation (ODE's).

The model is valid for any type of length pore size distribution $l(a_0)$ defined in the interval $[0, +\infty]$. Actually the measured pore size distributions are defined in a finite size range $[r_{0^*}, r_{0_*}]$. Consequently, the density length distribution $l(a_0)$ is based on the range $[a_{0^*}, a_{0_*}]$ that comes from the experimental data analysis. Bhatia [10] suggested a log-normal length size distribution of the non-overlapped pore system. However, in this work of thesis the log-normal distribution was applied to the pore size distribution. Consequently, the pore length size distribution is obtained from the pore size distribution by dividing for $\pi\, r_0^2$:

$$l(r_0) = \frac{b_{\mathrm{LN}}}{\pi\sqrt{2\pi}\,\sigma_{N_0}\, r_0^3} \exp\left\{\frac{1}{2\sigma_{N_0}^2}\left[\ln(r_0) - \mu_{N_0}\right]^2\right\}, \tag{3.174}$$

where μ_{N_0} and σ_{N_0} are respectively the mean and the variance of the normal distribution of the random variable $\ln(r_0)$; b_{LN} represents the total non-overlapped porosity of the solid phase that is V_{E_0}. The mean and variance of log-normal distribution are related to the normal distribution parameters by the following relations

$$M_0 = \exp\left(\mu_{N_0} + \frac{\sigma_{N_0}^2}{2}\right) \tag{3.175}$$

$$V_0 = \exp\left(2\,\mu_{N_0} + \sigma_{N_0}^2\right)\left[\exp\left(\sigma_{N_0}^2\right) - 1\right]. \tag{3.176}$$

Using dimensionless variables Eq. (3.174) becomes

$$l(a_0) = \frac{b_{\mathrm{LN}}}{\pi\sqrt{2\pi}\,\sigma_{N_0}\, M_0^3\, a_0^3} \exp\left\{\frac{1}{2\sigma_{N_0}^2}\left[\ln(a_0) + \ln(M_0) - \mu_{N_0}\right]^2\right\}. \tag{3.177}$$

[13] The β parameter is still a ratio between the kinetic of the reaction and the product layer diffusion.

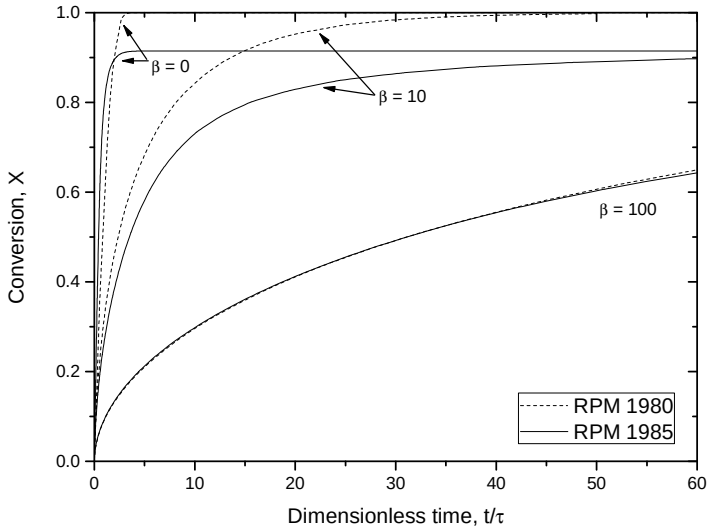

Figure 3.21: Comparison of conversion predictions for random pore model 1985 and random pore model with thin product layer assumption (1980). Curves obtained for $Z = 2$.

In order to obtain a numerical solution, the range size $[a_{0^*}, a_{0_*}]$ is discretized obtaining nr grid point, following the Numerical Method of Lines (NUMOL) by Schiesser [52]. Eqs. (3.170),(3.171), (3.172) are simultaneously solved at each grid point. The number of ODEs is $nr \times n_{\text{ode}}$ where n_{ode} in this case is 3. Eq. (3.173) is integrated over the grid points using the Simpson's Rule (that requires a equally spacing grid point).
To reduce the computational costs of the numerical method, Eq. (3.155) is solved assuming cylindrical coordinates, which allows to reduce the number of ODEs for each grid point down to 2. In fact, once integrated Eq. (3.157) becomes

$$y = \left[\frac{1}{(1-X)}\ln\left(\frac{r_s}{a_0}\right) + \frac{1}{[1+(Z-1)X]}\ln\left(\frac{a_0}{\eta_p}\right)\right]\frac{1}{(1-\varepsilon_0)}, \tag{3.178}$$

and is substituted in Eq. (3.170), avoiding the numerical solution of one ODE at each grid point.

Conversion-time behaviour

In order to compare the conversion-time predictions of this random pore model (RPM 1985) to the older one (RPM 1980), the length size distribution reported in Eq. (3.177) for the non-overlapped pore system was adopted. The values of the parameters are $\mu_{N_0} = 5.526\,\text{Å}$ (namely $M_0 = 256.562\,\text{Å}$), $\sigma_{N_0} = 0.204$ and $b_{LN} = 0.650$. Integration of this distribution gives $S_0 = 3.652 \times 10^7\,\text{m}^2\,\text{m}^{-3}$, $\varepsilon_0 = 0.478$ and $\psi = 2.171$. Comparing Eq. (3.93) with Eq. (3.169), the following relation may be obtained

$$\beta_{\text{TLM}} = \frac{2}{M_0\,S_0}\beta \tag{3.179}$$

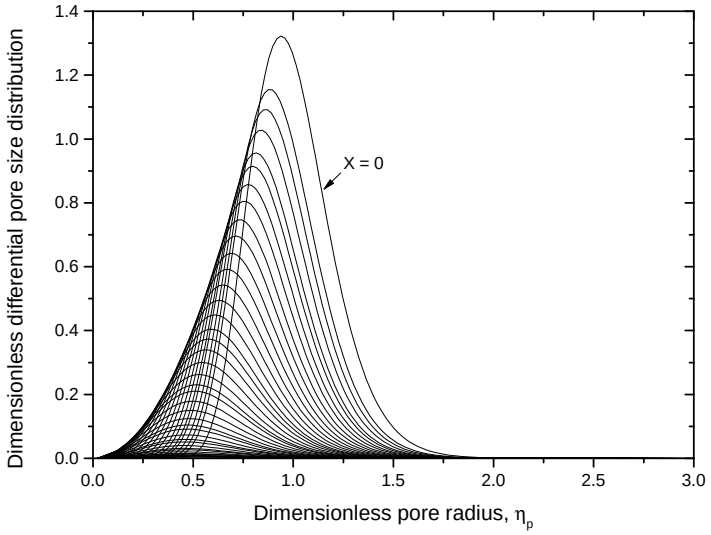

Figure 3.22: Variation of the porosity density function with conversion.

where, for simplicity, β_{TLM} is refers to the thin layer model (RPM 1980) that is abbreviated as "TLM", whereas β is referred to the last RPM (1985). In addition, the dimensionless time of Eq. (3.95) is related with Eq. (3.169) by

$$\tau_1 = \frac{S_0\, M_0}{1-\varepsilon_0}\,\tau, \tag{3.180}$$

where the previous notation is assumed. Fig. 3.21 shows the conversion-time predictions of the two models for $Z = 2$, and for $\beta = 0$ (reaction control), as well as for $\beta = 10$ and $\beta = 100$ (that may be considered as product layer diffusion control). Eq. (3.105) predicts a maximum conversion of 0.916. The dashed curves in Fig. 3.21 result from Eq. (3.96) having care to estimate β and τ with Eqs. (3.179) and (3.180). Eq. (3.96) continues to complete conversion contradicting Eq. (3.105). The solid lines represent the random pore model developed independently by Bhatia and Sotirchos at al. This model asymptotically approaches the maximum conversion always showing some reaction proceeding, even close to the maximum conversion, but with a very small rate. However, the two results agree remarkably well, deviating after about 60 % of the maximum conversion, as reported by Bhatia [10]. This lack of accuracy of the thin layer model beyond about 60 % of the maximum conversion arises out of the assumption of a linear concentration gradient in the product layer, as well as of neglecting the progressive closure of the smaller pores. In fact, the thin layer model is not capable to represent the abrupt transition between the kinetic and the product layer diffusion regime.

Variation of the porosity density function

The progressive change in the pore size distribution is shown in Fig. 3.22, which depicts the porosity density function at various level of conversion for $\beta = 10$ and $Z = 2$. The figure shows the gradual shift of the distribution as the smaller and more reactive pores close preferentially to the larger ones.

Fig. 3.23 shows the surface reaction and pore evolution from initial to final time at various values of β and Z. Clearly, pore closure is more evident in the kinetic controlled regime ($\beta = 0$) and for $Z > 2$ as depicted in Fig. 3.23b. On the contrary, a remarkable evolution of surface reaction takes place when chemical controlled regime is established and for Z values close to 1 (Fig. 3.23a). The larger values of β the smaller effects occur in pore and reaction surfaces. For reaction surfaces with a constant value of β, the smaller value of Z the more remarkable variation of η_s. On the contrary, for pore surfaces the larger value of Z the higher are the effects on pore closure. Fig. 3.24 shows the tree-dimensional evolution of pore and reaction surfaces for $Z = 2$.

Variation of internal surface area

One of the difficulties of many structural models for gas-solid reactions is their inability to predict the change of the internal surface area with conversion. This random pore model estimates the change of the internal surface with conversion by integration of Eq. (3.154) and the results are reported in Fig. 3.25 using the pore length distribution of Eq. (3.177). For $Z = 1.5$, Eq. (3.105) predicts that porosity does not becomes zero even at $X = 1$, so that some internal surface must remain at complete conversion.
A further interesting feature of the curves in Fig. 3.25 is the relatively small effect of the product layer diffusion parameter β. For $\beta > 10$ the surface area at any conversion is essentially independent of β. The weak dependence on β also means a small effect of temperature on the surface area.

Incomplete conversion

In Fig. 3.21 incomplete conversion is seen for $Z = 2$, as predicted by Eq. (3.105). This is due to reduction of the porosity to zero or to a small value close to zero. Bhatia and Perlmutter [13] showed with experimental results that apparent incomplete conversion for the CaO-CO_2 reaction arises even when sufficient initial porosity exists for the reaction to reach completion. This was qualitatively attributed to closure of the small pores, leaving behind only a small amount of pore volume in larger and less reactive pores. Fig. 3.26 shows conversion-time curves for various values of β taking $Z = 2$. The model is clearly in agreement with Eq. (3.105) by accounting incomplete conversion due to pore closure.

3.7 Choice of the model

Several models were proposed during the the second half of the 20^{th} century for gas-solid reactions. Szekely [29] in 1976 proposed a structural model ("grain model") capable to represent the solid phase evolution during reaction assuming the whole process to be controlled by intrinsic kinetics and product layer diffusion. Such model assumed porous particles made of non-porous grains of any shape (spherical, cylindrical and flat geometry) uniformly sized. Each grain evolved following a shrinking-core model. However, this model works for reactions without product layer generation and for particles made of fine compacted powder.

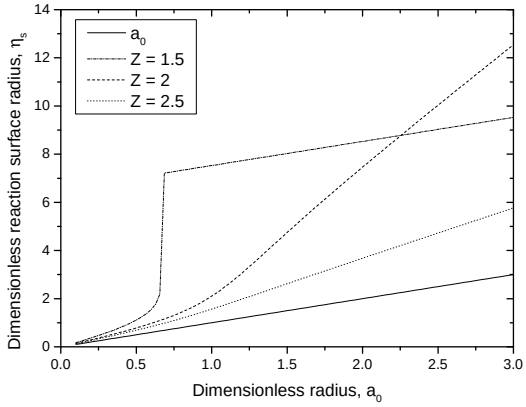

(a) $\beta = 0$.

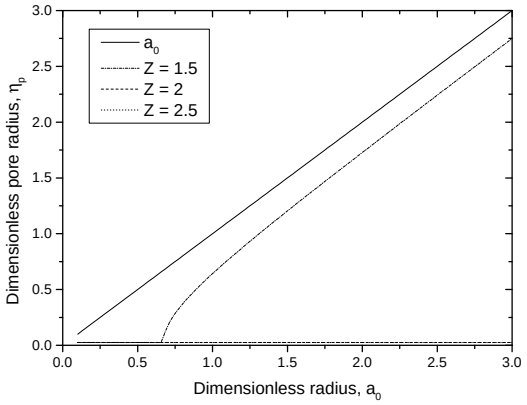

(b) $\beta = 0$.

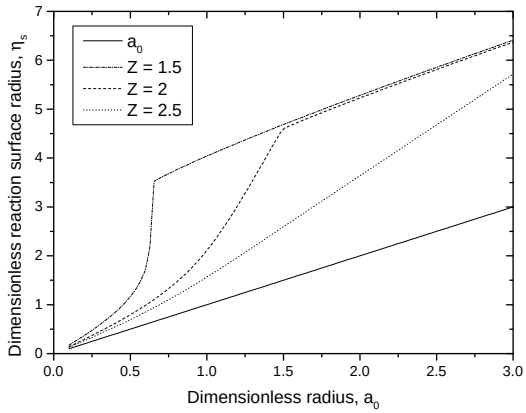

(c) $\beta = 10$.

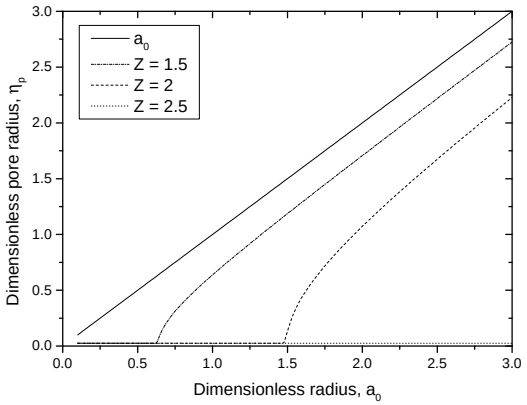

(d) $\beta = 10$.

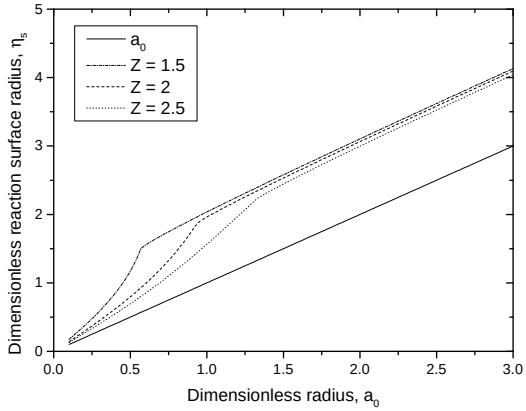

(e) $\beta = 100$.

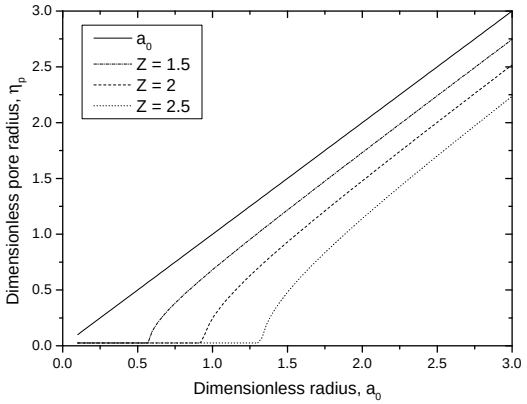

(f) $\beta = 100$.

Figure 3.23: Dimensionless reaction surface and pore radius at initial and final time.

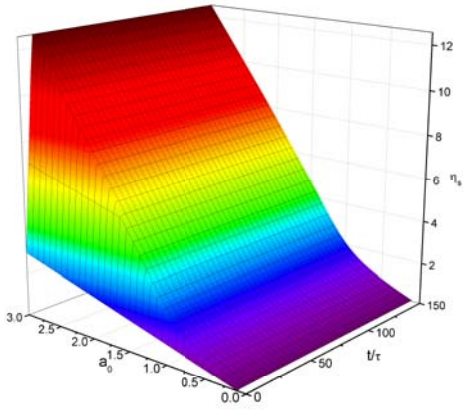

(a) $\beta = 0$.

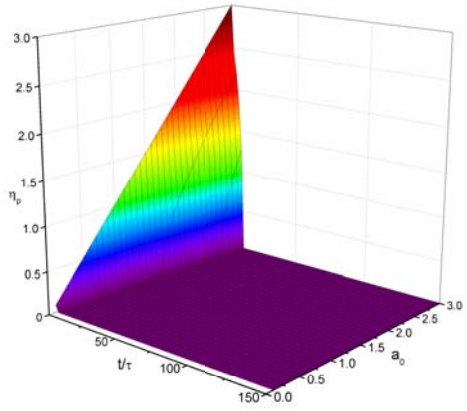

(b) $\beta = 0$.

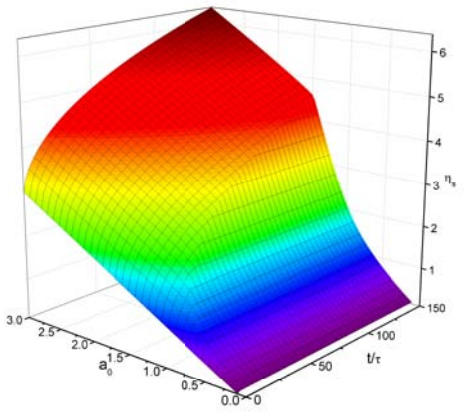

(c) $\beta = 10$.

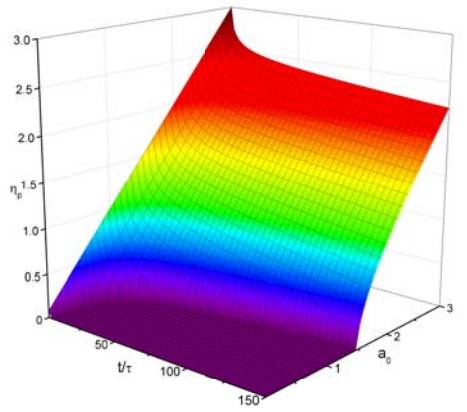

(d) $\beta = 10$.

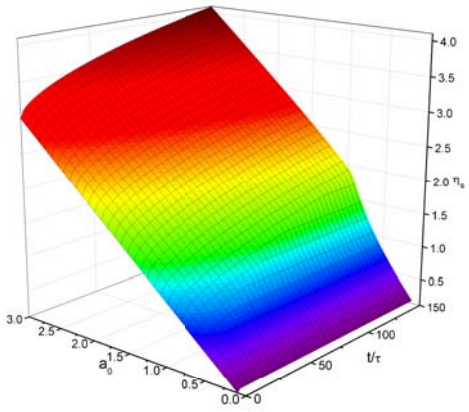

(e) $\beta = 100$.

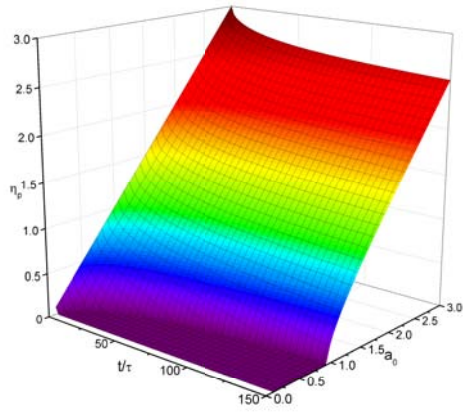

(f) $\beta = 100$.

Figure 3.24: Variation of dimensionless reaction surface and pore radius with dimensionless time obtained for $Z = 2$.

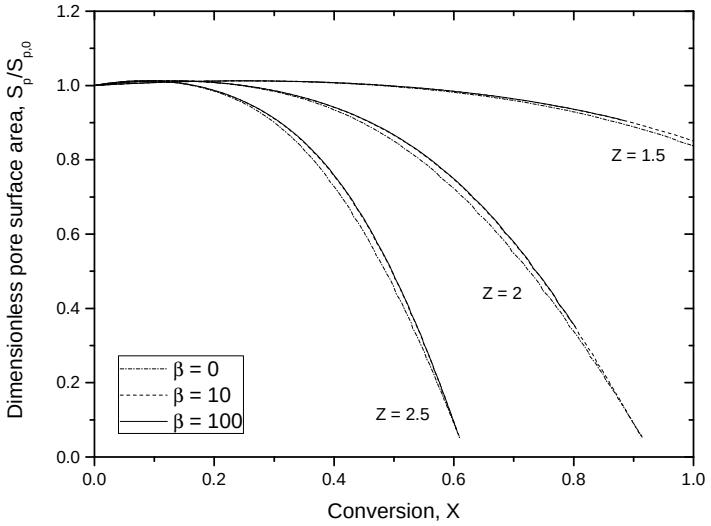

Figure 3.25: Effect of β and Z on the variation of pore surface area vs conversion.

When grain models were applied to gas-solid reactions with solid product, it was assumed that the shrinking solid reactant grain was surrounded by a dense layer of solid product of uniform thickness. Georgakis in 1978 [23] modified the grain models to account for grain expansion as the more voluminous product is formed. He showed that density differences between the solid product and the solid reactant may readily be incorporated in the grain model by means of an equation relating the overall grain size to the local conversion. However, this extension produced the anomaly that the total internal grain surface area increased monotonically while the porosity reduced to zero.

Because of the drawbacks of the grain models, several pore models were studied during the 20^{th} century in order to develop structural models capable to represent the evolution of the void fraction of porous particles during the reaction. One of the first pore models was developed by Petersen in 1957 [46] who proposed a structural model in which he recognized the importance of pore intersections and overlap [57]. He analysed the pore structure assuming that all pores were of the same size and that no new intersections occurred as the reaction surfaces within the solid particle grow. Because no solid product was considered, the reaction surface of the solid was always the same as the internal surface of the pores [11]. Indeed, the number and geometry of intersections were not linked to the random geometry of the pores, and, as a result, the expressions derived for porosity and surface area was quite empirical, according to [22].

A more refined random pore model for a distributed pore size system was presented by Gavalas [22] and Bhatia and Perlmutter [11] in 1980. Gavalas [22] recognized the importance of pore overlap, he developed a random capillary model in which the number of intersections, length of pore segment and evolution of pore volume and surface area were derived from a single probability-density function characterizing the porous particles. On the basis of Gavalas'work, Bhatia and Perlmutter [11] proposed a new random pore model. Three parameters of pore volume, surface area and length were required to characterize the internal structure of porous particles when an arbitrary pore size distribution is available. The following year, Bhatia and

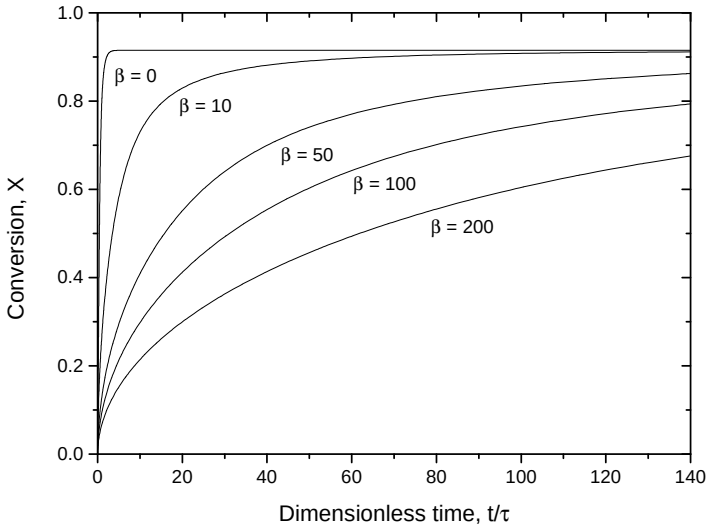

Figure 3.26: Predicted conversion-time behaviour, at various values of β.

Perlmutter [12] modified their model including simultaneous chemical reaction and product layer diffusion. However, they assumed a thin product layer close to the surface area, and therefore, pore reaction and surface areas were equal [13]. In 1983 they applied their random pore model to experimental data on CO_2-lime reaction. They found that their model agreed well only for the kinetic and diffusion control regimes, but not for the transition between the two regimes. They recognized the importance of pore closure since the molar volume of product layer is larger than the reactant one [13]. In 1983 they corrected the random pore model with thin layer approximation distinguishing the individual evolution of pore and reaction surfaces. However, not even this model was able to represent pore closure.

Because of the drawbacks of the previous random pore models, in 1985 Bhatia [10] and Sotirchos at al. [57] independently developed a random pore model accounting for pore closure in gas-solid reactions. They recognized that for gas-solid reactions with solid product that occupies a larger volume than the reactant consumed the porosity of the solid was gradually reduced with conversion because of pore closure. This kind of reactions could not be modeled with averaged properties (such as structural parameters L_0, S_0 and V_0), but pore size distributions must be taken into account in order to represent local structural changes in porous particles [10]. In this way, a structural model was developed to study gas-solid reactions with solid product formation under reaction conditions controlled by kinetics and diffusion through the product layer. Its development was based on the assumption that the reaction and pore surfaces can be generated at all times by a population of growing or shrinking, overlapping cylinders co-axial with the randomly distributed capillaries that represent the initial pore structure, according to [57].

Among the several models for gas-solid reactions proposed and discussed during the 20^{th} century, the random pore model developed by Bhatia [10] and Sotirchos at al. [57] is likely to be the most appropriate one for modeling carbonation reaction. In fact, for this kind of reaction $Z > 1$ and pore closure characterizes CO_2-lime reaction (Bhatia [13] and Ping Sun [58]). For these reasons the following chapters apply this model to the carbonation reaction having care to

consider the intra-particle diffusion and the external mass transfer.

Chapter 4

Application of the RPM to the Carbonation Reaction

In this chapter the RPM developed by Bhatia [10] and Sotirchos et al. [57] and presented in Chapter 3 is applied to the carbonation reaction by using a continuous pore size distribution. Afterwards, in the following chapter, the model is coupled with the intra-particle diffusion in order to consider the particle size effect on the kinetics of the carbonation reaction. This approach was never explored in the literature earlier and this work of thesis is the first that applies the continuous RPM [10, 57] coupled with the intra-particle diffusion to the carbonation reaction. Before the model application to the carbonation reaction, several features are analyzed, such as: the operative conditions, the pore size distribution and the parameter estimation. In § 4.2 the validity of the ideal gas assumption is checked at typical operative conditions. Afterwards, the most relevant literature contributors are analyzed in § 4.3 focusing on the model application to the carbonation reaction, kinetic and product layer diffusivity estimation and proposed reaction mechanism. Then, § 4.4 deals with the problem of fitting the pore size distribution. The goal is to represent the pore distribution with a continuous function in order to obtain the RMP in continuous form. In § 4.5 the RPM independently developed by Bhatia [10] and Sotirchos et al. [57] is modified in order to account for the continuous pore size distribution, the equilibrium concentration and the reaction rate switch from zero to first order. The chapter ends with a comparison between the experimental results (from TGA analysis) and the model predictions of the carbonation kinetics.

4.1 Introduction

The carbonation kinetic data presented in this chapter were obtained by using a TGA instrument (Chapter 2). In this way, assuming isothermal and isobaric conditions, gas-solid reaction occurs simultaneously with other phenomena, which can determine a number of physical limitations. Such resistances[1] depend on the instrument, the solid reactant and the operative conditions and can be listed as follows:

[1] A more detailed list is reported in § 2.6.

Table 4.1: Critical constants and acentric factors of carbon dioxide and nitrogen. Source: Green et Perry [26].

Species	T_c [K]	P_c [MPa]	v_c $[m^3\,kmol^{-1}]$	ω [adim]
CO_2	304.21	7.383	0.094 00	0.223 60
N_2	126.20	3.400	0.089 21	0.0377

1. external diffusion;

2. inter-particle mass diffusion;

3. intra-particle mass diffusion;

This chapter aims to analyze the carbonation reaction in both the kinetic and product layer diffusion regime. All the above mentioned physical resistances are neglected in the RPM used in this chapter. Following this approach, the resulting global reaction rate consists of two mechanisms: the intrinsic kinetics and the product layer ($CaCO_3$) diffusivity. The overall reaction rate is modeled in this chapter taking into account these steps simultaneously and considering the pore closure due to the product layer.

4.2 Ideal gas assumption

During the carbonation reaction the reaction chamber of the TGA is continuously fed with gas reactant that is CO_2 or mixtures of CO_2-N_2. The explored temperature range of each run is $30 \div 650\,°C$ (from the room temperature to the carbonation reaction one[2]). In this chapter the presented TGA tests were performed using the DynTHERM MP-ST by RUBOTERM GMBH TGA (instead of the TA SDT Q600), which can work up to 40 bar. This instrument is a vertical TGA, and the sample weight measurement is performed by a suspension magnetic balance.

Since the TGA analysis performed using the TGA SDT Q600 were at room pressure, the gas phase is retained to be an ideal gas mixture (or a pure ideal gas if CO_2 is the only gas employed) because of the low pressure and the high carbonation temperature (450 °C, 550 °C and 650 °C). For these reasons the gas phase behavior is modeled using the ideal gas equation.
However, using the DynTHERM MP-ST that can to operate at pressures up to 40 bar, the ideal gas phase behaviour may become a rough approximation during the carbonation reaction.

Consequently, the following paragraph investigates the pressure and temperature ranges in which pure CO_2 or CO_2-N_2 mixtures can be modeled with the idea gas law. The operative conditions at which the carbonation reaction was performed were 650 °C and 750 °C at 5 bar in CO_2.

4.2.1 Pure species: the carbon dioxide behaviour

Carbon dioxide is a linear non-polar molecule that can be modeled with a cubic Equation Of State (EOS). For this work the Soave-Redlich-Kwong (SRK) equation was selected. As can be seen from Tab. 4.1, the critical temperatures of each species are well below the operative conditions where TGA tests were performed. Thus, the fluid is in the gaseous phase and this simplifies the the gas molar volume estimation, namely v.
The Gibbs'phase rule states that the number of degree of freedom is 2, since temperature and pressure are imposed. In this way, v becomes the only unknown quantity.
Following the procedure reported by Soave [54] and Prausnitz [48] for a pure component the SRK is expressed as

$$P = \frac{R_{\text{gas}}\, T}{v - b_{\text{SRK}}} - \frac{a_{\text{SRK}}(T)}{v\ (v + b_{\text{SRK}})}, \tag{4.1}$$

where $a_{\text{SRK}}(T)$ depends on temperature according to

$$a_{\text{SRK}}(T) = a_{\text{SRK}}(T_c)\, \alpha(T). \tag{4.2}$$

$\alpha(T)$ for fluids such as carbon dioxide or nitrogen is

$$\alpha(T) = \left[1 + \left(0.480 + 1.574\,\omega - 0.176\,\omega^2\right)\ \left(1 - \sqrt{\frac{T}{T_c}}\right)\right]^2 \tag{4.3}$$

and $a(T_c)$ is defined as

$$a_{\text{SRK}}(T_c) = \gamma_a\, \frac{(R_{\text{gas}}\, T_c)^2}{Pc}, \tag{4.4}$$

as reported by Poling [47]. The acentric factor (ω[3]) is reported in Tab. 4.1.
The constant $b_{\text{SRK}}(T)$ is given by

$$b_{\text{SRK}} = \gamma_b\, \frac{R_{\text{gas}}\, T_c}{P_c}, \tag{4.5}$$

that is the same of the Redlich-Kwong equation. The constants in Eqs. (4.4) and (4.5) are given by

$$\gamma_a = 0.42747, \tag{4.6}$$

$$\gamma_b = 0.08664. \tag{4.7}$$

Since no phase transition occurs, the cubic EoS Eq. (4.1) is solved in order to obtain a solution in terms of molar volume. A numerical method is required to find the roots of the cubic equation.

[2] This range excludes the calcination reaction that is performed up to 900 °C.
[3] If the acentric factor is not known, it can be calculated by its definition: $\omega = -1 - \log_{10} P_r^{\text{sat}}\big|_{T_r=0.7}$.

For this reason Eq. (4.1) is rewritten in terms of dimensionless variables ("reduced properties"):

$$P_r = \frac{P}{P_c}, \qquad T_r = \frac{T}{T_c}, \qquad v_r = \frac{v}{v_c}, \tag{4.8}$$

so that Eq. (4.1) becomes:

$$P_r = \frac{T_r}{\mathbb{Z}_c \left(v_r - \frac{\gamma_b}{\mathbb{Z}_c} \right)} - \frac{\gamma_a \, \alpha(T_r)}{\mathbb{Z}_c^2 \, v_r \left(v_r + \frac{\gamma_b}{\mathbb{Z}_c} \right)}, \tag{4.9}$$

where for the SRK equation of state the compressibility factor at the critical conditions is $\mathbb{Z}c = 1/3$ by definition.
Once P_r and T_r are known, the only unknown in Eq (4.9) is v_r. A numerical method, as Newton's method, can be used to find the solution of Eq (4.9), that is rewritten in terms of $f(v_r) = 0$. Since the Newton's method is an iterative numerical method with a quadratic but local convergence, a good initial guess is needed to find the correct root. For this aim the ideal gas equation is employed to give the initial guess:

$$v_r^{(0)} = \frac{R_{\text{gas}} T}{P} \frac{1}{v_c}. \tag{4.10}$$

The results are elaborated in terms of compressibility factor, named $\mathbb{Z}$ and reported in Fig. 4.1. Fig. 4.1a shows that the compressibility factor of carbon dioxide deviates from the ideal behavior when the operative conditions are close to the critical point or when temperature and pressure are large. However, when the pressure remains below 15 bar and at temperature larger that T_c, the compressibility factor is close to 1. Fig. 4.1b shows the pressure parametric curves of $\mathbb{Z}$ as a function of T. This graph is useful for TGA tests. In fact, by using the TA SDT Q600 only isobaric tests (at 1 bar) can be performed, whereas the DynTHERM MP-ST can work at pressure up to 40 bar.

This study highlights that pure CO_2 follows an ideal behavior ($\mathbb{Z} \cong 1$) when the total pressure is below 10 bar and when the temperature is larger than about 400 K. For these reasons the ideal gas equation is justified within the temperature and pressure ranges used in the TGA experiments.

4.2.2 Extension to carbon dioxide-nitrogen mixtures

In order to reduce the CO_2 partial pressure, the gaseous reactant is fed with an inert species as nitrogen. Consequently, also for this case the ideal assumption of the mixture is verified. Following the approach reported by Prausnitz [48], the SRK is generalized for the case of the mixture N_2-CO_2.

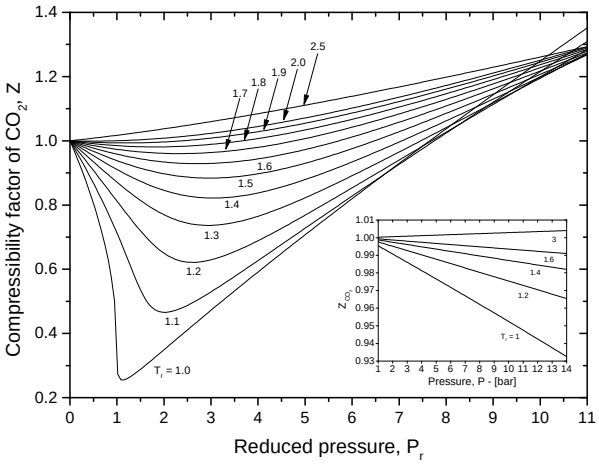

(a) $\mathbb{Z}$ *vs* P_r *and* P.

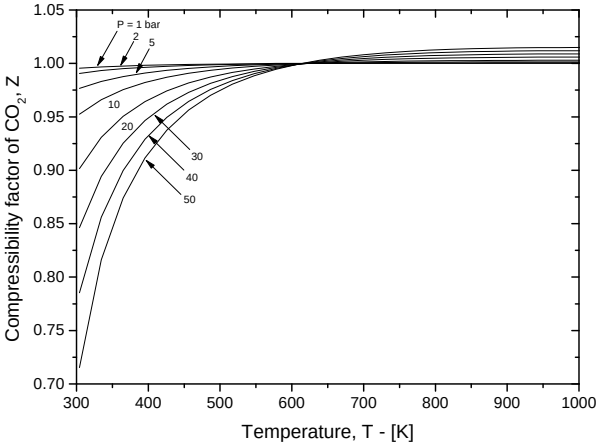

(b) $\mathbb{Z}$ *vs* T.

Figure 4.1: Predicted compressibility factor for CO_2 with the SRK equation of state.

The procedure requires mixing rules for $a_{\mathrm{SRK}}(T)$ and b_{SRK}, as reported by Poling [47]:

$$a_{\mathrm{SRK,\,mix}}(T) = \sum_{i=1}^{NC}\sum_{j=1}^{NC} y_i\, y_j\, a_{\mathrm{SRK},\,ij}(T), \tag{4.11}$$

$$b_{\mathrm{SRK\,mix}} = \sum_{i=1}^{NC} y_i\, b_{\mathrm{SRK}\,i}, \tag{4.12}$$

where NC is the number of components of the mixture (for this work $NC = 2$), y_i is the molar fraction of species i, $a_{\mathrm{SRK},\,ii}(T)$ and $b_{\mathrm{SRK}\,i}$ are the EOS parameters for pure components. The binary parameter $a_{\mathrm{SRK},\,ij}(T)$ is defined as

$$a_{\mathrm{SRK},\,ij}(T) = \left[a_{\mathrm{SRK},\,ii}(T)\, a_{\mathrm{SRK},\,jj}(T)\right]^{1/2} \left(1 - k_{\mathrm{SRK},\,ij}\right), \tag{4.13}$$

where the binary parameter $k_{\mathrm{SRK},\,ij}$ for CO_2-N_2 mixture is taken as -0.028 as reported by Pellegrini at al. [45].

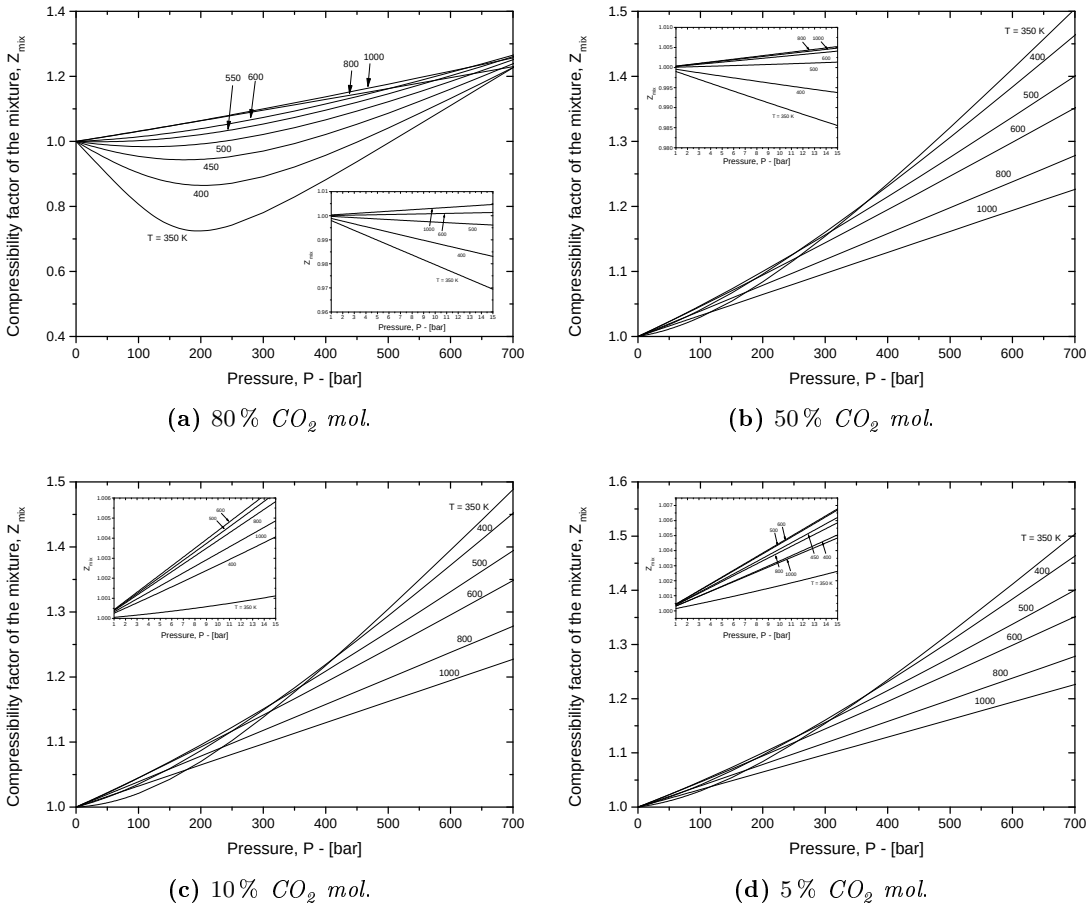

(a) 80 % CO_2 *mol.* **(b)** 50 % CO_2 *mol.*

(c) 10 % CO_2 *mol.* **(d)** 5 % CO_2 *mol.*

Figure 4.2: Predicted compressibility factor for CO_2-N_2 mixtures for various CO_2 molar fractions with the SRK equation of state extended to mixture ($k_{\mathrm{SRK},ij} = -0.028$ [45]).

Consequently, Eq (4.1) is rewritten in terms of mixture and the same numerical method was adopted as for the case of pure component. All the results are expressed in term of the compressibility factor $\mathbb{Z}_{\mathrm{mix}}$ for mixtures and reported in Fig. 4.2. Clearly, Fig. 4.2 shows that the ideal gas behavior of the mixture is reasonable for low pressure (less than 10 bar) and high temperature (more than 500 °C).

4.3 Literature results

In order to simplify the nomenclature, the carbonation reaction represented by Eq. (2.1) is rewritten in terms of

$$\begin{aligned} &\mathrm{CO}_{2(g)} + \mathrm{CaO}_{(s)} = \mathrm{CaCO}_{3(s)} \\ &A_{(g)} + B_{(s)} = Q_{(s)} \end{aligned} \tag{4.14}$$

where the stoichiometric coefficient of each species is 1.
The kinetic rate constant is commonly expressed in terms of Arrhenius law, that is

$$k_s = A_k \exp\left(-\frac{E_{ak}}{R_{\text{gas}}\,T}\right), \tag{4.15}$$

where A_k is the pre-exponential factor, E_{ak} is the activation energy of the reaction, R_{gas} is the universal constant of gases and T is the temperature of the system expressed in K.

According to Bhatia and Perlmutter [13] the product layer diffusion coefficient is also retained a temperature activated mechanism that follows an Arrhenius-like equation, such as

$$D_{pl} = A_D \exp\left(-\frac{E_{aD}}{R_{\text{gas}}\,T}\right), \tag{4.16}$$

where A_D is the pre-exponential factor, E_{aD} is the activation energy of the product layer diffusion.

These parameters can be obtained once k_s and D_{pl} are known for various temperatures, by a linear regression into the Arrhenius-plot ($\ln(k_s)$ or $\ln(D_{pl})$ vs $1/T$).

The literature contributors on the carbonation reaction commonly describe the conversion-time curves as sigmoid-shape, generally interpreted as composed by two main steps: a rapid (growth) reaction followed by a slower second stage reaction at high conversion [13]. The selected model must represent these steps in order to simulate the reaction behavior.

4.3.1 Bhatia and Perlmutter

Bhatia and Perlmutter [13] in 1983 studied the carbonation of calcined limestone particles (particle size equal to $74 \div 88\,\mu$m) carried out in an atmospheric thermogravimetric analyzer (ATGA) with $0 \div 42$ vol % of CO_2. They modeled the porous material with their RPM 1980 (with thin product layer assumption, § 3.4).
According to such model, in regime of reaction control, the conversion for a reversible first order reaction (as the carbonation reaction) is given by Eq. (3.75). Once integrated it becomes

$$\frac{1}{\psi}\left[\sqrt{1-\psi\,\ln(1-X)}-1\right] = \frac{k_s\,S_0\,(C_A - C_{A,\,eq})\,t}{2\,(1-\varepsilon_0)}, \tag{4.17}$$

where $C_{A,\,eq}$ is the equilibrium CO_2 concentration that can be estimated with Eq. (2.2).
Bhatia and Perlmutter [11] also derived a general rate expression for the instantaneous local reaction rate applicable in the presence of product layer diffusion resistance, as reported by Eq. (3.92). In the limit of product layer diffusion control, $k_s/D_{pl} \to \infty$ as well as β, where the expression of β is given by Eq. (3.93). Thus, in regime of product layer diffusion control, Eq. (3.92) is integrated to the limiting form

$$\frac{1}{\psi}\left[\sqrt{1-\psi\,\ln(1-X)}-1\right] = \sqrt{\frac{M_B\,D_{pl}\,S_0^2\,C_{A,s}\,t}{2\,\rho_s\,Z\,(1-\varepsilon_0)}} = \frac{S_0}{(1-\varepsilon_0)}\sqrt{\frac{D_{\text{eff}}\,t}{2\,Z}}, \tag{4.18}$$

where D_{eff} is the apparent product layer diffusion coefficient and $C_{A,s}$ is the concentration of diffusing species on the pore surface (assuming zero concentration at the carbonate/oxide interface). For the other physical properties in Eqs. (4.17) and (4.18) refer to Tab. 2.1.
Bhatia and Perlmutter [13] first investigated the effect of the gas reactant composition on reaction rate. Eq. (4.17) suggests a linearity trend between the relative reaction rate

$$\frac{d}{dt}\left[\frac{\sqrt{1-\psi\,\ln(1-X)}-1}{\psi}\right], \tag{4.19}$$

and the gas concentration . The relative reaction rate reduces to $1/2\,dX/dt$ at low conversion. Therefore, they plotted the relative reaction rate vs $(C_A - C_{A,\,eq})$ demonstrating with experimental results that the rapid initial stage of the carbonation reaction follows a reversible first order kinetics. Afterwards, they showed that the slow second stage reaction rate is independent of CO_2 partial pressure, except close to equilibrium concentration.
The sharp change in the conversion-time curves between the rapid initial stage and the second slow stage was attributed to the closure of the small pores of a rather narrow size range. Such change occurred at about 60 % of conversion.
In order to evaluate the intrinsic kinetic parameters, Bhatia and Perlmutter considered only the linear growth stage of the conversion-time curves. The rate constant k_s did not exhibit a significant variation with change in temperature. Thus, they concluded that the carbonation reaction followed a zero activation kinetic constant:

$$k_s = A_k = (5.95 \pm 0.18) \times 10^{-10}\,\text{m}^4\,\text{mol}^{-1}\,\text{s}^{-1} \tag{4.20}$$

between 823 K and 998 K.

The second limiting step controlled by product layer diffusion follows Eq. (4.18). The appropriate diffusivity coefficient was estimated from the slope of a linear relation between the ratio $\left[\sqrt{1-\psi\,\ln(1-X)}-1\right]/\psi$ and the square root of time. They found that experimental data follow the linear pattern to about 55 to 60 % of conversion. In this way, the values of the effective diffusivity coefficient for each sample were computed from the linear slope consistent with Eq. (4.18). Using the Arrhenius coordinates they found two different activation energies for D_{eff} for two different temperature ranges:

$$E_{aD} = \begin{cases} 88.9 \pm 3.7\,\text{kJ mol}^{-1} & \text{for} \quad T < 788\,\text{K} \\ 179.2 \pm 7.0\,\text{kJ mol}^{-1} & \text{for} \quad T > 788\,\text{K}. \end{cases} \tag{4.21}$$

The abrupt increase of the activation energy may suggest a change in the reaction mechanism (Bhatia and Pelmutter [13]). However, the RPM 1980 developed by Bhatia and Pelmutter [11] and applied to carbonation reaction ([13]) was not able to reproduce the abrupt transition from the first fast kinetic controlled regime to the second slow product layer diffusion regime.

Reaction mechanism

Bhatia and Perlmutter [13] noticed that the relatively low diffusivity in the product layer and the relative large activation energy are inconsistent with the gas molecular diffusion theory. In addition, the observed change in activation energy at 788 K was to be expected for a solid state process, since the Tammann temperature[4] for $CaCO_3$ is about 800 K. According to [13], Ca^{+2} and CO_3^{-2} were retained to be the main ions in the product layer and the most plausible species for ionic motion. Once CO_3^{-2} moved to the product layer, then a counter-current motion of a negatively charged species was postulated to preserve the electroneutrality of the solid. In the system CaO-$CaCO_3$-CO_2 the most probable species for this purpose was retained to be O^{-2}. Consequently, the following plausible mechanism for the carbonation reaction was suggested:

$$CO_3^{-2} + CaO \rightarrow CaCO_3 + O^{-2} \tag{4.22}$$

at the CaO-$CaCO_3$ interface, and

$$CO_{2_g} \rightleftharpoons CO_{2_{ads}} \tag{4.23}$$

$$CO_{2_{ads}} + O^{-2} \rightarrow CO_3^{-2} \tag{4.24}$$

at the pore surface. In the experiments conducted by the authors, the CO_2 concentration was far from equilibrium and the reaction was found to be independent of gas concentration. Following the above mechanism this must imply that the absorbed gas concentration had reached its saturation value.

On the other hand at elevated temperature above 788 K the activation energy value of $179.2 \pm 7.0\,\mathrm{kJ\,mol^{-1}}$ agreed closely with the $CaCO_3$ heat of decomposition ($178.5\,\mathrm{kJ\,mol^{-1}}$). Thus they suggested a second diffusion mechanism assuming that CO_2 motion is given by the sequential decompositions of CO_3^{-2} in the calcium carbonate layer. A CO_3^{-2} ion momentarily decomposes to give carbon dioxide and an oxygen ion. The carbon dioxide molecule then moves to a neighboring similarly vacated site, while another carbon dioxide so produced elsewhere moves to take its place and reform the carbonate ion. Consequently, the CO_2 molecule diffuses site to site through the product layer up to the CaO-$CaCO_3$ interface.

They concluded explaining that the first stage chemically controlled reaction is compatible with either of the two hypothesized mechanisms if the initial product layer has an high diffusivity causing the intrinsic kinetic reaction at the CaO-$CaCO_3$ interface to control the overall process. This is due to anomalies such as channels and grain boundaries in the surface layer of $CaCO_3$, which favour diffusion. As a result, according to Bhatia and Pelmutter [13] the rapid transition from the fast initial reaction to the second stage represents the formation of a more compact layer with a much lower diffusivity.

[4]The Tammann temperature is the temperature at which the mobility and reactivity of the molecules in a solid become appreciable. It is approximately half of the melting point in kelvin. Source Merkle et al. [41].

4.3.2 Sun et al.

Sun et al. (in their works [59] and [58]) obtained kinetic and product layer diffusion parameters for the carbonation reaction of calcium oxide having a particle size of $38 \div 45\,\mu m$. Two fixed-bed thermogravimetric analyzers were used, one operated at atmospheric pressure (ATGA) and the other under pressurized conditions (PTGA) up to a total pressure of 800 kPa.

The main purpose of Sun et al.'s work [59] was to investigate the intrinsic rate constant of the CaO-CO_2 reaction starting from TGA results. Therefore, a grain model with kinetic control was chosen for the kinetic-controlled region. Following the work of Szekely [29], they applied Eq. (3.28) adopting Eq. (3.12) as reaction rate formulation. In this way, the differential reaction rate of Eq. (3.28) is changed into

$$\frac{dX}{dt} = M_B\, k'_{s,p}\, (p_A - p_{A,\,eq})^n\; S_g\; (1-X)^{2/3} \tag{4.25}$$

having care to follow Eqs. (3.13), (3.26) and (3.5) to express the kinetic constant in terms of CO_2 partial pressure (from k_s to $k'_{s,p}$) and the particle surface are per unit of volume in terms of surface area per unit of weight (from S_p to S_g). Eq. (4.25) assumes that the stoichiometric coefficient b is 1 as reported in Eq. (4.14). M_B is $56.077\,g\,mol^{-1}$ as in Tab. 2.1.
As previous reported in Chapter 3, Eq. (4.25) shows that when the reaction is under kinetic control, a plot of $\left[1-(1-X)^{1/3}\right]$ vs t should give a straight line with a slope providing the reaction rate constant. From TGA tests, Sun et al. observed that at the beginning of the reaction, there was a lower slope induction period. After this, a short linear stage occurred, whose slope identified the intrinsic reaction rate. Following the kinetic control region, the slow-down stage is controlled by both surface reaction and product-layer diffusion, showing lower slopes. As carbonation proceeds further, product-layer diffusion becomes more important, resulting in much slower carbonation. Therefore, the value of the intrinsic reaction rate constant in the kinetic-controlled region obtained from the linear plot slope can also be extended to represent the true rate at the zero conversion point, such as

$$R_0 = \left.\frac{dX}{dt}\right|_{t=0} = M_B\, k'_{s,p}\, (p_A - p_{A,\,eq})^n\; S_{g,0}. \tag{4.26}$$

where $S_{g,0}$ is the specific surface area at the initial time. In logarithmic form Eq. (4.26) becomes

$$\ln(R_0) = \ln\left(M_B\, k'_{s,p}\right) + n\, \ln(p_A - p_{A,\,eq}) + \ln S_{g,0}. \tag{4.27}$$

The slope of $\ln(R_0)$ vs $\ln(p_A - p_{A,\,eq})$ gives the order of reaction with respect to the CO_2 partial pressure. From experimental results Sun et al. demonstrated that at low CO_2 partial pressure driving force $(p_A - p_{A,\,eq})$ values, the CO_2-CaO reaction is first order. However, for higher $(p_A - p_{A,\,eq})$ a transition in the reaction order occurred. This change appeared to be sharp, suggesting a sudden change in the controlling mechanism. Driving force $(p_A - p_{A,\,eq})$ at ~ 10 kPa was taken as the transition value. As a result of a non-linear fitting in the Arrhenius

plot, they obtained

$$k_s^{(0)} : \begin{cases} A_k^{(0)} = 2.8 \times 10^{-8}\,\mathrm{m\,s^{-1}} \\ E_{a,k}^{(0)} = 29.4 \pm 4\,\mathrm{kJ\,mol^{-1}} \end{cases} \quad \text{for} \quad \left(p_{\mathrm{CO_2}} - p_{\mathrm{CO_2},eq}\right) > 10\,\mathrm{kPa} \tag{4.28}$$

for the zero-order region. Since $(p_A - p_{A,eq}) = 10\,\mathrm{kPa}$ at the transition from the first-order to zero-order reaction, the specific reaction rate predicted for zero-order carbonation reaction was equal the first-order kinetics at the transition point. Consequently, they derived for the first-order region:

$$k_{s,p}^{(1)} : \begin{cases} A_k^{(1)} = 2.8 \times 10^{-12}\,\mathrm{m\,s^{-1}\,Pa^{-1}} \\ E_{a,k}^{(1)} = 29.4 \pm 4\,\mathrm{kJ\,mol^{-1}} \end{cases} \quad \text{for} \quad \left(p_{\mathrm{CO_2}} - p_{\mathrm{CO_2},eq}\right) \leq 10\,\mathrm{kPa} \tag{4.29}$$

where the limits on the activation energy correspond to 95 % confidence level. Clearly, the relationship between $k_{s,p}^{(1)}$ and $k_s^{(1)}$ follows Eq. (3.13), once a reaction temperature is selected.

Reaction mechanism

With the purpose to explain the shift in the reaction order, Sun et al. suggested that the CaO-CO_2 reaction consisted of a series of elementary steps. Each one of these steps followed a Langmuir mechanism such as:

$$\mathrm{CaO} + \mathrm{CO_2} \underset{k_2}{\overset{k_1}{\rightleftharpoons}} \mathrm{CaO \cdot CO_2} \quad \text{step 1} \tag{4.30}$$

$$\mathrm{CaO \cdot CO_2} \underset{k_4}{\overset{k_3}{\rightleftharpoons}} \mathrm{CaCO_3} \quad \text{step 2.} \tag{4.31}$$

where $\mathrm{CaO \cdot CO_2}$ was an intermediate complex. Step 1 was retained to be a reversible process where the CO_2 gaseous molecules were adsorbed on CaO sites to give $\mathrm{CaO \cdot CO_2}$. The second step considered the complex reaction to $CaCO_3$, according to Sun et al. [59]. Assuming that step 2 is at equilibrium, the first step is the rate controlling one. Following the Langmuir theory:

$$k_3\,\theta - k_4 = 0, \tag{4.32}$$

so that

$$\theta = \frac{k_4}{k_3}, \tag{4.33}$$

where θ is the fractional site coverage. Then

$$R = k_1\,(1-\theta)\,p_{\mathrm{CO_2}} - k_2\,\theta. \tag{4.34}$$

where R is the reactivity of the reaction according to Eq. (3.15). Substituting Eq. (4.33) into Eq. (4.34),

$$R = k_1 \left[\left(1 - \frac{k_4}{k_3} \right) p_{CO_2} - \frac{k_2\, k_4}{k_1\, k_3} \right]. \tag{4.35}$$

Considering the reaction equilibrium, $k_2\, k_4/(k_1\, k_3) = 1/K = p_{CO_2,eq}$, where K is the equilibrium constant of the carbonation reaction, Eq. (4.35) becomes

$$R = k_1 \left[\left(1 - \frac{k_4}{k_3} \right) p_{CO_2} - \frac{1}{K} \right]. \tag{4.36}$$

Assuming that step 2 was fast, site coverage of the $CaO \cdot CO_2$ complex was very low, so that $\theta = k_4/k_3 \ll 1$ and Eq. (4.36) becomes

$$R = k_1 \left(p_{CO_2} - p_{CO_2,eq} \right). \tag{4.37}$$

Eq. (4.37) indicates that Eq. (4.25) is explained by a Langmuir mechanism. However, from experimental data Sun et al. found that the apparent first-order dependence occurs when $\left(p_{CO_2} - p_{CO_2,eq}\right) \leq 10\,\text{kPa}$, above which a zero-order dependence was observed. Consequently they concluded that there must be a shift in reaction mechanism when $\left(p_{CO_2} - p_{CO_2,eq}\right)$ exceeds this critical value. When the driving force $\left(p_{CO_2} - p_{CO_2,eq}\right)$ is larger than the critical value, the concentration of the transition complex $CaO \cdot CO_2$ is high enough that the CaO sites are mostly saturated so that $\theta \to 1$. Thus, the assumption of low site coverage of complex $CaO \cdot CO_2$ is no longer valid. At this stage, step 2 becomes rate-limiting, so that the overall reaction rate becomes $R = k_3 \times \theta - k_4 = k_3 - k_4$.
At the critical value of $\left(p_{CO_2} - p_{CO_2,eq}\right)$ of $\sim 10\,\text{kPa}$, the kinetic rate determined from Eq. (4.37) reaches its maximum value, numerically equal to the rate determined as $R = k_3 - k_4$.
As a result of the previous analysis,

$$R^{(1)} = k_1 \left(p_{CO_2} - p_{CO_2,eq} \right) \quad \text{for} \quad \left(p_{CO_2} - p_{CO_2,eq} \right) \leq 10\,\text{kPa}, \tag{4.38}$$

$$R^{(0)} = k_3 - k_4 = k_1 \times 10\,\text{kPa} \quad \text{for} \quad \left(p_{CO_2} - p_{CO_2,eq} \right) > 10\,\text{kPa}. \tag{4.39}$$

Eqs. (4.38) and (4.39) represent the reaction rates of the carbonation reaction following a Langmuir mechanism, consistent with Sun et al.'s experimental results, as reported by Eqs. (4.28) and (4.29).

In their following work [58] Sun et al. recognized several disadvantages of the grain model reported in § 3.3.4: for example, the monotonically increase of the surface area (even when the porosity approaches to zero) or the non overlapping behavior. Consequently, they applied a pore model to account for the pore evolution and, specifically, they applied the RPM developed by Bhatia [10] and Sotirchos [57], previously discussed in § 3.6. However, instead of a continuous pore-size distribution they used a discrete one. In this work they used calcined CaO particles having a size of $38 \div 45\,\mu\text{m}$ and $212 \div 250\,\mu\text{m}$ respectively.
Using the kinetic parameters of their previous work [58], the solid-state diffusivity in the product

layer D_{pl} was the only unknown parameter. Thus, from ATGA and PTGA results they fitted the product layer diffusivity for the CO_2-CaO reaction obtaining the following result

$$D_{pl} : \begin{cases} A_D = 0.27\,\mathrm{m^2\,s^{-1}} \\ E_{a,D} = 215\,\mathrm{kJ\,mol^{-1}} \end{cases} \quad \text{for} \quad 773 \leq T \leq 1123\,\mathrm{K}. \tag{4.40}$$

Sun et al. outline that during the first step of the reaction if $\left(p_{CO_2} - p_{CO_2,eq}\right) > 10\,\mathrm{kPa}$, $\left(p_{CO_2} - p_{CO_2,eq}\right) > 10\,\mathrm{kPa}$ at the reaction surface and reaction remains in the zero order zone. During this stage the CO_2 concentration does not affect the kinetics. When the product layer thickness becomes relevant, the slower stage of carbonation occurs. The reaction falls in the first-order zone because of the decrease of the CO_2 concentrations at the reaction front due to the concentration gradient in the product layer. At this stage, the reaction is slow than the first stage,because of the controlling product-layer diffusion.
Sun et al. [58] investigated the reason of the sudden shift of carbonation reaction from a fast to a slow stage of reaction. Based on their pore size distribution estimations at different degree of conversion, they attributed the two stage pattern of reaction to a small pore closure having an initial radius $< 250\,\mathrm{nm}$. In fact smaller pores contributed more to the surface area. In this way, the reaction proceeds very slowly in the second stage because of the loss of the most surface area.

Since the use of a discrete pore size distribution that makes the model easily to implement, on the other hand it presents some disadvantages. In fact, when the number of pore radius classes are low, a discrete form of the pore size distribution may not be able to well represent the particle porosity of specific surface. For this reason a continuous pore size distribution should be employed.

4.3.3 Grasa et al.

Grasa et al.'s works [25] and [24] are focused in kinetic parameter estimation of carbonation reaction for highly cycled particles of CaO in order to represent the CO_2 capture capacity in a carbonator reactor. Indeed high reaction rates between the CO_2 in the flue gas and the sorbent particles are required in order to design compact absorbers. Fresh calcined lime is known to be able to carbonate very readily at appropriate temperatures, but the average sorbent particle in the system must experience many carbonation/calcination cycles and the sorbent capture capacity decreases rapidly in these conditions.

In their work [25] they study the reactivity of highly cycled lime particles with the purpose to determine the carbonation rate over cycles. The cyclic carbonation and calcination reactions were experimentally studied in a TGA instrument. From experimental results they recognized the two stage pattern of CO_2-CaO reaction and they focused only on the fast reaction stage in order to obtain kinetic constant estimations. The calcium oxide particles used had a particle diameter of $0.25 \div 1\,\mathrm{mm}$, with operative conditions ranging from $550 \div 700\,^{\circ}\mathrm{C}$ for carbonation temperature and $0.01 \div 0.1\,\mathrm{MPa}$ of CO_2 partial pressure. Each sample was cycled up to 500 times.
The carbonation rate was described with a fist order kinetic with two different models: the

grain model and the thin product layer RPM both under kinetic control (respectively Eqs. (3.28) and (3.75)). Carbonation was considered as a first order reversible reaction and the driving force force $\left(C_{CO_2} - C_{CO_2,eq}\right)$ was used in place of CO_2 concentration. As Bhatia and Perlmutter [13], Grasa et al. considered carbonation reaction had a zero activation energy at their experimental temperatures. As a result of their fittings, they obtained the following results:

$$k_s = (3.2 \div 8.9) \times 10^{-10} \mathrm{m^4\,mol^{-1}\,s^{-1}} \tag{4.41}$$

for the grain model, and

$$k_s = (3.1 \div 8.7) \times 10^{-10} \mathrm{m^4\,mol^{-1}\,s^{-1}} \tag{4.42}$$

for the thin product layer RPM.
In their following work [24] they investigated both kinetic and product layer diffusion control using particle lime having a particle diameter of $50 \div 75\,\mu\mathrm{m}$. Two different types of limestone were used during the experiments: a Spanish limestone called "Imeco" and a Polish limestone called "Katowice".
They adopted Eq. (4.17) for the kinetic controlled regime and Eq. (4.18) for the product layer controlled regime. These expressions were used to derive intrinsic kinetic constant and product layer diffusivity respectively. The fitting results of the experimental data give the following parameters. For intrinsic kinetic parameters:

$$k_s = \begin{cases} A_k = 5.59 \times 10^{-9}\,\mathrm{m^4\,mol^{-1}\,s^{-1}}; & E_{a,k} = 21.3\,\mathrm{kJ\,mol^{-1}} \quad \text{Imeco} \\ A_k = 5.29 \times 10^{-9}\,\mathrm{m^4\,mol^{-1}\,s^{-1}}; & E_{a,k} = 19.2\,\mathrm{kJ\,mol^{-1}} \quad \text{Katowice.} \end{cases} \tag{4.43}$$

For intrinsic product layer diffusivity:

$$D_{pl} = \begin{cases} A_D = 3.37 \times 10^{-6}\,\mathrm{m^2\,s^{-1}}; & E_{a,D} = 163\,\mathrm{kJ\,mol^{-1}} \quad \text{Imeco} \\ A_D = 4.32 \times 10^{-6}\,\mathrm{m^2\,s^{-1}}; & E_{a,D} = 163\,\mathrm{kJ\,mol^{-1}} \quad \text{Katowice.} \end{cases} \tag{4.44}$$

As reported in Eq. (4.43) the activation energies for carbonation reaction are in close agreement with the values of Sun et al. [59], Eqs. (4.28) and (4.29). However, Grasa et al. [24] did not assume a zero activation energy for carbonation reaction, differently with respect to their previous work [25] and Bhatia and Perlmutter [13].
They attributed the sharp drop of the reaction rate due to a critical product layer thickness. Before this step, Grasa et al. [24] stated that the carbonation reaction was characterized by both a component of an intrinsic kinetic nature and a component associated to the diffusivity of CO_2 in the product layer. This process occurred until the small pores are filled up to the critical value of $\sim 50\,\mathrm{nm}$, after which CO_2 diffusion tends to be very low. This last point is consistent with the findings of Mess et al. [42] who found that CO_2 diffusion in the carbonate product layer decreased rapidly with increasing carbonate conversions.
Finally, their experimental results showed that the carbonation reaction was found to be first order with respect to the CO_2 concentration up to $0.1\,\mathrm{MPa}$ of CO_2 partial pressure. This

appeared to be in contrast with the results of Sun et al. [59] who considered the reaction to be first order up to 0.01 MPa and zero order for higher CO_2 partial pressures (with respect to the equilibrium value).

4.3.4 Mess et al.

Mess et al. [42] investigated the product layer diffusion in the CO_2-CaO reaction. Specifically, their purpose was to measure product layer diffusion rates as a function of CO_2 pressure and temperature when all the physical resistances were negligible. This was achieved by carbonating nonporous, high purity CaO particles in a TGA which has been modified for pressurized operation.
In their work single crystal lumps of calcium oxide were used. The material was 99.9 % pure having a size fraction of $15 \div 20\,\mu m$. The temperature range was from 550 to 1100 °C and the CO_2 pressure range from 1 to 11.7atm.
The observed morphologies through SEM supported the concept of a product layer whose thickness is approximately uniform but made of grains which were characteristic of a recrystallized structure.
Mess et al. chose the grain model under product layer control to represent their experimental results. Consequently, Eq. (3.34) was applied to the whole spherical particles in order to estimate the apparent effective product layer diffusivity D_{eff} as the unique fitting parameter. From their experimental results they found a first order dependence of the reaction rate on the concentration gradient at high temperature ($950 \div 1000\,°C$). Effective diffusivities for product layer diffusion of the high-temperature runs were calculated from Eq. (3.34):

$$D_{\text{eff}} : \begin{cases} A_D = 6.5 \times 10^{-5}\,\text{m}^2\,\text{s}^{-1} \\ E_{a,D} = 237.3\,\text{kJ mol}^{-1}. \end{cases} \tag{4.45}$$

Mess at al. proposed that two independent and parallel processes take place:

1. a diffusional process that was proportional to the grain boundary length and is independent of the CO_2 driving force;

2. a bulk diffusional process of CO_2 through the $CaCO_3$ crystals which cover the surface but increase in thickness with time.

Their experimental results indicate a distinct carbonation rate at low conversions. This rate at low conversions was modeled by assuming that CO_2 accessed the CaO surface by grain boundary diffusion independently by the CO_2 pressure driving force. Consequently, the carbonation rate under product layer diffusion control was due to two main terms: $L_A\,D_{gb}$ and D_{eff}, where L_A is the grain boundary length, D_{gb} is the grain boundary diffusion and D_{eff} is the effective diffusivity through the crystal product layer. The first term describes diffusion through the grain boundaries and is proportional to the grain boundary length, which decreases with time as the carbonate crystals grow by coalescence and is independent of the CO_2 driving force. The second term

represents diffusion through the crystals to the surface of the calcium oxide where it reacts to form the carbonate.

4.3.5 Kyaw at al.

Kyaw at al. [32] studied the carbonation reaction using CaO particles of 5 µm diameter, carried out at $400 \div 900\,^{\circ}\mathrm{C}$ under various CO_2 partial pressures ($20 \div 101\,\mathrm{kPa}$ at atmospheric pressure). They noticed that the form of their conversion-time curves suggested two reaction stages: the first consisted of rapid reaction with CO_2 and the second of a much slower reaction rate that falls off with time. They assumed that the porous calcined particles were composed by calcium oxide of uniform spherical grains. Accordingly, they considered the grain model under kinetic control as structural model, using the following form

$$\frac{dX}{dt} = k''_{s,p}\ (p_A - p_{A,\,eq})^n\ (1-X)^{2/3}. \tag{4.46}$$

Eq. (4.46) agrees with Eq. (4.25) including M_B and S_g into $k''_{s,p}$, so that

$$k''_{s,p} = k'_{s,p}\, M_B\, S_g, \tag{4.47}$$

whose unit are $\mathrm{kPa^{-n}\,s^{-1}}$. By plotting dX/dt values vs $(p_A - p_{A,\,eq})$ for the carbonation reaction at $400 \div 900\,^{\circ}\mathrm{C}$, they found that n was about 0.1. Moreover, the estimated activation energy was found to be about $78\,\mathrm{kJ\,mol^{-1}}$.

In their following work [31] they considered again the grain model under kinetic control applied to the carbonation reaction under kinetic control. They assumed the carbonation reaction to be composed by two steps following Eqs. (4.30) and (4.31) respectively. By these equations, a Langmuir mechanism was applied assuming the $CaO \cdot CO_2$ concentration small, $k_1 \gg k_2$ and $k_3 \gg k_4$. With these assumptions they derived:

$$\frac{dX}{dt} = k_x\ (1-X)^{2/3}\ \left(\frac{p_A - p_{A,eq}}{p_{A,eq}}\right)^n, \tag{4.48}$$

where k_x is dimensionless.
The experimental TGA data were plotted in terms of dX/dt vs $(p_A - p_{A,eq})\,/p_{A,eq}$ on logarithmic scale giving straight lines whose slope was 0.4 in the temperature range of $600 \div 850\,^{\circ}\mathrm{C}$. Finally, they achieved the following reaction rate parameters:

$$k_x = \begin{cases} A_k = 248.5; \\ E_{a,k} = 76.67\,\mathrm{kJ\,mol^{-1}}. \end{cases} \tag{4.49}$$

4.3.6 Other literature works

Dedman et al. in 1962 [21] studied the second slower stage of the carbonation reaction using a pressurized reaction vessel surrounded by a furnace with a manometer to follow the progress of reaction. Between $200 \div 600\,^{\circ}\mathrm{C}$ the estimated activation energy was $397.7\,\mathrm{kJ\,mol^{-1}}$.

Oakeson et al. in 1979 [43] studied the effect of temperature and CO_2 pressure of the carbon-

ation reaction using a TGA instrument. Non-porous dense disks of CaO with 40 µm in diameter were used. The operative condition were $853 \div 1044\,°C$ for temperature and $2.35 \div 24.87\,atm$ for CO_2 partial pressure. Focusing on the slower reaction step, they considered a Langmuir mechanism. The estimated activation energy from experimental results was $121\,kJ\,mol^{-1}$.
Finally, both the authors suggested that the last reaction stage is due to a counterdiffusion of ions mechanism of species CO_3^{-2} and O_2^{-2} at the CaO-$CaCO_3$ interface.

4.4 Determination of the pore size distribution

The RPM developed by Bhatia [10] and Sotirchos et al. [57] requires the knowledge on the pore size distribution of the porous solid reactant. As reported in § 3.6, Bhatia [10] suggested a log-normal distribution in order to represent the differential length size distribution. In order to apply such RPM to the carbonation reaction, the pore size distribution is first obtained from N_2 adsorption experimental data. These data are fitted in order to have the pore size distribution in the analytical form.

In Chapter 2 the reported pore size distributions were obtained from N_2 adsorption tests in terms of void volume per unit of sample weight (cumulative distribution) and void volume per unit of sample weight and pore radius (differential distribution). In order to estimate the porosity, surface area and length size distributions based on the unit of geometrical volume, it is useful to convert N_2 adsorption results from a weight basis to a volume basis multiplying by the particle bulk density, defined as

$$\rho_{p,s} = \rho_s\,(1 - \varepsilon_0)\,, \tag{4.50}$$

where ρ_s is the solid skeleton density[5] and ε_0 is the initial sample porosity. In this way, the sample porosity becomes

$$\varepsilon_0 = \frac{\rho_s\,V_g}{1 + \rho_s\,V_g} \tag{4.51}$$

where V_g is the void volume of the sample per unit of weight.
r_0 is the initial pore radius and is the random variable of the log-normal distribution defined as

$$\varepsilon_0(r_0) = \frac{b_{LN}^{(o)}}{\sqrt{2\,\pi}\sigma_{N_0}\,r_0}\exp\left[-\frac{(\ln r_0 - \mu_{N_0})^2}{2\,\sigma_{N_0}^2}\right] \tag{4.52}$$

where μ_{N_0} and σ_{N_0} are respectively the mean and the variance of the normal distribution of the random variable $\ln(r_0)$; $b_{\mathrm{LN}}^{(o)}$ represents the total porosity of the sample, hence the total overlapped void fraction, according to Bhatia [11]. The mean (M_0) and variance (V_0^{LN}) of the log-normal distribution are related to the normal distribution parameters by Eqs. (3.175) and (3.176).

[5]Skeleton density is defined as the mass of dense solid per unit of geometrical volume. This quantity refers to non-porous materials.

The cumulative log-normal distribution is defined as

$$E_0(r_0) = \int_0^{r_0} \varepsilon_0(r_0')\, dr_0' = b_{LN}^{(o)} \left[\frac{1}{2} + \frac{1}{2}\,\mathrm{erf}\left(\frac{\ln r_0 - \mu_{N_0}}{\sqrt{2}\,\sigma_{N_0}}\right)\right] \tag{4.53}$$

where erf is the Gauss error function[6].
In order to estimate the three unknown parameters, namely $b_{LN}^{(o)}$, μ_{N_0} and σ_{N_0}, a non linear fitting to the N_2 adsorption data was performed. The selected experimental curve for the fitting procedure was the cumulative one that provides the correct valued of the porosity when the experimental points are few instead of the differential one. It is useful for the numerical fitting to consider dimensionless variables using the following change of variable

$$a_0 = \frac{r_0}{M_0}. \tag{4.54}$$

Following Eq. (4.54), Eqs. (4.52) and (4.53) become

$$\varepsilon_0(a_0) = \frac{b_{LN}^{(o)}}{\sqrt{2\,\pi}\sigma_{N_0}\, M_0\, a_0} \exp\left[-\frac{\left(\ln a_0 + \ln\left(M_0\right) - \mu_{N_0}\right)^2}{2\,\sigma_{N_0}^2}\right], \tag{4.55}$$

$$E_0(a_0) = \int_0^{a_0} M_0\, \varepsilon_0(a_0')\, da_0' = b_{LN}^{(o)} \left[\frac{1}{2} + \frac{1}{2}\,\mathrm{erf}\left(\frac{\ln a_0 + \ln\left(M_0\right) - \mu_{N_0}}{\sqrt{2}\,\sigma_{N_0}}\right)\right]. \tag{4.56}$$

Because of the non linear behavior of the problem, a numerical method is required to estimate the unknown parameters. To this end, the selected MATLAB® routine is "fminsearch", that minimizes an objective function, called "FOB":

$$\mathrm{FOB} = \left\|\mathbf{E_{0,\,exp}} - \mathbf{E_{0,\,calc}}\right\|_2, \tag{4.57}$$

where $\mathbf{E_{0,\,exp}}$ is a vector whose components are the cumulative experimental porosity values, whereas, $\mathbf{E_{0,\,calc}}$ contains the analytical porosity evaluated at each experimental point a_0. The symbolism $\|\cdot\|_2$ refers to the Euclidean norm of a vector[7]. The "fminsearch" routine finds the minimum of a multidimensional function by solving the following problem:

$$\min_{\mathbf{s}}\left(\mathrm{FOB}\right) = \min_{\mathbf{s}}\left(\left\|\mathbf{E_{0,\,exp}} - \mathbf{E_{0,\,calc}}\right\|_2\right), \tag{4.58}$$

which is a three dimensional minimization whose solution is a three dimensional vector, $\mathbf{s}$, whose components have the values of $b_{LN}^{(o)}$, μ_{N_0} and σ_{N_0}.

The results of the fitting procedure are reported in Fig. 4.3. Fitting results was retained to be satisfactory especially for Figs. 4.3f and 4.3a samples, where more experimental points were obtained from N_2 adsorption. Clearly the whole experimental procedure requires more time than tests with fewer points (up to twice). The CaO samples were obtained by calcination at 800 °C for 120 min and 900 °C for 15, 30 and 180 min.

[6] Gauss error function is defined as $\mathrm{erf}\,(x) = 2/\sqrt{\pi}\,\int_0^{\infty} e^{-x'^2}\, dx'$ where x is a random variable.

[7] On an n-dimensional Euclidean space $\mathbb{R}^n$ the Euclidean norm of a vector $\mathbf{x} \in \mathbb{R}^n$ is defined as $\|\mathbf{x}\|_2 = \left(\sum_{i=1}^{n} x_i^2\right)^{1/2}$.

Table 4.2: Results of the numerical fitting for CaO samples obtained by calcination at different temperatures/times.

Sample	$b_{LN}^{(o)}$ [−]	$b_{LN}^{(E)}$ [−]	μ_{N_0} [Å]	σ_{N_0} [Å^{-1}]	M_0 [Å]	V_0^{LN} [Å^{-1}]
800 °C, 120 min	0.514	0.721	5.212	0.234	188.612	2.010×10^3
900 °C, 5 min	0.520	0.734	5.114	0.462	185.044	8.141×10^3
900 °C, 10 min	0.484	0.661	5.115	0.402	180.453	5.698×10^3
900 °C, 15 min	0.486	0.666	5.069	0.346	168.850	3.626×10^3
900 °C, 30 min	0.498	0.689	5.492	0.612	294.536	4.086×10^3
900 °C, 180 min	0.489	0.672	5.649	0.455	314.955	2.284×10^4

The RPM developed by Bhatia [10] and Sotirchos [57] required a length pore size distribution, named $l(a_0)$. For these reason, Eq. (4.55) is divided by $\pi\, M_0^2\, a_0^2$ obtaining the pore length size distribution:

$$l(a_0) = \frac{b_{LN}^{(o)}}{\pi\sqrt{2\,\pi}\sigma_{N_0}\, M_0^3\, a_0^3} \exp\left[-\frac{\left(\ln a_0 + \ln\left(M_0\right) - \mu_{N_0}\right)^2}{2\,\sigma_{N_0}^2}\right]. \tag{4.59}$$

Eq. (4.59) refers to the overlapped situation. However, the RPM requires a non-overlapped length size distribution. Consequently, the fitted parameter $b_{LN}^{(o)}$ must be rescaled to $b_{LN} = b_{LN}^{(E)}$ which refers to non-overlapped configuration. To this end, Eq. (3.58) was applied in the inverted form,

$$b_{LN} = b_{LN}^{(E)} = -\ln\left(1 - b_{LN}^{(o)}\right). \tag{4.60}$$

Substituting b_{LN} instead of $b_{LN}^{(o)}$, Eq. (4.59) matches exactly Eq. (3.177). All the results of the fitting procedure are reported in Tab. 4.2.

Sun et al. [58] considered a discrete pore size distributions that were measured with a mercury porosimeter. With these distributions Sun et al. applied the RPM of Bhatia [10] and Sotirchos et al. [57] to the carbonation reaction. However, a continuous pore size distribution is recommended because the number of classes may affect the accuracy of the results in terms of total particle porosity. Indeed, a pore size distribution that presents a low number of experimental points may lead to unphysical results. In fact, considering Eq. (3.173), if few classes in the discrete pore size distribution are employed, the quadrature may not match the total particle porosity and the conversion prediction may exhibit negative values.

4.5 The random pore model applied to the carbonation reaction

In this section the carbonation reaction is modeled following the RPM developed by Bhatia [10] and Sotirchos et al. [57] as reported in § 3.6. Bhatia and Sotirchos et al. assumed a first order irreversible reaction. However, on the basis of Sun et al.'s analysis ([59] and [58]), Eq. (4.14) is reversible and switches its reaction order depending on CO_2 partial pressure. Since

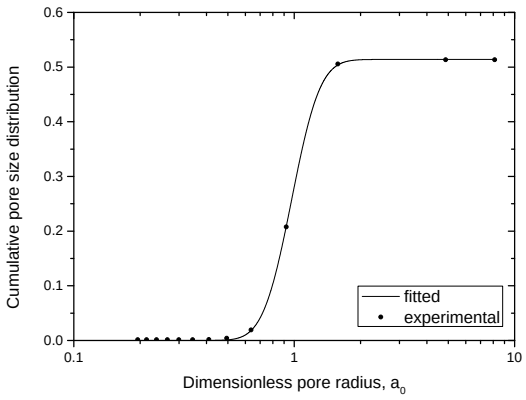

(a) 800 °C, 120 min.

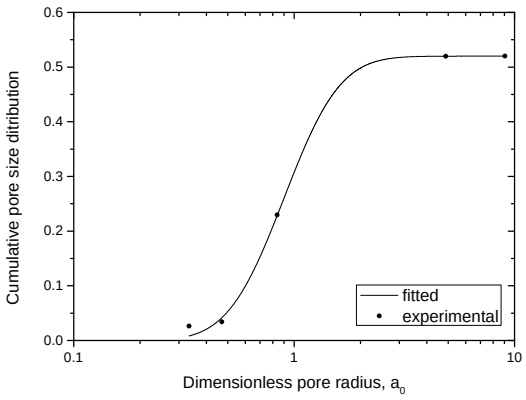

(b) 900 °C, 5 min.

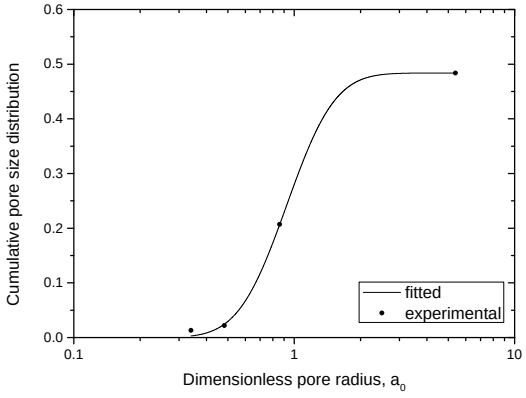

(c) 900 °C, 10 min.

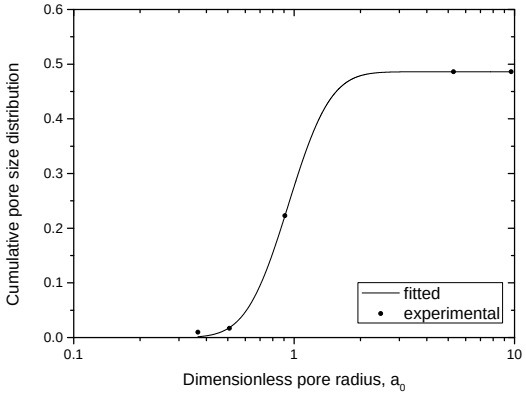

(d) 900 °C, 15 min.

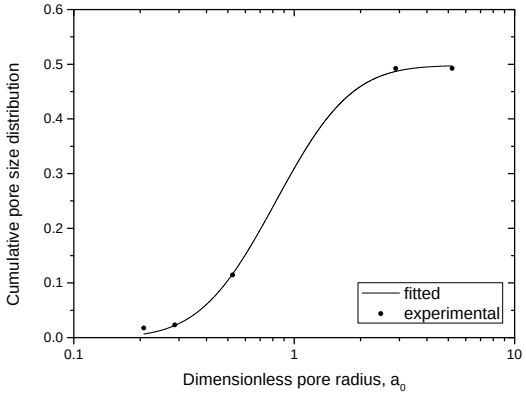

(e) 900 °C, 30 min.

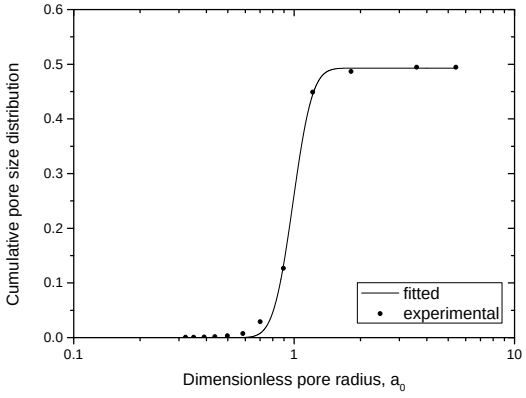

(f) 900 °C, 180 min.

Figure 4.3: Comparison between experimental and analytical cumulative distributions. Temperatures and permanence times refer to the calcination reaction.

the carbonation reaction is a reversible reaction, the carbon dioxide partial pressure is expressed in terms of driving force with respect to the equilibrium, such as $(p_{CO_2} - p_{CO_2,eq})$. Consequently, Eqs. (3.170), (3.171), (3.172) and (3.173) must be modify to account the reaction order switch and the equilibrium condition.
Following the analysis presented § 3.6 the modeling problem can be initially split into two cases: the first order reversible, and the zero order reaction behavior.

4.5.1 First order reaction

Assuming a first order reversible reaction, whose stoichiometry follows Eq. (4.14), the intrinsic kinetic rate is

$$\frac{\partial r_s}{\partial t} = b\, k_s^{(1)} \left(C^s_{A,\,\mathrm{int}} - C_{A,\,eq}\right) \tag{4.61}$$

where r_s is the reaction surface radius, $k_s^{(1)}$ the first order kinetic constant and $C_{A,\,\mathrm{int}}$ is the concentration of species A at the reaction front. In cylindrical coordinates the pseudo-steady-state diffusion equation of species A is reported by Eq. (3.139), whose boundary conditions are

$$\begin{aligned} C_A = C^p_{A,\,\mathrm{int}} &= C_{A,\,\mathrm{bulk}}, \qquad \text{at } r = r_p \\ -D_{pl}\,\frac{\partial C_A}{\partial r} &= a\, k_s^{(1)}\,\frac{\rho_s}{M_B}\,\left(C^s_{A,\,\mathrm{int}} - C_{A,\,eq}\right), \qquad \text{at } r = r_s, \end{aligned} \tag{4.62}$$

where the first condition states that all the external resistances are neglected as well as inter-particle and intra particle diffusion. Consequently, the concentration of species A at the pore surface is exactly the same of the concentration of A in the bulk.
Once integrated assuming cylindrical pores, Eq. (3.139) represents the concentration profile of A inside the product layer and gives the following general solution:

$$C_A(r) = c_1\, \ln(r) + c_2. \tag{4.63}$$

However, Eq. (4.63) does not consider $C_{A,\,eq}$ and Eq. (3.139) can not be integrated with Eq. (4.62) as boundary condition. Thus, the following change of variable is introduced:

$$C^*_A = C_A - C_{A,\,eq}, \tag{4.64}$$

where $dC^*_A = dC_A$. On the basis of Eq. (4.64), Eq. (4.61) becomes

$$\frac{\partial r_s}{\partial t} = b\, k_s^{(1)}\, C^{s*}_{A,\,\mathrm{int}}, \tag{4.65}$$

Eq. (3.139) changes into

$$\frac{\partial}{\partial r}\left(S(r, r_0)\,\frac{\partial C^*_A}{\partial r}\right) = 0 \qquad r_p \le r \le r_s. \tag{4.66}$$

whose boundary conditions are

$$\begin{aligned} C_A^* &= C_{A,\,\text{int}}^{p*} = C_{A,\,\text{bulk}}^*, \qquad \text{at } r = r_p \\ -D_{pl}\,\frac{\partial C_A^*}{\partial r} &= a\,k_s^{(1)}\,\frac{\rho_s}{M_B}\,C_{A,\,\text{int}}^{s*}, \qquad \text{at } r = r_s. \end{aligned} \tag{4.67}$$

This approach allows to bring Eqs. (4.61) and (4.62) back to normal form reported in § 3.6, whose general solution follows Eq. (4.63):

$$C_A^* = c_1\,\ln(r) + c_2. \tag{4.68}$$

Once the boundary conditions are imposed, Eq. (4.68) becomes

$$C_A^*(r) = \frac{C_{A,\,\text{bulk}}^*}{1 + \dfrac{a\,k_s^{(1)}\,\rho_s}{M_B\,D_{pl}}\,r_s\,\ln\left(\dfrac{r}{r_p}\right)} \tag{4.69}$$

with $r_p \leq r \leq r_s$. Taking $r = r_s$, the reaction surface concentration of A is

$$C_{A,\,\text{int}}^{s*} = \frac{C_{A,\,\text{bulk}}^*}{1 + \dfrac{a\,k_s^{(1)}\,\rho_s}{M_B\,D_{pl}}\,r_s\,\ln\left(\dfrac{r_s}{r_p}\right)}. \tag{4.70}$$

4.5.2 Zero order reaction

On the basis of Eqs. (4.28) and (4.29), the carbonation reaction switches to a zero-order as long as $C_{A,\,\text{int}}^{s*} = C_{A,\,c}$, where $C_{A,\,c}$ is the critical concentration, below which the reaction follows a first order kinetics.
In this case the kinetic rate becomes

$$\frac{\partial r_s}{\partial t} = b\,k_s^{(0)}, \tag{4.71}$$

where $k_s^{(0)}$ is the zero order kinetic constant. The boundary conditions of the pseudo-steady-state balance of A are

$$\begin{aligned} C_A &= C_{A,\,\text{int}}^{p} = C_{A,\,\text{bulk}}, \qquad \text{at } r = r_p \\ -D_{pl}\,\frac{\partial C_A}{\partial r} &= a\,k_s^{(0)}\,\frac{\rho_s}{M_B}, \qquad \text{at } r = r_s. \end{aligned} \tag{4.72}$$

Considering the change of variable given by Eq. (4.64), Eq. (4.72) are rewritten in terms of C_A^*. Once integrated with Eq. (4.72) in terms of C_A^*, Eq. (4.66) becomes:

$$C_A^* = C_{A,\,\text{bulk}}^* - a\,k_s^{(0)}\,\frac{\rho_s\,r_s}{M_B\,D_{pl}}\,\ln\left(\frac{r}{r_p}\right), \tag{4.73}$$

and for $r = r_s$, the concentration of A at the reaction front is

$$C^{s*}_{A,\,\text{int}} = C^{*}_{A,\,\text{bulk}} - a\,k^{(0)}_s\,\frac{\rho_s\,r_s}{M_B\,D_{pl}}\ln\left(\frac{r_s}{r_p}\right). \tag{4.74}$$

4.5.3 Model assembling

The analysis presented in § 3.6 is modified considering the equilibrium condition and the reaction rate switch from zero to first order. As a results, following the stoichiometry of Eq. (4.14), Eq. (3.156) becomes

$$\frac{\partial r_s}{\partial t} = k^{(0)}_s, \qquad \text{for 0 order reaction} \tag{4.75}$$

and

$$\frac{\partial r_s}{\partial t} = \frac{k^{(1)}_s\,C^{*}_{A,\,\text{bulk}}}{1 + \dfrac{k^{(1)}_s\,\rho_s}{M_B\,D_{pl}}\,r_s\,(1-\varepsilon_0)\,(1-X)\,y}, \qquad \text{for } 1^{\text{st}} \text{ order reaction.} \tag{4.76}$$

Because of the the high non linearity of model a numerical method is needed to find a solution. For this reason it is useful to convert the previous equations in dimensionless form. For this purpose, the following dimensionless variables are considered

$$a_0 = \frac{r_0}{M_0}, \qquad \eta_s = \frac{r_s}{M_0}, \qquad \eta_p = \frac{r_p}{M_0}, \tag{4.77}$$

and

$$\beta = \frac{k^{(1)}_s\,\rho_s\,M_0\,(1-\varepsilon_0)}{M_B\,D_{pl}}, \tag{4.78}$$

$$\hat{t} = \frac{k^{(0)}_s}{M_0}\,t = \frac{t}{\tau}, \tag{4.79}$$

$$\hat{C}_A = \frac{C_A - C_{A,eq}}{C_{A,\,\text{bulk}} - C_{A,eq}} = \frac{C^{*}_A}{C^{*}_{A,\,\text{bulk}}}, \tag{4.80}$$

where $C_A = \hat{C}_A\,(C_{A,\,\text{bulk}} - C_{A,eq}) + C_{A,eq}$. Differentiating Eq. (4.80) gives

$$d\hat{C}_A = \frac{1}{C^{*}_{A,\,\text{bulk}}}\,dC_A. \tag{4.81}$$

Consequently, the RPM for the carbonation reaction on the basis of the previous equations become:

Zero order reaction:

$$\hat{C}_{A,\,\mathrm{int}} = 1 - \frac{k_s^{(0)}}{k_s^{(1)}} \frac{\beta}{(1-\varepsilon_0)\, C^*_{A,\,\mathrm{bulk}}} \eta_s \ln\left(\frac{\eta_s}{\eta_p}\right), \tag{4.82}$$

$$\frac{\partial \eta_s}{\partial \hat{t}} = 1, \tag{4.83}$$

Eqs. (3.171), (3.173) and (3.178). (4.84)

First order reaction:

$$\hat{C}_{A,\,\mathrm{int}} = \frac{1}{1 + \dfrac{\beta}{(1-\varepsilon_0)} \eta_s \ln\left(\dfrac{\eta_s}{\eta_p}\right)}, \tag{4.85}$$

$$\frac{\partial \eta_s}{\partial \hat{t}} = \frac{C^*_{A,\,\mathrm{bulk}}\, k_s^{(1)}/k_s^{(0)}}{1 + \beta\, \eta_s\, y\, (1-X)}, \tag{4.86}$$

Eqs. (3.171), (3.173) and (3.178). (4.87)

The zero order kinetic constant $k_s^{(0)}$ is clearly related with the first order kinetic constant $k_s^{(1)}$ by $C_{A,c}$ through the following relation

$$k_s^{(0)} = k_s^{(1)}\, C_{A,c}, \tag{4.88}$$

where $C_{A,c}$ is the corresponding CO_2 concentration of the 10 kPa that is the transition CO_2 partial pressure, according to Sun et al. [59]. Assuming the ideal gas behavior of the gaseous reactant, $C_{A,c} = 10\,\mathrm{kPa}/\left(R_{\mathrm{gas}}\, T\right)$. Consequently, the condition on the CO_2 partial pressure according to Eqs. (4.28) and (4.29) changes into a concentration conditions:

$$C^*_{A,\,\mathrm{int}} \gtreqless C_{A,c}, \tag{4.89}$$

and dividing both the sides of Eq. (4.89) by $C^*_{A,\,\mathrm{bulk}}$,

$$\hat{C}^*_{A,\,\mathrm{int}} \gtreqless \check{C}_{A,c}, \tag{4.90}$$

where

$$\check{C}_{A,c} = \frac{C_{A,c}}{C^*_{A,\,\mathrm{bulk}}}. \tag{4.91}$$

As explained in § 3.6.2, when the pore size becomes small than $a_{0,\,\mathrm{min}}$, no reaction occurs and the pore is retained to be totally closed.

Pore length size distribution is discretized into nr computational grid points following the NUMOL[8] procedure. Consequently, Eqs. (4.82) and (4.83) or Eqs. (4.85) and (4.86) must be computed for each grid point. Such approach allows to build a set of $2 \times nr$ ODEs, that can be solved with a MATLAB® ODE solver. Algorithm 1 shows the procedure for the assembling of

[8] The Numerical Method of Lines.

flag = 0
X = Eq. (3.173)
y = Eq. (3.178)
for $i = 1 : nr$ **do**
  if flag = 0 **then**
    $\hat{C}_{A,\,\mathrm{int}}$ = Eq. (4.82)
  else
    $\hat{C}_{A,\,\mathrm{int}}$ = Eq. (4.86)
  end if
  if flag = 0 **then**
    $\partial\eta_s/\partial\hat{t}(i)$ = Eq. (4.83)
  else
    $\partial\eta_s/\partial\hat{t}(i)$ = Eq. (4.86)
  end if
  $\partial\eta_p/\partial\hat{t}(i)$ = Eq. (3.171)
  if $\eta_p(i) \leq 0.025$ **then**
    $\partial\eta_s/\partial\hat{t}(i) = 0$
    $\partial\eta_p/\partial\hat{t}(i) = 0$
  end if
  if $\hat{C}_{A,\,\mathrm{int}} > \check{C}_{A,\,c}$ **then**
    flag = 0
  else
    flag = 1
  end if
end for

Algorithm 1: Implementation of the RPM with equilibrium concentration and reaction switch from zero to first order.

the ODEs system.

4.6 Comparison with experimental data

Several literature contributions were presented in § 4.3, and each of them studied the carbonation reaction in specific controlling regimes. None of them was able to develop a model which can simulate the whole experimental conversion-time curve and which is capable to describe the transition between the two regimes (kinetic and product layer diffusion regime) except Sun et al.Ȯnly Sun et al. [58] predicted the whole behavior of the carbonation reaction in terms of conversion-time curve. However, some important assumptions were made by Sun et al. [58], namely, the pore size distributions were discretized and all the physical resistances were neglected (external, inter-particle and intra-particle resistances). Moreover, they obtained a nice agreement with their experimental data only for extremely long time scale (namely 2000 s) and no details about the initial kinetic regime were provided.

In order make a comparison of the simulation results of the RPM proposed in this chapter with the experimental data, TGA tests obtained from the DynTHERM MP-ST by RUBOTERM

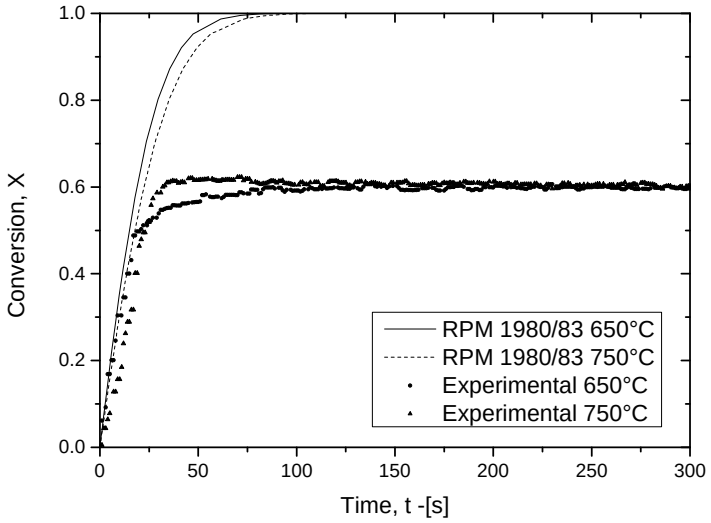

Figure 4.4: Comparison of experimental results with RPM 1980/1983 with a zero order kinetics ($\psi = 1.48$). Experimental data were both obtained at 5 bar and 100 % of CO_2.

GMBH were considered. These tests were performed using 100 % of carbon dioxide with a total pressure of 5 bar. From Fig. 2.2 or Eq. (2.2) it is easy to understand that $(p_{CO_2} - p_{CO_2,eq})$ is much higher than 10 kPa at this pressure. In this way the carbonation reaction always follows a zero order kinetic rate (assuming that all the external resistances and inter/intra-particle diffusion were negligible). Fig. 4.4 shows the comparison between the experimental data and the RPM 1980/83 respectively at 650 °C and 750 °C. Only the kinetic zone is sufficiently accurate. Fig. 4.4 demonstrates that the RPM 1980/83 (Bhatia and Pelmutter [11, 14]) is not consistent with Eq. (3.105) which predicts a conversion below 100 %. Moreover, the sharp transition between the two regimes (kinetics and product layer diffusion regime) is not represented.

These model simplify the structural changes (in terms of porosity ans specific surface area) that occur during the reaction even if a first order kinetic rate is considered. Fig. 4.5 shows the conversion-time curves for the carbonation reaction using RPM 1980 and RPM 1983 and considering a first order carbonation reaction. Both Figs. 4.5a and 4.5b do not follow Eq. (3.105), but the conversion-time curves reach the complete conversion. This means that pore closure is not contemplated in these models. Moreover, Figs. 4.5a and 4.5b appear to overestimate the product layer diffusion even at high temperature, especially for low total pressure. In fact, this can be easily showed by plotting $F_\psi(X)$ vs X, following Eq. (3.97). Fig. 4.6 shows that the product layer diffusion term (that is $F_\psi(X)$ for RPM 1980) becomes large for $X \to 1$ and increases of 2-3 orders of magnitude as conversion progresses. However, as reported by Figs. 4.6a and 4.6b the product layer diffusion process is smaller than the reaction when the temperature is below 650 °C[9]. The kinetic constant and the product layer diffusivity are estimated following Eqs. (4.29) and (4.40) respectively(Sun et al. [59, 58]).

Tab. 4.3 reports the RPMs (1980 and 1983 [11, 14]) parameters of each sample (Tab. 4.2 and

[9]The parameter β is an index of the ratio between the carbonation intrinsic kinetics and the product layer diffusion process.

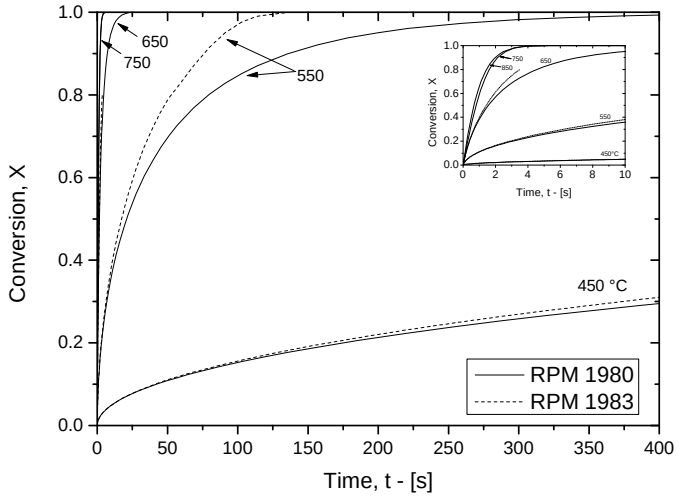

(a) *Total pressure,* $P = 1\,\text{bar}$.

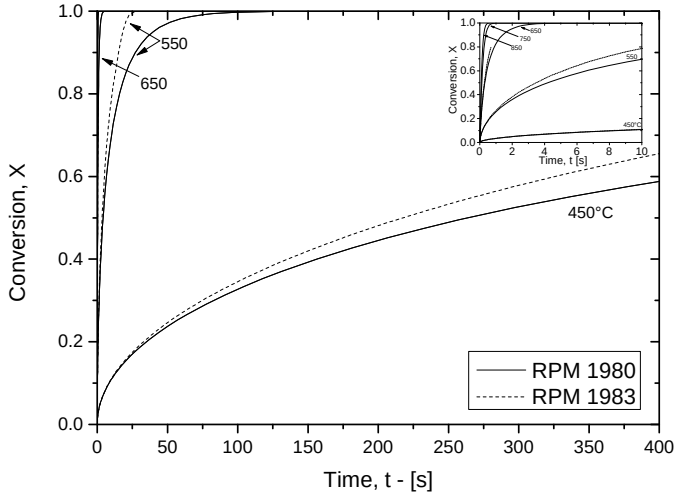

(b) *Total pressure,* $P = 5\,\text{bar}$.

Figure 4.5: Comparison of RPM 1980 with RPM 1983 for different temperatures, considering a first order kinetic rate for the carbonation reaction.

Fig. 4.3). These are the CaO samples that were typically used for the carbonation reaction. For these sample the N_2 adsorption was performed and the structural parameters were calculated (ψ and σ). Clearly, the assumption of $\sigma \to \infty$[10] reported in § 3.4.1 and suggested by Bhatia and Pelmutter [11] is largely satisfied, so that the external particle surface is negligible respect to the internal surface.

Since the RPM developed by Bhatia and Pelmutter (in their works [11], [12] and [14]) in 1980 and 1983 are not able to represent the conversion-time of the carbonation reaction, a more detailed model for non-catalytic gas-solid reactions was considered. Specifically, as reported by Sun et al. [58] the conversion of the carbonation reaction is strictly related to the pore size, so that the conversion consists of a number of contributors, and each of them is related to a specific pore size. Indeed, only an analysis accounting for the pore closure phenomena or the

[10] The particle diameter of CaO is 150 µm.

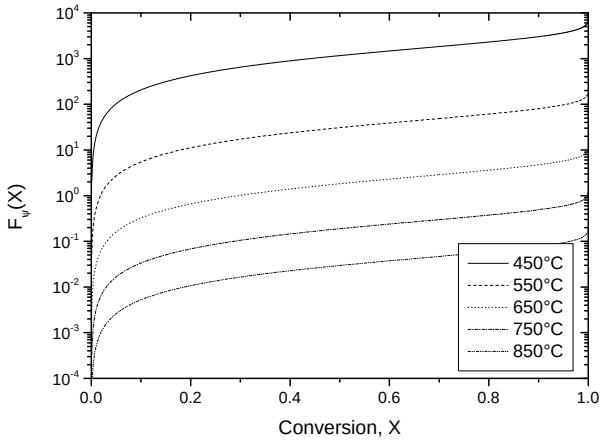

(a) $F_\psi(X)$.

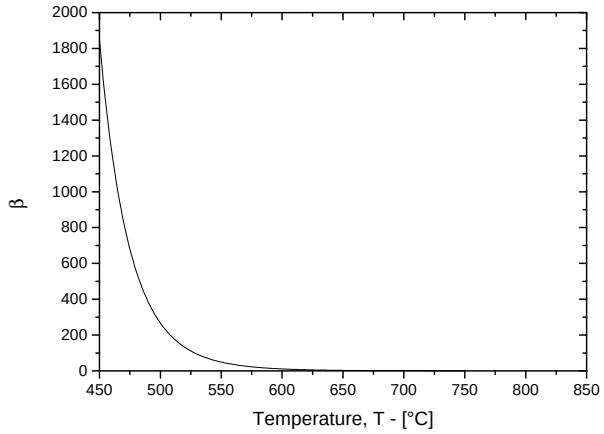

(b) β *vs* T.

Figure 4.6: Product layer diffusion contributors ($F_\psi(X)$ refers to RPM 1980).

different product layer thickness between small pores and large pores is required. In fact, it is reasonable consider that smaller pores contribute to more surface area, so that they are more reactive than larger ones (according to Sun et al. [58]). Moreover, as reported in Chapter 2 the BJH analysis on calcined samples showed that pores follow a probability distribution inside the CaO particle. Consequently, the RPM 1980/83 cannot be represent the local conversion of the carbonation reaction because all the pore-size dependent properties are mediated through the structural parameter ψ.

According to these reasons, the attention was focused on the pore-size dependent pore models as the RPM developed by by Bhatia [10] and Sotirchos et al. [57] in 1985. Following the development presented in § 4.5, the model was applied to the carbonation reaction including the equilibrium conditions and the reaction rate switch from zero to first order.

Unfortunately, the BET/BJH analysis were not available for the TGA tests performed using Dyn-THERM MP-ST. Therefore, a parameter estimation was performed in order to match the experimental TGA data. For the comparison of the simulation results with the experimental data, two TGA tests were considered at two different temperatures, respectively at

Table 4.3: Specific surface and structural parameters of RPMs [11, 14] for the calcined samples listed in Tab. 4.2.

Sample	S_g $[\mathrm{m^2\,g^{-1}}]$	ψ [–]	σ [–]
800 °C, 120 min	21.02	1.29	7798.51
900 °C, 5 min	15.60	4.65	7054.61
900 °C, 10 min	15.31	4.08	4916.83
900 °C, 15 min	15.40	3.37	5144.71
900 °C, 30 min	14.00	6.42	4281.33
900 °C, 180 min	8.46	2.02	4936.89

650 °C and 750 °C. Both tests were performed with a total pressure of 5 bar and with pure carbon dioxide. For the TGA result performed at 650 °C the following parameters for the pore size distribution were chosen: $\mu_{N_0} = 4.939\,\text{Å}$, $\sigma_{N_0} = 0.285$ and $\epsilon_0 = b_{LN}^{(o)} = 0.424$. For these values the corresponding mean pore radius, log-normal variance and specific surface are: $M_0 = 145.38\,\text{Å}$, $V_0 = 1794.82$ and $S_g = 37.30\,\mathrm{m^2\,g^{-1}}$. Whereas, for the experimental results at 750 °C: $\mu_{N_0} = 5.432\,\text{Å}$, $\sigma_{N_0} = 0.285$ and $\epsilon_0 = b_{LN}^{(o)} = 0.424$, which correspond to the following quantities: $M_0 = 250.28\,\text{Å}$, $V_0 = 5319.57$ and $S_g = 21.67\,\mathrm{m^2\,g^{-1}}$. These porosity values seem to be small respect to the experimental results (Tab. 4.2) which shows a particle porosity never below 0.47. However, the selected values well represented the final conversion and seem to be consistent with Eq. (3.105). On the other hand the calculated specific surface is larger respect the experimental data listed in Tab. 4.3.

Fig. 4.7 shows the comparison of the simulation results with the TGA data. For this purpose Eqs. (4.28), (4.29) and (4.40) were considered for the kinetic parameter and product layer diffusivity estimation, using $A_k^{(1)} = 1.54 \times 10^{-12}\,\mathrm{m\,s^{-1}\,Pa^{-1}}$ ($A_k^{(0)} = A_k^{(1)} \times 10\,\mathrm{kPa}$) namely, about half of the value of Sun et al. [59] (Eq. (4.29)). Activation energy and product layer diffusivity were taken from Sun et al. [59] and [58].

The results showed in Fig. 4.7 are extremely interesting: the modified RPM 1985 is able to represent the whole conversion-time curve of the carbonation reaction including the sharp transition between the two regimes. It is remarkable that the TGA data are accurately predicted both at short and at long times. Moreover, such agreement, at low degree of conversions, was never presented in literature. Particularly, at 650 °C (Fig. 4.7a) the simulation results are in agreement with the experimental data for the first instants of reactions. The results at 750 °C (Fig. 4.7b) present a lower degree of accuracy. However this behavior is suspected to be due to high temperature, which may increase the sources of error of the TGA analysis.

According to Eq. (3.105), the conversion of CaO is strictly related to ε_0. Figs. 4.7a and 4.7b show that the particle porosity is slightly overestimated because the final predicted conversions do not exact match the experimental results. The mismatch may be due to the assumptions of negligible external resistances and inter/intra-particle diffusion. Fig. 4.8 shows the porosity profile during the reaction. The two porosity-time curves are quite similar, likely because of the similarity between the two pore size distributions (they differ only for μ_{N_0}).

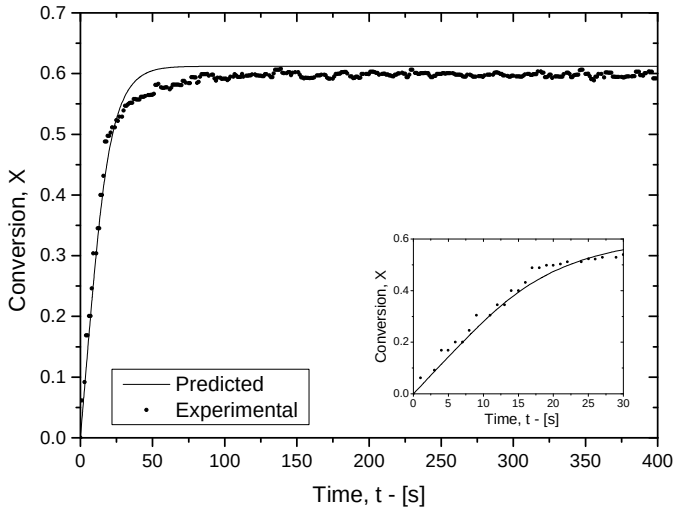

(a) $T = 650\,^{\circ}\mathrm{C}$.

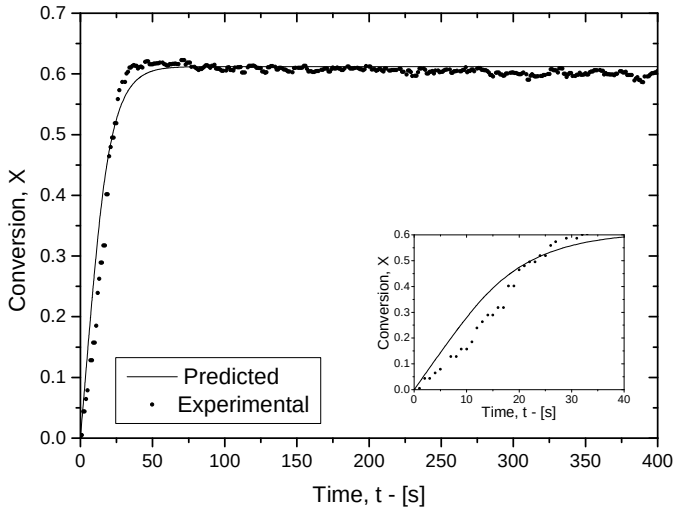

(b) $T = 750\,^{\circ}\mathrm{C}$.

Figure 4.7: Comparison of the modified RPM 1985 with experimental results. TGA tests refer to 5 bar and pure CO_2.

Fig. 4.9 shows the differential pore size distributions (non-overlapped case) for each case which shows that the porosity is progressively reduced as reaction takes place. Specifically, most of the porosity is lost in the kinetic control regime that occur in the first $40 \div 50$ s. Furthermore, the pore and reaction surface areas are quite similar in the two cases (Fig. 4.10). Moreover, according to the small activation energy of the carbonation reaction, the temperature effect is very low and it becomes significant only at low temperatures.

Fig. 4.11 shows the total pore and reaction surface evolution with conversion. The pore surface does not reduces to zero because the larger pores do not totally close. Clearly, when this situation occurs, the reactivity of the solid is close to zero because the smaller pores contribute to the majority of particle reactivity. As reaction progresses, each reaction surface increases up to intersect with another reaction surface. The continuous overlapping of the reaction surfaces

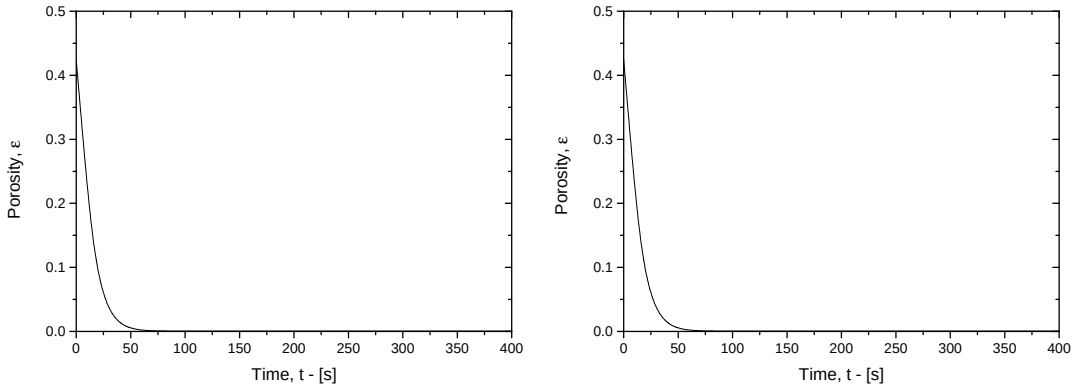

(a) $T = 650\,^{\circ}\mathrm{C}$. **(b)** $T = 750\,^{\circ}\mathrm{C}$.

Figure 4.8: Predicted porosity by the modified RPM 1985.

leads to a continuous loss of the reaction surface (Figs. 4.11c and 4.11d) and, consequently, of the solid reactivity.

Finally, Fig. 4.12 shows the CO_2 concentration profiles at the reaction front. The abrupt change in slope of $\hat{C}_{A\,\mathrm{int}}$ is due to pore closure. When pore closure occurs $\hat{C}_{A\,\mathrm{int}}$ becomes zero according to Eq. (4.85) and this appear to be in contrast with concentration predictions reported in Fig. 4.12. This is not exactly true because the numerical method represents the pore closure by imposing $\eta_p \leq 0.025$, in order to avoid stiffness. In this way, $\hat{C}_{A\,\mathrm{int}}$ does not become zero but remains to a constant value because of η_p, according to Eqs. (4.82) and (4.85).
Fig. 4.13 shows the prediction of CO_2 concentration profiles at each reaction front after imposing a total pressure of 1 bar and 5 % of carbon dioxide in mole. Considering the smaller pores, Fig. 4.13 shows that the reaction front remains always in the zero order zone up to pore closure, when CO_2 concentration remains constant. On the other hand, the larger pores start to react with a zero order kinetic rate and when the driving force ($\hat{C}^*_{A,\,\mathrm{int}}$) becomes lower than the transition CO_2 concentration, the reaction order switches from zero to first order. This change in mechanism is represented by Eqs. (4.82) and (4.85). The switch of the reaction order is represented by the progressively decrease of the reactant concentration at the reaction surface that occurs until the pore closure, as shown in Fig. 4.13.

4.7 Discussion

In this chapter a modified RPM was presented and applied to the carbonation reaction. First, starting from the typical operative conditions (temperature, pressure and CO_2 concentration) of the carbonation, a thermodynamic study was made in order to predict the compressibility factor of pure carbon dioxide and of the CO_2-N_2 mixtures at different CO_2 concentrations. The results show that both pure species and mixtures can retained to be ideal up to 15 bar. The temperature effect is not significant and below 15 bar the ideal behavior is always verified.

Afterwards, the more relevant literature contributions on the carbonation reaction were presented. Specifically, the attention was focused on the carbonation reaction kinetic models, the

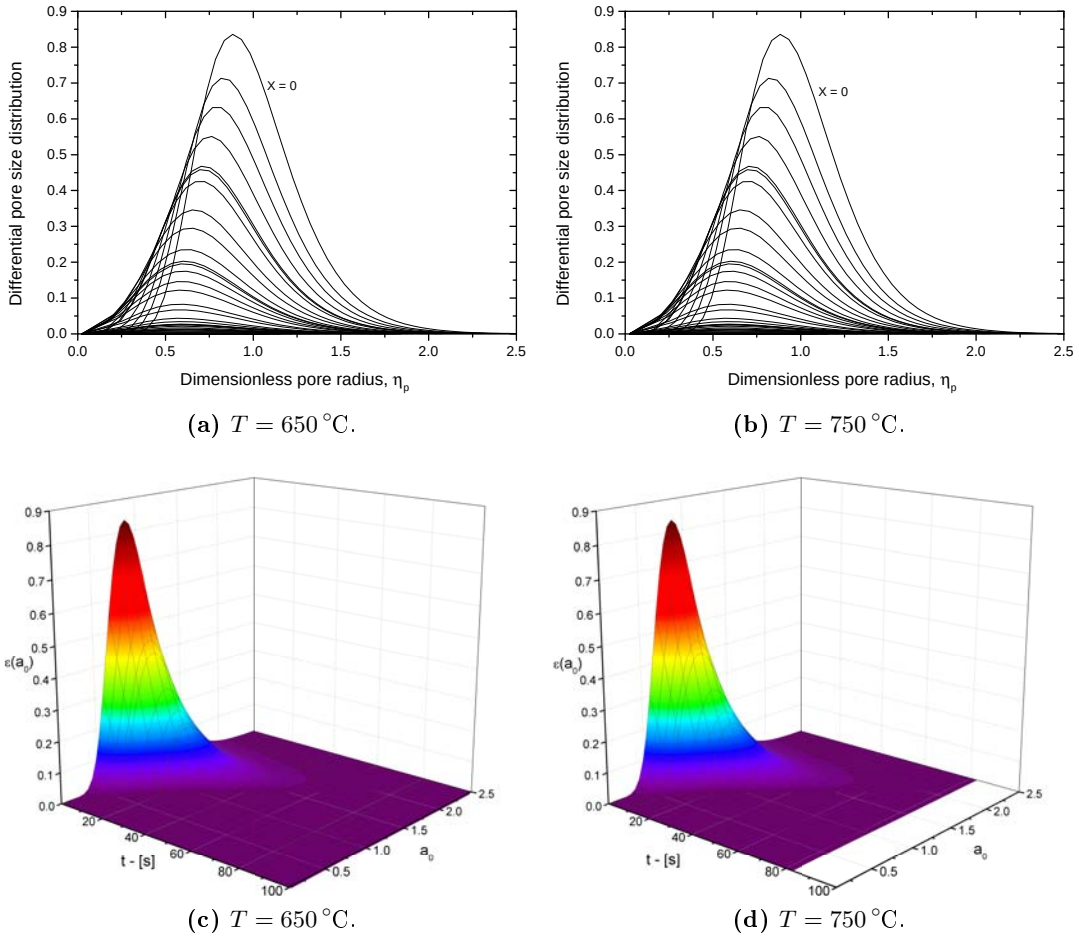

(a) $T = 650\,^{\circ}\mathrm{C}$. **(b)** $T = 750\,^{\circ}\mathrm{C}$.

(c) $T = 650\,^{\circ}\mathrm{C}$. **(d)** $T = 750\,^{\circ}\mathrm{C}$.

Figure 4.9: Predicted pore size distributions.

parameters estimation (intrinsic kinetics and product layer diffusivity) and the reaction mechanism. For this work of thesis the most significant contributions are due to Sun et al. [59, 58]. In fact, Sun et al. [59] first proposed a kinetic reaction rate that switches from zero to first order depending on the CO_2 partial pressure at the reaction front.
The kinetic of the carbonation reaction presents several features that are related to several mechanism that simultaneously occurs:

1. the carbonation switches the reaction order from first to zero order depending on the CO_2 concentration at the reaction surface;

2. since it is a reversible reaction the equilibrium concentration is to be included in the kinetics equation;

3. the reaction rate shows two regimes: the kinetic and the product layer diffusion;

4. the transition between the two regime is sharp;

5. because the molar volume of the product layer is larger than the molar volume of the reactant, pore closure occurs.

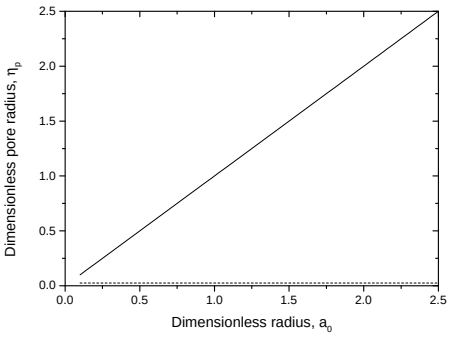

(a) $T = 650\,^{\circ}\mathrm{C}$.

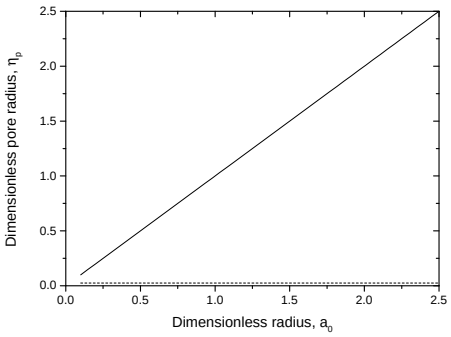

(b) $T = 750\,^{\circ}\mathrm{C}$.

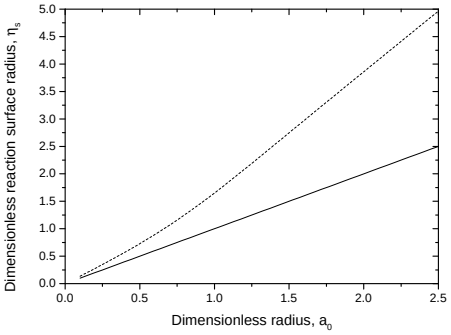

(c) $T = 650\,^{\circ}\mathrm{C}$.

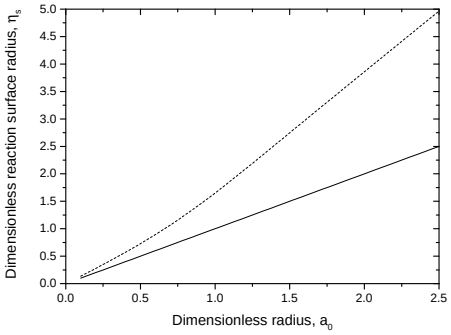

(d) $T = 750\,^{\circ}\mathrm{C}$.

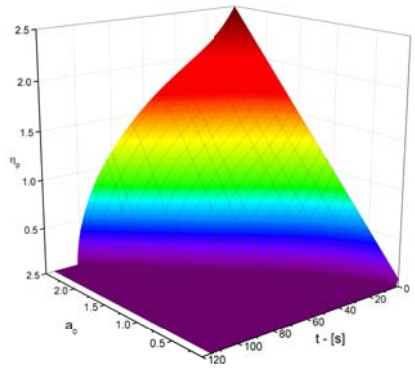

(e) $T = 650\,^{\circ}\mathrm{C}$.

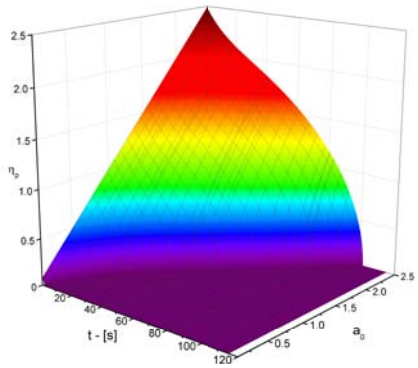

(f) $T = 750\,^{\circ}\mathrm{C}$.

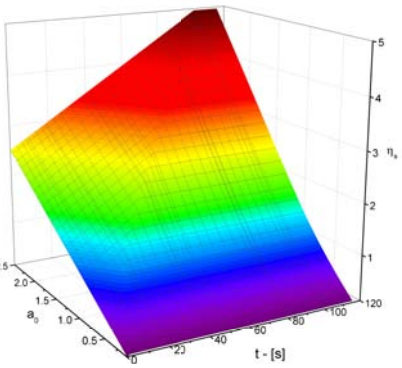

(g) $T = 650\,^{\circ}\mathrm{C}$.

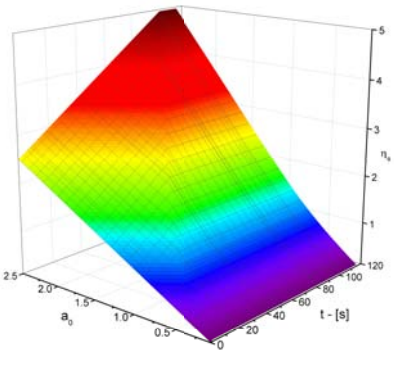

(h) $T = 750\,^{\circ}\mathrm{C}$.

Figure 4.10: Predicted dimensionless pore and reaction surfaces. The dotted lines represents the pore and the reaction surface radii at the final time of the reaction.

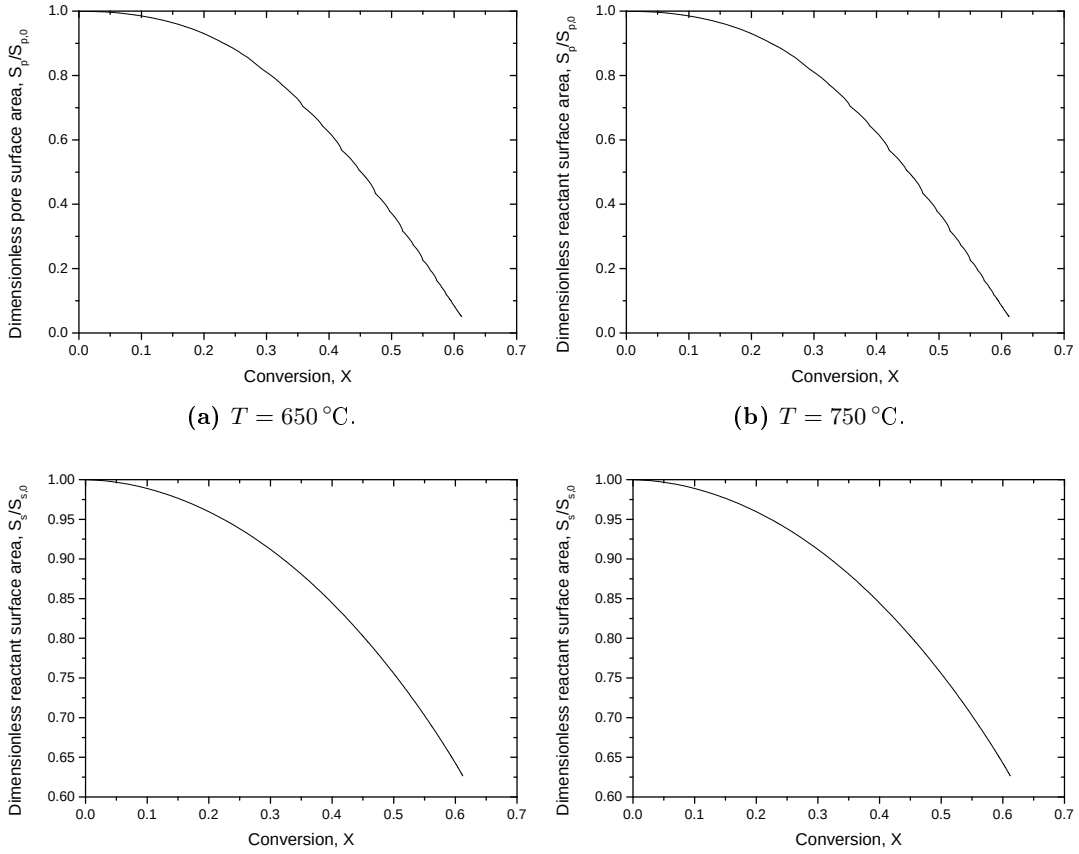

(a) $T = 650\,^{\circ}\mathrm{C}$. **(b)** $T = 750\,^{\circ}\mathrm{C}$.

(c) $T = 650\,^{\circ}\mathrm{C}$. **(d)** $T = 750\,^{\circ}\mathrm{C}$.

Figure 4.11: Total pore and reaction surface evolution with conversion.

All the proposed models for the carbonation reaction do not represent the whole experimental conversion-time curve except for the model of Sun et al. [59, 58]. However, Sun et al. considered a discrete pore size that may lead to unphysical behavior when the number of classes are low.

With the aim to apply a random pore model to the carbonation reaction, the pore size distribution must be known. Therefore, the pore size distribution was represented with a continuous distribution (log-normal distribution). In this way, three parameters were identified in order to completely characterize the porosity distribution. A fitting procedure allowed to estimate such parameters. However, even if the fitting procedure shows a nice agreement an improved analysis of the continuous pore size distributions could be obtained using a more detailed function in terms of shape parameters.

After the pore size estimation, the RPM (Bhatia [10] and Sotirchos et al. [57], 1985) presented in § 3.6 was modified in order to account for the continuous pore size distribution, the equilibrium concentration and the reaction switch. Consequently, a new random pore model was presented and applied to the TGA experimental results, that differs from the model of Sun et al. [59, 58] to the use of a continuous pore size distribution. In the discrete approach the number of classes may affect the accuracy of the predictions and leads to unphysical results.

To simplify the analysis, the external resistances and the inter/intra-particle diffusion were ne-

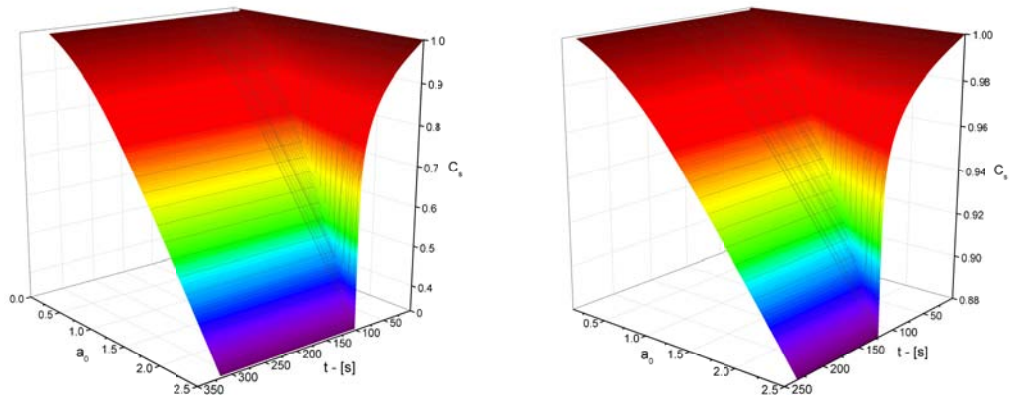

(a) $T = 650\,°C$. **(b)** $T = 750\,°C$.

Figure 4.12: Predicted CO_2 concentrations at reaction front. C_s is the dimensionless CO_2 concentration at the reaction surface, namely $\hat{C}_{A\,\mathrm{int}}$.

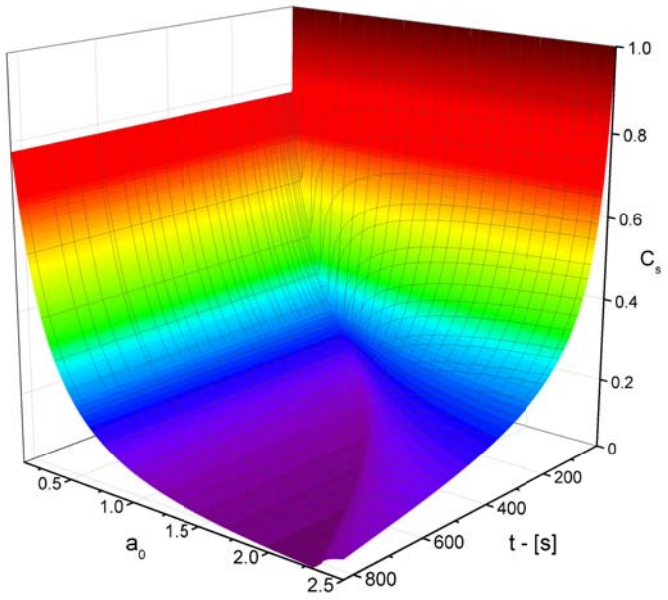

Figure 4.13: Predicted CO_2 concentrations at reaction front when the temperature id 650 °C, the total pressure is $P = 1$ bar and the molar fraction of CO_2 is 0.05.

glected. The comparison of the previous models (RPM 1980/83) with TGA tests shows that no one was able to represent the whole conversion-time behavior of the carbonation reaction. Specifically, they neglected the smaller pore properties that are retained to be essential to represent the carbonation behavior (pore closure).

Afterwards, the RPM (1985) developed in § 4.5 was applied to the TGA data. The results show that the modified RPM has an excellent versatility once the pore size distribution is known. Furthermore, the degree of detail appears to be very high especially at the beginning of the reaction. Such a degree of accuracy was never be achieved in the literature on the CO_2 carbonation. In fact, all the papers in the literature consider a longer time scale with respect to this work. In this way, all the initial details on the kinetic regime are lost and the whole fitting results appear

to be nice even if the beginning of the reaction and the transition between the kinetic to the product layer diffusion regime were not well simulated.
Once the sample pore size distribution is known and the kinetic and product layer diffusion parameters are available, such model is able to predict the whole conversion-time curve of the carbonation reaction.
However, the simulation results were obtained using structural parameters that were not be estimated from experimental data (as N_2 adsorption). Instead, these parameters were selected in order to represent the experimental results on the basis of the structural parameters of similar samples. Thus, the model must be tested with TGA data whose structural parameters are experimentally known, in order to test the predictive capacity of the proposed model.

Chapter 5

Influence of the Intra-Particle Diffusion on the Carbonation Reaction

This chapter is a continuation of Chapter 4, where a new RPM was developed and applied to the carbonation reaction, following the approach of Bhatia [10] and Sotirchos et al. [57]. In Chapter 4 all the external resistances were neglected, instead in this chapter the intra-particle diffusion is accounted for. For this purpose, a new model was developed in order to include the simultaneous CO_2 diffusion in porous CaO particles and a non-catalytic gas-solid reaction, such as the carbonation. This study is relevant because no one in the literature had ever included the intra-particle diffusion to the carbonation reaction whose reaction kinetics is modeled with the RPM of Bhatia [10] and Sotirchos et al. [57].

5.1 Introduction

The previous chapter demonstrates that the RPM by Bhatia [10] and Sotirchos [57] applied to the carbonation reaction is capable to reproduce the conversion-time curve of the reaction. Specifically, the model well represents the sudden change from the first rapid period to the slower second stage. This is very interesting because all the older structural models are not able to represent the whole sigmoid shape of the conversion curves and only the limiting regimes were represented. However, up to this chapter the RPM does not contemplate any type of external resistances or inter/intra-particle diffusion.

The intra-particle diffusion effects increases when large particle size is used, when the kinetics of the gas-solid reaction is very fast compared to the diffusion inside the particle, when the CO_2 partial pressure is slow and when the mean pore radius is small. In these cases, the model must account for the intra-particle diffusion in order to represents the diffusional effects that may arises due to the porous particle.

For this purpose a local material balance on CO_2 is needed. However, since the gaseous reactant must diffuse inside a porous system (as the porous CaO particle), the material balance on carbon dioxide must consider the particle porosity. Moreover, the diffusivity coefficient should consider the several obstacles present in the porous particle, such as pores, pore intersection, pore section

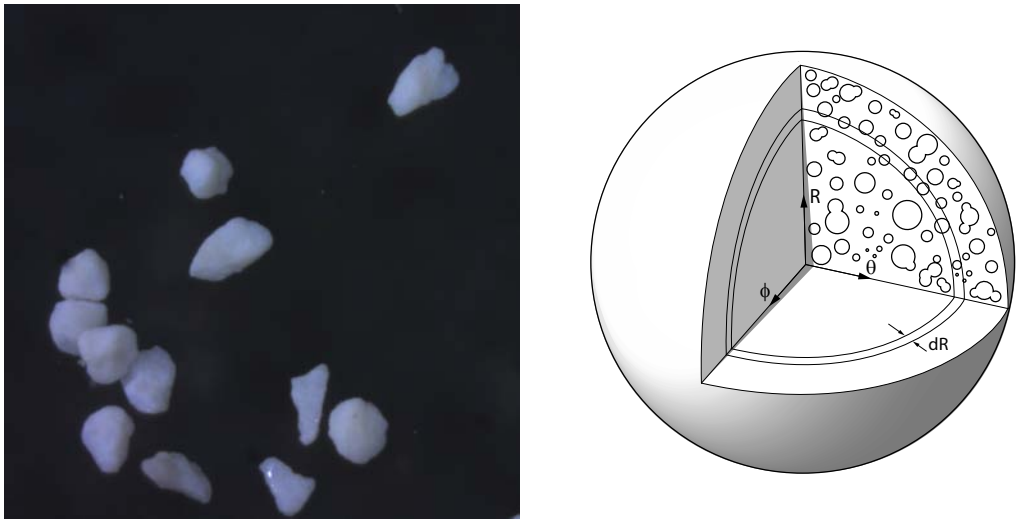

(a) *CaO particles of* 150 µm *in diameter.* **(b)** *Ideal representation.*

Figure 5.1: Real calcium oxide particles and idealized representation of one particle.

shrinkage, etc. Therefore, an effective diffusivity must be employed.
Finally, a numerical method is necessary to solve such a model, because the local material balance of CO_2 is governed by a partial difference equation (PDE).

5.2 Governing equations

The mathematical analysis of the intra-particle diffusion considers the simultaneous reaction and diffusion inside the porous network of a calcium oxide particle. The model is based on several assumptions listed as follows:

1. each porous CaO particle is spherical with a particle radius R_0, as shown in Fig. 5.1;
2. the whole process is isothermal;
3. the diffusion of the gaseous reactant within the porous structure is represented by the Fick's first law;
4. the gas solid reaction, namely the carbonation, is reversible and switches from zero order to first order kinetics depending on the driving force of the process that is $\left(C_{\mathrm{CO}_2} - C_{\mathrm{CO}_2,eq}\right)$;
5. the pore size distribution is homogeneous inside each particle and each differential annular shell has the same porous pattern in term of pore size distribution;
6. a spherical coordinates frame is assumed (according to Fig. 5.1b) and the particle is assumed to be isotropic.

On the basis of the previous assumptions, the local balance of species A in spherical coordinates is

$$\frac{\partial \left(C_{A,p}\, \varepsilon_p\right)}{\partial t} = \frac{1}{R^2}\, \frac{\partial}{\partial R} \left(R^2\, \mathscr{D}_{\mathrm{eff}}\, \frac{\partial C_{A,p}}{\partial R} \right) - \frac{dX}{dt}\, \frac{\rho_s\, (1 - \varepsilon_{p,0})}{M_B}, \tag{5.1}$$

where $C_{A,p}(t,R)$ is the concentration of species A inside the particle, $\varepsilon_p(t,R)$ is the local particle porosity, ε_{p_0} is the particle porosity at the initial time ($t=0$), $\mathscr{D}_{\text{eff}}$ is the effective diffusivity of CO_2 within the porous medium according to Satterfield [51], and dX/dt is the local reaction rate following the RPM by Bhatia [10] and Sotirchos [57]. Eq (5.1) is a second order partial differential equation (PDE) and once integrated gives the concentration profile of A inside the particle as time progresses. Consequently, a local reaction conversion is estimated for each differential annular shell and the overall conversion of the whole particle is the mean of all the local conversions.
Since Eq (5.1) is a second order PDE, an initial condition and a two boundary conditions are required. The initial condition imposes a concentration at $t=0$ for each point of the particle. Since no CO_2 is present before the reaction, the initial condition states that

$$C_{A,p}(0,R) = 0 \qquad \forall\, R \in [0,\, R_0]\,. \tag{5.2}$$

The two boundary conditions for Eq (5.1) are

$$C_{A,p}(t,R_0) = C^{\text{s}}_{A,p} = C_{A,\,\text{bulk}} \quad \text{at} \quad R = R_0, \tag{5.3}$$

$$\frac{\partial C_{A,p}}{\partial R} = 0 \quad \text{at} \quad R = 0. \tag{5.4}$$

Eqs (5.3) and (5.4) are respectively a Dirichlet and Neumann boundary conditions. Eq (5.3) assumes that the external surface of the particle is exposed to a finite concentration value that is $C^{\text{s}}_{A,p}$. Assuming that the external resistance is negligible as well as the inter-particle diffusion, the particle surface concentration is equal to the bulk concentration $C^{\text{s}}_{A,p} = C_{A,\,\text{bulk}}$.
The reaction rate is modeled with the RPM Bhatia [10] and Sotirchos [57] applied to the carbonation reaction. As reported in § 4.5, the reaction rate switches from zero order to first order depending on $C_{A,p}(t,R)$. Thus, Eqs. (4.75), (4.76), (3.164), (3.157) and (3.168) must be simultaneously solved with Eq (5.1) in order to obtain the conversion-time curve for each radial point of the particle reactant. Precisely, dX/dt is obtained by deriving Eq. (3.168) with time:

$$\frac{dX}{dt} = \left[\int_0^{\infty} 2\pi\, r_s\, \frac{\partial r_s}{\partial t} l(r_0)\, dr_0\right] \frac{\exp\left[-\displaystyle\int_0^{\infty} \pi r_s^2(r_0,t)\, l(r_0)\, dr_0\right]}{1-\varepsilon_{p,0}}, \tag{5.5}$$

which is substituted into Eq (5.1).

5.3 Effective diffusivity coefficient in the porous particle

The experimental procedure reported in § 2.5.5 states that the TGA reaction chamber is heated at $450 \div 650\,^{\circ}\text{C}$ meanwhile nitrogen is continuously fluxed. When isothermal conditions are reached, the inert gas flow switches to carbon dioxide and the carbonation reaction takes place. At the switch time CO_2 diffuses inside the porous particle throughout the stagnant

nitrogen following the Fick's law, which is written in the general form:

$$\mathbf{J_{i,j}} = -\mathscr{D}_{i,j}\,\nabla C_{i,p} \tag{5.6}$$

according to Cunningham and Williams [19], where $\mathbf{J_{i,j}}$ is the molecular flux of i in j (that is CO_2 in N_2) and $\mathscr{D}_{i,j}$ is the binary molecular diffusivity. However, since the particle consists of a porous network, the pores generate wall effects that become obstacles to the diffusing molecules because the pore walls decrease the free area of the cross section and increase the diffusion path, as stated by Cunningham and Williams [19]. If the porous network is ignored a correction factor must be introduced, that accounts for the effect of the pore walls on the molecular flux. Consequently, the diffusivity $\mathscr{D}_{i,j}$ is replaced by an effective coefficient that takes the form of

$$\mathscr{D}_{i,j,\text{eff}} = \mathscr{D}_{i,j}\,Q_p, \tag{5.7}$$

where Q_p is the obstruction factor, as reported by Cunningham and Williams [19]. According to Satterfield [51], this obstruction factor is proportional to the particle porosity ε_p and inversely proportional to the particle tortuosity factor τ_p that is characteristic of the porous solid. Thus, Eq (5.7) becomes

$$\mathscr{D}_{i,j,\text{eff}} = \mathscr{D}_{i,j}\,\frac{\varepsilon_p}{\tau_p}. \tag{5.8}$$

where τ_p accounts for both varying direction of diffusion and varying pore cross section. For an accurate estimation the tortuosity factor must be determined experimentally. However, according to the model of Wakao and Smith [64]

$$\tau_p = \frac{1}{\varepsilon_p}, \tag{5.9}$$

suggesting that tortuosity varies as reaction proceeds through the porosity.

When a gas species diffuses through a porous network two characteristic lengths must considered, according to Cunningham and Williams [19]: the mean distance between two molecular collisions, called the mean free path λ, and the average distance λ_p between two neighboring pore walls (that is the average pore diameter). When $\lambda \ll \lambda_p$ the molecules inside the particle collide with other molecules. The molecules of the gaseous phase collide with molecules in the intermediate vicinity, thus, interaction is between molecules. In this way, the molecules are completely not influenced by the pore walls and the molecular diffusivity coefficient follows the classical kinetic theory of gases. The molecular diffusivity becomes the molecular diffusion coefficient $\mathscr{D}_{i,j,\text{eff}}$ as reported by Eq (5.8), according to Cunningham and Williams [19], named "bulk diffusion" following Satterfield's nomenclature [51].
Considering the opposite condition $\lambda \gg \lambda_p$[1], the probability of a molecule-molecule collision is negligible compared to that of molecule-pore wall collision. This kind of molecule-wall interaction

[1] This situation can also be expressed in term of Knudsen number, $\text{Kn} = \lambda/\lambda_p$ as reported by Cunningham and Williams [19]. In this case $\text{Kn} \gg 1$.

is called "Knudsen diffusion" and the corresponding phenomenon is called the "Knudsen regime" (Cunningham and Williams [19]). Consequently, in a multi-component mixture in the Knudsen regime a given species cannot be influenced by the other species and the diffusivity coefficient becomes $\mathscr{D}_{k,i}$ that is the Knudsen diffusivity of species i. Following Satterfield [51], the Knudsen diffusivity of species i can be evaluated with the following

$$\mathscr{D}_{k,i} = \frac{2}{3} M_0 \left(\frac{8000\, R_{\text{gas}}\, T}{\pi\, M_i} \right)^{1/2}, \tag{5.10}$$

where R_{gas} is the ideal gas constant in $\left[\text{m}^3\,\text{Pa}\,\text{K}^{-1}\,\text{mol}^{-1}\right]$, T is the system temperature in K, M_i is the molecular weight of species i and M_0 is the average pore radius expressed in m. By using these units $\mathscr{D}_{k,i}$ is in $\text{m}^2\,\text{s}^{-1}$.
Bulk diffusion occurs when the collisions of molecules with the pore walls are unimportant compared to molecular collisions between molecules. Knudsen diffusion occurs when this condition is reversed. In a given pore there is a range of molecular concentrations in which both types of collisions are important. This is the "transition" region and in this case the diffusivity coefficient is evaluated as

$$\frac{1}{\mathscr{D}_{\text{eff}}} = \frac{1}{\mathscr{D}_{k,i\,\text{eff}}} + \frac{1}{\mathscr{D}_{i,j\,\text{eff}}}, \tag{5.11}$$

where $\mathscr{D}_{\text{eff}}$ is the overall effective molecular diffusivity, following Satterfield [51] and Szekely et al. [29]. Each effective diffusion coefficient of Eq (5.11) is calculated with Eq (5.8).

The mean free path of the gaseous molecules defines the diffusion regime and, thus, the equations for the diffusion coefficient estimation. According to Bird et al. [15], the mean free path is given by

$$\lambda_i = \frac{1}{\sqrt{2}\,\pi\,\sigma_{LJ,i}^2\, n}, \tag{5.12}$$

where $\sigma_{LJ,i}$ is the "collision diameter" of species i, a Lennard-Jones parameter expressed in m, n is the number of molecules per unit of volume. Assuming ideal gas behaviour, $n = P\,N_A/(R_{\text{gas}}T)$ where N_A is the Avogadro number[2]. Eq (5.12) becomes

$$\lambda_i = \frac{k_B\, T}{\sqrt{2}\,\pi\,\sigma_{LJ,i}^2\, P}, \tag{5.13}$$

where k_B is the Boltzmann constant[3]. The Lennard-Jones parameters are reported in Tab. 5.1, where $\varepsilon_{LJ\,i}$ is a Lennard-Jones parameter that represents the energy of molecular interaction of the species i. Tab. 5.2 shows the mean free path for carbon dioxide at various temperature and pressure. Considering that the mean pore diameter is around $30 \div 80\,\text{nm}$, at room pressure λ_i is slightly larger than $\lambda_p = 2\,M_0$ and, thus, a first approximation of $\mathscr{D}_{\text{eff}}$ may consider only the Knudsen diffusion. However, as pressure increases, intermediate regimes take place up to reach

[2]The Avogadro number is $6.0221 \times 10^{23}\,\text{mol}^{-1}$.
[3]The Boltzmann constant is $1.3806 \times 10^{-23}\,\text{J}\,\text{K}^{-1}$.

Table 5.1: Lennard-Jones parameters for carbon dioxide and nitrogen. Source Bird et al. [15].

Species	σ_{LJ} [Å]	ε_{LJ}/k_B [K]	MW [g mol^{-1}]
CO_2	3.996	190	44.01
N_2	3.667	99.8	28.01

Table 5.2: Mean free path in nm of carbon dioxide for various temperature and pressure.

	P - [atm]					
	1	2	5	10	20	50
T - [°C]						
450	138.89	69.44	27.78	13.89	6.94	2.78
500	148.49	74.24	29.70	14.85	7.42	2.97
550	158.09	79.05	31.62	15.81	7.90	3.16
600	167.69	83.85	33.54	16.77	8.38	3.35
650	177.30	88.65	35.46	17.73	8.86	3.55
700	186.90	93.45	37.38	18.69	9.35	3.74
750	196.50	98.25	39.30	19.65	9.83	3.93

the conditions of bulk diffusion regime. Therefore, in order to obtain a more accurate diffusion coefficient estimation, Eq. (5.11) must be considered.
According to Eqs. (5.8), (5.9) and (5.11), the effective diffusion coefficient may be calculated as

$$\mathscr{D}_{\text{eff}} = \varepsilon_p^2 \, \mathscr{D}_{\text{global}} \tag{5.14}$$

where

$$\frac{1}{\mathscr{D}_{\text{global}}} = \frac{1}{\mathscr{D}_{k,i}} + \frac{1}{\mathscr{D}_{i,j}}. \tag{5.15}$$

In this work the bulk diffusivity is calculated using the Chapman and Enskog equation according to Poling et al. [47].

5.4 Model development

Eq. (5.1) is the governing equation that describes the concentration profile of the gaseous reactant due to the molecular diffusion inside the porous spherical particle meanwhile the carbonation reaction occurs. However, Eq. (5.1) states that the $C_{A,p}(t, R)$ function can be obtained only if a suitable function of the porosity with time $\varepsilon_p(t)$ is known. In fact, differentiating the left hand size of Eq. (5.1), gives

$$\frac{\partial \left(C_{A,p} \, \varepsilon_p \right)}{\partial t} = \varepsilon_p \, \frac{\partial C_{A,p}}{\partial t} + C_{A,p} \, \frac{d\varepsilon_p}{dt}, \tag{5.16}$$

where $d\varepsilon_p/dt$ is unknown. Such relation is obtained considering Eq. (3.105) that relates the particle porosity to the reaction conversion. Thus, by deriving Eq. (3.105) with time, the following differential equation is obtained:

$$\frac{d\varepsilon_p}{dt} = (1 - Z)(1 - \varepsilon_{p,0})\,\frac{dX}{dt}, \tag{5.17}$$

which is the sought for porosity-time function. Substituting Eq. (5.17) into Eq. (5.1), the local balance of species A becomes

$$\frac{\partial C_{A,p}}{\partial t} = \frac{1}{\varepsilon_p\, R^2}\,\frac{\partial}{\partial R}\left(R^2\,\mathscr{D}_{\text{eff}}\,\frac{\partial C_{A,p}}{\partial R}\right) - \frac{dX}{dt}\,(1 - \varepsilon_{p,0})\left[\frac{\rho_s}{M_B} + C_{A,p}\,(1 - Z)\right]\frac{1}{\varepsilon_p}, \tag{5.18}$$

that is a non-linear second order partial difference equation (PDE).

Eq. (5.18) represents the intra-particle model that must be simultaneously solved with the equations of § 5.2. Clearly, a numerical method must be used in order to obtain a solution. Thus, the governing equations should be rewritten in term of dimensionless quantities. For this purpose the following changes of variable are considered:

$$\hat{C}_{A,p} = \frac{C_{A,p} - C_{A,\,eq}}{C_{A,\,\text{bulk}} - C_{A,\,eq}} = \frac{C^*_{A,p}}{C^*_{A,\,\text{bulk}}}, \tag{5.19}$$

$$\hat{R} = \frac{R}{R_0}, \tag{5.20}$$

$$\hat{\varepsilon}_p = \frac{\varepsilon_p}{\varepsilon_{p,0}}, \tag{5.21}$$

as well as Eqs. (4.77) and (4.79). After some algebra, the molar balance of species A becomes

$$\begin{aligned}\frac{\partial \hat{C}_{A,p}}{\partial \hat{t}} = \frac{\hat{\mathscr{D}}_{\text{eff}}}{\hat{\varepsilon}_p\,\phi_p^2}\left[\frac{2}{\hat{R}}\,\frac{\partial \hat{C}_{A,p}}{\partial \hat{R}} + \frac{\partial^2 \hat{C}_{A,p}}{\partial \hat{R}^2}\right] + \\ - \frac{dX}{d\hat{t}}\,\frac{(1 - \varepsilon_{p,0})}{C^*_{A,\,\text{bulk}}\,\varepsilon_{p,0}}\left[\frac{\rho_s}{M_B} + (\hat{C}_{A,p}\,C^*_{A,\,\text{bulk}} + C_{A,\,eq})\,(1 - Z)\right]\frac{1}{\hat{\varepsilon}_p},\end{aligned} \tag{5.22}$$

where $\hat{\mathscr{D}}_{\text{eff}}$ is a dimensionless diffusivity coefficient defined as

$$\hat{\mathscr{D}}_{\text{eff}} = \frac{\mathscr{D}_{\text{eff}}}{\mathscr{D}_{\text{eff},0}}, \tag{5.23}$$

where $\mathscr{D}_{\text{eff}}$ is a function of time because of the particle porosity, according to Eqs. (5.8), (5.9) and (5.15) and $\mathscr{D}_{\text{eff},0}$ is the diffusivity at the initial time. Then, considering the dimensionless porosity of Eq. (5.21), Eq. (5.23) becomes

$$\hat{\mathscr{D}}_{\text{eff}} = \hat{\varepsilon}_p^2. \tag{5.24}$$

Moreover, the dimensionless term ϕ_p present in Eq. (5.22) is defined as

$$\phi_p = R_0 \sqrt{\frac{k_s^{(0)}\,\varepsilon_{p,0}}{M_0\,\mathscr{D}_{\text{eff},0}}} \tag{5.25}$$

that is the particle Thiele diffusion modulus, according to Satterfield [51].

Following the continuous RPM presented in § 4.5, Eqs. (4.82), (4.85) and (4.86) must be adjusted in order to account for the intra-particle diffusion. Thus, Eq. (4.82) becomes

$$\hat{C}_{A,\,\text{int}} = \hat{C}_{A,p} - \frac{k_s^{(0)}}{k_s^{(1)}}\,\frac{\beta}{(1-\varepsilon_0)\;C^*_{A,\,\text{bulk}}}\,\eta_s\,\ln\left(\frac{\eta_s}{\eta_p}\right). \tag{5.26}$$

Whereas, Eqs. (4.85) and (4.86) become

$$\hat{C}_{A,\,\text{int}} = \frac{\hat{C}_{A,p}}{1 + \dfrac{\beta}{(1-\varepsilon_0)}\,\eta_s\,\ln\left(\dfrac{\eta_s}{\eta_p}\right)}, \tag{5.27}$$

$$\frac{\partial \eta_s}{\partial \hat{t}} = \frac{\hat{C}_{A,p}\,C^*_{A,\,\text{bulk}}\,k_s^{(0)}/k_s^{(1)}}{1 + \beta\,\eta_s\,y\,(1-X)}. \tag{5.28}$$

Once the intra-particle corrections are applied, Eq. (5.23) must be simultaneously solved with Eqs. (5.26), (4.83), (3.170), (3.173) and (3.178) when the carbonation reaction is in the zero order zone. On the contrary, Eq. (5.23) must be simultaneously solved with Eqs. (5.27), (5.28), (3.170), (3.173) and (3.178) for the reaction to follow a first order kinetic rate.
Finally, the reaction rate $dX/d\hat{t}$ is obtained from Eq. (5.5) and it is rewritten in dimensionless form, giving

$$\frac{dX}{d\hat{t}} = \left[\int_0^\infty 2\pi\,M_0^3\,\eta_s\,\frac{\partial \eta_s}{\partial \hat{t}}\,l(a_0)\,da_0\right]\,\frac{\exp\left[-\displaystyle\int_0^\infty \pi\,M_0^3\,\eta_s^2\,l(a_0)\,da_0\right]}{1-\varepsilon_{p,0}}. \tag{5.29}$$

5.5 The particle Thiele modulus and the effectiveness factor for the carbonation reaction

Following the procedure reported by Satterfield [51], the particle Thiele modulus is evaluated at different temperatures in order to estimate the particle effectiveness factor η_{particle}, that is defined as

$$\eta_{\text{particle}} = \frac{\text{rate of reaction with pore diffusion resistance}}{\text{rate of reaction at the particle surface conditions}}, \tag{5.30}$$

according to Thiele [63] and Aris [4]. In spherical coordinates Eq. (5.30) becomes

$$\eta_{\text{particle}} = \frac{3}{\tanh\phi_p}\left[\frac{1}{\tanh\phi_p} - \frac{1}{\phi_p}\right] \tag{5.31}$$

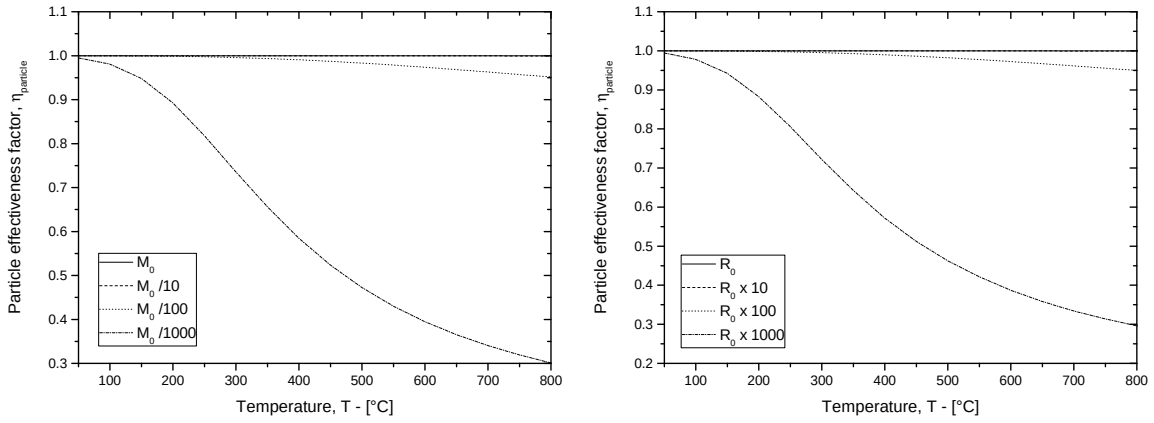

(a) *Varying* M_0. **(b)** *Varying* R_0.

Figure 5.2: Predicted particle effectiveness factors. The mean pore radius is $M_0 = 145.38\,\text{Å}$ and the particle radius is $R_0 = 75\,\mu\text{m}$.

as reported by Thiele [63], Aris [4] and Satterfield [51].

Fig. 5.2 shows the particle effectiveness factor profiles vs temperature for various mean pore radius and particle size. As reported in Fig. 5.2a, the diffusion resistance becomes significant only when the mean pore radius is 1000 times lower than M_0. Clearly, this results is consistent with Eq. (5.10) which states that the Knudsen diffusivity is directly proportional to the mean pore radius. On the other hand, as the porous particle increases, the concentration gradient of the gaseous reactant becomes large according to the Fik's law. In fact, Fig. 5.2b shows the particle effectiveness factor for various particle radii. However, appreciable gaps form the ideal behavior ($\eta_{\text{particle}} = 1$) appears only for porous particles having radius of $R_0 \times 1000$.

The method of the effectiveness factor is largely employed in catalytic reaction where the solid phase remains invariant during the reaction. However, several literature works considered the effectiveness factor approach in modeling the non-catalytic gas-solid reactions such as the carbon black oxidation (Song et al. [56]) or the char gasification (Ollero et al. [44], Mani et al. [40]). This method does evidently not work for the case of carbonation reaction because of the porosity decreasing, the pore closure and the product layer diffusion are not accounted for.

5.6 Numerical approach

The local molar balance of species A (Eq. (5.22)) provides the concentration profile of the gaseous reactant inside the porous particle meanwhile the carbonation reaction occurs. In order to solve Eq. (5.22) the Numerical Method of Lines (NUMOL, by Shiesser [52]) was used. This method states that the variation of $\hat{C}_{A,p}$ with respect to the spatial coordinate $\hat{R}$ takes place in a computational grid[4]. In this way, $\hat{C}_{A,p}$ is continuous along the time coordinate and discretized along the spatial one, so that Eq. (5.22) is reduced to a system nR ODEs, where nR is the total number of the grid points along $\hat{R}$. Afterwards, the ODEs system can be easily solved using an

[4]For this work of thesis an equally spaced grid was used.

ODE solver.
The partial derivatives in Eq. (5.22) are replaced with algebraic approximations and the finite difference method was used.

Following the NUMOL approach the $\hat{R}$ coordinate is discretized with $nR-1$ intervals, obtaining nR grid points. Thus, $\hat{R}(1)$ correspond to $\hat{R}=0$ and $\hat{R}(nR)$ to $\hat{R}=1$. Considering Eq. (5.22), its discretization along $\hat{R}$ becomes

$$\frac{d\hat{C}_{A,p}(i)}{d\hat{t}} = \frac{\hat{\mathscr{D}}^{p}_{\text{eff}}}{\hat{\varepsilon}_p(i)}\left[\frac{2}{\hat{R}(i)}\frac{d\hat{C}_{A,p}(i)}{d\hat{R}} + \frac{d^2\hat{C}_{A,p}(i)}{d\hat{R}^2}\right]\frac{1}{\phi_p^2} - \frac{dX(i)}{d\hat{t}} \ldots \quad i=2,\ldots,nR-1. \tag{5.32}$$

The two grid points, whose index is $i=1$ and $i=nR$, refer to the boundary conditions reported by Eqs. (5.3) and (5.4)and for this reason they are independently considered. The Dirichlet boundary condition (that is Eq. (5.3)) imposes a constant value of $\hat{C}_{A,p}$ at $\hat{R}=1$. Thus, in this point Eq. (5.22) becomes

$$\frac{d\hat{C}_{A,p}(nR)}{d\hat{t}} = 0. \tag{5.33}$$

Then, the Neumann boundary condition (Eq. (5.4)) is imposed at $\hat{R}=0$.
Eq. (5.32) with the boundary conditions at $\hat{R}=0$ and at $\hat{R}=1$ represent a set of ODEs and once integrated it gives the solution of Eq. (5.22) according to NUMOL. In this way, the initial condition (Eq. (5.2)) of Eq. (5.22) becomes the initial condition of each ODE.

Such equations must be simultaneously solved with the equations of the RPM reported in § 4.5. Thus, a second computational grid is considered in order to discretize the pore radius coordinate a_0 into nr grid points. For each $a_0(i)$ two ODEs must be solved to evaluate η_s and η_p. Consequently, for each computational point $\hat{R}(i)$, $(1+2\,nr)$ ODEs must be simultaneously solved and the total number of the ODEs system becomes $[nR\times(1+2nr)]$. This can be visualized considering a matrix of ODEs:

$$\begin{bmatrix} \frac{d\hat{C}_{A,p}(1)}{d\hat{t}} & \frac{d\eta_s(1,1)}{d\hat{t}} & \cdots & \frac{d\eta_s(1,nr)}{d\hat{t}} & \frac{d\eta_p(1,nr+1)}{d\hat{t}} & \cdots & \frac{d\eta_p(1,2nr)}{d\hat{t}} \\ \vdots & & & \cdots & & & \vdots \\ \frac{d\hat{C}_{A,p}(nR)}{d\hat{t}} & \frac{d\eta_s(nR,1)}{d\hat{t}} & \cdots & \frac{d\eta_s(nR,nr)}{d\hat{t}} & \frac{d\eta_p(nR,nr+1)}{d\hat{t}} & \cdots & \frac{d\eta_p(1,2nr)}{d\hat{t}} \end{bmatrix}, \tag{5.34}$$

whose dimension is $[nR\times(1+2nr)]$. The RPM equations (§ 4sec:RPMcarbonation) are applied to each grid point $\hat{R}(i)$ having care to consider Eq. (5.29) in order to evaluate the local reaction rate $dX(i)/d\hat{t}$. Moreover, the local particle porosity is calculated using Eq. (3.105) by substituting the respective local quantities.

Finally, once the ODEs system is integrated the global particle conversion is evaluated as the mean along the radial coordinate of all the local conversions that are calculated at each grid point.

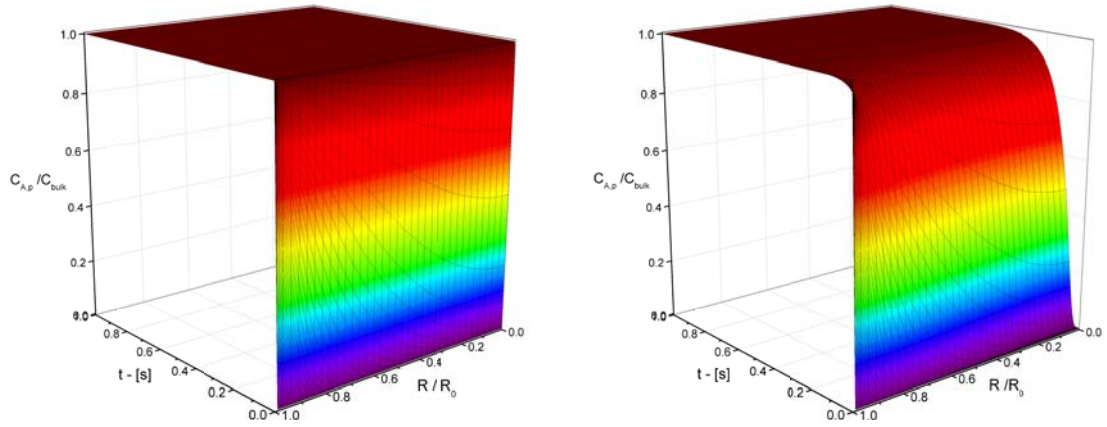

(a) $\varepsilon_0 = 0.424$. **(b)** $\varepsilon_0 = 0.424/100$.

Figure 5.3: Predicted concentration profiles inside a porous particle with a diameter of 150 µm. The operative conditions are 650 °C and 5 bar.

5.7 Intra-particle diffusion without reaction

When the carbonation reaction is neglected, the only mechanism is the diffusion of the gaseous reactant inside the porous particle. Thus, Eq. (5.18) reduces to:

$$\frac{\partial C_{A,p}}{\partial t} = \frac{\mathscr{D}_{\text{eff}}}{\varepsilon_p}\left[\frac{2}{R}\frac{\partial C_{A,p}}{\partial R} + \frac{\partial^2 C_{A,p}}{\partial R^2}\right]. \tag{5.35}$$

Following the NUMOL approach Eq. (5.35) becomes a set of nR ODEs that can be easily solved with the MATLAB® routine named "ode45". The numerical results are shown in Fig. 5.3. From Fig. 5.3a, the diffusion process seems to be very fast, and the bulk concentration is reached with a time scale below 1 s. No concentration gradients appeared along the $\hat{R}$ coordinate. However, significant concentration gradients occurs when the particle porosity is reduced to 100 times. In this case, the whole process is slower respect to the previous one, but also in this case the bulk concentration in reached in less than 1 s.

5.8 Influence of the intra-particle diffusion on the carbonation reaction

The pure intra-particle diffusion without any reaction is a simple process that completes in less than 1 s. However, when the reactant diffusion inside the CaO particles is coupled with the carbonation reaction, several complications occur because of the reactant consumption due to the reaction. In fact, as carbonation occurs, the total particle porosity is gradually reduced according to Eq. (3.105). For this reason, the diffusion coefficient of Eq. (5.22) progressively

[5] The activation energy of the carbonation reaction comes from Sun et al. [59], as reported by Eq. (4.28). The product layer diffusivity follows Sun et al. [58], as stated by Eq. (4.40).

Table 5.3: Values of the parameters employed in the intra-particle diffusion/carbonation simulation.

Parameter	value	units
R_0	75	Å
M_0	145.38	Å
V_0^{LN}	1794.822	-
μ_{N_0}	4.939	Å
σ_{N_0}	0.285	-
$b_{LN}^{(o)}$	0.424	-
$b_{LN}^{(E)}$	0.552	-
S_g	37.30	$m^2\,g^{-1}$
$A_k^{(1)}$	1.54×10^{-12}	$m\,s^{-1}\,Pa^{-1}$
$E_{a,k}$	29.4	$kJ\,mol^{-1}$
A_D	0.27	$m^2\,s^{-1}$
$E_{a,D}$[5]	215	$kJ\,mol^{-1}$

reduces to zero:

$$\frac{\hat{\mathscr{D}}_{\text{eff}}}{\hat{\varepsilon}_p\,\phi_p^2} = \frac{\hat{\varepsilon}_p}{\phi_p^2} \tag{5.36}$$

where $\hat{\mathscr{D}}_{\text{eff}}$ is expressed according to Eq. (5.24). As reaction progresses $\hat{\varepsilon}_p \to 0$ and the diffusion contribution becomes gradually smaller down to the closure of pores. This occurs over the external surface ($\hat{R} = 1$) of the particle where the pores are completely exposed to the bulk concentration, so that the reactivity of these is larger respect to the internal one. Since the external pores presents a larger reaction rate, pore closure occurs earlier respect to the particle interior. This situation is critical because, when the external shell plugs, the reactant diffusion stops as well as reaction itself.

The intra-particle diffusion coupled with a gas-solid reaction model accounting for pore closure, such as the RPM of Bhatia [10] and Sotirchos et al. [57], was never be proposed in the literature. In fact, as reaction progresses, structural changes occur inside the porous particle, as the particle specific surface and porosity variations. In this way the transport properties (that depends on the porosity) also vary during the whole process. As well, the kinetic of the gas-solid reaction is deeply influenced by the structural changes: both specific surface and CO_2 concentration decrease during the reaction. This situation is accentuated when a fast chemical reaction occurs, such as the carbonation.

Following the numerical method reported in § 5.4 and § 4.5, a process simulation was performed. The parameters used are listed in Tab 5.3.
The results are obtained at 600 °C and 1 bar considering the gaseous reactant composed by 100 % of CO_2.

Fig. 5.4 shows the results of the simulation in terms of local concentration and conversion surfaces. Particularly, Fig. 5.4a presents the concentration evolution of the carbon dioxide inside the particle as a function of time. During the first instants of the reaction, the porous particle

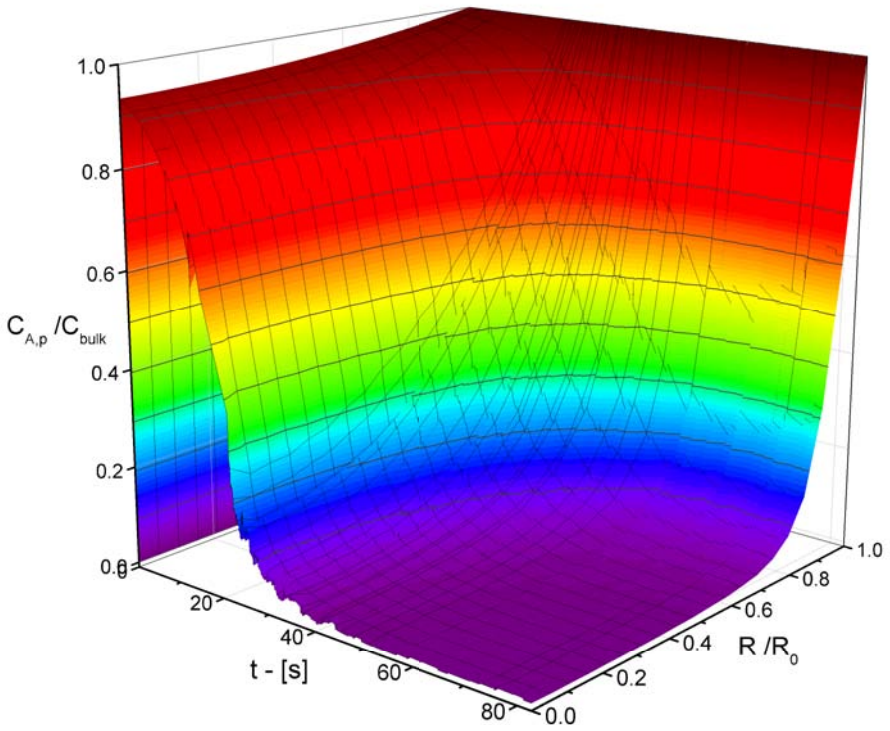

(a) *CO_2 concentration surface as a function of time and $\hat{R}$.*

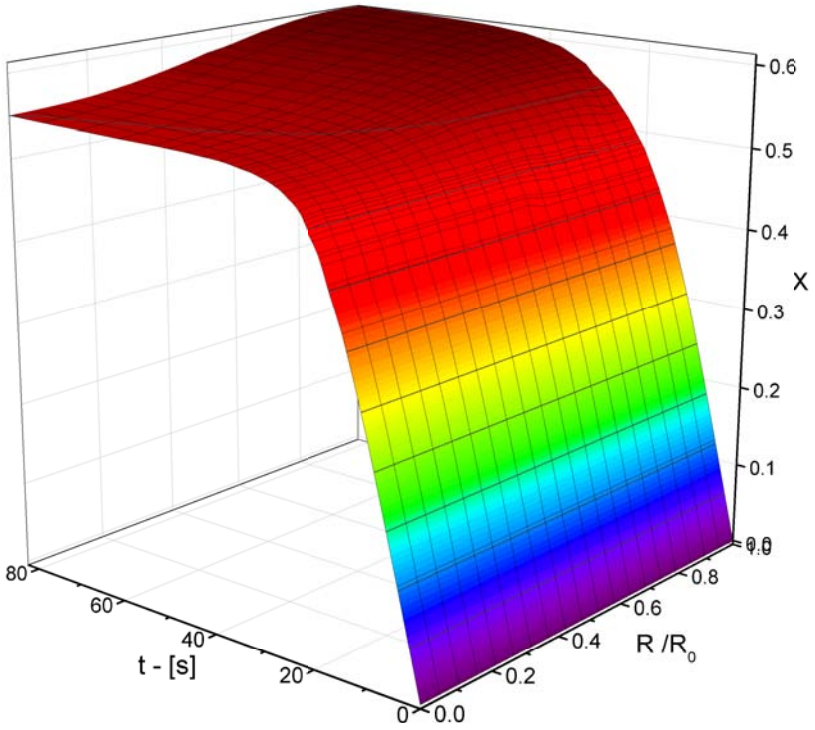

(b) *Local conversion X as a function of time and $\hat{R}$.*

Figure 5.4: Intra-particle diffusion and carbonation: local CO_2 concentration and conversion inside the CaO porous particle at 600 °C and 1 bar of CO_2.

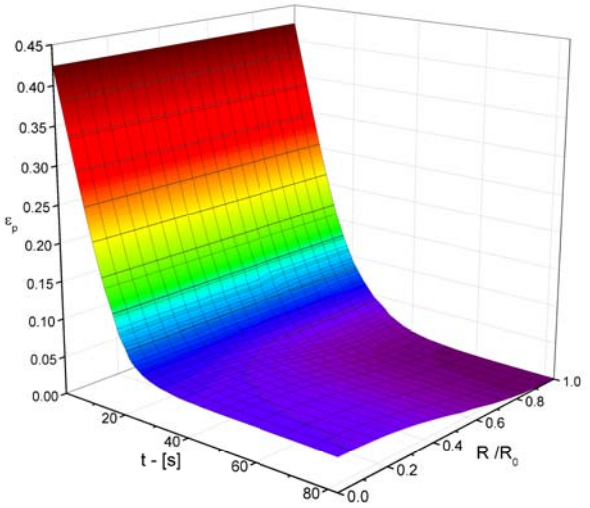

(a) *Particle porosity surface.*

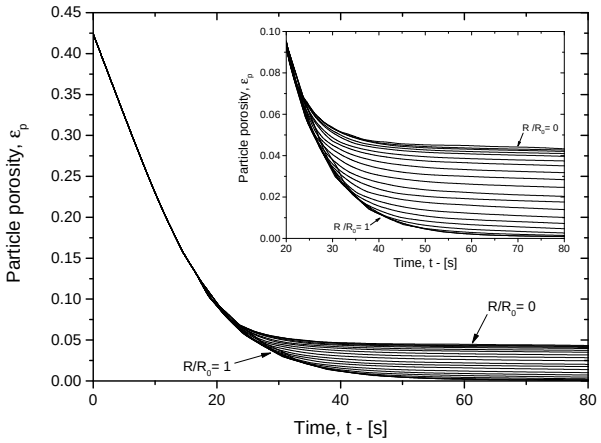

(b) *Parametric porosity curves.*

Figure 5.5: Local particle porosity evolution inside the CaO particle.

is filled by CO_2. Afterwards, as reaction occurs carbon dioxide is progressively consumed. In this way, the abrupt decrease of the concentration is due to the kinetic control regime as shown by Fig. 5.4b. During this step the kinetic rate is high, the reactant is quickly consumed and the particle porosity decreases. For these reasons, after the reaction control regime, the CO_2 local concentration approaches to zero. In fact, as shown in Fig. 5.5, the particle porosity is completely lost and the dense product layer prevents the CO_2 diffusion inside the particle.

This concentration profile is very different with respect to Fig. 5.3a where no reaction was considered. The differences between the two concentration surfaces are due to the structural changes that occur in the porous particle during the carbonation reaction.

However, Fig. 5.4a shows some numerical oscillation probably caused by the numerical method used. The decrease of the particle porosity and the low particle radius discretization could be the reasons such oscillations.

For this simulation the total number of grid points for the radial coordinate were $nR = 30$, whereas, for the pore distribution $nr = 30$. Thus, 1220 ODEs were simultaneously solved. Since

the computational cost significantly increases with the discretization, the number of grid points was limited, especially for the particle radial coordinate. Certainly, better results can be obtained using more refined computational grids.

The local conversion evolution inside the particle is reported in Fig. 5.4b. The result is consistent with the concentration profile of Fig. 5.4a: the local conversion progressively decreases from the outside to the particle center. The global conversion of the particle is the average value along the radial coordinate.

Fig. 5.5 shows the local particle porosity as a function of time. Since the external shell of the particle is continuously exposed to the bulk concentration, in this region the local reactivity is higher respect to the center of the particle. For this reason, the external shell of the particle undergoes a progressive loss in porosity, down to the complete closure. When the external pores are completely filled by the product layer, reaction stops even if the porosity inside the particle is yet available. The parametric curves in Fig. 5.5b clarify the phenomena with a detailed view of the porosity evolution with time for each grid point $\hat{R}$.

Since the particle porosity evolves in a different manner between the external and the center of the particle, Fig. 5.6 shows the evolution of the pore/reaction radii and the pore size distribution at $\hat{R} = 1$ and $\hat{R} = 0$ respectively. Figs. 5.6a and 5.6b clearly emphasized the different pore evolution at the extremities of the computational grid. As well as pore radius, also the reaction surface shows a different evolution as reported by Figs. 5.6c and 5.6d. The pore size distributions are also reported (Figs. 5.6e and 5.6f), which demonstrate that the reaction at $\hat{R} = 0$ could virtually occurs when the external porosity is completely lost. However, in this situation no reactant diffusion can occur because of the complete pore closure at the particle surface.

5.8.1 The importance of the intra-particle diffusion in non-catalytic gas-solid reactions

The assumption of no intra-particle diffusion can be roughly in non-catalytic gas-solid reactions and may lead to a wrong kinetic parameter estimation. According to Eq. (5.22), the intra-particle diffusion depends on the the operative conditions, on the kinetics and on the porous particle physical properties. The temperature, the total pressure and the CO_2 concentration may affect the CO_2 diffusivity inside the porous network of the particle. Specifically, the temperature effect is weak because of the low temperature dependence of the bulk diffusion coefficient $\mathscr{D}_{i,j}$ and the low activation energy of the carbonation reaction. However, if an high activation energy reaction is considered, the temperature dependence should be studied more in detail. The role of the CO_2 partial pressure is significant, as shown in Fig. 5.7. As the reactant partial pressure increases the CO_2 diffusion progressively increases. Consequently the higher carbon dioxide partial pressure the better the match between the RPM with and without intra-particle diffusion (§ 4.5).

The conversion-time curves reported in Fig. 5.8 were obtained at 650 °C and 1 bar with 100 % in CO_2. The kinetic rate parameter employed are the same of Eqs. (4.28) and (4.29) (Sun et al. [59]). A parametric study was performed increasing and reducing the pre-exponential factor of 100 times. Fig. 5.8 shows that if the reaction kinetics is reduced the two RPMs match because

the whole process becomes reaction rate controlled. On the other hand, if the kinetic rate is increased, the intra-particle diffusion becomes the limiting mechanism, and the whole process becomes particle-diffusivity controlled.
Also the physical properties of the solid reactant can influence the intra-particle diffusion. As the particle diameter increases the reactant concentration gradient along the radial coordinate increases and the porous particle does not uniformly react. However, in this study the CaO particle diameter was set at 150 µm and the particle size effect is not so relevant. For bigger particle size the intra-particle diffusion modeling can be critical. The pore size influences both the Knudsen diffusion and the kinetic rate. The larger the pore radius the higher the reactant diffusivity. However, since the pore opening is performed during the calcination step, it is difficult to have a careful control of the pore radius. Additionally, if the void fraction of the porous particle increases the gaseous reactant can diffuse more inside the particle, so that the reaction takes place uniformly.
Thus, when a TGA experiment is performed the intra-particle diffusion needs to be considered in order to avoid apparent reaction rate estimations. However, a careful choice the operative conditions and the physical properties of the solid reactant can improve the experiments confusion between the intrinsic and the apparent kinetic rate.
The comparison between the predicted conversion time curves with the experimental data is reported in Fig. 5.9. Since the intra-particle effect is not to so relevant the match with the experimental results is improved, compared to whose reported in Fig. 4.7.
The RPM with intra-particle diffusion was applied to the experimental data of the previous chapter. The comparison between the predicted conversion time curves and the TGA results is reported in Fig. 5.9. The figure shows that the intra-particle effect is limited at 650-750 °C and 5 bar[6]. Finally, Figs.5.10 and shows a comparison between the model predictions respectively obtained with and without the intra-particle diffusion. Since the CO_2 partial pressure is large (5 bar) the overall effect low respect to the results of Fig.5.7.

5.9 Conclusions

The modified RPM developed in Chapters 4 and 5 considers several mechanisms that simultaneously occur during a TGA experiment:

1. the gas-solid reaction kinetics;
2. the product layer diffusion;
3. the intra-particle diffusion.

Moreover, structural changes that occur inside the porous particle are modeled considering a continuous pore size distribution, in order to describe the various pore radius classes in an efficient way.

[6]The distribution parameters employed for the TGA tests at 750 °C were: $\mu_{N_0} = 5.432$ Å, $\sigma_{N_0} = 0.285$ Å^{-1} and $b_{LN}^{(o)} = 0.424$, according to § 4.6,.

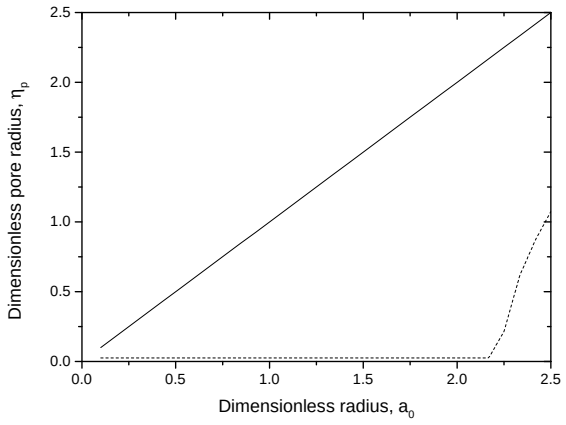

(a) η_p *at* $\hat{R} = 1$.

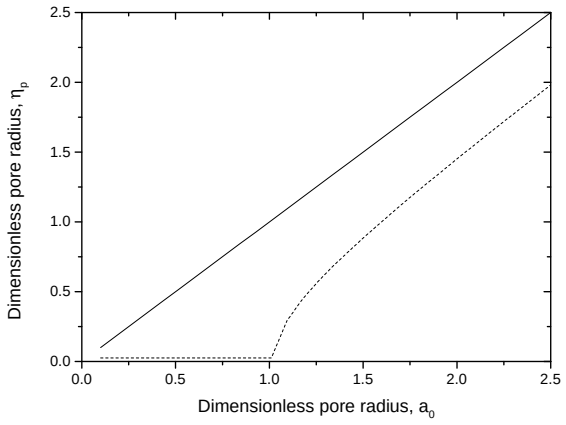

(b) η_p *at* $\hat{R} = 0$.

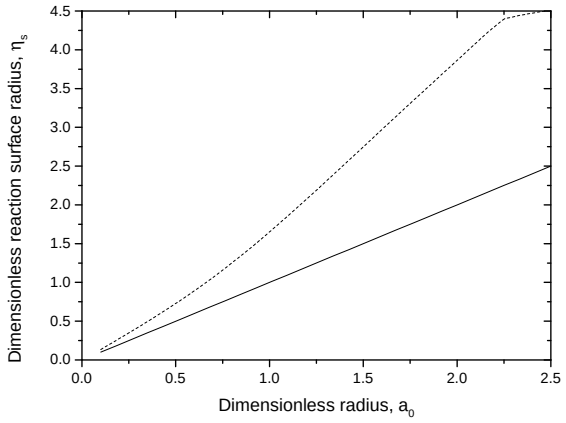

(c) η_s *at* $\hat{R} = 1$.

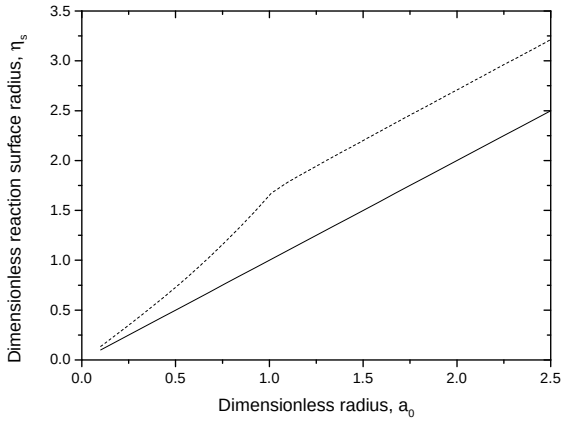

(d) η_s *at* $\hat{R} = 0$.

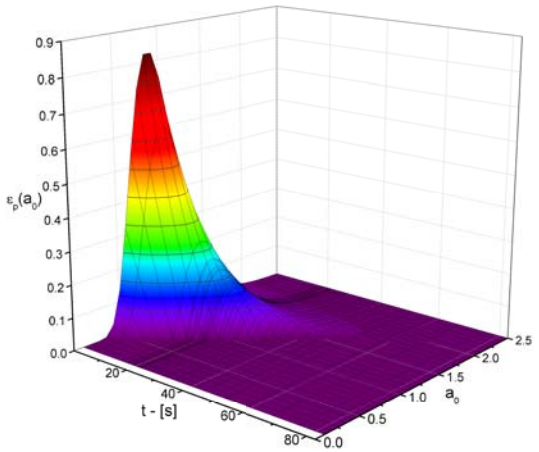

(e) *Evolution of pore size distribution at* $\hat{R} = 1$.

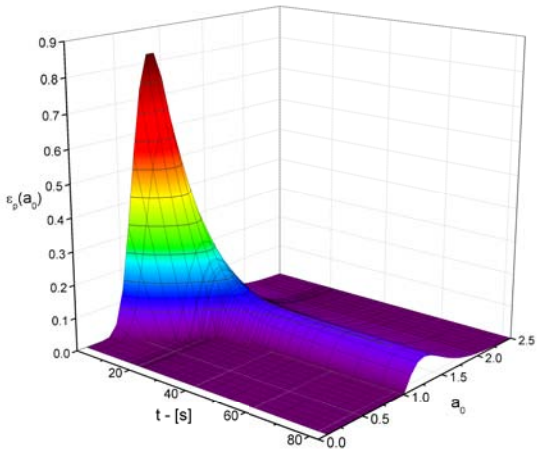

(f) *Evolution of pore size distribution at* $\hat{R} = 0$.

Figure 5.6: Evolution of the pore and surface reaction (at initial and final time) and evolution of the pore size distribution.

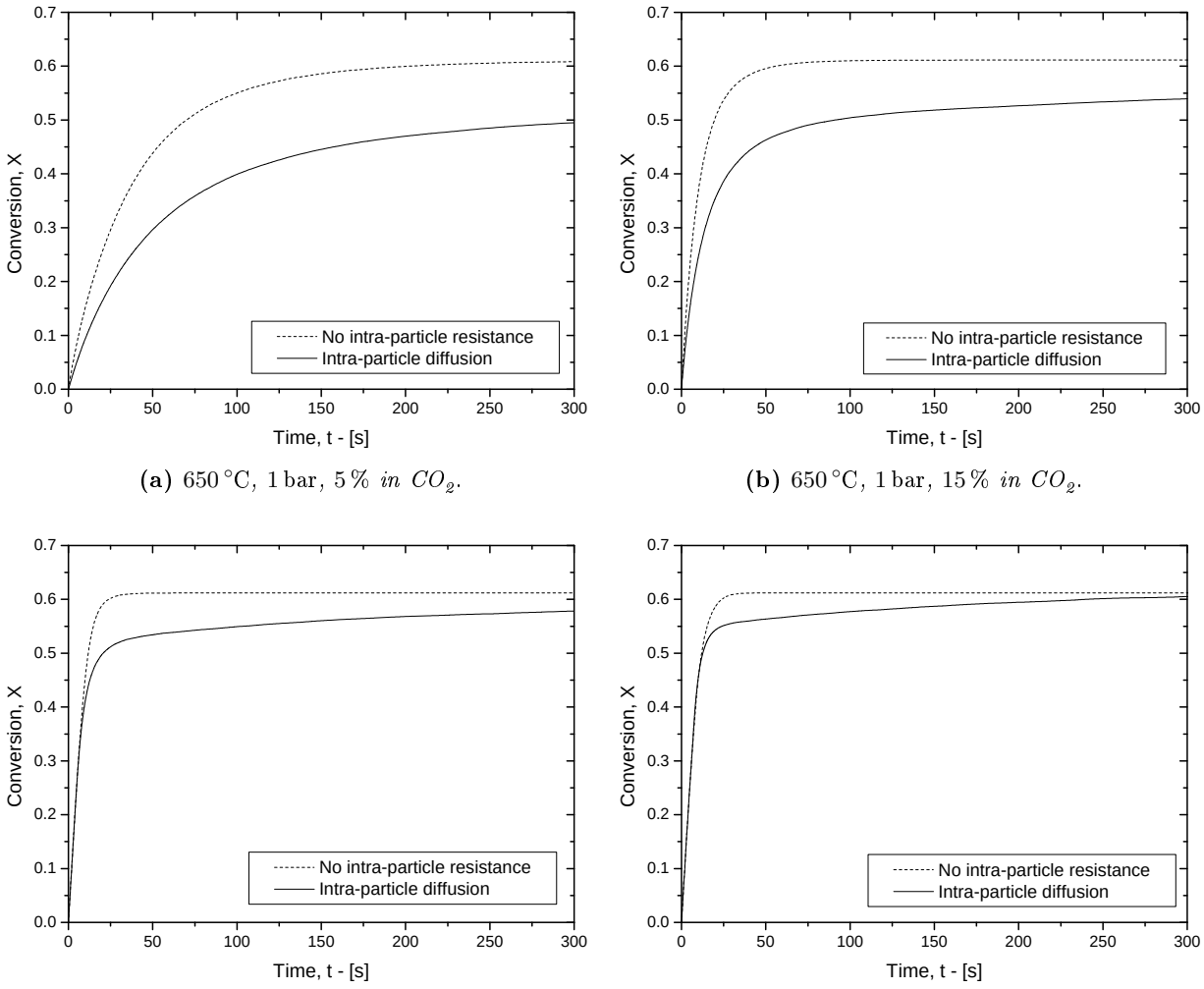

(a) 650 °C, 1 bar, 5 % *in* CO_2.

(b) 650 °C, 1 bar, 15 % *in* CO_2.

(c) 650 °C, 1 bar, 50 % *in* CO_2.

(d) 650 °C, 1 bar, 100 % *in* CO_2.

Figure 5.7: Comparison between the modified RPM with and without intra-particle diffusion varying the CO_2 partial pressure.

The coupling between the a random pore model accounting for pore closure and intra-particle diffusion was never proposed in the literature and applied to a fast gas-solid reaction such as the carbonation. Only Sun et al. [58] applied the RPM by Bhatia [10] and Sotirchos et al. [57] to the carbonation reaction. However, Sun et al. considered a discrete pore size distribution and all the external resistances and gas phase diffusion processes were neglected.

One of the main purpose of this chapter was to demonstrate that intra-particle diffusion cannot be neglected when the carbonation reaction is considered. In fact, the previous section shows the concentration and conversion profile inside the CaO particles, in which both concentration and conversion gradients should not be ignored, especially for low CO_2 partial pressure and large particle size.

The intra-particle analysis becomes important both in TGA test planning and in the interpretation of the experimental results. On the other hand, if the intra-particle diffusion is not considered, a zero-resistance model may lead to apparent kinetic rate estimations, that can be

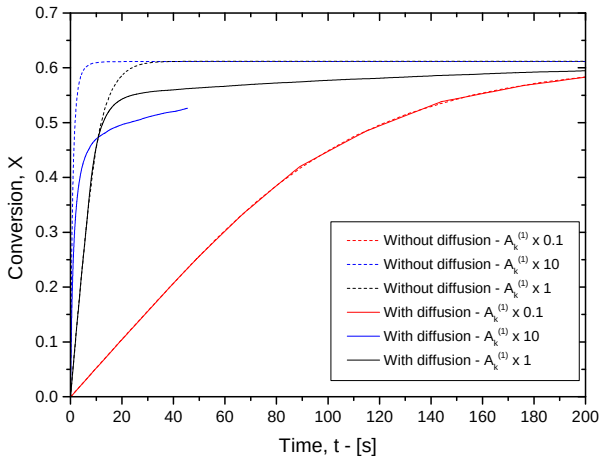

(a) *Long time scale.*

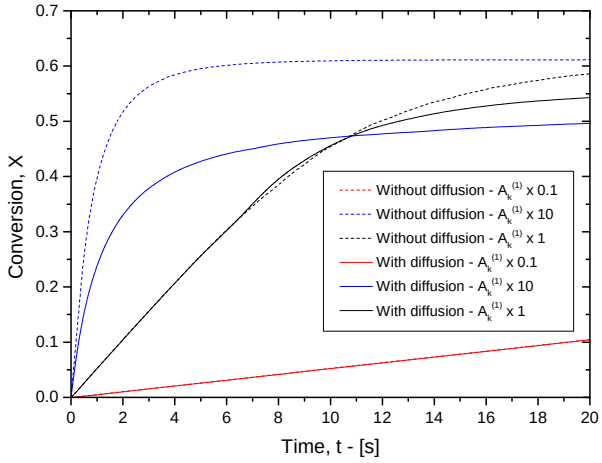

(b) *Short time scale.*

Figure 5.8: Comparison between the modified RPM with and without intra-particle diffusion varying the pre-exponential factor. 650 °C, 1 bar, 100 % in CO_2.

different from the intrinsic reaction. Consequently, the apparent kinetic rate can be very slow compared to the intrinsic kinetic, because it can be considered as the sum of the real reaction rate and the intra particle diffusivity. This especially for fast reactions.

The analysis proposed in this chapter indicates that the TGA results of Chapter 4 (that were performed at 650 °C and 750 °C and 5 bar of CO_2) are not influenced by the intra-particle diffusion because of the large CO_2 partial pressure.

A limit of the work presented in this chapter is the instability of the applied numerical method. The future development of the work will require an investigation of the the causes of the numerical instabilities as well as a more efficient and refined implementation.

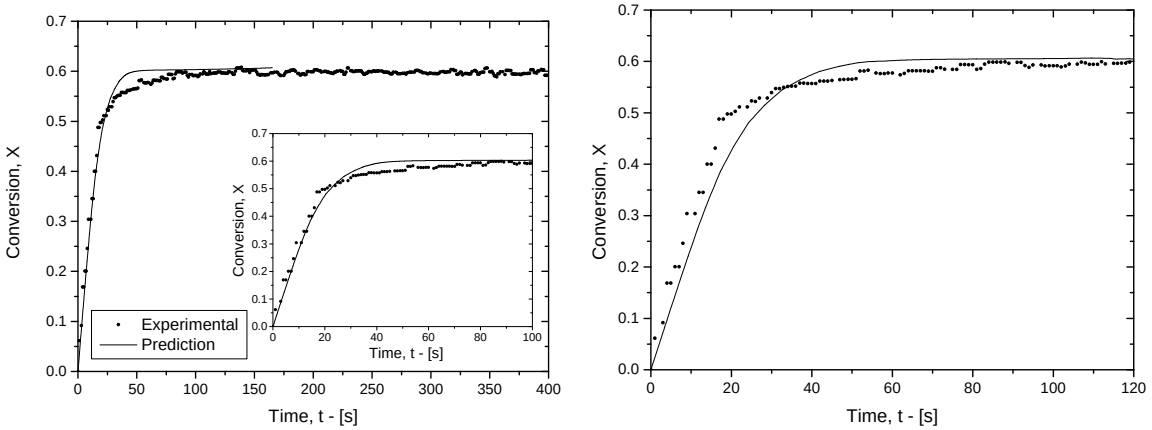

(a) $T = 650\,^{\circ}\mathrm{C}$. **(b)** $T = 750\,^{\circ}\mathrm{C}$.

Figure 5.9: Comparison of the predicted conversion-time curves with experimental results, 5 bar and 100 % in CO_2.

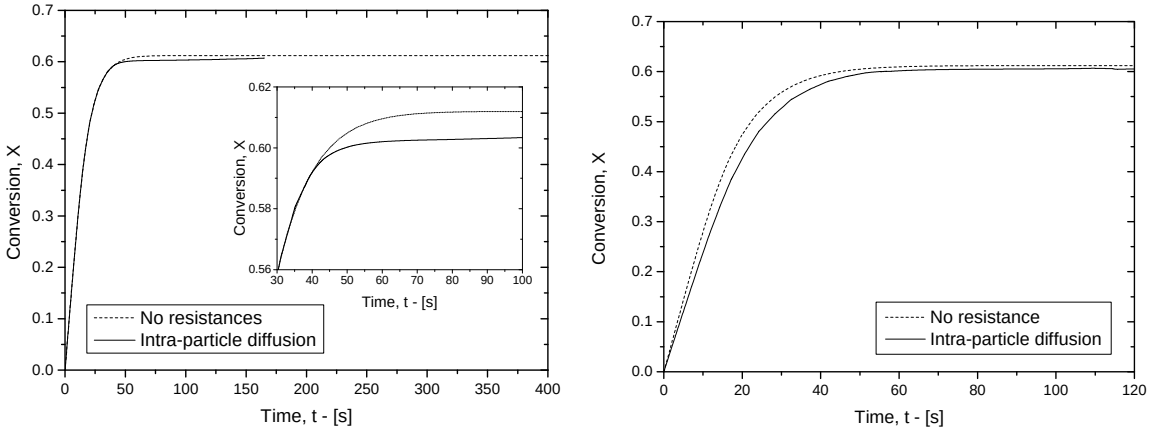

(a) $T = 650\,^{\circ}\mathrm{C}$. **(b)** $T = 750\,^{\circ}\mathrm{C}$.

Figure 5.10: Comparison between the modified RPM with and without the intra-particle diffusion at 5 bar and 100 % in CO_2.

Chapter 6

CFD Analysis of TG carbonation experiments

In this chapter a CFD analysis was performed on horizontal TGA systems in which the carbonation reaction occurs at the surface of a crucible. The goal of the simulation is to study the external mass transfer resistance inside a TGA and the discrepancy between the apparent kinetics and the intrinsic kinetics that arises in these TGA systems. The intra-particle and inter-particle diffusion were neglected.

6.1 Introduction

The kinetic measurements of a gas-solid reaction using the thermogravimetric analysis may lead to inaccurate results if the mass transfer of the gaseous reactant is neglected. In fact, when determining the kinetic constant of gas-solid reactions the gaseous reactant mass transfer to the reactive surface of the solid may become the controlling step depending on the following factors:

1. the kinetics of the gas-solid reaction;
2. the geometry of the TGA;
3. the operative conditions in the TGA.

When a fast gas-solid reaction occurs, the mass transfer of the gaseous reactant may become the limited controlling mechanism. TGA results with such reactions are affected by mass transfer limitations (external diffusion) and the measured kinetic rate may be slower compared to the intrinsic reactivity. These situations occur when the dynamic of the mass transfer is slower respect to the reaction.

The geometries of the TGA reaction chamber may be complex and the gas flow may not reach stationary conditions at the reactant surface. In fact, in TGA tests the sample is charged into a crucible which is placed into a sample holder. Depending on the crucible geometry, the velocity field around and inside the crucible may be not trivial. In this way, the assumption of stagnant gas may underestimate the reactant mass transfer from the bulk to the reaction surface.

The gas flow inside the crucible may recirculate generating eddies that can improve the overall mass transfer. This means that the gas reactant flux that is fed into the crucible may present both diffusive and both convective components.

In some cases, the diffusional limitations in a TGA can be reduced experimentally. For example, the reactant mass flow may progressively increase up to reduce or eliminate the external limitations. However, in some cases the TGA cannot operate with too high flow rate, because the upper limit for the flow rate could be imposed by the mechanical limits of the instrument. For example, the maximum volumetric flow rate at which the TA SDT-Q600 can operate is $1000\,\mathrm{Ncm^3\,min^{-1}}$.

Therefore, a computational fluid dynamics (CFD) study was performed on the TA SDT Q600 which is an horizontal type TGA, according to § 2.5.2. The study was performed using the CFD commercial code ANSYS FLUENT® 14.0. The main purpose of the work is to investigate the velocity field around and inside the crucible where reaction occurs as well as the reactant concentration gradients, in order to evaluate the effect of these operative conditions on the kinetic reaction measurements. In fact, an incorrect apparent kinetics rate may be measured instead of the intrinsic reaction rate if the fluid-dynamics and the reactant mass transfer are not reduced or accurately simulated.
Moreover, in this study the inter-particle resistance is neglected as well as the intra-particle one. The assumption of no inter-particle diffusion may experimentally obtained by using low sample weight.

6.2 TGA gas flow regime

In this fluid-dynamics study the temperature was set at 650 °C, the pressure at 1 bar and the total amount of CO_2 at 100 % in mole fraction. However, the CFD simulations considered also a gas flow of pure N_2 which was typically fed before switching to CO_2. Following these operative conditions, the Reynolds number was calculated both for the furnace and the reactive gas tube . Precisely, the definition of the Reynolds number employed refers to cylindrical pipe:

$$Re_{i,j} = \frac{\rho_i \, \bar{v}_j \, d_j}{\mu_i} \tag{6.1}$$

where i refers to the N_2 or CO_2 species, j to the reactive gas tube (RGT) or to the furnace (F), ρ is the density of species i, $\bar{v}_j$ is average gas velocity inside the furnace, d_j is the reactive gas tube diameter (0.08 mm) and the furnace diameter (22.86 mm), μ_i is the viscosity of the gaseous species i. According to Eq. (6.1), the Reynolds number was calculated for each species varying the gas flow rate at the inlet. The results are listed in Tab. 6.1, which shows that for the explored gas flow rate the flow regime remains in the laminar flow zone ($Re_i \leq 2100$) in both the furnace and the reactive gas tube.
These results shows that the gas flow rate inside the furnace is always laminar. In this way, CFD simulations were performed considering only a laminar model.

Table 6.1: Gas flow regime inside the TGA furnace and the reactive gas tube.

Flow rate		Furnace			Reactive gas tube		
$\dot{V}_{T0}$ $[\mathrm{Nm^3\,min^{-1}}]$	$\dot{V}_T$ $[\mathrm{m^3\,s^{-1}}]$	$\bar{v}_F$ $[\mathrm{m\,s^{-1}}]$	$Re_{\mathrm{N_2}}$ $[-]$	$Re_{\mathrm{CO_2}}$ $[-]$	$\bar{v}_{\mathrm{RGT}}$ $[\mathrm{m\,s^{-1}}]$	$Re_{\mathrm{N_2}}$ $[-]$	$Re_{\mathrm{CO_2}}$ $[-]$
100	5.633E-06	0.014	2.947	4.822	11.383	84.862	138.872
250	1.408E-05	0.034	7.366	12.055	28.458	212.154	347.181
400	2.253E-05	0.055	11.786	19.288	45.533	339.447	555.490
500	2.816E-05	0.069	14.733	24.110	56.916	424.309	694.362
800	4.506E-05	0.110	23.573	38.576	91.065	678.894	1110.979
1000	5.633E-05	0.137	29.466	48.220	113.832	848.617	1388.724

6.3 Geometry

As shown in Fig. 2.14, the geometry of the TA SDT Q600 consists of several components. However, for this CFD study only the furnace was considered as reported in Fig. 2.16. Actually, a simplified furnace geometry was employed in order to maintain the computational cell number lower than the limit value due to the available FLUENT® license. Specifically, the sample holder, the beams and the tapering zone were neglected.

Another important assumption of the geometry consists of the neglecting of the reactive gas tube, in order to avoid to model the sudden flow expansion when the gas flow is fed from the reactive gas tube into the furnace. This simplification seems to be reasonable when the gas flow rate is low because the completely developed flow regime occurs in lower space. However, for large gas flows this assumption may lead to non-realistic results.

The computational domain cannot be reduced along the axial coordinate because of the importance of the CO_2 gas flow from the inlet during the first instants of the reaction. When the gas flow switches to CO_2, the reactant front moves forward to the crucibles due the convection and diffusion mechanisms. These first steps of the process are the most significant for the gas solid reaction (especially if the reaction rate is fast). Because of the diffusion the CO_2 species progressively arrives at the reaction surface. In this way the reaction occurs with a low reactant concentration and these instants are external mass transfer controlled. Therefore, the simulated geometry must be the whole TGA furnace and its 3D representation is shown in Fig 6.1.

In order to reduce the external mass transfer resistance the reaction was performed in the smaller crucible (2 mm in height).

6.4 Meshing

Once the geometry of the system was assembled, the computational domain is meshed. The mesh process is critical because it requires a compromise between an accurate domain discretisation and the computational costs. Thus, an hybrid mesh was chosen to achieve such compromises. Close to the furnace wall a structured mesh was imposed as reported in Fig. 6.2a, whereas an unstructured mesh was used for the other parts of the domain. Specifically, tetrahedron cells

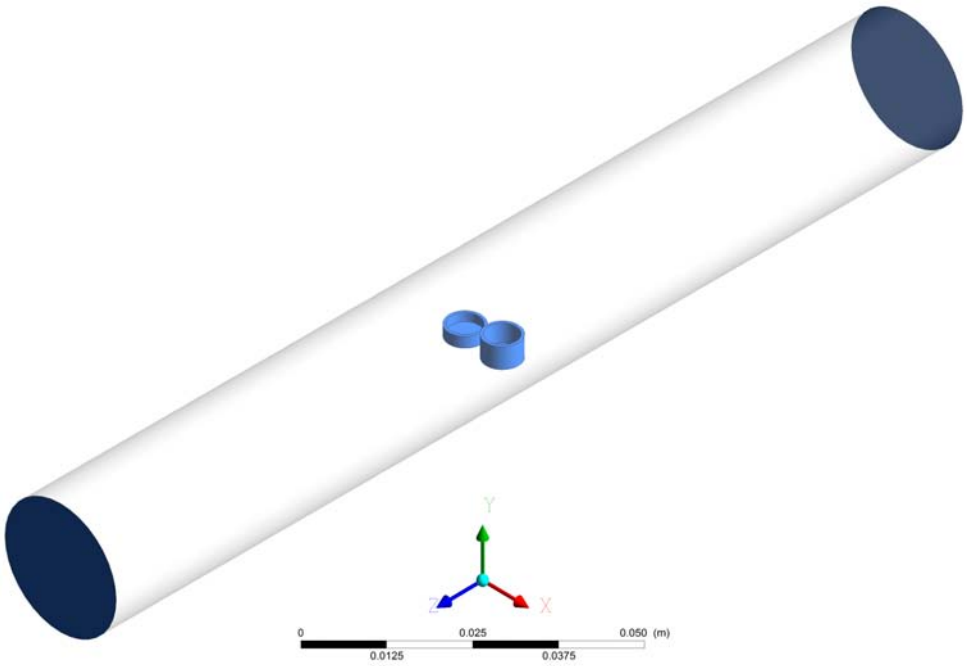

Figure 6.1: Geometry for the CFD simulations with ANSYS FLUENT® 14.0.

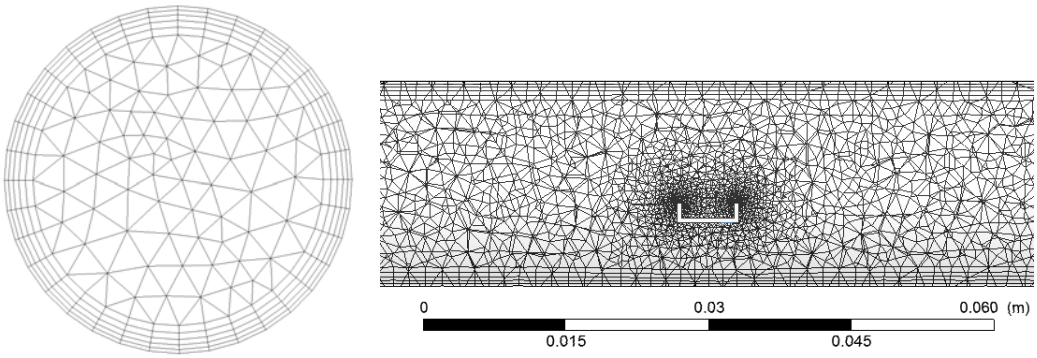

(a) *Radial meshing.* **(b)** *Domain mesh side..*

Figure 6.2: The hybrid mesh employed for the simulations.

were chosen and the proximity function was selected in order to increase the number of cells close to the crucible (Figs. 6.2b and 6.3) where a more degree of accuracy is needed. The cell max size was set to 2 mm, whereas the minimum was set to 2.5×10^{-2} mm. In this way, 273 892 computational cells and 63 114 nodes were obtained. With this number of elements, each simulation requires about $3 \div 4$ h.

6.4.1 Verification of the numerical approach

Tests were preliminarily performed in order check the correctness of the numerical approach used. For these tests a pure N_2 gas flow was considered with a mean velocity of $0.01\,\mathrm{m\,s^{-1}}$ that was imposed at the inlet of the furnace with an uniform profile. Afterwards, the results were

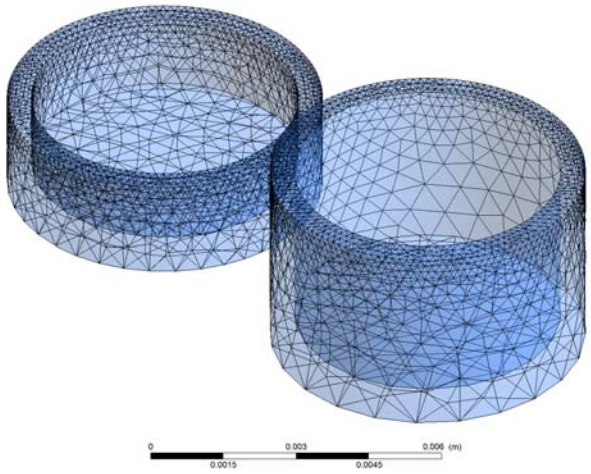

Figure 6.3: The geometry and mesh of the two crucibles.

compared with the Poiseuille flow[1] and reported in Fig 6.4. Simulations results were obtained varying the maximum mesh size. The figure shows that the best simulations were obtained with a cell max size of 2 mm and 1.5 mm which correspond to a cell number of 273 892 and 384 914 respectively. For this work the 2 mm cell max size was selected in order to obtain a good compromise between the accuracy of the results and the computational costs. The graphs showed in Figs. 6.4f and 6.4h confirm the correctness of the numerical approach through a nice agreement with the Poiseuille flow.

6.5 The simulated kinetic rate for the carbonation reaction

In this CFD study a simple reaction rate model was considered. In fact, the attention was focused on the fat kinetic regime of the carbonation reaction, because in the second slower product layer regime the external diffusion is negligible. In this way, only the kinetic regime was simulated and the following phenomena were neglected: the equilibrium concentration, the switch to zero reaction order, the pore closure, the abrupt transition to the product layer diffusion and the intra-particle diffusion. Consequently, the following reaction rate was employed

$$\frac{dX}{dt} = \frac{k_s\, C_{\mathrm{CO_2}}\, (1 - X)\, S}{1 - \varepsilon_0}, \tag{6.2}$$

where X is the reaction conversion, k_s is the kinetic constant, C_A is the CO_2 concentration at the crucible surface, S is the specific surface area and ε_0 is the sample porosity. Following Bhatia and Perlmutter [13] the kinetic constant value is given by Eq. (4.20).
Since the inter-particle diffusion resistances is assumed to be negligible, the whole reaction is assumed to occur at the crucible surface, where the CaO moles are expressed in terms of surface density. This quantity represents the reactant mass loaded into the crucible and in this study

[1] The Poiseuille flow states that $v_z(R) = 2\,\bar{v}_z \left[1 - \left(\frac{r}{R}\right)^2\right]$ where $v_z(R)$ is the axial z-velocity, $\bar{v}_z$ is the mean velocity with respect to the pipe radius ($\bar{v}_z = 1/2\, v_{z,\,\max}$), r is the radial coordinate and R is the pipe radius.

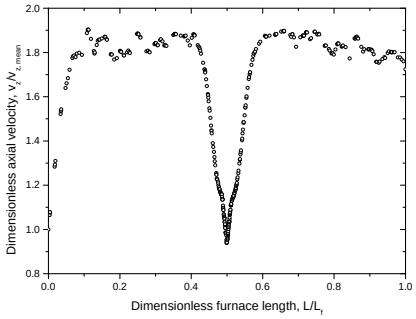

(a) *Maximum velocity along z-axis. Cell max size* 10 mm.

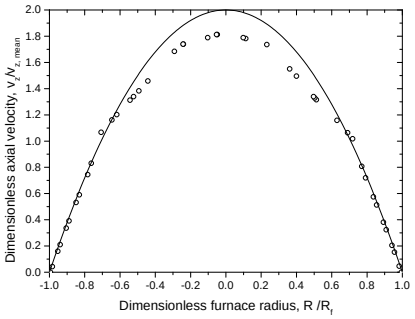

(b) *Radial velocity. Cell max size* 10 mm.

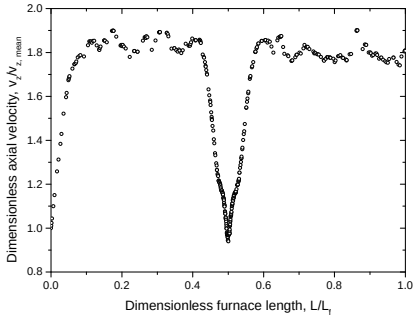

(c) *Maximum velocity along z-axis. Cell max size* 4 mm.

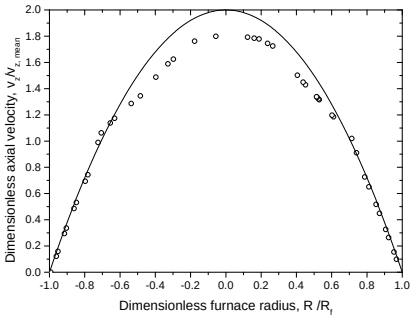

(d) *Radial velocity. Max size* 4 mm.

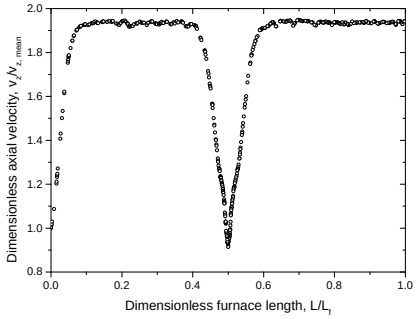

(e) *Maximum velocity along z-axis. Cell max size* 2 mm.

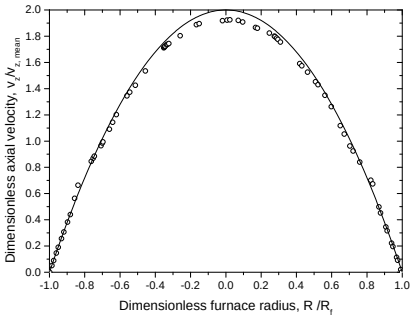

(f) *Radial velocity. Max size* 2 mm.

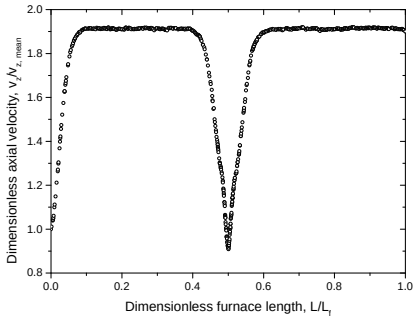

(g) *Maximum velocity along z-axis. Cell max size* 1.5 mm.

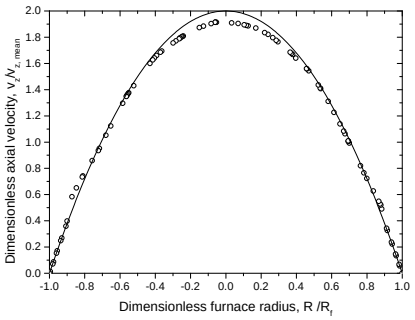

(h) *Radial velocity. Max size* 1.5 mm.

Figure 6.4: Simulation results of N_2 flow inside the furnace for different mesh max size. The continuous line represents the analytical solution of the Poiseuile flow.

was 10 mg.

6.6 Results

The goal of this chapter is to study the behaviour of a fast gas-solid reaction, as the carbonation reaction, inside an horizontal TGA (the TA SDT Q600). The simulation results consists of the velocity field, the CO_2 concentration field and the conversion-time curves.

6.6.1 Velocity field

A parabolic velocity profile was imposed at the inlet of the furnace according to the Poiseuille flow. Before the reaction simulation, N_2 was fed for 2 s before starting to feed CO_2. In this way, the velocity field was generated and the continuity and momentum the equations converged easier after the gas switch.

Fig. 6.5 shows the velocity field inside the furnace for different slices corresponding to the radial center of the furnace and the radial center of the two crucibles and parallel to the furnace axis. Since the effective cross section of the furnace is reduced due to the crucibles, the flow rate accelerate and the velocity increase above the crucibles, as shown in Fig. 6.5a. However, because of the different heights of the two crucibles the local axial velocity above them is larger for the smaller crucible, because of the lower resistance to the gas flow, instead of the higher crucible. Figs. 6.6 shows a detailed view of the velocity field around and inside the crucibles. However, in both cases the local gas velocity approaches to zero at the surface of the crucible.
Fig 6.7 shows a 3D representation of the velocity field inside the furnace.

6.6.2 Carbon dioxide concentration field

When the gas flow is switched from N_2 to CO_2, an axial carbon dioxide profile is established due to convection and diffusion. The reactant does not move forward to the crucible with an uniform front due to diffusion. In this way, it takes some time for the bulk concentration to reach the reactive surface of the crucible. Figs. 6.8 and 6.9 show the CO_2 reactant front at the first instants after the gas switch. As time progresses, the surface of the crucible is progressively reached CO_2 whose concentration gradually increases. The bulk front of carbon dioxide requires about $3 \div 4$ s to reach the crucible position. Afterwards, the only concentration gradient is due to the surface reaction as shown in Fig. 6.9c.

6.6.3 Surface reaction

The carbonation reaction occurs at the surface of the smaller crucible according to Eq. (6.2). The goal of the analysis is to study the reaction dependence on the external mass transfer. In fact, because the carbonation reaction shows a fast reaction rate, the limiting step is the CO_2 mass transfer from the bulk to the surface of the reaction. Thus, a parametric study was performed varying the total flow rate at 650 °C, 1 bar and 100 % of CO_2. The results are reported in Fig. 6.10a which shows the CO_2 mole fraction profile at the reaction surface (average value) vs

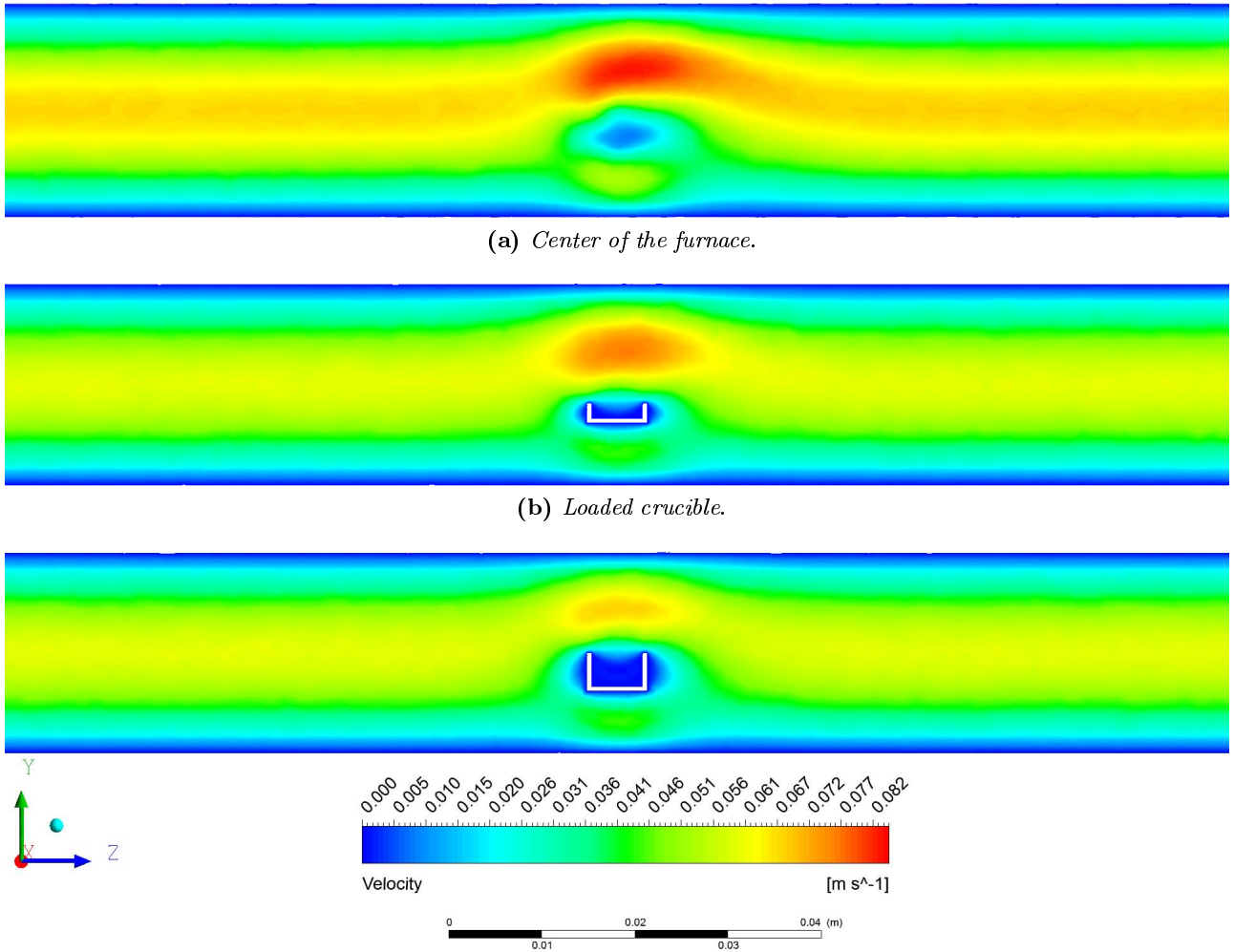

(a) *Center of the furnace.*

(b) *Loaded crucible.*

(c) *Empty crucible.*

Figure 6.5: Velocity contours along different planes. 650 °C, 1 bar, 100 % in CO_2 and 250 $Ncm^3\,min^{-1}$.

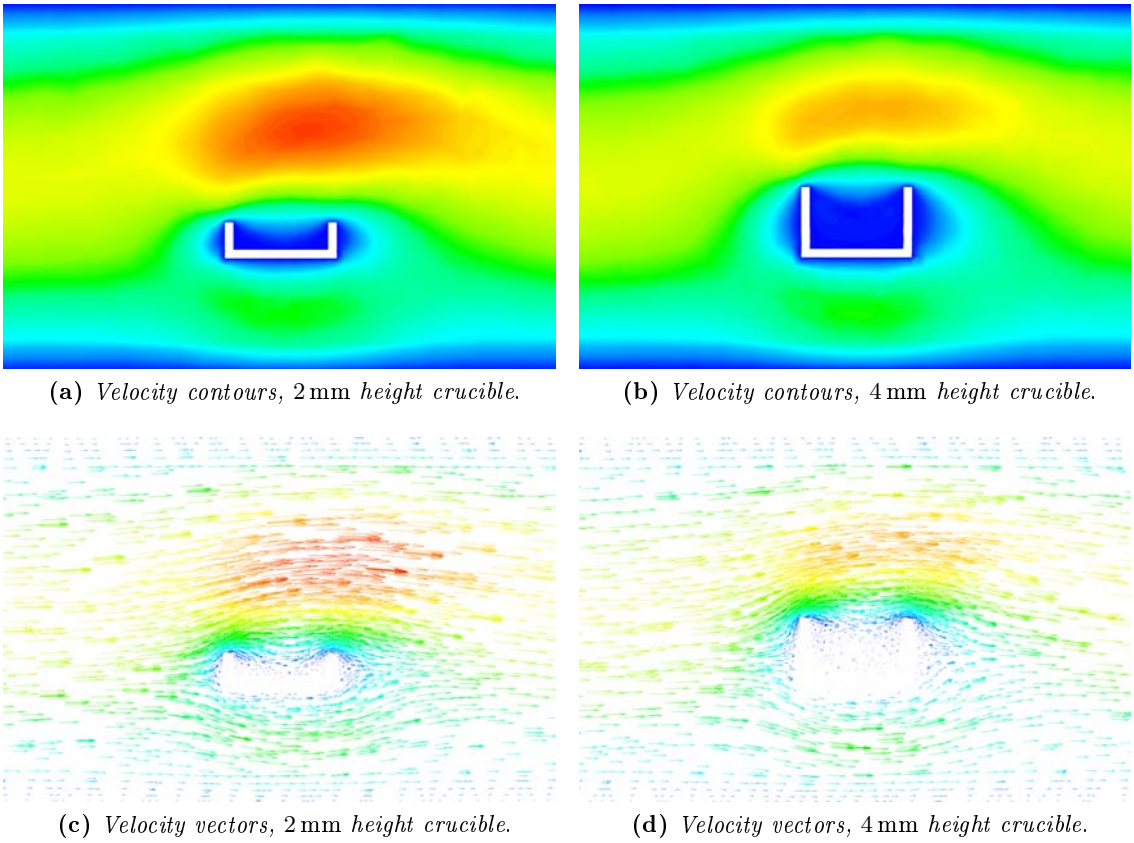

(a) *Velocity contours,* 2 mm *height crucible.*

(b) *Velocity contours,* 4 mm *height crucible.*

(c) *Velocity vectors,* 2 mm *height crucible.*

(d) *Velocity vectors,* 4 mm *height crucible.*

Figure 6.6: Predicted velocity field around and inside the two crucibles. 650 °C, 1 bar, 100 % in CO_2 and 250 $Ncm^3\,min^{-1}$.

time for various flow rates. The mole fraction vs time curves are the result of the incoming CO_2 from the bulk flow and the reactant consumption due to the reaction. According to Figs. 6.8 and 6.9 the carbon dioxide profile at the reaction surface increases as long as the bulk front arrives at the crucible. Afterwards, the mole fraction profile change in slope and monotonically increases up to reach the bulk composition at the end of the reaction. These phenomena can be increased by imposing a smaller mass of reactant in the crucible. Clearly, this profile can not be predicted without a CFD simulation and the constant CO_2 bulk concentration at the reaction surface becomes a rough assumption for the horizontal TGA as the TA SDT Q600.

The CO_2 profile vs time influences the reaction kinetics because the reaction rate depends on the local reactant concentration (according to Eq. (6.2)). Thus, the conversion time curves obtained from the simulations are shown in Fig. 6.10b. The figure shows the apparent kinetic rates for various flow rates compared to the solution of Eq. (6.2) that represents the intrinsic kinetics. Even if the gas flow rate is increased up to 1000 $Ncm^3\,min^{-1}$ (that is the maximum flow rate permitted of the TA SDT Q600), the conversion time curve is drastically conditioned by the flow regime. Clearly, this reaction rate is an apparent kinetic rate that depends on the external mass transfer. Specifically, the intrinsic conversion-time curve has an initial slope of 0.284 s^{-1} whereas at 1000 $Ncm^3\,min^{-1}$ the apparent kinetics has a initial slope of about 0.074 s^{-1} that is significantly low respect to the intrinsic. However, the recommended flow rate suggested by the

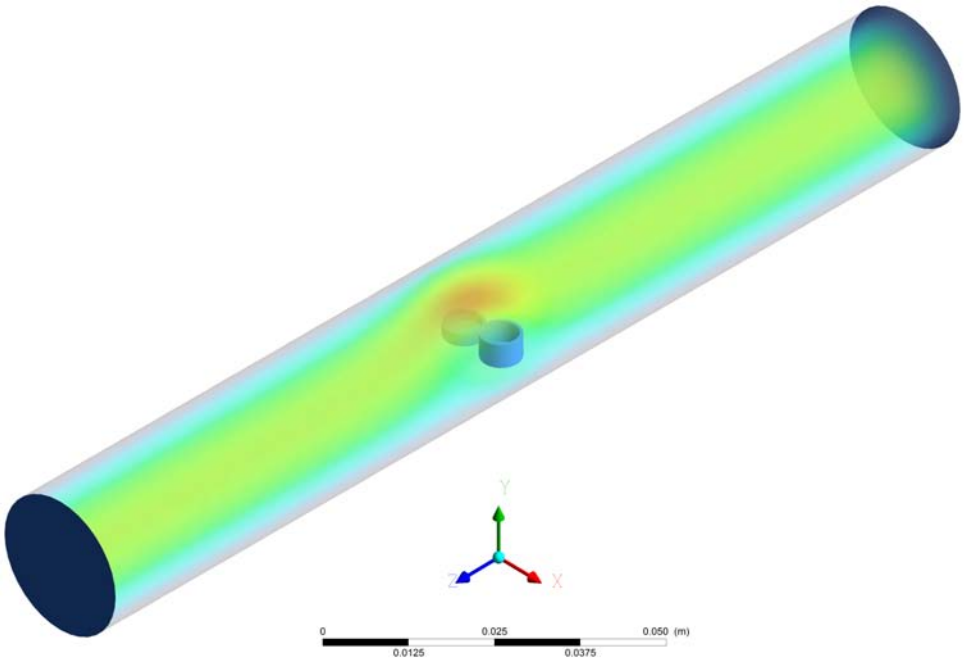

Figure 6.7: A three-dimensional representation of the velocity field. 650 °C, 1 bar, 100 % in CO_2 and 250 $Ncm^3\,min^{-1}$.

constructor of the TA SDT Q600 is about 100 $Ncm^3\,min^{-1}$, for which the slope of the apparent kinetic rate is about 0.032 s^{-1}.

6.7 Discussion

In this chapter the horizontal TGA TA SDT Q600 was considered in order to study the fluid-dynamics inside the furnace while the CO_2 carbonation reaction occurs assuming a first order kinetics. In this type of TGA, the computed conversion-time curves depend on the operative conditions of the experiment, such as the gas flow rate. Thus, an apparent kinetic rate is obtained of instead the intrinsic kinetics.

Several informations were obtained from the CFD simulations. The first is the complexity of velocity field inside the TGA furnace, especially around and inside the crucible, in which the gas flows with a very low velocity (that never becomes zero, except at the reaction surface). Thus, the gas reactant arrives at the reactive surface with both convective and diffusive components. In this way, the assumption of stagnant gas is a rough approximation that could underestimate the reactant mass transfer from the bulk to the crucible.

Consequently, when the gas flow switches from the inert gas (N_2) to the reactant (CO_2), at the reaction surface the CO_2 concentration gradually increases up to reaching of the bulk concentration. In the meanwhile, the reaction occurs with a reactant concentration that can be significantly lower than the bulk one. If the kinetic is fast the whole reaction may occur with a low time-variable reactant concentration and the conversion-time curve may be different from the curves obtained from the intrinsic kinetics due to the non-stationary local conditions.

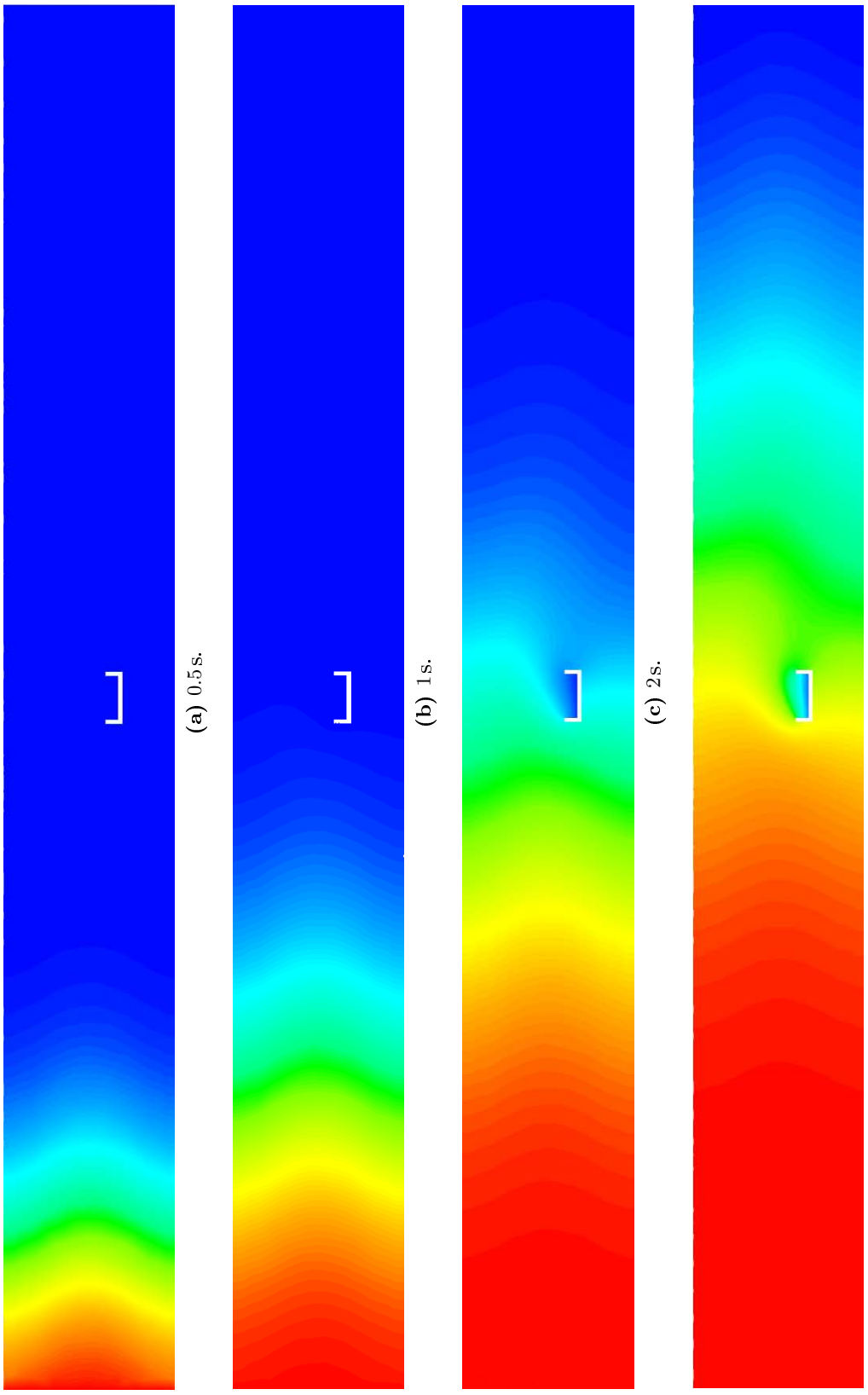

(a) 0.5 s. **(b)** 1 s. **(c)** 2 s. **(d)** 3 s.

Figure 6.8: Contours of the CO_2 mass fraction in the first seconds of the simulation. 650 °C, 1 bar, 100 % in CO_2 and 250 $Ncm^3 min^{-1}$.

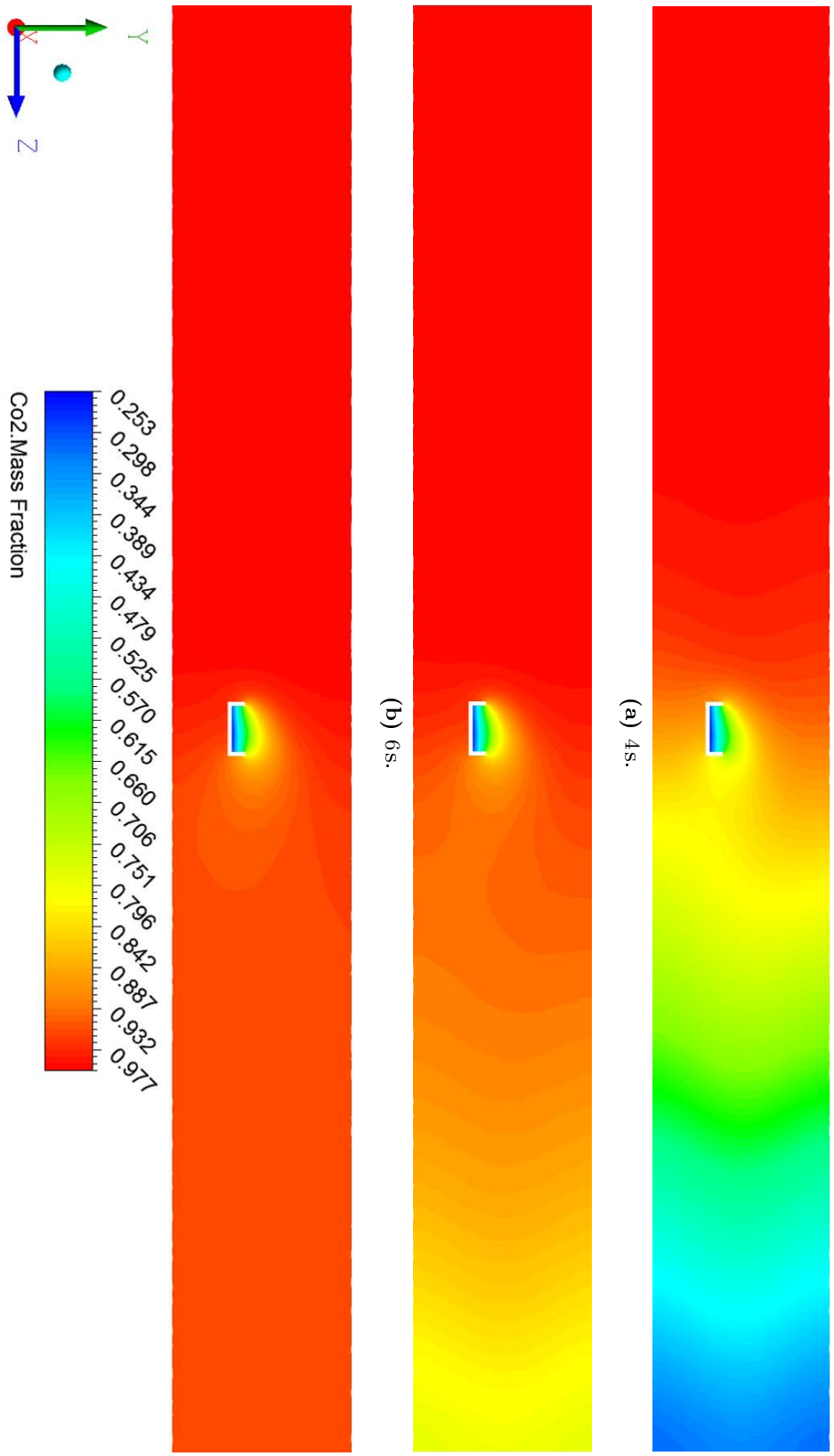

(a) 4 s. (b) 6 s. (c) 12 s.

Figure 6.9: Contours of the CO_2 mass fraction in the first seconds of the simulation. 650 °C, 1 bar, 100 % in CO_2 and 250 $Ncm^3 min^{-1}$.

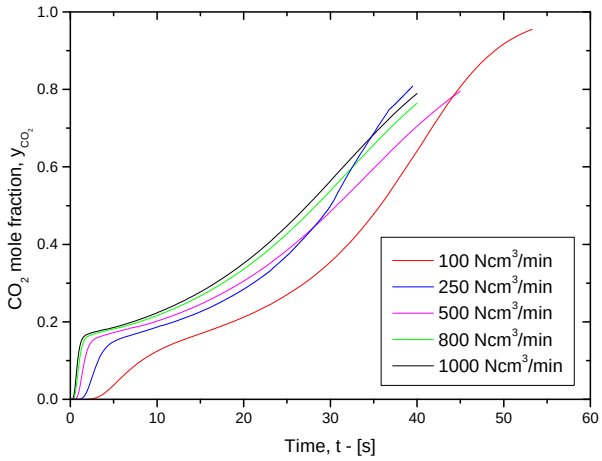

(a) *CO_2 mole fraction profiles vs time.*

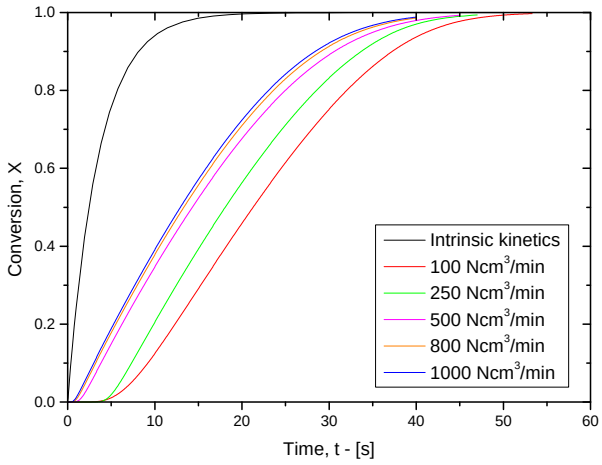

(b) *Conversion vs time curves.*

Figure 6.10: Simulation results of the conversion-time curves and the CO_2 mole fraction at the crucible reaction surface (average value) varying the flow rate. 650 °C, 1 bar, 100 % in CO_2.

If the local reactant concentration is assumed to be constant and equal to the bulk, the estimated kinetic parameters from the experimental data may be strongly affected by the operative conditions. These effects may increase when using more solid reactant mass. In this case the reaction itself severally affects the local reactant mass balance.

However, this study presents a few limitations. First, the reactive gas tube was neglected as well as the flow expansion from the outlet of the reactive gas tube to the furnace. When the gas flow rate is low this assumption is reasonable and the velocity field does not differ form the real situation. On the other hand, if large flow rates are used the sudden expansion from the reactive gas tube to the furnace cannot be neglected and the velocity field may significantly differ from the results obtained from this study. Future developments of this works will include a more detailed simulation of the gas expansion inside the furnace. Particularly, in this case the meshing process become critical because a large number of computational cells are required.
Another important assumption was made on the kinetic rate of the carbonation reaction. The

equilibrium conditions and the switch from the two reaction order between order zero/first order kinetics were neglected and should be future CFD simulations to obtain more accurate results.

Conclusions

The carbon dioxide capture with calcium based solid sorbents is a promising technology to reduce the CO_2 emissions from fossil fuel combustion power plants, that is included in the Carbon Capture and Storage (CCS) processes. This technology is considered part of a mitigation strategy of the unequivocal global scale climate change and is based on the CO_2 carbonation reaction.

This work of thesis deals with the kinetics of the CO_2 carbonation reaction that is classified as a non-catalytic gas solid reaction. As such reaction progresses the solid reactant is gradually consumed and the structural properties of the solid phase (namely, the porosity and the specific surface of the reactant in the particle) change.

More specifically, as the reaction occurs a calcium carbonate layer is progressively generated and interposes between the calcium oxide solid reactant and the gas phase (carbon dioxide). Since the molar volume of the product layer is larger than the reactant one, each pore of the particle shrinks down to closure. In this way, the active reaction surface and the particle porosity reduce until pore closure is reached. Consequently, this reaction is characterized by incomplete conversion because of the loss in particle porosity due to pore closure. Referring to the carbonation reaction, the literature contributions commonly describe the conversion-time curves composed by two steps: a rapid kinetic controlled one followed by a slower second one at high conversions. Indeed, the transition between the kinetic regime to the product layer diffusivity occurs suddenly due to a drastic change in the pore structure. This feature is attributed to the closure of the smaller pores that contribute more to the reactive surface area but are the first to reach the closure.

Since the structural properties of the porous phase evolve during the reaction, a kinetic model must include these features in order to account for specific surface and porosity changes and pore closure. These models are named "structural models". During the 20^{th} several structural models were developed in literature in order to represent the conversion-time curves of such reactions. Therefore, in this work the advantages and the drawbacks of each model (grain models and pore models) were studied in order to identify the most appropriate one to represent the carbonation kinetics.

The only gas-solid reaction model which was found capable to account for pore closure, pore overlapping and for the abrupt transition from a kinetic regime to the product layer diffusion regime is the Random Pore Model (RPM) development independently by Bhatia [10] and Sotirchos et al. [57]. The model development is based on the assumption that the reaction and pore

surfaces are described by a population of growing or shrinking overlapping cylinders co-axial with the original pore distribution.
Consequently, this RPM was selected to represent the kinetic behaviour of the carbonation reaction.

According to Sun et al. [59, 58] the carbonation kinetic rate switches its reaction order from first to zero depending on the CO_2 partial pressure. Thus, the RPM developed by Bhatia [10] and Sotirchos et al. [57] was modified in order to include the reaction order switch and the equilibrium condition. A log-normal functional form was used for the pore size distribution which requires three parameters: the particle porosity, the mean and the variance of pore radius. These quantities were estimated by fitting the N_2 adsorption data of the calcined samples. This modified RPM was applied to experimental data on the carbonation reaction. The results shows that this model represents accurately the whole conversion-time curve (obtained experimentally at 5 bar of CO_2) in terms of kinetic regime and product layer diffusion regime. Also the abrupt transition due to pore closure is well represented. Furthermore, the model capability to simulate the experimental data is high even at the first instants of the reaction. Such degree of detail was never be explored in the literature on the carbonation. Indeed, this RPM with a continuous pore size distribution was never applied before to carbonation reaction.
However, the pore size distribution was not known for the CaO samples used in the TGA experiments. Consequently, the distribution parameters were estimated from typical N_2 adsorption results for CaO calcined samples, except for the porosity. In fact, this parameter was selected in order to represent the final experimental conversion and the chosen values are lower respect to the typical particle porosities. Additionally, the calculated specific surfaces are larger than the experimental measurements. On the other hand, the imposed kinetic constant is about half of the value of Sun et al. [59] which balances the high specific surface. The future development of this work will require to improve the agreement with the experimental porosity and the literature kinetic constant.

A similar work was proposed by Sun et al. [58], in which a discrete pore size distribution was used. This approach works fine when a large number of classes are used and this means a large number of experimental points in terms of N_2 adsorption. On the other hand, if few classes are used in the discrete pore size distribution the predicted conversion may become unphysical.
Finally, the proposed modified RPM is relevant because it can predict the conversion-time curve for the carbonation reaction once the initial pore size distribution of the CaO, the kinetic constant and the product layer diffusivity are known.

The intra-particle diffusion was also considered and applied to the carbonation reaction. The analysis considers the coupling between the proposed modified RPM that accounts for pore closure and the intra-particle diffusion. The intra-particle diffusion effects increase when large particle size are used, when the kinetics of the gas-solid reaction is fast compared to the diffusion inside the particle, when the CO_2 partial pressure is low and when the mean pore radius is small. However, the model simulations demonstrate that even when small particles are used the intra-particle diffusion may still be significant. In fact, when pore shrinking or pore closure occur at the external shell of the particle, the gaseous reactant diffusivity decreases and the intra-particle

diffusion may decrease and thus becomes controlling.
This model is relevant because no literature contribution applied simultaneously the intra-particle diffusion and the RPM accounting for pore closure to the carbonation reaction. In the previous literature studies the influence of the intra-particle diffusion was verified using the Thiele modulus, but this dimensionless number does not account for the pore closure (and for the pore size distribution). In this way, the influence of intra-particle diffusion is strongly be underestimated for the carbonation reaction.
Because of some oscillations of the numerical method used, the future developments of this work will require an investigation of the causes of these oscillations and an improvement of the stability and the efficiency of the method.

The experimental conversion-time curves of the carbonation reaction were obtained using a termogravimetric analyzer (TGA). This type of analysis can be affected by several mass-transfer resistances, such as: external mass transfer, inter-particle mass diffusion and intra-particle mass diffusion.
Consequently, if these resistance are not reduced or accounted for through accurate models, the measured kinetic rate may differs from the intrinsic kinetics of the reaction, especially when a fast reaction is analysed.

The intra-particle diffusion can be reduced experimentally by loading a small amount of sample. Instead, the external diffusion cannot always be neglected, even if the TGA is operated at high flow rates. When a fast gas-solid reaction takes place in a TGA instrument, the mass transfer from the bulk to the surface of the reactant (external diffusion) may become the controlling mechanism. Specifically, this effect was investigated considering the horizontal TGA systems. A CFD study was developed in which the TGA (TA SDT Q600) geometry was replicated and the carbonation reaction was assumed to occur at the surface of a crucible with a first order dependence on the local CO_2 concentration.
Additionally, the geometry was simplified by neglecting the reactive gas tube from which the gas flow is fed as well as the balance beams and the tapering zone.
A parametric study was performed varying the flow rate up to the maximum limits of the TGA (that is $1000\,\mathrm{Ncm^3\,min^{-1}}$); even at high flow rate the regime was laminar. The CFD simulation result show that the reactant front moves forward to the crucible with both convective and diffusion components. Thus, the CO_2 concentration profile at the crucible surface never reaches stationary condition. In this way, the fast carbonation reaction occurs with a non constant concentration profile the resulting kinetic rate is slower with respect to the reaction that occurs at the bulk concentration (that is reached only asymptotically). The conversion-time curves obtained from the simulations are compared with the intrinsic kinetic rate (evaluated at the bulk concentration). The results shows that the apparent kinetic rates are strongly influenced by the gas flow rate and are significantly slower respect to the intrinsic kinetics. This effects may increase when larger solid reactant mass is used.
The assumption that the gas flow rate is not fed from the gas reactive tube may become a rough approximation especially at high flow rates. In fact, even if the flow rate regime inside the reactive tube is laminar, the gas velocity is high because of the small diameter of the pipe.

However, the recommended flow rate suggested by the constructor of the TA SDT Q600 is about $100\,\mathrm{Ncm^3\,min^{-1}}$ for which the expansion effect of the reactive tube may be likely low.
The future development of the TGA CFD study will require the investigation of the sudden expansion of the gas flow rate from the reactive gas tube. Moreover, the modified RPM presented in this work of thesis should be considered to check the fluid dynamics effects on the two stage and order switching reaction rate of the carbonation. Once intra-particle diffusion will be included as well, the CFD simulations will likely represent the complete physics inside the termogravimeter analysis.

Nomenclature

a, b	=	stoichiometric coefficients
a_0	=	dimensionless pore radius
A_k	=	pre-exponential factor of the Arrhenius'law
A_D	=	pr-exponential factor of the Arrhenius'law for product layer diffusivity - m^2/s
a_{SRK}	=	constant of the Soave-Redlich-Kwong
$a_{\mathrm{SRK,mix}}$	=	constant of the Soave-Redlich-Kwong for mixture
$b_{LN}^{(E)}$	=	parameter distribution of the non-overlapped system
$b_{LN}^{(0)}$	=	parameter distribution of the overlapped system
b_{SRK}	=	constant of the Soave-Redlich-Kwong
$b_{\mathrm{SRK,mix}}$	=	constant of the Soave-Redlich-Kwong for mixture
C_A	=	molar concentration of species A - $\mathrm{mol\,m^{-3}}$
$C_{A\,\mathrm{bulk}}$	=	bulk molar concentration of species A - $\mathrm{mol\,m^{-3}}$
$C_{A,c}$	=	molar concentration of species A at the core surface - $\mathrm{mol\,m^{-3}}$
$C_{A,eq}$	=	equilibrium molar concentration of species A - $\mathrm{mol\,m^{-3}}$
$C_{A,g}$	=	molar concentration of species A inside the grain - $\mathrm{mol\,m^{-3}}$
$C_{A,g}^{s}$	=	molar concentration of species A at the surface of the grain - $\mathrm{mol\,m^{-3}}$
$C_{A,\,\mathrm{int}}$	=	molar concentration of species A at the interface - $\mathrm{mol\,m^{-3}}$
$C_{A,\,\mathrm{int}}^{p}$	=	molar concentration of species A at the pore interface - $\mathrm{mol\,m^{-3}}$
$C_{A,\,\mathrm{int}}^{s}$	=	molar concentration of species A at the surface reaction interface - $\mathrm{mol\,m^{-3}}$
$\mathscr{D}_{\mathrm{eff}}$	=	effective diffusivity - m^2/s
$\mathscr{D}_{\mathrm{eff},0}$	=	initial effective diffusivity - m^2/s
$\mathscr{D}_{\mathrm{eff}}^{p}$	=	effective particle diffusivity - m^2/s
$\mathscr{D}_{\mathrm{global}}$	=	global particle effective diffusivity - m^2/s
$\mathscr{D}_{i,j}$	=	binary molecular diffusivity - m^2/s
$\mathscr{D}_{i,j}$	=	effective binary molecular diffusivity - m^2/s
$\mathscr{D}_{k,i}$	=	Knudsen diffusivity of species i - m^2/s
$\mathscr{D}_{k,i\,\mathrm{eff}}$	=	effective Knudsen diffusivity of species i - m^2/s
D_{pl}	=	product layer diffusivity - m^2/s
$E_{a,D}$	=	activation energy of the product layer diffusion - $\mathrm{kJ\,mol^{-1}}$
$E_{a,k}$	=	activation energy of the reaction - $\mathrm{kJ\,mol^{-1}}$
E_0	=	cumulative pore size distribution
F_ψ	=	product layer diffusion contributor
h	=	radial coordinate

h_p = radial coordinate at the pore surface

h_s = radial coordinate at the reaction surface

k_B = the Boltzmann constant - $1.3806 \times 10^{-23}\,\mathrm{J\,K^{-1}}$

k_s = kinetic constant - $\mathrm{m^4/mol/s}$

$k_{s,p}$ = kinetic constant - $\mathrm{m\,s^{-1}\,Pa^{-1}}$

$k'_{s,p}$ = kinetic constant - $\mathrm{mol\,s^{-1}\,m^{-2}\,Pa^{-1}}$

$k_{\mathrm{SRK},ij}$ = binary parameter of the Soave-Redlich-Kwong

k_v = kinetic constant - $\mathrm{m^3\,mol^{-1}\,s^{-1}}$

k'_v = kinetic constant - $\mathrm{s^{-1}}$

l = differential length size distribution - $\mathrm{m\,m^{-3}}$

l_0 = initial differential length size distribution - $\mathrm{m\,m^{-3}}$

L = total length size per unit of volume - $\mathrm{m\,m^{-3}}$

L_0 = initial total length size per unit of volume - $\mathrm{m\,m^{-3}}$

L_E = total length size per unit of volume for non-overlapped system - $\mathrm{m\,m^{-3}}$

L_{E_0} = initial total length size per unit of volume for non-overlapped system - $\mathrm{m\,m^{-3}}$

m = sample mass - kg

m_{calcined} = sample mass after calcination - kg

M_0 = mean pore radius - $\mathrm{g\,mol^{-1}}$

M_i = molecular weight of specie i - $\mathrm{g\,mol^{-1}}$

MP = melting point - °C

n_i = moles of species i - mole

$n_{i,0}$ = initial moles of species i - mole

N_A = the Avogadro number - $6.0221 \times 10^{23}\,\mathrm{mol^{-1}}$

P = pressure - bar

p_i = partial pressure of specie i - bar

$p_{i,eq}$ = equilibrium partial pressure of specie i - bar

P_c = critical pressure - bar

P_r = reduced pressure

P_r^{sat} = reduced saturation partial pressure

Q_p = obstruction factor

r = pore radius m

r_0 = initial pore radius

r_c = core radius m

r_g = grain radius m

r_p = radius of the pore surface m

r_s = radius of the reaction surface m

R = particle radius - m

R_0 = initial particle radius - m

R_{gas} = the universal constant of gas - $\mathrm{m^3\,Pa\,mol^{-1}\,K^{-1}}$

R_m = solid reactivity - $\mathrm{s^{-1}}$

R_s = reaction rate based per unit of surface area - $\mathrm{mol\,s^{-1}\,m^{-2}}$

R_s = reaction rate based per unit of volume - $\mathrm{mol\,s^{-1}\,m^{-3}}$

S = specific surface per unit of volume - $\mathrm{m^2\,m^{-3}}$
S_0 = initial specific surface per unit of volume - $\mathrm{m^2\,m^{-3}}$
S_c = core surface - m
S_E = distribution function of non overlapped surface area - $\mathrm{m^2\,m^{-3}}$
S_{E_0} = initial distribution function of non overlapped surface area - $\mathrm{m^2\,m^{-3}}$
S_g = specific surface per unit of mass - $\mathrm{m^2\,g^{-1}}$
S_{grain} = grain surface
S_p = total pore surface per unit of volume - $\mathrm{m^2\,m^{-3}}$
t = time - s
T = temperature - °C
T_c = critical temperature - °C
T_r = reduced temperature
v = molar volume - $\mathrm{m^2\,mol^{-1}}$
v_c = critical molar volume - $\mathrm{m^2\,mol^{-1}}$
v_r = reduced molar volume
V = volume enclosed by the reaction surface per unit of volume (overlapped)
V_0 = initial volume enclosed by the reaction surface per unit of volume (porosity)
V_0^{LN} = variance of the log-normal distribution
V_c = core volume
V_E = volume enclosed by the reaction surface in the non-overlapped system
V_{E_0} = initial volume enclosed by the reaction surface in the non-overlapped system
V_g = void volume per unit of weight - $\mathrm{m^3\,g^{-1}}$
$V_{g,0}$ = initial void volume per unit of weight - $\mathrm{m^3\,g^{-1}}$
X = conversion
y, x = molar fraction
$\mathbf{J_{i,j}}$ = molecular flux of i in j - $\mathrm{mol\,m^{-2}\,s^{-1}}$
Z = ratio of the volume of the solid phase after reaction to that before reaction
$\mathbb{Z}$ = compressibility factor
$\mathbb{Z}_c$ = the compressibility factor at the critical conditions
$\mathbb{Z}_{\mathrm{mix}}$ = mixture compressibility factor

Greek Letters

α = coefficient of the Soave-Redlich-Kwong
β = dimensionless number that is the ratio between the kinetic rate and the product layer diffusion
γ_a = constant of the Soave-Redlich-Kwong
γ_b = constant of the Soave-Redlich-Kwong
ΔG_f° = standard Gibbs energy of formation - $\mathrm{kJ\,mol^{-1}}$
ΔH_f° = standard enthalpy of formation - $\mathrm{kJ\,mol^{-1}}$
ΔH_r° = standard enthalpy of reaction - $\mathrm{kJ\,mol^{-1}}$
ε = porosity
ε_0 = initial porosity

$\varepsilon_{LJ,i}$ = a Lennard-Jones parameter - J
ε_p = particle porosity
$\varepsilon_{p,0}$ = initial particle porosity
η_p = dimensionless pore radius
η_s = dimensionless reaction surface radius
λ_i = mean free path of species i - m
λ_p = mean free path equal to $2\,M_0$ - m
μ_{N_0} = mean of the normal distribution of the random variable - $\ln(r_0)$ - Å
ρ_p = solid product density - $\mathrm{g\,m^{-3}}$
$\rho_{p,s}$ = particle density - $\mathrm{g\,m^{-3}}$
ρ_r = solid reactant density - $\mathrm{g\,m^{-3}}$
ρ_s = skeleton density - $\mathrm{g\,m^{-3}}$
$\rho_{s,0}$ = initial skeleton density - $\mathrm{g\,m^{-3}}$
ζ = the extent of reaction
$\sigma_{LJ,j}$ = "collision diameter" of species i (a Lennard-Jones parameter) - Å
σ_{N_0} = variance of the normal distribution of the random variable - $\ln(r_0)$
τ = the factor used to dimensionless time - s
τ_p = particle tortuosity
ϕ_p = particle Thiele modulus
ψ = structural factor of random pore model
ω = acentric factor

Superscript

$\hat{\cdot}$ = dimensionless variable
$\cdot^*$ = refers to reduced variable, i.e. $C_A^* = C_A - C_{A,eq}$
$\tilde{\cdot}$ = extensive variable
$\bar{\cdot}$ = average variable

Bibliography

[1] J. Carlos Abanades and Diego Alvarez. "Conversion Limits in the Reaction of CO_2 with Lime". In: *Energy & Fuels* 17.2 (2003), pp. 308–315.

[2] M. Alonso et al. "Undesired effects in the determination of CO_2 carrying capacities of CaO during TG testing". In: *Fuel* 127.0 (2014), pp. 52 –61.

[3] Diego Alvarez and J. Carlos Abanades. "Determination of the Critical Product Layer Thickness in the Reaction of CaO with CO_2". In: *Industrial & Engineering Chemistry Research* 44.15 (2005), pp. 5608–5615.

[4] Rutherford Aris. "On shape factors for irregular particles - I: the steady state problem. diffusion and reaction". In: *Chemical Engineering Science* 6.6 (1957), pp. 262–268.

[5] Melvin Avrami. "Kinetics of Phase Change. I General Theory". In: *The Journal of Chemical Physics* 7.12 (1939), pp. 1103–1112.

[6] Melvin Avrami. "Kinetics of Phase Change. II Transformation-Time Relations for Random Distribution of Nuclei". In: *The Journal of Chemical Physics* 8.2 (1940), pp. 212–224.

[7] E. H. Baker. "The calcium oxide-carbon dioxide system in the pressure range 1-300 atmospheres". In: *J. Chem. Soc.* (0 1962), pp. 464–470.

[8] Ihsan Barin, Ottmar Knacke, and Oswald Kubaschewski. *Thermochemical properties of inorganic substances: supplement*. Vol. 380. Springer-Verlag Berlin, 1977.

[9] Heleen de Coninck Bert Metz Ogunlade Davidson. *Carbon Dioxide Capture and Storage*. Cambridge University Press, 2005.

[10] S. K. Bhatia. "Analysis of distributed pore closure in gas-solid reactions". In: *AIChE Journal* 31.4 (1985), pp. 642–648.

[11] S. K. Bhatia and D. D. Perlmutter. "A random pore model for fluid-solid reactions: I. Isothermal, kinetic control". In: *AIChE Journal* 26.3 (1980), pp. 379–386.

[12] S. K. Bhatia and D. D. Perlmutter. "A random pore model for fluid-solid reactions: II. Diffusion and transport effects". In: *AIChE Journal* 27.2 (1981), pp. 247–254.

[13] S. K. Bhatia and D. D. Perlmutter. "Effect of the product layer on the kinetics of the CO_2-lime reaction". In: *AIChE Journal* 29.1 (1983), pp. 79–86.

[14] S. K. Bhatia and D. D. Perlmutter. "Unified treatment of structural effects in fluid-solid reactions". In: *AIChE Journal* 29.2 (1983), pp. 281–289.

[15] R.B. Bird, W.E. Stewart, and E.N. Lightfoot. *Transport Phenomena*. Wiley, 2001.

[16] Stephen Brunauer, P. H. Emmett, and Edward Teller. "Adsorption of Gases in Multimolecular Layers". In: *Journal of the American Chemical Society* 60.2 (1938), pp. 309–319.

[17] A. Calvelo and J. M. Smith. "Intrapellet transport in gas-solid non-catalytic reactions". In: *CHEMECA '70*. Vol. 1. 1970.

[18] Jose M. Criado et al. "The effect of the CO_2 pressure on the thermal decomposition kinetics of calcium carbonate". In: *Thermochimica Acta* 254.0 (1995), pp. 121 –127.

[19] Roberto E Cunningham and RJJ Williams. *Diffusion in gases and porous media*. Springer, 1980.

[20] C.C. Dean et al. "The calcium looping cycle for CO_2 capture from power generation, cement manufacture and hydrogen production". In: *Chemical Engineering Research and Design* 89.6 (2011), pp. 836 –855.

[21] A. J. Dedman and A. J. Owen. "Calcium cyanamide synthesis. Part 4.-The reaction CaO + CO_2= $CaCO_3$". In: *Trans. Faraday Soc.* 58 (1962), pp. 2027–2035.

[22] George R. Gavalas. "A random capillary model with application to char gasification at chemically controlled rates". In: *AIChE Journal* 26.4 (1980), pp. 577–585.

[23] Christos Georgakis, CW Chang, and J Szekely. "A changing grain size model for gas-solid reactions". In: *Chemical Engineering Science* 34.8 (1979), pp. 1072–1075.

[24] Gemma Grasa et al. "Application of the random pore model to the carbonation cyclic reaction". In: *AIChE Journal* 55.5 (2009), pp. 1246–1255.

[25] Gemma S. Grasa et al. "Reactivity of highly cycled particles of CaO in a carbonation/calcination loop". In: *Chemical Engineering Journal* 137.3 (2008), pp. 561 –567.

[26] D.W. Green and R.H. Perry. *Perry's Chemical Engineers' Handbook, Eighth Edition*. McGraw Hill professional. McGraw-Hill Education, 2007.

[27] Robert Ian Harker and Orville Frank Tuttle. "Studies in the system CaO-MgO-CO_2; Part 1, The thermal dissociation of calcite, dolomite and magnesite". In: *American Journal of Science* 253.4 (1955), pp. 209–224.

[28] M. Ishida and C.Y. Wen. "Comparison of zone-reaction model and unreacted-core shrinking model in solid-gas reactions - I isothermal analysis". In: *Chemical Engineering Science* 26.7 (1971), pp. 1031 –1041.

[29] J. W. Evans J. Szekely and H. Y. Sohn. *Gas-Solid Reactions*. Ed. by Academic Press. Academic Press, 1976.

[30] O. Knacke, O. Kubaschewski, and K. Hesselmann. *Thermochemical properties of inorganic substances*. Thermochemical Properties of Inorganic Substances v. 1. Springer-Verlag, 1991.

[31] Kyaw Kyaw et al. "Study of Carbonation of CaO for High Temperature Thermal Energy Storage". In: *Journal of Chemical Engineering of Japan* 31.2 (1998), pp. 281–284.

[32] Kyaw Kyaw et al. "Study of Carbonation Reactions of Ca-Mg Oxides for High Temperature Energy Storage and Heat Transformation". In: *Journal of Chemical Engineering of Japan* 29.1 (1996), pp. 112–118.

[33] Normand M. Laurendeau. "Heterogeneous Kinetic of Coal Char Gasification and Combustion". In: *Progress in Energy and Combustion Science* 4 (1978), pp. 221–2270.

[34] Deuk Ki Lee. "An apparent kinetic model for the carbonation of calcium oxide by carbon dioxide". In: *Chemical Engineering Journal* 100 (2004), pp. 71 –77.

[35] O. Levenspiel. *Chemical reaction engineering*. Wiley, 1999.

[36] D.R. Lide. *CRC Handbook of Chemistry and Physics, 84th Edition*. Taylor & Francis, 2003.

[37] Wen Liu et al. "An investigation of the kinetics of CO_2 uptake by a synthetic calcium based sorbent". In: *Chemical Engineering Science* 69.1 (2012), pp. 644 –658.

[38] Seymour Lowell. *Characterization of porous solids and powders: surface area, pore size and density*. Vol. 16. Springer, 2004.

[39] B. Arias M. E. Diego and J.C. Abanades. "Modeling the solids circulation rates and solids inventories of an interconnected circulating fluidized bed reactor system for CO_2 capture by calcium looping". In: *Chemical Engineering Journal* 198-199 (2012), pp. 228 –235.

[40] Thilakavathi Mani, Nader Mahinpey, and Pulikesi Murugan. "Reaction kinetics and mass transfer studies of biomass char gasification with CO_2". In: *Chemical Engineering Science* 66.1 (2011), pp. 36 –41.

[41] Rotraut Merkle and Joachim Maier. "On the Tammann-Rule". In: *Zeitschrift fr anorganische und allgemeine Chemie* 631.6-7 (2005), pp. 1163–1166.

[42] Derek Mess, Adel F. Sarofim, and John P. Longwell. "Product Layer Diffusion during the Reaction of Calcium Oxide with Carbon Dioxide". In: *Energy & Fuels* 13.5 (1999), pp. 999–1005.

[43] Wendell G. Oakeson and Ivan B. Cutler. "Effect of CO_2 Pressure on the Reaction with CaO". In: *Journal of the American Ceramic Society* 62.11-12 (1979), pp. 556–558.

[44] P. Ollero et al. "Diffusional effects in {TGA} gasification experiments for kinetic determination". In: *Fuel* 81.15 (2002), pp. 1989 –2000.

[45] Laura A. Pellegrini et al. "Prediction of vapor-liquid equilibrium for reservoir mixtures with cubic equations of state: Binary interaction parameters for acidic gases". In: *Fluid Phase Equilibria* 326.0 (2012), pp. 45 –49.

[46] E. E. Petersen. "Reaction of porous solids". In: *AIChE Journal* 3.4 (1957), pp. 443–448.

[47] Bruce E Poling et al. *The properties of gases and liquids*. Vol. 5. McGraw-Hill New York, 2001.

[48] J.M. Prausnitz, R.N. Lichtenthaler, and E.G. de Azevedo. *Molecular Thermodynamics of Fluid-Phase Equilibria*. Prentice-Hall international series in the physical and chemical engineering sciences. Pearson Education, 1998.

[49] Terry Renner. *Quantities, Units and Symbols in Physical Chemistry*. Ed. by E Richard Cohen et al. The Royal Society of Chemistry, 2007.

[50] Lydie Rouchon, Loic Favergeon, and Michele Pijolat. "Analysis of the kinetic slowing down during carbonation of CaO by CO_2". In: *Journal of Thermal Analysis and Calorimetry* 113.3 (2013), pp. 1145–1155.

[51] C.N. Satterfield. *Mass transfer in heterogeneous catalysis*. M.I.T. Press, 1970.

[52] W.E. Schiesser. *The Numerical Method of Lines: Integration of Partial Differential Equations*. Academic Press, 1991.

[53] T. Shimizu et al. "A Twin Fluid-Bed Reactor for Removal of CO_2 from Combustion Processes". In: *Chemical Engineering Research and Design* 77.1 (1999), pp. 62 –68.

[54] Giorgio Soave. "Equilibrium constants from a modified Redlich-Kwong equation of state". In: *Chemical Engineering Science* 27.6 (1972), pp. 1197 –1203.

[55] Susan Solomon. *Climate change 2007, The physical science basis: Working group I contribution to the fourth assessment report of the IPCC*. Vol. 4. Cambridge University Press, 2007.

[56] Qiang Song et al. "Influence of Diffusion on Thermogravimetric Analysis of Carbon Black Oxidation". In: *Energy & Fuels* 20.5 (2006), pp. 1895–1900.

[57] Stratis V. Sotirchos and Huei-Chung Yu. "Mathematical modelling of gas-solid reactions with solid product". In: *Chemical Engineering Science* 40.11 (1985), pp. 2039 –2052.

[58] Ping Sun et al. "A discrete-pore-size-distribution-based gas-solid model and its application to the CaO+CO_2 reaction". In: *Chemical Engineering Science* 63.1 (2008), pp. 57 –70.

[59] Ping Sun et al. "Determination of intrinsic rate constants of the CaO-CO_2 reaction". In: *Chemical Engineering Science* 63.1 (2008), pp. 47 –56.

[60] J Szekely and JW Evans. "A structural model for gas-solid reactions with a moving boundary". In: *Chemical Engineering Science* 25.6 (1970), pp. 1091–1107.

[61] J. Szekely and JW Evans. "Studies in gas-solid reactions: Part I. A structural model for the reaction of porous oxides with a reducing gas". In: *Metallurgical Transactions* 2.6 (1971), pp. 1691–1698.

[62] D. Qin T. F. Stocker. *Climate change 2013: The physical science basis*. Cambridge University Press, 2013.

[63] EW Thiele. "Relation between catalytic activity and size of particle". In: *Industrial & Engineering Chemistry* 31.7 (1939), pp. 916–920.

[64] N. Wakao and J.M. Smith. "Diffusion in catalyst pellets". In: *Chemical Engineering Science* 17.11 (1962), pp. 825 –834.

[65] Y.S. Yu et al. "Modeling of the carbonation behavior of a calcium based sorbent for CO_2 capture". In: *International Journal of Greenhouse Gas Control* 10.0 (2012), pp. 510 –519.

Ringraziamenti

Nel concludere questo lavoro di tesi vorrei ringraziare tutte quelle persone che mi hanno aiutato, sostenuto e incoraggiato in questi anni e, in particolar modo, nel periodo di tesi.
Il mio primo pensiero va ai miei genitori, che hanno permesso di realizzare il mio sogno di diventare ingegnere. A loro va il mio primo grazie e la mia infinita gratitudine per avermi sempre sostenuto e spronato in tutti questi anni malgrado le difficoltà incontrate, certi del mio impegno nel portare a termine questo percorso. Dedico a loro il mio entusiasmo e la mia soddisfazione nel essere diventato "dottore", sicuro che tutto questo non sarebbe stato possibile senza il loro sostegno.
Un grazie di cuore a mio fratello Stefano per essere stato un punto di riferimento costante specialmente in quest'ultimo periodo. Grazie per non avermi mai negato l'aiuto di cui avevo bisogno malgrado gli importanti impegni di lavoro.
Il mio pensiero va poi a Francesco, il bambino che in questi anni ho visto crescere e diventare ragazzo, e che ormai è diventato fin troppo alto per essere chiamato "fratellino". Grazie per l'entusiasmo e la vitalità che ti hanno sempre contraddistinto e che sono state per me fonte d'ispirazione e stimolo per i miei studi.
Ringrazio la nonna Margherita sempre pronta ad offrirmi un buon caffè, sicura che avrei trovato la carica necessaria per studio. Sono certo che in questo momento saresti entusiasta e orgogliosa di me.
Ringrazio con tutto il cuore Mario e Pina, che mi hanno accolto come un figlio. Li ringrazio della loro calda ospitalità che mi ha fatto sentire più a casa. A loro va la mia riconoscenza più sincera per l'impagabile aiuto che mi hanno dato.
Sarebbe stato impensabile affrontare tutto questo senza i miei amici, che mi hanno accompagnato in questi anni: Matteo, il mio compagno di stanza; Antonio, che ancora adesso stento a capire; Gauli e suo infinito entusiasmo; Tito e Lorenzo, anche se ora si trovano distanti centinaia di chilometri. Grazie di cuore per aver reso la mia permanenza a Padova più serena.
Un sincero grazie va a Paolo per tutto l'aiuto e i buoni consigli che mi ha sempre fornito. Anche se ci siamo incontrati alla fine, spero sia l'inizio di una bella amicizia.
Ringrazio Andrea per il sostegno che in questi ultimi tempi mi ha generosamente fornito. Un "in bocca al lupo" per la tua discussione e laurea.
Un grazie sincero ad Alberto per avermi seguito nei primi mesi di tesi e per lo sforzo fatto nell'introdurmi gli argomenti. Grazie per il tuo sostegno che mi hai sempre dato e che hai continuato a darmi anche oltreoceano.

Uno speciale ringraziamento va al prof. Strumendo. Grazie della sua infinita pazienza che ha sempre avuto nei miei confronti, grazie per avermi insegnato che anche le sfide più difficili e insormontabili possono essere vinte con l'impegno e la dedizione. Grazie per avermi sempre spronato a fare il massimo, grazie per il sostegno e l'aiuto che mi ha costantemente dato in tutti questi mesi di tesi.
Per ultimo, ma non per questo meno importante, va il mio più sentito grazie alla mia Roberta che mi ha sempre capito, difeso e spronato, specie in quest'ultimo periodo. Grazie per esserci stata anche nei momenti più difficili, grazie per non aver mai dubitato delle mie capacità, grazie per il tuo immenso aiuto e sostegno, grazie per essere semplicemente quella giusta.

Padova, 18 luglio 2014

Alberto Benedetti